# Dynamics of Bose-Einstein Condensation

**MATTHEW JOHN DAVIS**

A thesis submitted in partial fulfillment of
the requirements for the degree of
Doctor of Philosophy at the University of Oxford

St John's College
University of Oxford
Hilary Term 2001

# DYNAMICS OF BOSE-EINSTEIN CONDENSATION

Matthew John Davis, St John's College.

Thesis submitted for the degree of Doctor of Philosophy
at the University of Oxford, Hilary Term 2001.

## ABSTRACT

This thesis is concerned with the dynamics of thermal Bose-Einstein condensates with two main areas of emphasis.

We summarise the development of the quantum kinetic theory of C. W. Gardiner, P. Zoller, and co-workers, and in particular its application to the problem of condensate growth. We extend an earlier model of the growth of a Bose-Einstein condensate to include the full dynamical effects of the thermal cloud by numerically solving a modified quantum Boltzmann equation. We find that the results can be easily interpreted by introducing an effective chemical potential for the thermal cloud. Our new results are compared with the earlier model and with the available experimental data. We find that in certain circumstances there is still a discrepancy between theory and experiment.

Beginning with the second-quantised many-body Hamiltonian we develop an approximate formalism for calculating the dynamics of a partially condensed Bose gas. We divide the Hilbert space into a highly-occupied coherent region described by a Gross-Pitaevskii equation, and an incoherent region described by a kinetic equation. We discuss the interpretation of the terms in the equations, and their relevance to recent experiments in the field.

We numerically solve the projected Gross-Pitaevskii equation we derive, and find that it evolves strongly non-equilibrium states towards equilibrium. We analyse the final distributions in terms of perturbative equilibrium theories, and find that the two approaches are in excellent agreement in their range of validity. We are therefore able to assign a temperature to the numerical simulations. However, the presently available equilibrium theories fail near the critical region, whereas the projected Gross-Pitaevskii equation remains valid throughout the Bose-Einstein condensation phase transition as long as the relevant modes remain highly occupied. This suggests that the equation will be useful in studying the role of vortices in the critical region, and the shift of the transition temperature with the atomic interaction strength.

# ACKNOWLEDGEMENTS

Over the past three and a bit years many people have helped make my life that little bit easier and more enjoyable.

Firstly, my heartfelt thanks go to Prof. Keith Burnett for his encouragement, humour, and emotional support. He always made me feel an important part of the team, and I greatly appreciate his friendship.

I have learnt a lot from working with Prof. Rob Ballagh and Prof. Crispin Gardiner, and would like to thank them both for being so patient with me. I hope that I can continue to interact with them in the future.

I have benefited greatly from countless discussions with Dr. Sam Morgan, and would like to thank him for putting up with my ignorance. He is the person responsible for all the errors in this thesis, as he was in charge of the proof-reading. (Cheers!)

I would like to thank all the stalwarts of the Burnett group during my time in Oxford. Dr. David Hutchinson, Dr. Martin Rusch, Dr. Stephen Choi, Jacob Dunningham and Mark Lee have all made the Clarendon a stimulating environment in which to work. David deserves a special mention for consistently lowering the tone of conversation (along with Dr. John Watson, gone but not forgotten).

I would also like to mention all the newcomers, who have ensured that I will miss Oxford when I leave. Thanks to Dr. Thomas Gasenzer, Dr. Vicki Ingamells, Dr. Thorsten Koehler, David Roberts, Alex Rau, Peter Kasprowicz and Karen Braun-Munzinger.

I have enjoyed interacting with all the BEC experimentalists, including Dr. Chris Foot, Dr. Jan Arlt, Onofrio Maragò, Eleanor Hodby, and Gerald Heckenblaikner. I would also like to thank the atom opticians: Dr. Gil Summy, Dr. Rachel Godun and Dr.(?) Michael D'Arcy.

I am grateful to the Clarendon laboratory for the use of facilities; and the

Commonwealth scholarship and St John's College for financial support.

Of course, I greatly appreciate the love and support of family. Thanks to Jonathan, for never letting me forget I am a physics geek, and to Mum and Dad for their belief in me, and for encouraging me to get this far.

Finally, I would like to mention my lovely wife Shannon, who has always been at my side emotionally (if not physically) throughout the course of this D. Phil. She has been a great source of motivation, and I would especially like to thank her for looking after me and cheering me up in the final period of writing.

# CONTENTS

# Chapter 1

# Introduction

## 1.1 Indistinguishable particles

In classical mechanics it is possible to label identical particles uniquely by their position and momentum coordinates at any given time. Each individual particle follows a well-defined phase-space trajectory, and although we can form a separate description by exchanging the particle labels, it is of no consequence as the physical predictions remain the same.

In quantum mechanics particles no longer have well-defined trajectories, and the fact that identical particles are indistinguishable has profound effects. If we arbitrarily form a wave function for a many-body system by assigning mathematical labels to each particle, an exchange of these labels can lead to different physical predictions—a situation which is obviously unacceptable.

To obtain unambiguous physical observables we must impose certain symmetries on the many-body wave function. We find that there are two such possibilities—the wave function must be either symmetric or antisymmetric with respect to the exchange of particle labels. This is expressed as

$$\Psi(\ldots \mathbf{r}_i, \ldots, \mathbf{r}_j, \ldots) = \pm\Psi(\ldots \mathbf{r}_j, \ldots, \mathbf{r}_i, \ldots). \tag{1.1}$$

Particles whose wave functions are antisymmetric ($-$) with respect to label exchange are said to obey Fermi-Dirac statistics and are called fermions. Those that are symmetric ($+$) with respect to label exchange obey Bose-Einstein statistics and are called bosons.

The spin-statistics theorem makes a remarkable connection between the intrinsic angular momentum of the particles and the quantum statistics they obey. From considering the relationship between relativity and the symmetry of the wave function, it is possible to deduce that particles with half-integer spin are fermions, while those with integer spin are bosons. The spin-statistics theorem applies rigorously to elementary particles, whereas atoms are composite particles made up of fermions. However, if they contain an even number of electrons and nucleons they will have integer spin. At energies sufficiently low that their internal structure cannot be probed, such atoms will behave as bosons.

The simple requirements on the symmetry of the wave function lead to dramatically different behaviour for the two types of particle. For fermions it results in the Pauli exclusion principle, which forbids the particles from sharing the same quantum state. Bosons, on the other hand, have a tendency to cluster together in the same state. Given suitable conditions this tendency can turn into an avalanche, resulting in the macroscopic occupation of a single quantum level. This phenomenon is a phase transition known as Bose-Einstein condensation (BEC). It is unusual in the fact that it is purely an effect of the quantum statistics, requiring no interaction between the particles themselves.

In 1924 Satyendra Nath Bose derived the Planck distribution by considering the statistics of a collection of photons [1]. A year later, Einstein utilised de Broglie's new ideas about matter waves to extend this work to massive particles [2, 3]. He realised that as the number of particles in a system must be conserved, this implied the existence of the phase transition that now famously bears his name.

## 1.2 BEC in an ideal gas

A discussion of BEC in an ideal gas can be found in most textbooks on statistical mechanics [4]. It is a useful illustration of the features of the transition, and we summarise the details in this section.

The system under consideration is a gas of $N$ non-interacting bosons with mass $m$ in a box of volume $\Omega$. We are interested in the thermodynamic properties of the system at a temperature $T$. The mean number of particles in a single quantum level $k$ is given by the Bose-Einstein distribution

$$f(\varepsilon_k) = \frac{1}{z^{-1}e^{\beta\varepsilon_k} - 1}, \tag{1.2}$$

where $\varepsilon_k$ is the energy of the level, $\beta = 1/k_BT$, $k_B$ is the Boltzmann constant, and $z$ is the fugacity of the system, related to the chemical potential $\mu$ by $z \equiv e^{\beta\mu}$. The chemical potential is the energy required to add a particle to the system at constant volume and entropy. It is uniquely determined by the constraint on the number of particles

$$N = \sum_k f(\varepsilon_k). \tag{1.3}$$

We can see that the chemical potential must always be less than the lowest energy level of the system, otherwise this state would have a negative occupation number. Usually this energy is taken to be zero so that for the ideal gas we have the condition $\mu < 0$.

If the Bose-Einstein distribution function varies slowly on the scale of the energy level spacing of the system, we can approximate the summation of Eq. (1.3) by an integral. We make the replacement

$$N = \sum_k f(\varepsilon_k) \approx \int d\varepsilon \, g(\varepsilon) f(\varepsilon_k), \tag{1.4}$$

where $g(\varepsilon)$ is the density of states of the system, representing the number of quantum levels between $\varepsilon$ and $\varepsilon + d\varepsilon$. For a homogeneous gas this is

$$g(\varepsilon) = \frac{\Omega}{4\pi^2} \frac{2m}{\hbar^2}^{3/2} \varepsilon^{1/2}, \tag{1.5}$$

and its derivation can be found in Ref. [4].

From Eq. (1.2) we see that if $\mu \to 0^-$ (and hence $z \to 1^-$), then the ground state of the system can have a very large occupation, given by $N_0 = z/(1-z)$. In addition, from Eq. (1.5) we find $g(0) = 0$. Thus, the ground state population is not well-represented by the integral of Eq. (1.4), and we single it out as

$$N = N_0 + \int d\varepsilon \, g(\varepsilon) f(\varepsilon). \tag{1.6}$$

Performing the integral leaves us with

$$N = N_0 + g_{3/2}(z)\Omega \left( \frac{mk_BT}{2\pi\hbar^2} \right)^{3/2}, \tag{1.7}$$

where the second term on the right-hand side represents the number of excited particles in the system $N^{\mathrm{ex}}$, and $g_{3/2}(z)$ is the Bose function defined by

$$g_{3/2}(z) = \sum_{j=1}^{\infty} \frac{z^j}{j^{3/2}}. \tag{1.8}$$

From Eq. (1.2) we can see that the Bose-Einstein distribution is a monotonically increasing function of both $\mu$ and $T$. If our system is cooled, $\mu$ and therefore $z$ must increase to conserve the total number of particles. The interesting feature is that the Bose function of Eq. (1.8) only converges for $|z| \leq 1$. It reaches a maximum of $g_{3/2}(1) = \zeta(3/2) \approx 2.612$, where $\zeta(x)$ is the Riemann zeta function. In the context of Eq. (1.7) we can see that for $\mu \to 0$ (i.e. $z \to 1$ ), at any temperature there is a maximum possible number of excited particles in the system given by

$$N^{\mathrm{ex}}_{\max} = 2.612\Omega \left(\frac{mk_BT}{2\pi\hbar^2}\right)^{3/2}. \tag{1.9}$$

At high temperatures $\mu \ll 0$, and therefore $N^{\mathrm{ex}}_{\max} \gg N$. However, as the system is cooled there will be a critical temperature at which $N^{\mathrm{ex}}_{\max} = N$ given by

$$T_c = \frac{2\pi\hbar^2}{mk_B}\left(\frac{N}{2.612\Omega}\right)^{2/3}. \tag{1.10}$$

Below this temperature the excited states can only accommodate a portion of the total number of particles in the system, so all remaining particles must be in the ground state.

We find that below the critical temperature we have $\mu \sim -1/N_0$, and so Eq. (1.9) gives the *total* number of excited particles in this region. Substituting this into Eq. (1.7) we find how the condensate population varies with temperature

$$\frac{N_0}{N} = 1 - \left(\frac{T}{T_c}\right)^{3/2}. \tag{1.11}$$

This macroscopic occupation of the lowest energy level is the phenomenon of Bose-Einstein condensation. Another characteristic of the system is that the specific heat reaches a maximum at the critical temperature; however, the entropy varies smoothly through this point and therefore BEC in an ideal gas is a continuous phase transition.

The physical significance of BEC can be found by identifying the thermal de Broglie wavelength $\Lambda = (2\pi\hbar^2/mk_BT/)^{1/2}$ of the particles. We find that the requirement for BEC of $T \leq T_c$ can be written as

$$n\Lambda^3 \leq 2.612, \tag{1.12}$$

where $n = N/\Omega$ is the number density. Thus BEC occurs when the de Broglie wave packets of the particles begin to overlap, and their quantum nature becomes important.

## 1.3 Interacting systems

After the observations of Einstein, little happened in the field of BEC until the first experiments on superfluid $^4$He. In 1938 Fritz London made the connection between the strange properties of this system and the phenomenon of BEC [5]. Part of his evidence was that the critical temperature predicted by Einstein's formula, Eq. (1.10), of 3.2 K was not far from the experimentally measured value of 2.17 K. Also, the specific heat of $^4$He peaks at this temperature[1], similar to the behaviour predicted for the ideal Bose gas.

Landau was the next person to make significant contributions to the new field of superfluidity [6]. He developed a very successful phenomenological hydrodynamic description of $^4$He that divided the system into superfluid and normal fluid components, similar to the 'two-fluid' model of Tisza [7]. Landau also introduced the idea that the liquid could be described in terms of a gas of weakly interacting quasiparticles, which had a simple energy spectrum for two types of excitations—phonons and rotons. The linear nature of his proposed dispersion relation at low momentum explained the phenomenon of frictionless flow.

A major breakthrough was made by Bogoliubov in 1947 [8]. He utilised the new ideas of second quantisation and many-body field theory to show quantitatively that the nature of BEC was not profoundly affected by the introduction of weak interactions. However, he demonstrated that the low-lying excitations of a Bose-condensed gas were significantly altered, and that the predicted phonon spectrum was exactly that assumed by Landau which ensured the stability of superfluid flow.

It turns out that superfluid $^4$He is not a good example of a weakly-interacting Bose gas (WIBG). It is a liquid, not a gas, and the interactions between the atoms are so strong that the actual condensate only makes up about 10% of the system at

---

[1] In fact the specific heat diverges at the critical temperature, and it is known as the lambda point as the curve resembles the Greek letter.

$T = 0$. However, the effects of Bose statistics play a major role in determining the characteristics of the fluid, and the weakly-interacting gas continued to be studied as a qualitative model of superfluid $^4$He. Many of the theoretical properties of the WIBG were determined in the 1950's and early 1960's in this context.

The background theory to the work presented in this thesis is presented in detail in Chapter 2. Comprehensive reviews of other aspects of BEC can be found in the recent publications of Refs. [9, 10, 11, 12, 13].

## 1.4 BEC in the laboratory

During the development of BEC theory in the middle of the 20th century, it was thought that there was little prospect of ever observing the BEC phase transition in the laboratory. In his book on statistical thermodynamics Schrödinger remarked that quantum statistics was at once satisfying, disappointing and astonishing [14]. It was satisfying as the theory reduces to that of a classical gas in the appropriate limits. He found it disappointing as he believed the densities required were so high and temperatures so low, that Van der Waals interactions would always mask any quantum statistical effects to the extent that it was impossible to separate the two. Finally, it was astonishing that such a simple difference in the statistical functions could result in such profound effects.

The system that seemed to offer the best possibility was atomic hydrogen, and attempts to reach quantum degeneracy began in the late 1970's. The first experiments used compressed, cryogenically cooled hydrogen and were soon able to reach a phase-space density of just a factor of 50 away from the BEC transition. However, from this point progress was slow and the experiments ran into several difficulties. Atoms sticking to the wall of the container, and large three-body recombination rates limited the densities that were achievable.

Progress in the cooling and trapping of neutral alkali atoms in the 1980's and early 1990's meant that these systems rapidly usurped hydrogen as the favourite for the first observation of BEC in a weakly interacting gas. After a very competitive race between several research groups, BEC was first reported by the group of Cornell and Wieman at JILA[2] in Boulder, Colorado in 1995 [15]. Anderson *et al.* described the observation of a Bose condensate of 2000 atoms in a gas of $^{87}$Rb atoms, with a critical temperature of 170 nK—a remarkable achievement indeed.

---

[2] Joint Institute for Laboratory Astrophysics.

Very soon afterwards, the Ketterle group at MIT[3] reported the observation of BEC in a gas of $^{23}$Na atoms [16]. Also, evidence was reported for BEC in a gas of $^{7}$Li atoms by the group of Hulet at Rice University in Houston, Texas [17]. Eventually the observation of BEC was reported in atomic hydrogen by the group of Kleppner at MIT in 1998 [18].

In the five year period to January 2001 since the first condensate was formed, a total of 23 different experiments around the world have reported the observation of BEC. In the 1990's more than one thousand papers have been published in the field, and it seems fair to say that the experimental achievements have sparked the recent rapid advances in this area.

### 1.4.1 Experimental procedure

In this section we give a summary of the procedures used in the production of alkali Bose-Einstein condensates. While the particular details vary between experiments, the broad outline is similar.

There are three principal steps in the formation of a Bose-Einstein condensate in the laboratory. They are

1. Laser cooling.
2. Magnetic trapping.
3. Evaporative cooling.

#### Laser cooling

The cooling and trapping of neutral atoms via the use of laser light was state-of-the-art technology in the 1980's, but today is essentially a routine experimental tool. For their contributions to the development of the procedure, the Nobel Prize in physics was awarded to Steven Chu, Claude Cohen-Tannoudji, and William Phillips in 1997.

A magneto-optical trap (MOT) is formed in a gaseous cell as follows. Three pairs of counter-propagating laser beams, slightly red-detuned below the atomic resonance with opposite circular polarisations, are superimposed on a magnetic quadrupole field produced by a pair of anti-Helmholtz coils. The Zeeman sublevels of an atom displaced from the centre of the trap are shifted by the local magnetic

---

[3] Massachusetts Institute of Technology.

field in such a way that the atom tunes into resonance with the laser field propagating in the opposite direction. The net force resulting on the atom is thus always towards the origin. There is also a velocity-dependent force due to the Doppler shift, and the effect is to cool and trap a sample of atoms in the region of the zero of the magnetic field.

This technique can produce clouds $\sim 10^{10}$ atoms at a density of $\sim 10^{11}$ cm$^{-3}$ and temperatures of tens of micro-Kelvin. While this is very cold, it it still approximately six orders of magnitude away from the phase-space density required for the BEC transition. The reader interested in further details of laser cooling and trapping is referred to one of several review papers on the subject [19, 20, 21, 22].

### Magnetic trapping and evaporative cooling

The development of magnetic trapping and evaporative cooling of alkali atoms is interlinked and so we discuss these procedures together. To reach the BEC transition, the atomic systems must be cooled to temperatures much lower than that attainable in a MOT. Therefore other techniques are required.

The method of evaporative cooling was first suggested by Hess, in the context of spin-polarised hydrogen in a magnetic trap [23]. Evaporative cooling for atoms works much as it does for hot liquids—if the hottest atoms are removed from the system, those remaining can rethermalise via collisions. Although particles are lost, the decrease in the temperature more than compensates and the phase-space density will increase.

If neutral atoms are optically pumped into a low-field seeking stretched $m_F$ state, they can be confined in a magnetic field such as that formed by a quadrupole trap. The most energetic atoms in the system will be able to move furthest from the centre of the trap and experience the largest magnetic field, where the Zeeman shift will be the greatest. With the application of a suitably tuned RF field, these hottest atoms can undergo a transition into a high-field seeking state, and thus be selectively ejected from the system. A slowly decreasing RF frequency will cut further into the atomic distribution as it rethermalises, continuously reducing the temperature.

There is a difficulty with this technique in a quadrupole trap. At the centre of the system the magnetic field is zero, and the atoms in this region are able to undergo Majorana spin flips to untrapped $m_F$ states. The problem is worse at lower temperatures as the cold atoms spend more time in the region of $B = 0$.

Two different traps were designed to avoid this pitfall. The first was the TOP[4] trap, developed at JILA [24]. In this configuration a rapidly rotating bias field is added to the static quadrupole field, such that on average the atoms experience a harmonic potential. At any time the zero of the magnetic field circulates about the centre of the trap, removing hot atoms rather than a cold ones. The MIT experiment initially used a blue-detuned laser as an “optical plug” to keep the atoms away from the centre of the quadrupole trap. However, they later developed a Ioffe-Pritchard type trap [25] with no region of $B = 0$. These traps have very tight confinement in two dimensions, and somewhat weaker confinement in the third.

### 1.4.2 Experiments today

The first BEC experiments were performed in a single vapour cell. This created something of a dilemma—on the one hand, the vapour pressure should be relatively high so that a large number of atoms could be captured in the MOT for transferal to the magnetic trap. This is desirable as it means that the initial collision rate would be high, increasing the rate of thermalisation and making the evaporative cooling process more efficient. On the other hand, a high background vapour pressure results in a large number of atoms at room temperature colliding with the trapped atoms, reducing the lifetime of the sample.

Many experiments today make use of a double-MOT arrangement. The first MOT is in a region of high vapour pressure so that many atoms can be trapped, and the second is at a very low pressure to increase the trap lifetime. The two MOTs are connected in such a manner that the pressure differential can be maintained. Atoms are moved from the first MOT to the second, before transferal to the magnetic trap and evaporative cooling. Experimental groups are divided between the use of TOP traps that produce a somewhat oblate condensate, and Ioffe-Pritchard traps that produce long, thin, “cigar”-shaped condensates.

Two techniques are utilised to image BECs. The first involves simply turning off the magnetic field, and using a time-of-flight expansion to measure the velocity distribution. In a non-spherical trap the condensate expands anisotropically due to both the uncertainty principle and the interactions between the atoms, and this provides one of the signatures for BEC. However, this method necessarily destroys the system, and so to make measurements in the time domain several identical

---

[4] Time-Orbiting Potential.

experiments must be repeated.

The second procedure is an *in situ* technique called phase-contrast microscopy. It utilises the phase profile of a far-detuned laser beam passing through the system to reconstruct a density image. While this is a non-destructive technique, it has much lower resolution than time-of-flight imaging.

### 1.4.3 Effect of the trapping potential

One major difference between the experiments of today and the early theory of BEC is the presence of a confining potential. In all cases this is well approximated by a harmonic trap.

The inhomogeneity has some important effects. Firstly, the density of states of the system has a different functional form (this is calculated for a harmonic trap in Appendix C). The same procedure as applied in Sec. 1.2 to the homogeneous ideal gas results in a critical temperature of

$$T_c = \frac{\hbar\omega}{k_B}\left(\frac{N}{\zeta(3)}\right)^{1/2}, \tag{1.13}$$

and the condensate population varies below $T_c$ as

$$\frac{N_0}{N} = 1 - \left(\frac{T}{T_c}\right)^3. \tag{1.14}$$

Secondly, BEC in the homogeneous case is condensation in momentum space—the condensate is uniformly distributed in real space. However, in a trap the condensate is localised, and below $T_c$ a sharp spike appears in the density profile of the system. This results in a large peak around zero velocity in a time-of-flight image, providing further experimental evidence of the phase transition.

## 1.5 Important experiments

To date there have been many fascinating experiments performed using Bose-Einstein condensates. In this section we mention a selection of these; however, the list is by no means exhaustive. We discuss a number of these in greater detail elsewhere in the thesis.

Both JILA and MIT have studied the excitations of BECs, at zero [26, 27] and finite temperatures [28]. The MIT group has also considered the propagation of sound [29, 30].

Many groups have performed output coupling of the condensate from the magnetic trap, forming rudimentary atom lasers. The first "pulsed" atom laser was observed at MIT [31], who have also observed the amplification of matter waves [32]. Other groups have extracted continuous beams of coherent atoms from their condensates [33, 34]. MIT have observed bosonic stimulation in the growth of a condensate [35].

Double condensates were first observed at JILA, by coherently transferring atoms to a second trapped magnetic state [36]. They have subsequently studied their dynamics [37] and measured their relative phase [38]. MIT were the first to move BECs to an optical dipole trap [39]. In this configuration they have studied spinor BECs where many $m_F$ states are trapped together [40, 41]. Also, they have tuned the scattering length of the atoms in the condensate using a Feshbach resonance [42]. Recently, a Feshbach resonance for $^{85}$Rb was utilised to tune the scattering length to be positive such that condensate formation was possible [43].

The atom-optical equivalent of four-wave mixing has been observed by researchers at NIST[5], by utilising Bragg pulses to coherently impart momentum to the condensate [44]. The group of Hau observed the slowing of light to 17 ms$^{-1}$ in a sodium BEC [45].

Experiments at Oxford [46] and MIT [47, 48] have offered evidence that a BEC has some of the characteristic properties of a superfluid. The group of Cornell at JILA have formed a vortex state in their BEC [49] and have studied its behaviour [50]. Finally, arrays of vortices have been observed by stirring a rubidium condensate in Paris [51, 52].

## 1.6 Thesis outline

This thesis is concerned with the dynamics of Bose-Einstein condensation, and in Chapter 2 we introduce much of the background theory. We begin with the many-body Hamiltonian for the Bose-field operator and derive the formal equations of motion. We then give derivations of two successful dynamical theories—the Gross-Pitaevskii equation and the quantum Boltzmann equation, and discuss their validity and application to trapped Bose gases.

In Chapter 3 we summarise the quantum kinetic theory of Gardiner, Zoller and co-workers, and discuss its application to the problem of condensate growth.

---

[5] National Institute for Standards and Technology.

We then consider our own work on this problem in Chapter 4. We describe our representation of the system and the method of solution, before comparing our results to other models of condensate growth, and finally to experimental data.

In Chapter 5 we develop a formalism for calculating the dynamics of thermal Bose-Einstein condensates. We derive equations of motion for the condensate and its coherent excitations, coupled to a kinetic equation for the higher lying modes of the gas. We discuss each of the terms that arise and their solution, and link these to experimental situations.

Chapter 6 is concerned with a simplification of the formalism of the previous chapter. We carry out numerical simulations at finite temperature, and analyse the resulting data in terms of equilibrium theories of BEC.

Finally in Chapter 7 we consider the future prospects of our formalism for calculating the thermal dynamics of Bose gases.

The appendices contain derivations of several results that we use in the main text, along with a discussion of some numerical techniques for evolving the Gross-Pitaevskii equation. We also include a reproduction of a paper on the effect of temperature on the excitations of a BEC with attractive interactions, to ensure this thesis is a complete record of the author's D. Phil. research.

# CHAPTER 2

# DYNAMICAL QUANTUM FIELD THEORIES

Thermal field theories are important in the description of a wide range of physical systems [53]. The achievement of Bose-Einstein condensation in a dilute gas [15, 16, 17] offers the possibility of studying the dynamics of a quantum field at finite temperatures in the laboratory. However, making theoretical predictions for such experiments poses many difficulties.

Equilibrium theories of BEC are now well developed [54, 55, 56], and have had success in calculating the excitation frequencies, damping rates and fluctuations of a condensate in the presence of non-condensed atoms. While there are still some discrepancies between experiment and theory, such as the $m = 2$ collective excitation measured at JILA [28], there are suggestions that more sophisticated calculations will resolve these differences [57].

The non-equilibrium dynamics of Bose-Einstein condensates in the presence of a thermal vapour poses an even greater theoretical challenge. The major difficulty lies in describing both the coherent and incoherent processes that can occur in the system when both a condensate and a significant thermal fraction are present.

In this chapter we introduce the second quantised many-body Hamiltonian from which all theories of BEC begin. We then outline how the real interatomic potential that appears in this Hamiltonian may be replaced by the two-body T-matrix. This simplifies the resulting theories because the T-matrix can by well approximated by a delta-function potential for low-energy scattering.

We then discuss the derivation of two successful dynamical theories of a Bose gas. The first, the Gross-Pitaevskii equation, is usually assumed to be valid in the $T = 0$ limit when the entire system is condensed. The second, the quantum Boltzmann equation, is valid for $T > T_c$ when there is no condensate present.

This thesis is concerned with the development and implementation of theoretical methods to describe Bose gases in the intermediate region between $T = 0$ and $T = T_c$. In Chapters 3 and 4 we extend the quantum Boltzmann description to describe the formation of a condensate. In Chapter 5 we develop a formalism based on the Gross-Pitaevskii equation to describe BECs at finite temperature, and in Chapter 6 we present results from simulations based on this approach.

## 2.1 The BEC Hamiltonian

Quantum field theories for Bose-Einstein condensation in dilute gases begin with the second quantised many-body Hamiltonian for a system of identical, structureless bosons with pair interactions. The gas is assumed to be dilute enough that three-body events are rare and can be neglected, a condition well-satisfied in experiments on evaporatively-cooled alkali atoms. The Hamiltonian can be written as

$$\hat{H} = \hat{H}_0 + \hat{H}_I, \tag{2.1}$$

$$\hat{H}_0 = \int d^3\mathbf{x}\; \hat{\Psi}^\dagger(\mathbf{x},t)\hat{H}_{sp}\hat{\Psi}(\mathbf{x},t), \tag{2.2}$$

$$\hat{H}_I = \frac{1}{2}\int d^3\mathbf{x} \int d^3\mathbf{x}'\; \hat{\Psi}^\dagger(\mathbf{x},t)\hat{\Psi}^\dagger(\mathbf{x}',t)V(\mathbf{x}-\mathbf{x}')\hat{\Psi}(\mathbf{x}',t)\hat{\Psi}(\mathbf{x},t). \tag{2.3}$$

The non-interacting part of the Hamiltonian, $\hat{H}_0$, corresponds to an ideal gas, and can be diagonalised exactly. The quantity $\hat{H}_I$ describes two-body interactions via the interatomic potential $V(\mathbf{x})$. The field operator $\hat{\Psi}(\mathbf{x},t)$ annihilates a single boson of mass $m$ at position $\mathbf{x}$ and time $t$, and obeys the equal time commutation relations

$$\left[\hat{\Psi}(\mathbf{x},t), \hat{\Psi}(\mathbf{x}',t)\right] = \left[\hat{\Psi}^\dagger(\mathbf{x},t), \hat{\Psi}^\dagger(\mathbf{x}',t)\right] = 0, \tag{2.4}$$

$$\left[\hat{\Psi}(\mathbf{x},t), \hat{\Psi}^\dagger(\mathbf{x}',t)\right] = \delta(\mathbf{x}-\mathbf{x}'). \tag{2.5}$$

The field operator is normalised such that

$$\int d^3\mathbf{x}\; \hat{\Psi}^\dagger(\mathbf{x},t)\hat{\Psi}(\mathbf{x},t) = \hat{N}, \tag{2.6}$$

where $\hat{N}$ is the particle number operator of the system. We find that the commutator $[\hat{N}, \hat{H}] = 0$, and so the number of particles $N$ is a constant of the motion.

The single particle Hamiltonian is

$$\hat{H}_{sp} = -\frac{\hbar^2}{2m}\nabla^2 + V_{\text{trap}}(\mathbf{x}), \tag{2.7}$$

where $V_{\text{trap}}(\mathbf{x})$ is the external confining potential of the system. If this is non-zero then the system is called *inhomogeneous*, because in equilibrium the field operator is dependent on position. However, in this thesis we also consider the *homogeneous* case, in which $V_{\text{trap}}(\mathbf{x})$ is set to zero. The ideal gas Hamiltonian $\hat{H}_0$, Eq. (2.2), can be diagonalised exactly by the eigenvectors of $\hat{H}_{sp}$, which we denote as the set $\{\phi_n\}$.

The interaction part of the Hamiltonian $\hat{H}_I$ describes binary collisions, and the term $V(\mathbf{x} - \mathbf{x}')$ is the actual interatomic potential between two particles. Using the Heisenberg equation

$$i\hbar\frac{d\hat{A}}{dt} = [\hat{A}, \hat{H}], \tag{2.8}$$

assuming that $\hat{A}$ has no explicit time dependence, we find the equation of motion for the field operator

$$i\hbar\frac{\partial\hat{\Psi}(\mathbf{x},t)}{\partial t} = \hat{H}_{sp}\hat{\Psi}(\mathbf{x},t) + \int d^3\mathbf{x}'\ \hat{\Psi}^\dagger(\mathbf{x}',t)V(\mathbf{x}-\mathbf{x}')\hat{\Psi}(\mathbf{x}',t)\hat{\Psi}(\mathbf{x},t). \tag{2.9}$$

Practically, this equation is impossible to solve for realistic systems.

### 2.1.1 Basis set representation

It is useful to expand the field operator on a basis set

$$\hat{\Psi}(\mathbf{x},t) = \sum_n \hat{a}_n(t)\phi_n(\mathbf{x}), \tag{2.10}$$

where $\hat{a}_n(t)$ annihilates a particle in mode $n$ at time $t$. These operators obey the equal-time commutation relations

$$[\hat{a}_m, \hat{a}_n] = \left[\hat{a}_m^\dagger, \hat{a}_n^\dagger\right] = 0, \tag{2.11}$$

$$\left[\hat{a}_m, \hat{a}_n^\dagger\right] = \delta_{mn}. \tag{2.12}$$

where we have dropped the time labels for clarity. If we substitute Eq. (2.10) into the Hamiltonian Eq. (2.1) and take the set $\{\phi_n\}$ to be the eigenvectors of $\hat{H}_{sp}$, we find

$$\hat{H} = \sum_n \hbar\omega_n \hat{a}_n^\dagger \hat{a}_n + \frac{1}{2}\sum_{pqmn} \langle pq|V|mn\rangle \hat{a}_p^\dagger \hat{a}_q^\dagger \hat{a}_m \hat{a}_n, \tag{2.13}$$

where we have defined the symmetrised matrix element

$$\begin{aligned} \langle pq|V|mn\rangle &= \frac{1}{2}\int d^3\mathbf{x}\int d^3\mathbf{x}'\; \phi_p^*(\mathbf{x})\phi_q^*(\mathbf{x}')V(\mathbf{x}-\mathbf{x}')\phi_m(\mathbf{x}')\phi_n(\mathbf{x}) \\ &+ \frac{1}{2}\int d^3\mathbf{x}\int d^3\mathbf{x}'\; \phi_p^*(\mathbf{x})\phi_q^*(\mathbf{x}')V(\mathbf{x}-\mathbf{x}')\phi_n(\mathbf{x}')\phi_m(\mathbf{x}). \end{aligned} \tag{2.14}$$

This definition may seem superfluous at this stage, but in Chapter 5 it significantly reduces the length of the equations of motion we derive. Equation (2.14) represents both direct and exchange collisions, which are physically indistinguishable for identical bosons.

The Heisenberg equation of motion for the individual mode operator $\hat{a}_p$ is therefore

$$i\hbar\frac{d\hat{a}_p}{dt} = \hbar\omega_p \hat{a}_p + \sum_{qmn}\langle pq|V|mn\rangle \hat{a}_q^\dagger \hat{a}_m \hat{a}_n. \tag{2.15}$$

We can eliminate the free evolution of the operators by defining

$$\tilde{a}_p = \hat{a}_p e^{i\omega_p t}, \tag{2.16}$$

so that the equation of motion for the annihilation operator becomes

$$i\hbar\frac{d\tilde{a}_p}{dt} = \sum_{qmn}\langle pq|V|mn\rangle \tilde{a}_q^\dagger \tilde{a}_m \tilde{a}_n e^{i(\omega_p+\omega_q-\omega_m-\omega_n)t}. \tag{2.17}$$

This will be useful later where we will assume, under certain circumstances, that the operator $\tilde{a}$ is slowly varying.

## 2.2 Effective low-energy Hamiltonian

The Hamiltonian described in the previous section contains spatial integrals over the bare interatomic potential $V(\mathbf{x})$ between two atoms. However, it is well-known that at low temperatures the scattering of neutral atoms in three dimensions can be described by the $s$-wave scattering length $a$ [58]. This parameter is often introduced into the theory by replacing the real interatomic potential by the contact potential

$$V(\mathbf{x}-\mathbf{x}') \rightarrow U_0\delta(\mathbf{x}-\mathbf{x}'), \qquad U_0 = \frac{4\pi\hbar^2 a}{m}. \tag{2.18}$$

The interaction strength $U_0$ can be shown to arise from the increase in kinetic energy of a two-particle wave function, when an excluded region of radius $a$ is introduced corresponding to a hard sphere interaction potential [59]. The contact potential approximation, however, can lead to ultraviolet divergences in theories of BEC if it is simply substituted into the Hamiltonian of Eq. (2.1). This is not surprising, as the delta-function potential can scatter high-energy atoms just as effectively as low-energy atoms. Physically this is unrealistic, as momentum transfer between atoms will vanish at high momenta ($k > 1/a$). The contact potential is a low-energy approximation, and care must be taken when summing over high energy states.

The ultraviolet renormalisation of the theory can be achieved by introducing the two-body T-matrix into the Hamiltonian, resulting in a high-momentum cutoff to the the states considered. We feel that this issue is important for this thesis and we give an outline of the procedure in this section. We closely follow Chapter 5 and Appendix C of the thesis of Morgan, and refer the reader to Ref. [54] for further details. The issue of renormalisation and the introduction of the two-body and many-body T-matrices has also been considered by Stoof [60] and Proukakis [61, 62].

### 2.2.1 The two-body T-matrix

The two-body T-matrix describes the scattering of two particles in a vacuum, and is defined by the Lippmann-Schwinger equation

$$T_{2b}(z) = V + V\frac{1}{z-\hat{H}_{sp}}T_{2b}(z), \tag{2.19}$$

where $z$ is the (generally complex) energy of the collision. Inserting a complete set of eigenfunctions of $\hat{H}_{sp}$ gives

$$T_{2b}(z) = V + V\sum_{pq}|pq\rangle\frac{1}{z-\epsilon_p-\epsilon_q}\langle pq|T_{2b}(z), \tag{2.20}$$

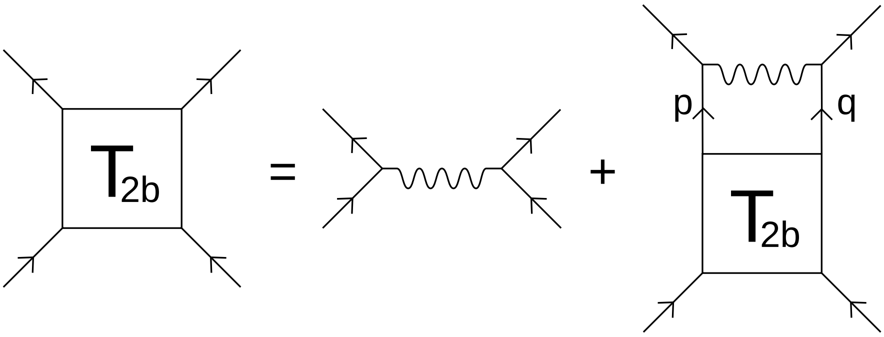

Figure 2.1: A diagrammatic representation of the Lippmann-Schwinger equation for the two-body T-matrix, Eq. (2.19).

where $\epsilon_p$, $\epsilon_q$ are single particle energies, and $|pq\rangle$ is a two-particle eigenstate describing an intermediate state in a collision. The two-body T-matrix includes all *ladder diagrams* that arise in the collision of two particles *in vacuo*, and is represented diagrammatically in Fig. 2.1.

In the homogeneous case the eigenfunctions of $\hat{H}_{sp}$ are plane-waves, and in the limit that the volume of the system $\Omega \to \infty$, the T-matrix can be written as

$$T_{2b}(\mathbf{k}', \mathbf{k}, z) = V(\mathbf{k}' - \mathbf{k}) + \frac{1}{(2\pi)^3} \int d^3\mathbf{k}'' \frac{V(\mathbf{k}'' - \mathbf{k}') T_{2b}(\mathbf{k}'', \mathbf{k}', z)}{z - (\hbar k'')^2/2\tilde{m}}, \tag{2.21}$$

where

$$\begin{aligned} V(\mathbf{k}) &= \int d^3\mathbf{x}\, V(\mathbf{x})\, e^{-i\mathbf{k}\cdot\mathbf{x}}, & (2.22) \\ T_{2b}(\mathbf{k}', \mathbf{k}, z) &= \int d^3\mathbf{x}' \int d^3\mathbf{x}\, e^{-i\mathbf{k}'\cdot\mathbf{x}'}\, T_{2b}(\mathbf{x}', \mathbf{x}, z)\, e^{i\mathbf{k}\cdot\mathbf{x}}, & (2.23) \end{aligned}$$

and $\hbar\mathbf{k}$, $\hbar\mathbf{k}'$ are the initial and final relative momenta of the colliding atoms, $\tilde{m} = m/2$ is the reduced mass, and $z$ has been redefined to include the centre of mass energy of the colliding pair.

Reference [58] shows that in the limit that the colliding pair of particles conserve energy and momentum, the homogeneous two-body T-matrix can be written as a partial-wave expansion in terms of the phase shifts $\phi_l(k)$ caused by the interatomic potential as

$$\lim_{\substack{\delta \to 0 \\ k' = k}} T_{2b}(\mathbf{k}', \mathbf{k}, \epsilon_k + i\delta) = -\frac{4\pi\hbar^2}{m} \sum_{l=0}^{\infty} \frac{(2l+1)}{k} e^{i\phi_l(k)} \sin\phi_l(k) P_l(\cos\theta), \tag{2.24}$$

where $\epsilon_k = \hbar^2 k^2/2\tilde{m}$ and $\theta$ is the angle between $\mathbf{k}$ and $\mathbf{k}'$.

At low energy (when $ka \ll 1$) only $s$-wave scattering is important. For a hard sphere of radius $a$ the $s$-wave phase shift is $\phi_0(k) = -ka$, and the same result applies for a wide range of more general potentials, where the quantity $a$ is interpreted as the $s$-wave scattering length. Therefore we can truncate the summation of Eq. (2.24) to the first term, and we have

$$\lim_{\substack{\delta\to 0\\ k'=k}} T_{2b}(\mathbf{k}', \mathbf{k}, \epsilon_k + i\delta) = \frac{4\pi\hbar^2 a}{m} + \mathrm{O}(ka). \tag{2.25}$$

Thus for low-energy scattering, the spatial representation of the T-matrix can be taken to be the contact potential

$$\begin{aligned} T_{2b}(\mathbf{x}', \mathbf{x}, z=0) &\sim \frac{4\pi\hbar^2 a}{m}\,\delta(\mathbf{x}'-\mathbf{x})\,\delta(\mathbf{x}), \\ &= U_0\,\delta(\mathbf{x}'-\mathbf{x})\,\delta(\mathbf{x}). \end{aligned} \tag{2.26}$$

Experimental measurements of the scattering length therefore correspond to the determination of the low-energy on-shell limit of the two-body T-matrix. To avoid ultraviolet divergences in calculations beyond first-order perturbation theory, we should replace not the interatomic potential $V(\mathbf{x})$, but rather the two-body T-matrix $T_{2b}(z)$ with the contact potential.

### 2.2.2 Elimination of high-energy states

In the previous subsection we discussed how the simple replacement of the interatomic potential with the contact potential is incorrect. In this subsection we identify how to introduce the two-body T-matrix into the theory.

We consider the equation of motion for the field operator in the basis diagonalising $\hat{H}_0$, Eq. (2.17). For dilute systems at low temperature only a finite energy-range of states will be occupied, and so the basis can be divided into two bands—a low-energy region $L$ that contains all the particles in the system, and a high-energy region $H$ that contains all the remaining unoccupied levels.

By arguing that matrix elements in Eq. (2.17) containing only one high index will be negligible, we can approximate the equation of motion for the low-energy state $p$ by

$$\begin{aligned} i\hbar\frac{d\tilde{a}_p}{dt} &= \sum_{qmn}^{L}\langle pq|V|mn\rangle \tilde{a}_q^\dagger\tilde{a}_m\tilde{a}_n e^{i(\omega_p+\omega_q-\omega_m-\omega_n)t} \\ &\quad+\sum_{q}^{L}\sum_{mn}^{H}\langle pq|V|mn\rangle \tilde{a}_q^\dagger\tilde{a}_m\tilde{a}_n e^{i(\omega_p+\omega_q-\omega_m-\omega_n)t}, \end{aligned} \tag{2.27}$$

where $\sum_{mn}^{H}$ means both the indices $m$ and $n$ are high, and $L$ indicates that only low-energy states are included in the summation.

The effect of interactions on the high-energy states is small, and they evolve on a time scale that is short compared to the characteristic time for the evolution of the low-energy states. Therefore it is possible to approximately integrate the equation of motion for the second term on the right-hand side of Eq. (2.27), and replace it with operators that act only on the low-energy states (see Appendix C of Ref. [54] for the details.) Inserting the result of this procedure into Eq. (2.27), we find

$$i\hbar\frac{d\tilde{a}_p}{dt} = \sum_{qmn}^{L}\langle pq|T_H|mn\rangle \tilde{a}_q^\dagger\tilde{a}_m\tilde{a}_n e^{i(\omega_p+\omega_q-\omega_m-\omega_n)t}, \tag{2.28}$$

where we have defined the *restricted* two-body T-matrix

$$T_H = V + \sum_{pq}^{H} V|pq\rangle \frac{1}{-(\varepsilon_p+\varepsilon_q)}\langle pq|T_H. \tag{2.29}$$

This is the same expression as for the full two-body T-matrix of Eq. (2.19), except for the fact that the sum over intermediate states is restricted to the high-energy subspace $H$.

The second step in the calculation is to replace the restricted T-matrix with the full two-body T-matrix. This can be done via a Born approximation on the expression for $T_{2b}$ in terms of $T_H$.[1] The major effect is simply to replace $T_H$ with $T_{2b}$ in all the matrix elements, whilst renormalising quantities that are otherwise infinite when the contact potential approximation is made. The Born approximation is valid as long as

$$na^3 \ll 1, \qquad \mathrm{T}=0, \tag{2.30}$$

$$a/\Lambda \ll 1, \qquad \mathrm{T}>0, \tag{2.31}$$

---

[1] We stress that this is *not* the same as a Born approximation for $T_{2b}$ in terms of the interatomic potential $V$, which is not valid at low energy.

i.e. the dilute gas criterion is satisfied at zero temperature, and the de Broglie wavelength of the atoms $\Lambda$ is much larger than the scattering length at finite temperature. The scattering length of the alkalis is typically a few nanometres, whereas the thermal de Broglie wavelength in the region of condensation is a few microns, so both these conditions are well satisfied in recent experiments on Bose-Einstein condensation above and below the critical temperature.

### 2.2.3 Conclusion

In this section we have shown that in the equation of motion for the occupied states of a dilute gas at low temperature, the interatomic potential can be replaced by a T-matrix if we introduce a high-energy cutoff to the states considered. Thus, the effective low-energy Hamiltonian is

$$\hat{H}_{\text{eff}} = \sum_{n}^{L} \hbar\omega_n \hat{a}_n^\dagger \hat{a}_n + \frac{1}{2} \sum_{pqmn}^{L} \langle pq|T_H|mn\rangle \hat{a}_p^\dagger \hat{a}_q^\dagger \hat{a}_m \hat{a}_n, \tag{2.32}$$

as this leads directly to the equation of motion Eq. (2.28).

In three dimensions we can replace the restricted T-matrix $T_H$ by a contact potential with two caveats:

1. There is a high-energy cutoff to the theory, and all particles in the system must fall well below this energy.

2. In any theory terms will arise that involve sums to the cutoff. Some of these have already been included in the theory with the replacement of $T_H$ with $T_{2b}$, and so such contributions must be renormalised.

These issues are explained in greater detail in Ref. [54]. For the remainder of this thesis we shall make use of the naive replacement of the interatomic potential by the contact potential, but we shall note where care must be taken.

## 2.3 The Gross-Pitaevskii equation at $T = 0$

The Gross-Pitaevskii equation (GPE) is a form of nonlinear Schrödinger equation (NLSE) that has been successfully used to describe the static and dynamic properties of Bose-Einsten condensates at very low temperatures. It was first derived in the early 1960's as a phenomenological description of superfluid helium [63], but has formed the basis of much research since the first observation of BEC in alkali gases. The form of the equation is simple, yet it contains a rich variety of features.

### 2.3.1 Derivation

The most usual form of the GPE can be derived from the spatial representation of the equation of motion for the Bose field operator, Eq. (2.9). We assume that the field operator has a mean value and can be written as

$$\hat{\Psi}(\mathbf{x},t) = \psi(\mathbf{x},t) + \hat{\delta}(\mathbf{x},t), \tag{2.33}$$

where $\psi(\mathbf{x},t) = \langle\hat{\Psi}(\mathbf{x},t)\rangle$, and $\hat{\delta}(\mathbf{x},t)$ represents the remaining quantum fluctuations of the field. The mean field description is equivalent to representing the condensate by a coherent state with a definite phase, and breaks the gauge symmetry of the Bose Hamiltonian. We substitute Eq. (2.33) into Eq. (2.9) and make use of the contact potential approximation. Taking the expectation value (while remembering that $\langle\hat{\delta}(\mathbf{x},t)\rangle = 0$ by definition), we find

$$i\hbar\frac{\partial\psi}{\partial t} = \hat{H}_{sp}\psi + U_0|\psi|^2\psi + U_0\left[\langle\hat{\delta}^\dagger\hat{\delta}\rangle\psi + \langle\hat{\delta}\hat{\delta}\rangle\psi^* + \langle\hat{\delta}^\dagger\hat{\delta}\hat{\delta}\rangle\right], \tag{2.34}$$

where we have dropped the space and time labels for clarity. The terms involving the operators $\hat{\delta}$ can be interpreted as follows:

$\langle\hat{\delta}^\dagger\hat{\delta}\rangle$ : The mean field of the uncondensed particles that acts on the condensate. For the case where the large majority of the particles are condensed this can be neglected.

$\langle\hat{\delta}^\dagger\hat{\delta}\hat{\delta}\rangle$ : Represents a collision between two uncondensed particles in which one of them is transferred to the condensate. Due to the lack of non-condensed particles in the limit of high condensate fraction, this can also be neglected.

$\langle\hat{\delta}\hat{\delta}\rangle$ : This term is known as the anomalous average. It represents the modification of the interaction between two condensate atoms due to virtual processes in which they make transitions to excited states before returning to the condensate. A naive calculation shows that this quantity is ultraviolet divergent; however, the dominant contribution from this term has already been accounted for by the introduction of the contact potential approximation. Thus it must be renormalised, and at $T = 0$ the remainder can be neglected [54, 61].

While these approximations are valid at zero temperature, terms involving $\hat{\delta}$ become important at finite temperature and this issue will be discussed in Chapter 5 of this thesis. For the case $T \to 0$, we are left with the famous and successful Gross-Pitaevskii equation

$$i\hbar\frac{\partial\psi(\mathbf{x},t)}{\partial t} = \hat{H}_{sp}\psi(\mathbf{x},t) + U_0|\psi(\mathbf{x},t)|^2\psi(\mathbf{x},t), \tag{2.35}$$

in which the wave function is normalised to the number of particles in the system. Often, the wave function is renormalised to unity, and as this is a nonlinear equation the coefficient of the nonlinear term becomes $NU_0$.

### 2.3.2 Time-independent GPE

If we make the substitution

$$\psi(\mathbf{x},t) = \psi(\mathbf{x})\, e^{-i\lambda t/\hbar}, \tag{2.36}$$

into the GPE of Eq. (2.35) we get the time-independent GPE

$$\lambda\psi(\mathbf{x}) = \hat{H}_{sp}\psi(\mathbf{x}) + U_0|\psi(\mathbf{x})|^2\psi(\mathbf{x}), \tag{2.37}$$

where $\lambda$ is the condensate *eigenvalue*. This is often written as $\mu$ and called the chemical potential, which is somewhat misleading. The chemical potential is a thermodynamic quantity that is determined by temperature and the number of particles in the system, and the two quantities are only identical in the thermodynamic limit. While $\lambda - \mu$ is very small when the system is condensed, there is an important difference between them at finite temperatures. If there are $n_0$ atoms in the condensate then in equilibrium we have

$$\lambda = \mu + k_B T \ln\left(1 + \frac{1}{n_0}\right). \tag{2.38}$$

In Chapters 3 and 4 of this thesis on the growth of a BEC we shall use the notation $\lambda = \mu_C(n_0)$.

In general Eq. (2.37) must be solved numerically, and methods for its solution have been discussed in the literature [64].

### 2.3.3 Thomas-Fermi solution

A very useful approximate solution for the ground state wave function in a trap can be found in the limit that there are a large number of atoms present. In this instance the kinetic energy is much smaller than the interaction energy or the potential energy due to the trap. Therefore, we can neglect the $\nabla^2$ operator in $\hat{H}_{sp}$ of Eq. (2.37) to find a solution for the wave function of

$$\psi(\mathbf{x}) \quad = \quad \sqrt{\frac{\lambda - V_{\text{trap}}(\mathbf{x})}{U_0}} \qquad \text{for } \lambda > V_{\text{trap}}(\mathbf{x}), \tag{2.39}$$

and zero elsewhere. If we consider a generic three-dimensional harmonic oscillator potential for the trap

$$V_{\text{trap}}(\mathbf{x}) = \frac{m}{2}\left(\omega_x^2 x^2 + \omega_y^2 y^2 + \omega_z^2 z^2\right), \tag{2.40}$$

and use the fact that the wave function is normalised to $N$, we find the Thomas-Fermi relationship between the condensate eigenvalue and the number of atoms in the system

$$\lambda = \left(\frac{15NU_0}{64\pi\hbar\bar{\omega}}\right)^{2/5}\left(\frac{2m\bar{\omega}}{\hbar}\right)^{3/5}, \tag{2.41}$$

where we have defined the geometrical average of the trap constants

$$\bar{\omega} = (\omega_x\omega_y\omega_z)^{1/3}. \tag{2.42}$$

We can see that the dependence of the condensate energy on the number of atoms is very weak in the large $N$ limit, having the form $\lambda \propto N^{2/5}$. The change in size of the condensate with the number of atoms in this limit is also very slow; the extent of the wave function along each axis being

$$r_i = \left(\frac{2\lambda}{m\omega_i}\right)^{1/2} \quad \propto \quad N^{1/5}, \tag{2.43}$$

with $i \in \{x, y, z\}$.

### 2.3.4 Collective excitations

The GPE can be used to find the shapes and frequencies of the excitations of a Bose-Einstein condensate. The collective excitations of the ground state are the normal modes of the system, and are hence quasiparticles.

The quasiparticle modes can be found by considering a small disturbance to the condensate and linearising with respect to it. Because the nonlinear term in Eq. (2.35) couples waves travelling in opposite directions, we look for a solution of the form

$$\psi(\mathbf{x},t) = e^{-i\lambda t/\hbar}\left[\psi_0(\mathbf{x}) + \sum_i \left\{u_i(\mathbf{x})c_i e^{-i\omega_i t} + v_i^*(\mathbf{x})c_i^* e^{+i\omega_i t}\right\}\right], \tag{2.44}$$

where the wave function $\psi_0(\mathbf{x})$ is the ground-state solution of the time-independent GPE, Eq. (2.37), with eigenvalue $\lambda$, and the coefficients $\{c_i\}$ are constants. If we substitute this into Eq. (2.35), linearise with respect to the $c_i$'s and equate coefficients of $e^{\pm i\omega_i t}$, we obtain the Bogoliubov-de Gennes (BdG) equations

$$\mathcal{L}u_i(\mathbf{x}) + U_0\psi_0(\mathbf{x})^2 v_i(\mathbf{x}) = \hbar\omega_i, \tag{2.45}$$

$$\mathcal{L}v_i(\mathbf{x}) + U_0\psi_0^*(\mathbf{x})^2 u_i(\mathbf{x}) = -\hbar\omega_i, \tag{2.46}$$

where

$$\mathcal{L} = \hat{H}_{sp} - \lambda + 2U_0|\psi_0(\mathbf{x})|^2. \tag{2.47}$$

The functions $\{u_i, v_i\}$ obey the orthogonality and symmetry relations

$$\int d^3\mathbf{x}\left\{u_i(\mathbf{x})u_j^*(\mathbf{x}) - v_i(\mathbf{x})v_j^*(\mathbf{x})\right\} = \delta_{ij}, \tag{2.48}$$

$$\int d^3\mathbf{x}\left\{u_i(\mathbf{x})v_j(\mathbf{x}) - v_i(\mathbf{x})u_j(\mathbf{x})\right\} = 0. \tag{2.49}$$

The BdG equations can be solved analytically in the homogeneous case, but in general they must be solved numerically.

While the BdG equations can be derived from the GPE, they were first derived from the fully quantum many-body Hamiltonian by Bogoliubov in 1947, when he considered the excitations of superfluid helium [8]. In this approach we make the substitution

$$\Psi(\mathbf{x},t) = e^{-i\lambda t/\hbar}\left[\psi_0(\mathbf{x}) + \hat{\delta}(\mathbf{x},t)\right], \tag{2.50}$$

in the Hamiltonian Eq. (2.1), and discard terms cubic and quartic in the $\hat{\delta}(\mathbf{x},t)$. This leaves us with a quadratic Hamiltonian, which can be diagonalised exactly by the Bogoliubov transformation

$$\hat{\delta}(\mathbf{x},t) = \sum_i \left\{ u_i(\mathbf{x})\hat{b}_i(t) + v_i^*(\mathbf{x})\hat{b}_i^\dagger(t) \right\}, \tag{2.51}$$

if the wave function $\psi_0(\mathbf{x})$ is a solution of the time-independent GPE and the functions $\{u_i, v_i\}$ satisfy

$$\int d^3\mathbf{x} \left\{ u_i^*[\mathcal{L}u_j + U_0\psi_0^2 v_j] + v_j^*[\mathcal{L}v_j + U_0\psi_0^{*2}u_j] \right\} = \hbar\omega_i\delta_{ij}, \tag{2.52}$$

$$\int d^3\mathbf{x} \left\{ u_i[\mathcal{L}v_j + U_0\psi_0^{*2}u_j] + v_j[\mathcal{L}u_j + U_0\psi_0^2 v_j] \right\} = 0, \tag{2.53}$$

where the space labels have been dropped for clarity. The operators $\{\hat{b}_i\}$ obey the usual Bose commutation relations, and for the transformation to be canonical the functions $\{u_i, v_i\}$ must also satisfy the orthonormality and symmetry requirements of Eqs. (2.48) and (2.49). Equations (2.52) and (2.53) are solved by the BdG equations (2.45) and (2.46).

### 2.3.5 Experimental verification

The GPE has been used very successfully to both quantitatively and qualitatively model several experiments on trapped Bose-Einstein condensates. In this section we briefly discuss a few of these.

#### Ballistic expansion

In the first observation of BEC at JILA [15], one piece of evidence that a condensate had formed was the anisotropy of the density distribution of the system after it underwent ballistic expansion. The tighter confinement in the $z$-direction meant that after release from the trap, the condensate expanded faster along the vertical axis. This was modelled quantitatively by Holland and Cooper who evolved a cylindrically symmetric GPE for the experimental conditions [65].

In Ref. [66] Castin and Dum derive a set of analytic equations to describe the evolution of a Thomas-Fermi limit BEC in a time-dependent harmonic trap. These are frequently used in experiments to model the ballistic expansion of condensates, and to determine the number of atoms present [67].

### Excitation frequencies

One of the first experiments carried out on the newly-formed BECs at both JILA and MIT was the measurement of the excitation frequencies, and their dependence on condensate number at zero temperature [26, 27]. The excitation frequencies of the JILA experiment for $T = 0$ were calculated by Edwards *et al.* [68]. They solve the BdG equations numerically, and the results are in excellent agreement with experiment. Other papers also consider condensate excitation frequencies using the GPE:

1. Fetter calculates the low-lying excitations of a condensate in an isotropic harmonic trap in the Thomas-Fermi limit [69].
2. Singh and Rokshar solve the BdG equations using a variational basis set method for the isotropic harmonic trap, for a range of interaction strengths including the attractive case [70].
3. Pérez-García *et al.* find the low-energy excitations by solving the time dependent GPE using a variational procedure with a gaussian ansatz for the wave function [71].
4. Stringari finds analytic formulae in the Thomas-Fermi limit for all excitation frequencies of a condensate in an isotropic harmonic trap, as well as for some modes of an anisotropic trap [72].

The excitation frequencies of a condensate at finite temperature were also measured at JILA [28]. It was found that the linearised GPE solutions gave good predictions of the frequencies up to $T = 0.6T_c$ if the number of atoms was taken to be the number measured in the condensate.

### Interference of two condensates

The interference of two BECs was suggested as an experiment by Hoston and You [73] as demonstration that a ground state condensate is well approximated by a coherent state. They used the GPE to demonstrate the formation of interference fringes, and Wallis *et al.* determined the experimental regime in which fringes could be measured [74].

Soon after in an experiment at MIT, Andrews *et al.* formed two separate Bose-Einstein condensates in a double-well potential. These were then released from the trap and allowed to ballistically expand. With the use of a clever imaging technique, they were able to observe interference between the two condensates [75]. Röhrl *et al.* [76] calculated the expected fringe spacing based on the parameters of Ref. [75], and found good agreement between theory and experiment.

### Four-wave mixing

In Ref. [77] Trippenbach *et al.* investigate the possibility of the atom-optical analogue of four-wave mixing (4WM). In nonlinear optics, 4WM is the interaction of three wavelengths of light in a nonlinear medium such that a fourth wavelength is generated. It can be thought of as a photon from each of two beams interacting via the medium. If energy and momentum can be conserved, one photon can be stimulated into the third beam, with a fourth beam also being produced.

Trippenbach *et al.* suggested that the same process could be observed with three BECs, each with a different momentum. They performed calculations using the 2D and 3D GPE suggesting that 4WM could be observed experimentally, although it would be different from the optical case due to the different energy-momentum dispersion relation.

An experiment was soon performed by the group of W. D. Phillips at NIST [44]. In the same paper, they model their experiment using the GPE, finding good agreement with their observations. The authors of Ref. [77] have recently carried out a more detailed study of 4WM with BECs in Ref. [78].

### Superfluidity

There has been much literature on the link between Bose-Einstein condensation and superfluidity. Here we concentrate on two situations that provide evidence that a trapped BEC is a superfluid.

In Ref. [79] Guèry-Odelin and Stringari propose an experiment that offers evidence of the superfluidity of a Bose condensate. They suggest that the “scissors” mode of a condensate in a cylindrically symmetric harmonic trap can be excited by a small, sudden rotation of the trap about the $x$-axis. In an uncondensed gas this would excite two modes of oscillation, one rotational and one irrotational. However, the GPE predicts that only irrotational flow should be observed for a Bose condensate, and this is a characteristic property of superfluids.

Soon afterwards, Maragó *et al.* performed this experiment for both a pure condensate and an uncondensed cloud [46]. As predicted, only irrotational flow was observed for the condensate. This experiment has now been extended to finite temperature, and the frequency shifts and damping rates have been measured [80].

Also, the MIT group have studied the effect of stirring a BEC with a blue-detuned laser beam. By the use of time-of-flight imaging they initially determined that there was a critical velocity of the laser beam above which significant heating of the condensate was observed [47]. Later they carried out a more quantitative analysis using non-destructive imaging techniques during the stirring process [48]. The observed flow pattern showed a critical velocity for the onset of a drag force between the laser beam and the condensate, in agreement with their earlier experiments. The existence of a critical velocity below which there is suppressed dissipation is another characteristic property of superfluids.

Similar scenarios have been studied using the GPE by Adams and co-workers [81]. They found that at velocities below a critical value, an almost negligible amount of energy is transferred to the system by the excitation of phonons at the motion extrema. Above the critical velocity, however, larger energy transfer occurs via vortex formation. This corresponds to significant heating in agreement with the MIT observations.

## 2.4 Kinetic theory

The problem of kinetic theory dates back to the late nineteenth century and the realm of classical physics. Part of its aim is to derive the thermodynamics of a dilute gas from a microscopic theory of particle collisions. In this section we introduce the Boltzmann transport equation that describes the evolution of a classical gas, and its extension to include the effects of quantum statistics. This extension is known as the quantum Boltzmann equation (QBE), and we derive it from the Bose field Hamiltonian of Eq. (2.1). Finally we consider this equation in the limit of large occupation numbers.

### 2.4.1 The Boltzmann transport equation

The system under consideration is a dilute gas of $N$ particles in a box of volume $\Omega$. The details of the dynamics of the individual molecules are not important; instead we are interested in the distribution function of the gas such that

$$f(\mathbf{p},\mathbf{x})\,\frac{d^3\mathbf{p}\,d^3\mathbf{x}}{h^3}, \tag{2.54}$$

is the number of molecules in the volume $d^3\mathbf{x}$ about position $\mathbf{x}$ with a momentum in the range $d^3\mathbf{p}$ about $\mathbf{p}$. By considering the motion of the particles between phase space volume elements, it can be shown that the distribution function obeys

$$\left(\frac{\partial}{\partial t} + \frac{\mathbf{p}}{m} \cdot \nabla_{\mathbf{x}} + \mathbf{F} \cdot \nabla_{\mathbf{p}}\right) f(\mathbf{p}, \mathbf{x}) = \left(\frac{\partial f}{\partial t}\right)_{\text{coll}}, \tag{2.55}$$

where $\mathbf{F}$ is the external force acting on a particle[2], and $(\partial f/\partial t)_{\text{coll}}$ describes the rate of change of the distribution function due to collisions.

The quantity $(\partial f/\partial t)_{\text{coll}}$ can be calculated using classical mechanics, or via quantum mechanical scattering theory [4]. For binary collisions in a classical gas we find

$$\begin{aligned} \left(\frac{\partial f}{\partial t}\right)_{\text{coll}} &= \frac{\sigma}{8\pi m^2 \hbar^3} \int d^3\mathbf{p}_2 d^3\mathbf{p}_3 d^3\mathbf{p}_4\, \delta(\mathbf{p} + \mathbf{p}_2 - \mathbf{p}_3 - \mathbf{p}_4)\, \delta(\epsilon + \epsilon_2 - \epsilon_3 - \epsilon_4) \\ &\times \left\{ f(\mathbf{p}_3, \mathbf{x}) f(\mathbf{p}_4, \mathbf{x}) - f(\mathbf{p}, \mathbf{x}) f(\mathbf{p}_2, \mathbf{x}) \right\}, \end{aligned} \tag{2.56}$$

where $\epsilon = p^2/2m$ is the energy of a particle with momentum $\mathbf{p}$, and $\sigma$ is the $s$-wave scattering cross-section, related to the scattering length via $\sigma = 8\pi a^2$. The delta functions in Eq. (2.56) ensure that momentum and energy are conserved in individual collisions. The combination of Eqs. (2.55) and (2.56) yield the classical Boltzmann transport equation.

Three assumptions are made in the derivation of the Boltzmann equation:

1. The thermal de Broglie wavelengths of the particles are much smaller than the interparticle separation, i.e.

   $$n\Lambda^3 \ll 1, \tag{2.57}$$

   where $n = N/\Omega$ and $\Lambda = \hbar/\sqrt{2mk_BT}$. This is the definition of the phase-space density, and this condition ensures that we are away from the realm of quantum degeneracy.

2. The dilute gas criteria $na^3 \ll 1$ is satisfied, so that only binary collisions need be considered.

3. The momenta of any two particles in a volume element $d^3\mathbf{x}$ are assumed to be uncorrelated, such that the probability of finding them simultaneously

---

[2] In a trap we will, of course, have $\mathbf{F} = -\nabla_{\mathbf{x}} V_{\text{trap}}(\mathbf{x})$.

> is simply the product of finding each individually. This is known as the assumption of molecular chaos. While collisions will cause correlations, we are effectively making the Markov approximation—that the correlation will be unimportant on the time scale that we are interested in.

In general these assumptions are well satisfied, and the Boltzmann equation gives an excellent dynamical description of cold alkali gases. It has been used to study the dynamics of a Bose gas from the point at which it is transferred to the magnetic trap and evaporatively cooled [82, 83, 84, 85]. It is only near the regime of quantum degeneracy that it fails.

The Boltzmann equation is difficult to solve numerically, and two important techniques have been applied in its solution. The first is a Monte Carlo method that simulates a large number of trajectories, each representing a sample of the atoms in the gas [86]. This has the advantage of being fully three-dimensional, but it introduces statistical noise into the calculations.

The second technique is to simplify the equation using the assumption of ergodicity—that the distribution function of the system depends only on the energy of the particles. By applying the operation

$$\int d^3\mathbf{x} \int d^3\mathbf{p} \;\; \delta(\varepsilon(\mathbf{p},\mathbf{x}) - \varepsilon), \tag{2.58}$$

to both sides of the full Boltzmann equation, it is possible to derive the ergodic Boltzmann equation [84]

$$g(\varepsilon)\frac{\partial f(\varepsilon)}{\partial t} = \frac{m\sigma}{\pi^2\hbar^3}\int d\varepsilon_2 d\varepsilon_3 d\varepsilon_4 \, \delta(\Delta) g(\varepsilon_{\min})\{f(\varepsilon_3)f(\varepsilon_4) - f(\varepsilon)f(\varepsilon_2)\}. \tag{2.59}$$

where $\Delta = \varepsilon + \varepsilon_2 - \varepsilon_3 - \varepsilon_4$, $\varepsilon_{\min} = \min(\varepsilon, \varepsilon_2, \varepsilon_3, \varepsilon_4)$ and the function $g(\varepsilon)$ is the density of states of the system. This describes the number of quantum levels of the system with energies between $\varepsilon$ and $\varepsilon + d\varepsilon$, and its functional form for a harmonic trap is derived in Appendix C.

The assumption of ergodicity greatly simplifies the numerical problem to be solved, and we make use of it in this thesis. There can be situations when it is not appropriate; however, studies have shown that any non-ergodicity in the initial distribution is damped on the scale of a few collision times [87, 82]. Therefore it seems a reasonable approximation to make if we are interested in longer time scales.

### 2.4.2 The quantum Boltzmann equation

The quantum Boltzmann equation (QBE) is the extension of the Boltzmann equation to include the quantum statistical effects of particle scattering in the system [88]. It can be written as

$$\begin{aligned}
&\left(\frac{\partial}{\partial t} + \frac{\hbar \mathbf{K}}{m} \cdot \nabla_{\mathbf{x}} - \frac{1}{\hbar} \nabla_{\mathbf{x}} V_{\text{trap}}(\mathbf{x}) \cdot \nabla_{\mathbf{K}}\right) f(\mathbf{K}, \mathbf{x}) \\
&\quad = \frac{U_0^2}{4\pi^3\hbar^2} \int d^3\mathbf{K}_2 \int d^3\mathbf{K}_3 \int d^3\mathbf{K}_4 \, \delta(\mathbf{K} + \mathbf{K}_2 - \mathbf{K}_3 - \mathbf{K}_4) \, \delta(\omega + \omega_2 - \omega_3 - \omega_4) \\
&\qquad \times \Big\{ \Big[1 \pm f(\mathbf{K}, \mathbf{x})\Big] \Big[1 \pm f(\mathbf{K}_2, \mathbf{x})\Big] f(\mathbf{K}_3, \mathbf{x}) f(\mathbf{K}_4, \mathbf{x}) \\
&\qquad\qquad - f(\mathbf{K}, \mathbf{x}) f(\mathbf{K}_2, \mathbf{x}) \Big[1 \pm f(\mathbf{K}_3, \mathbf{x})\Big] \Big[1 \pm f(\mathbf{K}_4, \mathbf{x})\Big] \Big\}, \qquad (2.60)
\end{aligned}$$

where the upper (lower) signs correspond to bosons (fermions), and we have redefined our distribution function in terms of $\mathbf{K} = \mathbf{p}/\hbar$. The factors $[1 \pm f(\mathbf{K}, \mathbf{x})]$ describe the stimulation (bosons) or suppression (fermions) of the scattering processes for each type of particle. We can see that if the number of particles in a phase-space cell $f(\mathbf{K}, \mathbf{x}) \ll 1$, then we can approximate $1 + f(\mathbf{K}, \mathbf{x}) \approx 1$ and the QBE reduces exactly to the Boltzmann equation.

As was the case with the Boltzmann equation, the QBE can also be converted to an ergodic form, and several authors have considered this simplified equation. For example, Snoke and Wolf used the ergodic QBE to determine whether BEC was possible in a gas of excitons [89], while Kagan *et al.* considered the time for formation of a condensate in a weakly-interacting Bose gas [90]. Holland *et al.* studied the formation of a condensate in an ideal gas in a spherical harmonic trap [91], and finally Yamashita *et al.* [92] extended the truncated Boltzmann approximation of Luiten *et al.* [84] to the QBE to study condensate formation.

### 2.4.3 Derivation of the QBE

The quantum Boltzmann equation gives an accurate description of the time evolution of a Bose gas well above the transition temperature. In this regime the mean time between particle collisions is long compared to the duration of a collision, and so the eigenstates of $\hat{H}_0$ provide a good basis. This means that the interaction part of the Hamiltonian $\hat{H}_I$ can be treated as a perturbation.

The operators $\tilde{a}_p$ have no mean value above the transition temperature, and so we want an equation of motion for the mean number of particles in mode $p$,

$\langle\hat{n}_p\rangle = \langle\tilde{a}_p^\dagger\tilde{a}_p\rangle$. From Eq. (2.17) we find

$$\frac{d\hat{n}_p}{dt} = -\frac{i}{\hbar}\sum_{qmn}\langle pq|V|mn\rangle\tilde{a}_p^\dagger\tilde{a}_q^\dagger\tilde{a}_m\tilde{a}_n e^{i(\omega_p+\omega_q-\omega_m-\omega_n)t} + h.c., \tag{2.61}$$

where *h.c.* is the hermitian conjugate. To attempt to find a closed expression for the evolution of $\hat{n}_p$, we can find an equation of motion for the quantity $\tilde{a}_p^\dagger\tilde{a}_q^\dagger\tilde{a}_m\tilde{a}_n$ which appears on the right-hand side of Eq. (2.61). However, this new equation for four operators contains terms involving six operators, and the equations of motion for six operators involve eight operators and so on. Instead, we truncate this series at the first iteration, approximately solve the equation for $\tilde{a}_p^\dagger\tilde{a}_q^\dagger\tilde{a}_m\tilde{a}_n$ and substitute the result back into Eq. (2.61).

One way to derive an equation of motion for $\tilde{a}_p^\dagger\tilde{a}_q^\dagger\tilde{a}_m\tilde{a}_n$ would be to commute it with the Hamiltonian. Another equivalent method (which will be useful for other purposes later) is simply to use the chain rule. We can formally write the solution as

$$\begin{aligned}
\tilde{a}_p^\dagger\tilde{a}_q^\dagger\tilde{a}_m\tilde{a}_n &= \int_{-\infty}^{t} dt'\frac{d}{dt'}\left(\tilde{a}_p^\dagger\tilde{a}_q^\dagger\tilde{a}_m\tilde{a}_n\right), \\
&= \int_{-\infty}^{t} dt'\left[\frac{d\tilde{a}_p^\dagger}{dt'}\tilde{a}_q^\dagger\tilde{a}_m\tilde{a}_n + \tilde{a}_p^\dagger\frac{d\tilde{a}_q^\dagger}{dt'}\tilde{a}_m\tilde{a}_n + \tilde{a}_p^\dagger\tilde{a}_q^\dagger\frac{d\tilde{a}_m}{dt'}\tilde{a}_n + \tilde{a}_p^\dagger\tilde{a}_q^\dagger\tilde{a}_m\frac{d\tilde{a}_n}{dt'}\right].
\end{aligned} \tag{2.62}$$

We now substitute Eq. (2.17) for each of the $d\hat{a}_k/dt$. This leaves us with a long and complicated expression, and working with it is predominantly an exercise in keeping track of subscripts. Instead, as an outline of the full calculation we consider only the last term of Eq. (2.62). We have

$$\begin{aligned}
&\int_{-\infty}^{t} dt'\left(\tilde{a}_p^\dagger\tilde{a}_q^\dagger\tilde{a}_m\frac{d\tilde{a}_n}{dt'}\right) \\
&= -\frac{i}{\hbar}\sum_{jkl}\delta_{in}\langle ij|V|kl\rangle\int_{-\infty}^{t} dt'\tilde{a}_p^\dagger\tilde{a}_q^\dagger\tilde{a}_m\tilde{a}_j^\dagger\tilde{a}_k\tilde{a}_l e^{i(\omega_i+\omega_j-\omega_k-\omega_l)t'}, \\
&= -\frac{i}{\hbar}\sum_{jkl}\delta_{in}\langle ij|V|kl\rangle\int_{-\infty}^{t} dt' \\
&\quad\times(\tilde{a}_p^\dagger\tilde{a}_q^\dagger\tilde{a}_j^\dagger\tilde{a}_m\tilde{a}_k\tilde{a}_l + \tilde{a}_p^\dagger\tilde{a}_q^\dagger\tilde{a}_k\tilde{a}_l\delta_{mj})e^{i(\omega_i+\omega_j-\omega_k-\omega_l)t'}.
\end{aligned} \tag{2.63}$$

where we have arranged the creation and annihilation operators in normal order.

It is at this stage that we introduce our first approximation. The free evolution of the operators has already been removed and so assuming the interaction is a perturbation, over the period of the integral most of the time dependence is contained in the exponential. We can therefore take the operators outside of the integral, and replace their time dependence by the time at the upper limit. (See Appendix A for further details of this approximation.) Implicit in this procedure is the Markov approximation, that assumes that correlations between the operators are unimportant on the time scale of interest. The integral then leaves us with a delta function when the frequencies of the modes add to zero, and a principal part when they do not. We assume that the principal part is negligible, which leaves us with

$$\begin{aligned}\int_{-\infty}^{t} dt' \left(\tilde{a}_p^\dagger \tilde{a}_q^\dagger \tilde{a}_m \frac{d\tilde{a}_n}{dt'}\right) &= -\frac{i\pi}{\hbar}\sum_{jkl}\delta_{in}\langle ij|V|kl\rangle\delta(\omega_i+\omega_j-\omega_k-\omega_l) \\ &\quad \times(\tilde{a}_p^\dagger \tilde{a}_q^\dagger \tilde{a}_j^\dagger \tilde{a}_m \tilde{a}_k \tilde{a}_l + \tilde{a}_p^\dagger \tilde{a}_q^\dagger \tilde{a}_k \tilde{a}_l \delta_{mj}). \qquad (2.64)\end{aligned}$$

Combining all the terms that arise out of this procedure, and making use of the symmetries of the indices, Eq. (2.61) becomes

$$\begin{aligned}\frac{d\hat{n}_p}{dt} &= \frac{2\pi}{\hbar^2}\sum_{\substack{qmn\\ijkl}}\langle pq|V|mn\rangle\langle ij|V|kl\rangle\delta(\omega_i+\omega_j-\omega_k-\omega_l) \\ &\quad \times\Big[\tilde{a}_i^\dagger \tilde{a}_j^\dagger \tilde{a}_p^\dagger \tilde{a}_l \tilde{a}_m \tilde{a}_n \delta_{kq} + \tilde{a}_i^\dagger \tilde{a}_j^\dagger \tilde{a}_q^\dagger \tilde{a}_l \tilde{a}_m \tilde{a}_n \delta_{kp} + \tilde{a}_i^\dagger \tilde{a}_j^\dagger \tilde{a}_m \tilde{a}_n \delta_{kq}\delta_{lp} \\ &\quad -\tilde{a}_p^\dagger \tilde{a}_q^\dagger \tilde{a}_i^\dagger \tilde{a}_m \tilde{a}_k \tilde{a}_l \delta_{jn} - \tilde{a}_p^\dagger \tilde{a}_q^\dagger \tilde{a}_i^\dagger \tilde{a}_n \tilde{a}_k \tilde{a}_l \delta_{jm} - \tilde{a}_p^\dagger \tilde{a}_q^\dagger \tilde{a}_k \tilde{a}_l \delta_{jn}\delta_{im}\Big]. \qquad (2.65)\end{aligned}$$

The next step is to take the expectation value of Eq. (2.65), as we are concerned with the time evolution of the *average* occupation of any individual level. In fact, it is most useful to take the ensemble average, which can be written as

$$\langle\hat{A}\rangle = \mathrm{Tr}(\hat{\rho}\hat{A}), \qquad (2.66)$$

where $\hat{\rho}$ is the density matrix of the system, and Tr denotes the trace operation. We are left to calculate quantities such as $\langle\tilde{a}_i^\dagger \tilde{a}_j^\dagger \tilde{a}_m \tilde{a}_n\rangle$. To do so, we assume that our system is near thermal equilibrium so that we can use Wick's theorem [93]. This states that for any system with a Hamiltonian that is a quadratic form in creation and annihilation operators, the ensemble average of any product of operators is simply the contraction of all possible pairings. For example we have

$$\langle\tilde{a}_i^\dagger \tilde{a}_j^\dagger \tilde{a}_m \tilde{a}_n\rangle = \langle\tilde{a}_i^\dagger \tilde{a}_j^\dagger\rangle\langle\tilde{a}_m \tilde{a}_n\rangle + \langle\tilde{a}_i^\dagger \tilde{a}_n\rangle\langle\tilde{a}_j^\dagger \tilde{a}_m\rangle + \langle\tilde{a}_i^\dagger \tilde{a}_m\rangle\langle\tilde{a}_j^\dagger \tilde{a}_n\rangle. \qquad (2.67)$$

This relation is exact at thermal equilibrium, and should be a very good approximation nearby.

We now make use of a further approximation, known as the random phase approximation (RPA). This states that if the density matrix for the system is diagonal, then we have

$$\langle \tilde{a}_i^\dagger \tilde{a}_j^\dagger \rangle = \langle \tilde{a}_i \tilde{a}_j \rangle = 0, \qquad \langle \tilde{a}_i^\dagger \tilde{a}_j \rangle = n_i \delta_{ij}. \tag{2.68}$$

This will be an excellent approximation away from condensation, as the interaction Hamiltonian $\hat{H}_I$ is only a small perturbation to the ideal gas Hamiltonian $H_0$. Thus we have

$$\begin{aligned}
\langle \tilde{a}_i^\dagger \tilde{a}_j^\dagger \tilde{a}_m \tilde{a}_n \rangle &= n_m n_n (\delta_{in}\delta_{jm} + \delta_{im}\delta_{jn}), && (2.69)\\
\langle \tilde{a}_i^\dagger \tilde{a}_j^\dagger \tilde{a}_p^\dagger \tilde{a}_l \tilde{a}_m \tilde{a}_n \rangle &= n_l n_m n_n (\delta_{il}\delta_{jm}\delta_{pn} + \delta_{il}\delta_{jn}\delta_{pm} + \delta_{im}\delta_{jl}\delta_{pn} \\
&\quad + \delta_{im}\delta_{jn}\delta_{pl} + \delta_{in}\delta_{jl}\delta_{pm} + \delta_{in}\delta_{jm}\delta_{pl}). && (2.70)
\end{aligned}$$

On substituting these relations into Eq. (2.65) the final result is

$$\begin{aligned}
\frac{dn_p}{dt} &= \frac{4\pi}{\hbar^2}\sum_{qmn} |\langle pq|V|mn\rangle|^2 \delta(\omega_p + \omega_q - \omega_m - \omega_n) \\
&\qquad \times [(n_p+1)(n_q+1)n_m n_n - n_p n_q (n_m+1)(n_n+1)] && (2.71a)\\
&+ \frac{8\pi}{\hbar^2}\sum_{qmn} \langle pq|V|pn\rangle \langle mn|V|mq\rangle n_p n_m (n_n - n_q)\delta(\omega_n - \omega_q) && (2.71b)\\
&+ \frac{8\pi}{\hbar^2}\sum_{qmn} \langle pq|V|qn\rangle \langle mn|V|mp\rangle n_q n_m (n_n - n_p)\delta(\omega_n - \omega_p). && (2.71c)
\end{aligned}$$

The first part of this expression, Eq. (2.71a) is the standard quantum Boltzmann equation; however, the lines of Eq. (2.71b) and (2.71c) do not appear in most definitions of the QBE. We would like to note the following about these terms:

1. The scattering processes described by the matrix elements of these terms involves a third particle, and hence these collision terms are of higher order than those described by Eq. (2.71a).

2. If we calculate the matrix elements using the contact potential approximation

in the homogeneous limit, then these terms become

$$\text{Eq. (2.71b)} \quad \to \quad \frac{8\pi U_0^2}{\hbar^2\Omega^2}\sum_{qmn}\delta(\mathbf{k}_q-\mathbf{k}_n)^2 n_p n_m (n_n-n_q)\delta(\omega_n-\omega_q), \tag{2.72a}$$

$$\text{Eq. (2.71c)} \quad \to \quad \frac{8\pi U_0^2}{\hbar^2\Omega^2}\sum_{qmn}\delta(\mathbf{k}_p-\mathbf{k}_n)^2 n_q n_m (n_n-n_p)\delta(\omega_n-\omega_p). \tag{2.72b}$$

The delta functions in momentum are equivalent to Kronecker delta functions in the quantum labels for the system, and hence these terms vanish.

3. For an ergodic system where the occupation of a level depends only on its energy, these terms are again identically zero.

4. The delta functions in frequency depend on only two of the particle indices, rather than four as for Eq. (2.71a). This means there will be far fewer matches for Eq. (2.71b) and (2.71c), and therefore these can be considered surface terms that become small in the thermodynamic limit.

We are therefore justified in neglecting these terms, and are left with the usual quantum Boltzmann equation

$$\begin{aligned}\frac{dn_p}{dt} &= \frac{4\pi}{\hbar}\sum_{qmn}|\langle pq|V|mn\rangle|^2\delta(\epsilon_p+\epsilon_q-\epsilon_m-\epsilon_n)\\ &\quad\times\Big\{(n_p+1)(n_q+1)n_m n_n - n_p n_q(n_m+1)(n_n+1)\Big\}.\end{aligned} \tag{2.73}$$

**Validity**

The approximations made in the above derivation require the following conditions to hold for the QBE to be valid:

1. The Markov approximation must be valid such that correlations induced by collisions are unimportant.

2. The system should be near equilibrium such that the factorisation of Wick's theorem is valid.

3. There must be a good basis such that the RPA is valid. In our derivation we have assumed that $\hat{H}_I$ should be a perturbation to the system for this to hold. However, if the average effect of $\hat{H}_I$ can be absorbed into $\hat{H}_0$ to form an effective Hamiltonian with a good basis, then the QBE derivation may still

be valid. It must be noted, however, that the Markov approximation may not be valid in this regime as the mean collision time will be much reduced.

### 2.4.4 The GPE kinetic equation

Finally, it is interesting to consider the kinetic equation that would result if we assume that the GPE is a good description of the system of interest.

We expand the time dependent wave function as

$$\psi(\mathbf{x},t) = \sum_k \tilde{c}_k \phi_k(\mathbf{x}) e^{-i\omega_k t}, \tag{2.74}$$

where the $\{\tilde{c}_k\}$ have had their free evolution removed. This is then substituted into the time dependent GPE, Eq. (2.35). Performing the operation $\int d^3\mathbf{x}\phi_p^*(\mathbf{x})$ on both sides results in the basis set representation of the GPE

$$i\hbar \frac{d\tilde{c}_p}{dt} = \sum_{qmn} \langle pq|V|mn\rangle \tilde{c}_q^* \tilde{c}_m \tilde{c}_n e^{i(\omega_p+\omega_q-\omega_m-\omega_n)t}. \tag{2.75}$$

If we compare Eq. (2.75) with the basis set equation of motion for the Bose field Eq. (2.17), we see that these are identical in form but for the replacement $\tilde{a}_k \leftrightarrow \tilde{c}_k$. In fact, we could have derived Eq. (2.75) directly from Eq. (2.17) by assuming the field operator was in a coherent state, and then taking the expectation value.

We can now carry out the same procedure on Eq. (2.75) as was applied to Eq (2.17) in the derivation of the QBE. The only difference is that we are now manipulating $c$-numbers rather than operators, and so any terms arising from commutators in the previous treatment will vanish. This means that the terms of the form $\tilde{a}^\dagger\tilde{a}^\dagger\tilde{a}\tilde{a}$ will disappear from Eq. (2.65), leaving only terms involving six $c$-numbers. With $n_p \equiv \tilde{c}_p^*\tilde{c}_p$ being the number of particles in mode $p$, the resulting GPE kinetic equation is

$$\begin{aligned} \frac{dn_p}{dt} &= \frac{4\pi U_0^2}{\hbar} \sum_{qmn} |\langle pq|mn\rangle|^2 \delta(\epsilon_p+\epsilon_q-\epsilon_m-\epsilon_n) \\ &\qquad \times \Big\{ (n_p+n_q)n_m n_n - n_p n_q (n_m+n_n) \Big\}. \end{aligned} \tag{2.76}$$

This is exactly the same form as the QBE, Eq. (2.73), except that the spontaneous collision terms are excluded. This equation was first considered by Svistunov in a study of the formation of a condensate in a weakly-interacting Bose gas [94].

Some of the approximations made in the derivation of the GPE kinetic equation may not hold in the presence of a condensate. In particular, the assumption of coherences decaying on a faster time scale than the collision time is unlikely to be valid. The GPE kinetic equation does, however, give us an understanding of the dynamics that are included in the full GPE.

### Interpretation

From Eq. (2.76) we can see that the GPE contains stimulated collision processes only. To understand this, consider the collision $p+q \to m+n$. This process will only be represented by the GPE if one of the levels $(m,n)$ is already occupied. This is in contrast to the QBE, for which the term in the curly brackets of Eq. (2.73) can be written

$$\Big\{(1+n_p+n_q)n_m n_n - n_p n_q(1+n_m+n_n)\Big\}. \tag{2.77}$$

Thus, due to the neglect of the quantum nature of the modes, the GPE can only accurately describe the evolution and interaction of modes which satisfy $n_p \gg 1$, such that $(1+n_p+n_q) \approx (n_p+n_q)$. This will be important in Chapter 5 of this thesis.

# CHAPTER 3

# QUANTUM KINETIC THEORY FOR CONDENSATE GROWTH

Quantum kinetic theory has been developed by Crispin Gardiner, Peter Zoller and co-workers in order to apply the quantum stochastic methods commonly used in quantum optics problems to the kinetics of weakly interacting Bose gases. It attempts to give a unified description of the entire range of Bose gas kinetics, combining both coherent and incoherent processes.

The theory has been developed over the last few years in a series of five papers. We refer to these several times, and so we use the following notation: QKI for [95], QKII for [96], QKIII for [97], QKIV for [98], and QKV for [99].

Each of the papers can be briefly described as follows:

- QKI derives a quantum kinetic master equation for spatially homogeneous systems with only a small amount of condensate present.
- QKII considers stochastic equations derived in QKI as a model of the initiation of a condensate.
- QKIII develops the formalism for the case of a trapped Bose gas. It considers the special situation where the large majority of the atoms are above a fixed energy $E_R$, and can be treated as a bath with a fixed chemical potential $\mu$ and temperature $T$.
- QKIV calculates the steady-state intensity and amplitude fluctuations of a trapped Bose gas at finite temperature using the formalism of QKIII.

- Most recently, QKV generalises the work of QKIII to allow the vapour of atoms above $E_R$ to be time dependent, using a quantum kinetic master equation of the form of QKI appropriately modified for the presence of a trap.

Another series of papers studying the formation of a Bose-Einstein condensate in a trapped gas have resulted from the formalism [100, 101, 102, 103, 104]. The first description of condensate growth [100] arose from QKIII, and considered only the dynamics of the condensate occupation coupled to a bath cooled to below the transition temperature. The second, more detailed treatment [101, 102] included the other low lying states of the system, but still treated the majority of the system as a thermal bath. A detailed description of this model was published as QKVI [103].

In Chapter 4 we present this author's most recent work on condensate growth, published as QKVII [104]. This arises from a combination of the methods of QKIII and QKV, and includes the time dependence of the vapour above the energy $E_R$. In this chapter we give an outline of the basis of quantum kinetic theory, and in particular the parts relevant to the growth of a BEC.

## 3.1 QKI : Homogeneous Bose gas

Quantum kinetic theory essentially involves the derivation of a *quantum kinetic master equation* (QKME) that describes the evolution of the density operator of a Bose gas.

For the homogeneous case the theory begins with the standard second quantised many-body Hamiltonian for an interacting Bose gas Eq. (2.1) with the trapping potential set to zero. In this chapter we make use of the replacement of the real interatomic potential by the two-body T-matrix, and hence use $V(\mathbf{x}) = U_0\,\delta(\mathbf{x})$.

Quantum kinetic theory proceeds in a similar spirit to the original description of the quantum Boltzmann equation, but uses a fully quantum mechanical description of the system. To derive the QKME, the phase space of the system is divided into cells of volume $h^3$, creating coarse-grained position and momentum variables. A wavelet basis is used, where (in one dimension) the wavelets are defined as

$$v_K(x,r) = \frac{1}{2\sqrt{\pi\Delta}}\int_{K-\Delta}^{K+\Delta} e^{ik(x-r)}dk, \tag{3.1}$$

$$\equiv \frac{e^{iK(x-r)}}{\sqrt{\pi\Delta}}\frac{\sin[\Delta(x-r)]}{x-r}. \tag{3.2}$$

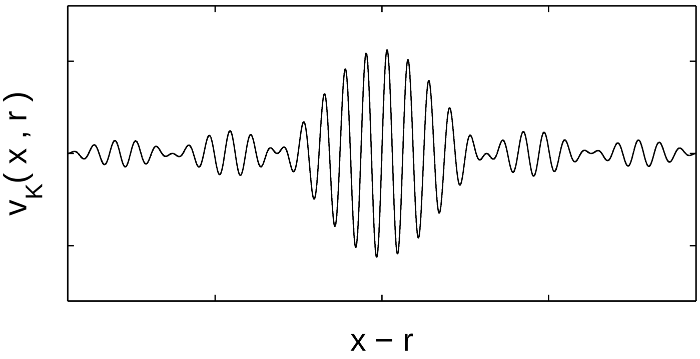

Figure 3.1: Representation of the shape of a wavelet function.

If $r = n\pi\Delta$ with $n$ an integer, then these functions form a complete orthonormal basis. Each wavelet has a momentum in the range $[\hbar(K-\Delta), \hbar(K+\Delta)]$, and is localised about the point $r$, as depicted in Fig. 3.1. In the three-dimensional generalisation of this basis, the field operator can be expanded as

$$\hat{\Psi}(\mathbf{x}) = \sum_{\mathbf{K},\mathbf{r}} v^*_{\mathbf{K}}(\mathbf{x},\mathbf{r})\hat{a}_{\mathbf{K}}(\mathbf{x},\mathbf{r}), \tag{3.3}$$

where the commutation relation for the ladder operators is

$$[\hat{a}_{\mathbf{K}}(\mathbf{x},\mathbf{r}), \hat{a}^\dagger_{\mathbf{K}}(\mathbf{x},\mathbf{r})] = \delta_{\mathbf{r}\mathbf{r}'}\delta_{\mathbf{K}\mathbf{K}'}. \tag{3.4}$$

The state of the system can thus be described quantum mechanically by the Fock state $|\mathbf{n}\rangle$, where $\mathbf{n} \equiv \{n_i\}$ is the set of the occupation numbers of the cells.

The substitution of the Hamiltonian expanded in this basis into the von Neumann equation of motion for the density operator and the application of standard techniques from quantum optics [105] yields the QKME, Eq. (75a–e) of QKI. No classical assumptions are made, so this equation should be valid from the classical to the quantum degenerate regime.

The principles involved in the derivation of the QKME are similar to those used in the derivation of quantum Boltzmann equation described in Sec. 2.4.3. The main difference is the use of a basis that does not diagonalise $\hat{H}_0$. The eigenstates in the homogeneous case are plane waves which have an infinite spatial extent. The wavelet basis functions used in the derivation of the QKME, however, have a width in momentum space. This causes them to be localised in real space allowing the system to be spatially varying.

The QKME description still suffers from some of the same problems as the

QBE. While it offers a probabilistic description of the kinetics of the gas, it does *not* take account of mean field effects on the motion of an individual particle due to the average of the interactions with all other particles. These effects change the eigenvalues of $\hat{H}_0$ when there is significant condensation, and thus the QKME is only valid in the limit of weak condensation.

The only other approximations that enter the theory are the replacement of the true interatomic potential by the two-body T-matrix, and the Markov approximation. The contact potential approximation is valid as long as $ka \ll 1$ for all occupied states, and the Markov approximation is valid when the separation between energy levels is smaller than the energy range of occupied states.

The full QKME is extremely unwieldy and difficult to solve. However, a simplified Quantum Boltzmann Master Equation (QBME) has also been derived, and results from using this are presented in QKII. The QBME neglects any position dependence of the system, and is an equation of motion for the probability $P_{\mathbf{n}}$ that the system will be in a Fock state $|\mathbf{n}\rangle$. The quantum Boltzmann equation can be derived from the QBME by averaging to find $\langle n_i \rangle = \sum_{\mathbf{n}} n_i P_{\mathbf{n}}$, and assuming that the factorisation $\langle n_i n_j \rangle \approx \langle n_i \rangle \langle n_j \rangle$ is valid.

## 3.2 QKIII : Trapped Bose gas

The description of a Bose gas in Sec. 3.1 is valid only for the homogeneous case when there is not a significant amount of condensate present. A different treatment is needed to describe the BECs formed in todays experiments, where there is both a trapping potential and strong condensation.

### 3.2.1 Description of the system

In a trap the major contribution to the mean field is due to the condensate, as it forms a very dense core at the centre of the cloud. For a gas with a positive scattering length, interactions with the condensate atoms cause a repulsive potential to be added to the confining potential, necessarily altering the eigenstates and eigenvalues of the system from that of the non-interacting case.

However, as the condensate is localised in the centre of the trap and the relative magnitude of its interaction with other atoms decreases as their energy increases, its effect will become negligible above some energy $E_R$. Hence, we divide our system into two separate bands:

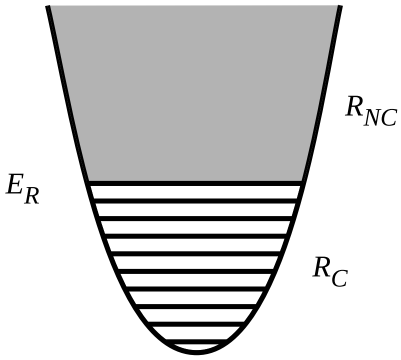

Figure 3.2: Schematic representation of the condensate and non-condensate bands for a harmonic trap

(i) The condensate band $R_C$, whose excitation spectrum is strongly modified by the presence of a condensate.

(ii) The non-condensate band $R_{NC}$, whose energies are sufficiently high that any modification due to the interaction with the condensate is negligible.

The division between the bands lies at the energy $E_R$. For harmonic traps, as is the case in experiments on Bose condensates, the lower lying levels of the trap are reasonably well separated. However, as the density of states of the trap increases as $E^2$, above a certain energy the levels effectively form a continuum. Thus for a large enough system, $E_R$ will be small enough that the overwhelming majority of atoms will be in the non-condensate band. This makes it possible to describe $R_{NC}$ by a phase space distribution function $f(\mathbf{K}, \mathbf{x})$. In QKIII this is taken to be thermalised, with a fixed chemical potential $\mu$ and temperature $T$. The dynamics of the condensate band, however, are treated fully quantum mechanically. The division of the system into the two bands is depicted in Fig. 3.2.

### 3.2.2 Derivation of the master equation

The standard Hamiltonian Eq. (2.1) is used, but this time with the trapping term included in $\hat{H}_0$. The field operator is split into condensate band and non-condensate band components

$$\hat{\Psi}(\mathbf{x}) = \hat{\phi}(\mathbf{x}) + \hat{\psi}_{NC}(\mathbf{x}), \tag{3.5}$$

and this is substituted into the Hamiltonian which is then separated into three parts. The first describes processes involving only $R_{NC}$, the second describes processes involving only $R_C$, and the third describes processes giving rise to population and/or energy transfer between the bands.

The density operator for the system can also be separated into the contribution from the condensate and non-condensate bands. The density operator for the non-condensate band is assumed to be fully thermalised and is given by

$$\hat{\rho}_{NC} = \exp\left(\frac{\mu\hat{N}_{NC} - \hat{H}_{NC}}{k_B T}\right). \tag{3.6}$$

The condensate band density operator is obtained by tracing over $R_{NC}$

$$\hat{\rho}_C = \mathrm{Tr}_{NC}(\hat{\rho}). \tag{3.7}$$

The master equation for the condensate band is derived using the same techniques as for the homogeneous case, and the result is given as Eq. (50a–f) in QKIII.

### 3.2.3 Bogoliubov transformation for the condensate band

The master equation described above gives an accurate description of the internal dynamics of the condensate band, and an approximate treatment of its coupling to $R_{NC}$. To use it in practice, however, requires the computation of the full spectrum of eigenstates of the condensate band, and some method of approximation is necessary. The Bogoliubov transformation, as outlined in Sec. 2.3.4, is the obvious choice.

In a Bose-condensed system the number of atoms in the ground state is macroscopically large, such that $\langle \hat{a}_0^\dagger \hat{a}_0 \rangle = n_0 \approx N$. This is very much larger than the commutator $[\hat{a}_0, \hat{a}_0^\dagger] = 1$, and therefore in the conventional Bogoliubov transformation the Hamiltonian is approximated by replacing the operator $\hat{a}_0$ by the $c$-number $\sqrt{n_0}$. This procedure breaks the global gauge symmetry of the many-body Hamiltonian, effectively choosing an absolute phase for the condensate. It assumes the condensate is in a coherent state with a *mean* population of $n_0$. However, as described in Chapter 1, the constraint on the number of particles of the system is crucial to the process of Bose condensation, and so there appears to be a contradiction here.

This difficulty can be resolved by arguing that the thermodynamics of the system should be described by the grand canonical ensemble, and we find that the quantity $\hat{H} - \mu N$ should be diagonalised rather than $\hat{H}$. The chemical potential $\mu$ is chosen to ensure that the mean number of particles is conserved. However, in quantum kinetic theory we want to consider processes in which the number of particles in the condensate band can change. This introduces a conceptual difficulty—how can the change in $N$ be accounted for properly if its value is uncertain in the first place?

To resolve this issue, Gardiner developed a *number-conserving* Bogoliubov method [106] similar to earlier treatments [107]. The usual Bogoliubov basis states are written in the form

$$|n_0, \mathbf{n}\rangle, \tag{3.8}$$

where $\mathbf{n} \equiv \{n_i\}$ is the vector of occupation numbers of all particles in excited states inside the condensate band. To solve the problem of number conservation, these basis states are rewritten to remove all explicit reference to $n_0$ by using the total number $N = n_0 + \sum_i n_i$, and hence the new basis is

$$|N, \mathbf{n}\rangle. \tag{3.9}$$

The condensate operators, rather than being replaced by $\sqrt{n_0}$, can now be written in terms of operators involving the total number and the excited states. The result is that the symmetry of the Hamiltonian is not broken, and number conservation is not violated as a consequence. The number-conserving approach gives results to the same accuracy as the usual Bogoliubov method via an expansion of $(1 - \sum_i n_i/N)^{1/2}$. In fact, to the order that they are actually computed in practice the two methods are identical. However, the major advantage of number conservation is that the concept of particle creation and destruction is separated from that of quasiparticles. This means the condensate band can be described by a configuration of a definite number of particles with a definite energy, and therefore can be described by a master equation.

In this formulation, the form of the condensate band field operator is

$$\hat{\phi}(\mathbf{x}) = \hat{B}\left[\xi_N(\mathbf{x}) + \sum_m \frac{\hat{b}_m f_m(\mathbf{x}) + \hat{b}_m^\dagger g_m(\mathbf{x})}{\sqrt{N}}\right]. \tag{3.10}$$

The annihilation operator $\hat{B}$ takes the $R_C$ system from the ground state with $N$ particles to the ground state with $N-1$ particles. The condensate wave function is $\xi_N(\mathbf{x})$, and $f_m(\mathbf{x})$, $g_m(\mathbf{x})$ are the amplitudes for the destruction and creation of a quasiparticle of an energy $\epsilon_N^m$ with the corresponding operators $\hat{b}_m, \hat{b}_m^\dagger$. These operators do not change the total number of particles in the condensate band, while the operator $\hat{B}$ [which multiples everything in Eq. (3.10)] reduces the total number of particles by one.

### 3.2.4 QKV

Before we move on to modelling the growth of a Bose-Einstein condensate, we shall briefly discuss the extension of the work of QKIII to allow the vapour to be time-dependent.

The system is still described by a condensate and a vapour interacting with each other, split into condensate and non-condensate bands as in QKIII. However, instead of $E_R$ being defined as the energy above which the levels are not greatly affected by the presence of a condensate, the division of the bands is made at an energy such that all phonon-like excitations are part of $R_C$, and particle-like excitations are part of $R_{NC}$.

A wavelet basis suitable for a trap is used to represent the vapour, and this obeys a quantum kinetic master equation that in most circumstances is equivalent to a quantum Boltzmann equation. The condensate is again described fully quantum-mechanically, often with the use of the Bogoliubov approximation. The two parts of the system interact via two mechanisms:

- Mean field terms, the largest part of which is estimated and included by defining effective potentials for the condensate and non-condensate bands.

- Master equation terms, which describe the transfer of particles and energy between the condensate and the vapour

The effective potential for each band gives rise to a basis from which the kinetic terms can be calculated. Assuming the non-condensate band is thermalised reduces the description of QKV to that of QKIII.

## 3.3 A model for condensate growth

The full master equation describing the evolution of the condensate band is very complex and rather unwieldy. To give some first insight into the basic structure of its predictions it is necessary to consider only those terms that are significant when there is a large amount of condensate present.

There are six main processes in the master equation that affect the size of the condensate through an atom scattering into or out of $R_C$. Each of these scattering events can be associated with the creation of a quasiparticle, the destruction of a quasiparticle, or no change in the number of quasiparticles. These six transition probabilities can be extracted from the master equation for the condensate defined in terms of the functions $R^{\pm}$ as

$$\begin{aligned} W^{+}(N) &= R^{+}(\xi_N, \mu_C(N)/\hbar), && (3.11)\\ W^{-}(N) &= R^{-}(\xi_{N-1}, \mu_C(N-1)/\hbar), && (3.12)\\ W^{++}_m(N) &= R^{+}(f_m, [\epsilon^m_N + \mu_C(N)]/\hbar), && (3.13)\\ W^{--}_m(N) &= R^{-}(f_m, [\epsilon^m_{N-1} + \mu_C(N-1))/\hbar), && (3.14)\\ W^{+-}_m(N) &= R^{+}(g_m, [-\epsilon^m_N + \mu_C(N)]/\hbar), && (3.15)\\ W^{-+}_m(N) &= R^{-}(g_m, [-\epsilon^m_{N-1} + \mu_C(N-1)]/\hbar). && (3.16) \end{aligned}$$

In these expressions $\mu_C(N)$ is the condensate energy as determined by the Gross-Pitaevskii equation for the condensate band with $N$ particles. Correspondingly, $\epsilon^m_N$ is the energy of the $m$th quasiparticle excitation measured relative to $\mu_C(N)$, for the case that there are $N$ particles in $R_C$. The first superscript of the function $W$ indicates whether a particle is transferred into (+) or out of (−) the condensate band, and the second indicates the creation (+) or destruction (−) of a quasiparticle. The absence of a second superscript indicates no change in the number of quasiparticles, and hence the particle is transferred to or from the condensate. The functions $R^{\pm}(y,\omega)$ are defined by

$$\begin{aligned} R^{+}(y,\omega) &= \frac{U_0^2}{(2\pi)^5\hbar^2}\int d^3\mathbf{x}\int d\Gamma\,\Delta(\Gamma,\omega) f_1 f_2 (1+f_3) W_y(\mathbf{x},\mathbf{k}), && (3.17)\\ R^{-}(y,\omega) &= \frac{U_0^2}{(2\pi)^5\hbar^2}\int d^3\mathbf{x}\int d\Gamma\,\Delta(\Gamma,\omega)(1+f_1)(1+f_2) f_3 W_y(\mathbf{x},\mathbf{k}), && (3.18) \end{aligned}$$

in which we use the notation

$$\begin{aligned} d\Gamma &\equiv d^3\mathbf{K}_1 d^3\mathbf{K}_2 d^3\mathbf{K}_3 d^3\mathbf{k}, && (3.19)\\ \Delta(\Gamma,\omega) &\equiv \delta(\Delta\omega_{123}(\mathbf{x}) - \omega)\delta(\mathbf{K}_1 + \mathbf{K}_2 - \mathbf{K}_3 - \mathbf{k}), && (3.20)\\ \Delta\omega_{123}(\mathbf{x}) &= \omega_{\mathbf{K}_1}(\mathbf{x}) + \omega_{\mathbf{K}_2}(\mathbf{x}) - \omega_{\mathbf{K}_3}(\mathbf{x}), && (3.21)\\ \hbar\omega_{\mathbf{K}}(\mathbf{x}) &= \frac{\hbar^2\mathbf{K}^2}{2m} + V_{\text{trap}}(\mathbf{x}). && (3.22) \end{aligned}$$

The function $f_i \equiv f(\mathbf{K}_i, \mathbf{x})$ is the number of non-condensate atoms per $h^3$ of phase space, and the Wigner function for the wave function $y(\mathbf{x})$ is written as

$$W_y(\mathbf{x}, \mathbf{k}) = \frac{1}{(2\pi)^3} \int d^3\mathbf{v} y^*(\mathbf{x} + \mathbf{v}/2) y(\mathbf{x} - \mathbf{v}/2) \exp(i\mathbf{k} \cdot \mathbf{v}). \tag{3.23}$$

The function $R^+(y, \omega)$ sums over all possible collisions of particles from $R_{NC}$ with momentum $\mathbf{K}_1$ and $\mathbf{K}_2$, resulting in a particle with momentum $\mathbf{K}_3$ remaining in $R_{NC}$ and one with momentum $\mathbf{k}$, energy $\hbar\omega$ and amplitude $y$ in $R_C$. The function $R^-(y, \omega)$ is the corresponding reverse rate.

From these rates we can write a stochastic master equation for the occupation probabilities of the condensate band $p(N, \mathbf{n}) \equiv \langle N, \mathbf{n}|\rho|N, \mathbf{n}\rangle$. This has the form

$$\begin{aligned}
\dot{p}(N, \mathbf{n}) &= 2NW^+(N-1)p(N-1, \mathbf{n}) - 2(N+1)W^+(N)p(N, \mathbf{n}) \\
&+ 2(N+1)W^-(N+1)p(N+1, \mathbf{n}) - 2(N)W^-(N)p(N, \mathbf{n}) \\
&+ \sum_m [2n_m W_m^{++}(N-1)p(N-1, \mathbf{n} - \mathbf{e}_m) - 2(n_m+1)W_m^{++}(N)p(N, \mathbf{n})] \\
&+ \sum_m [2(n_m+1)W_m^{--}(N+1)p(N+1, \mathbf{n} + \mathbf{e}_m) - 2n_m W_m^{--}(N)p(N, \mathbf{n})] \\
&+ \sum_m [2(n_m+1)W_m^{+-}(N-1)p(N-1, \mathbf{n} + \mathbf{e}_m) - 2n_m W_m^{+-}(N)p(N, \mathbf{n})] \\
&+ \sum_m [2n_m W_m^{-+}(N+1)p(N+1, \mathbf{n} - \mathbf{e}_m) - 2(n_m+1)W_m^{-+}(N)p(N, \mathbf{n})],
\end{aligned} \tag{3.24}$$

where the vector $\mathbf{e}_m$ describes the change of the configuration due to the collision, and as such it has two $+1$ and two $-1$ entries, with all others being zero.

To understand this equation, let us consider the first line. The first term is the rate by which a configuration with ($N-1$,$\mathbf{n}$) atoms gains an atom in the condensate $[NW^+(N-1)]$, multiplied by the probability that the system is in this configuration $[p(N-1, \mathbf{n})]$, and thus is added. The second term is the probability that the system is already in the configuration ($N$,$\mathbf{n}$), and gains another atom in the condensate, and therefore this rate is subtracted. The following five lines correspond to similar types of terms but for the five other transition probabilities.

## 3.4 Model A: the first approximation

The terms on the first two lines of Eq. (3.24) represent transitions to the ground state of the condensate and exhibit a stimulated increase in collision rate of order $N$. All other terms involving quasiparticles with transition probabilities $W_m^{\pm\pm}$ are multiplied only by the population $n_m$ which does not become nearly as large. Therefore, as a first approximation for condensate growth we neglect these smaller terms. Multiplying what remains by $N$, and taking expectation values over the probabilities leaves a simple rate equation for the mean number of particles in the condensate band

$$\dot{N} = 2(N+1)W^{+}(N) - 2NW^{-}(N). \tag{3.25}$$

Our final step is to make an attempt at calculating the quantities $W^{\pm}(N)$. To do so we make the following approximations:

1. In practice the condensate wave function is sharply peaked at $\mathbf{x} = 0$ in comparison with the phase space distribution function $f(\mathbf{K}, \mathbf{x})$. Therefore we replace $\mathbf{x}$ wherever it occurs by zero except in the Wigner function, which integrates to give the condensate density in momentum space $|\tilde{\xi}_N(\mathbf{k})|^2$.

2. If the energy range of the condensate band is small (as we have assumed it to be), the range of $\mathbf{k}$ will be small compared with the range of $\mathbf{K}$ in $f(\mathbf{K}, 0)$, and so we can carry out the $\mathbf{k}$ integral (which gives unity).

3. We make the ergodic assumption that the distribution function depends only on energy, and so we replace $f(\mathbf{K}, 0)$ with $f(\varepsilon)$.

This leaves us with the simplified integrals

$$\begin{aligned} W^{+}(N) &= \frac{4ma^2}{\pi\hbar^3} \int d\varepsilon_1\, d\varepsilon_2\, d\varepsilon_3\, f_1 f_2 (1+f_3)\, \delta(\varepsilon_1 + \varepsilon_2 - \varepsilon_3 - \mu_C(N)), & (3.26) \\ W^{-}(N) &= \frac{4ma^2}{\pi\hbar^3} \int d\varepsilon_1\, d\varepsilon_2\, d\varepsilon_3\, (1+f_1)(1+f_2) f_3\, \delta(\varepsilon_1 + \varepsilon_2 - \varepsilon_3 - \mu_C(N)), & (3.27) \end{aligned}$$

where we have written $f_1 \equiv f(\varepsilon_1)$. We note that with these approximations the rates are simply those that would be calculated from the standard quantum Boltzmann equation in ergodic form. From these expressions it is simple to show that in equilibrium

$$W^{+}(N) = \exp\left(\frac{\mu - \mu_C(N)}{k_B T}\right) W^{-}(N), \tag{3.28}$$

where $\mu$ is the chemical potential and $T$ is the temperature of the distribution function $f(\varepsilon)$.

As we are only considering the equation of motion for the mean condensate occupation, we extend the lower limit of the integrals in Eqs. (3.26) and (3.27) from $E_R$ to zero. To simplify the calculation of these rates, we approximate the Bose distribution function $f(\varepsilon)$ for $R_{NC}$ by the Boltzmann distribution

$$f(\varepsilon) = \left[\exp\left(\frac{\varepsilon-\mu}{k_BT}\right) - 1\right]^{-1} \approx \exp\left(\frac{\mu-\varepsilon}{k_BT}\right), \tag{3.29}$$

which will be valid at sufficiently high energies such that $\varepsilon/k_BT \gg 1$. On calculating the integral of Eq. (3.26) we find

$$W^{+}(N) = \frac{4m(ak_BT)^2}{\pi\hbar^3}\mathrm{e}^{2\mu/k_BT}\left\{\frac{\mu_C(N)}{k_BT}K_1\left(\frac{\mu_C(N)}{k_BT}\right)\right\}, \tag{3.30}$$

where $K_1(z)$ is a modified Bessel function. For $\mu_C(N)/k_BT \ll 1$ as is appropriate for most experiments, the quantity in the curly brackets is very close to one.

Making the assumption that the majority of atoms in $R_C$ form the condensate by replacing $N \to n_0$, the overall behaviour of the master equation Eq. (3.24) is described by the rate equation

$$\dot{n}_0 = 2W^{+}(n_0)\left\{\left[1 - \exp\left(\frac{\mu_C(n_0)-\mu}{k_BT}\right)\right]n_0 + 1\right\}, \tag{3.31}$$

where $n_0$ represents the number of atoms in the condensate, and we have made use of Eq. (3.28). This has been called the *simple growth* equation, and solutions were first considered in Ref. [100].

The simple growth equation describes a condensate level in contact with a particle and heat bath with a chemical potential $\mu$ and at temperature $T$. It is in equilibrium when the term in the curly brackets is zero, so solving for the equilibrium number in the ground state $n_{0,\mathrm{eq}}$ we find

$$n_{0,\mathrm{eq}} = \left[\exp\left(\frac{\mu_C(n_0)-\mu}{k_BT}\right) - 1\right]^{-1}, \tag{3.32}$$

i.e. the expected equilibrium occupation for the Bose-Einstein distribution. Above the transition temperature the condensate population is small, and hence $\mu_C(n_0) \approx \varepsilon_0$, the lowest bare energy level of the trap. However, we can imagine an experiment in which the thermal bath has been rapidly cooled below the transition temperature, and the atoms in $R_{NC}$ have come to quasi-equilibrium with a chemical potential $\mu > \mu_C(n_0)$. The condensate level is therefore out of equilibrium with the bath, and the exponential term in the simple growth equation (3.31) will be small. Hence the condensate population will initially obey

$$\dot{n_0} = 2W^+(n_0)\,[n_0 + 1]\,. \tag{3.33}$$

As soon as $n_0$ becomes much larger than one, the process of *bosonic stimulation* will occur, and the growth of the condensate will be exponential.

As the condensate population grows, so does its mean field and hence so does its eigenvalue $\mu_C(n_0)$. If we can assume that the condensate wave function grows adiabatically in its ground state, then for all but the smallest condensates the Thomas-Fermi approximation of Eq. (2.41) gives a good estimate of $\mu_C(n_0)$. As the eigenvalue increases, the exponential term in Eq. (3.31) will cause the stimulated growth to die off, until once again the condensate is in equilibrium with the bath.

Sample growth curves for the first BEC experiment at JILA [15], and the first MIT experiment in their harmonic cloverleaf trap [25] are shown in Fig. 3.3. In these graphs the reported critical temperature and the final number of condensate atoms have been used as input parameters. The predictions for the time of growth, published in Ref. [100], seemed to be of the right order of magnitude—at the time of publication there had been no experimental study of condensate growth. The behaviour should be reasonably well described by the simple growth equation once $n_0$ becomes large, but it was expected that the neglected terms may have a significant effect during the initial stages of growth.

## 3.5 Bosonic stimulation experiment

Soon after the publication of the simple growth paper [100], the Ketterle group at MIT carried out a study of the growth of a BEC [35]. In these experiments a cloud of sodium atoms confined in a “cigar”-shaped magnetic trap was evaporatively cooled to just above the Bose-Einstein transition temperature. Then, in a period of 10 ms the high-energy tail of the distribution was removed with a rapid and rather severe RF cut. The following equilibration resulted in conditions very similar to those described in the above theoretical model. The subsequent appearance of a sharp peak in the density distribution indicated the formation of a condensate.

If we assume condensate growth is initially Bose-stimulated, but the growth

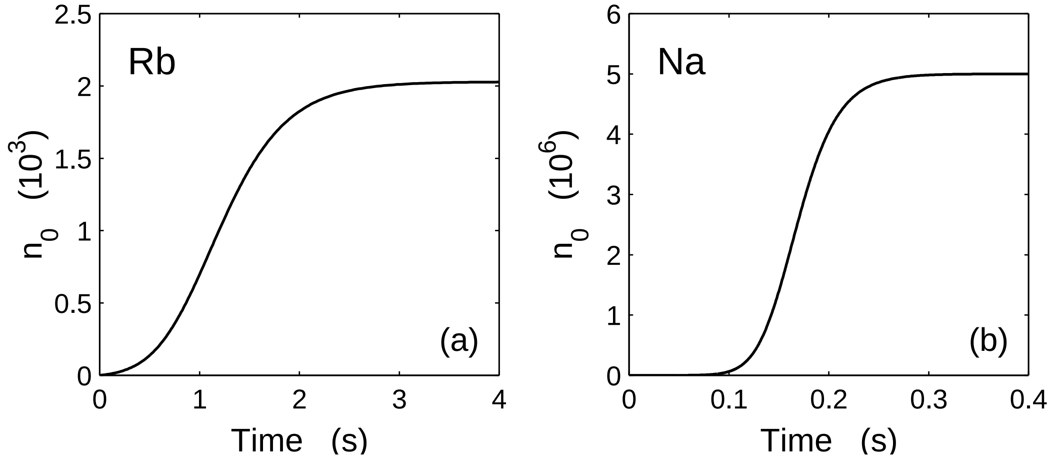

Figure 3.3: Sample solutions to the simple growth equation (3.31). (a) Rubidium atoms with $n_{0,\mathrm{eq}} = 2000$ and $T_c = 170$ nK, as for the first report of BEC [15]. (b) Sodium atoms with $n_{0,\mathrm{eq}} = 5 \times 10^6$ and $T_c = 2$ $\mu$K, matching the first reported parameters for the MIT cloverleaf trap [25].

rate tends to zero as the system nears equilibrium, we can guess at a rate equation for the number of condensate atoms of the form

$$\dot{n}_0(t) = \gamma n_0(0) \left[ 1 - \left( \frac{n_0(t)}{n_0(\infty)} \right)^{\delta} \right]. \tag{3.34}$$

This agrees with the simple growth equation (3.31) if we

1. Neglect the spontaneous term.
2. Assume that $\mu, \mu_C(n_0) \ll k_B T$ and expand the exponential to first order.
3. Use the Thomas-Fermi approximation for $\mu_C(n_0)$, and identify

$$\begin{aligned} \delta &= 2/5, & (3.35) \\ \gamma &= 2W^+(n_0)\frac{\mu}{k_B T} \quad \propto \quad n_0(\infty)^{2/5} T. & (3.36) \end{aligned}$$

The solution to Eq. (3.34) is

$$n_0(t) = n_0(0) e^{\gamma t} \left[ 1 + \left( \frac{n_0(0)}{n_0(\infty)} \right)^{\delta} (e^{\delta \gamma t} - 1) \right]^{-1/\gamma}, \tag{3.37}$$

and the MIT group analysed their growth data by fitting to this function. Their free parameters were the initial condensate population $n_0(0)$ and the growth rate $\gamma$—

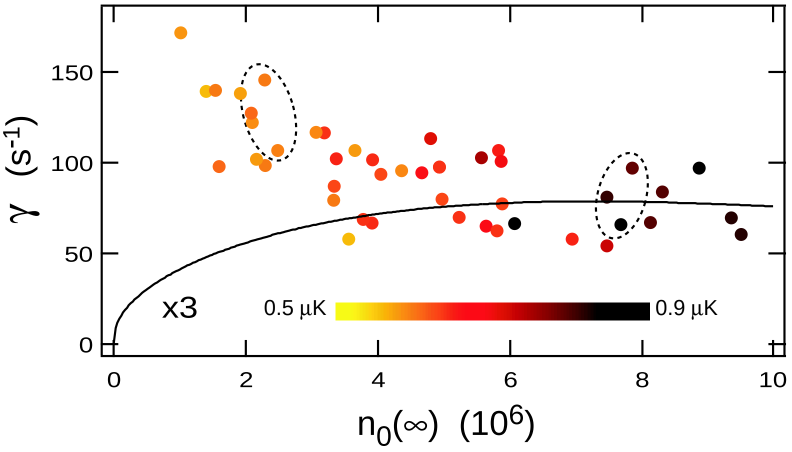

Figure 3.4: Experimental data for the growth of a sodium BEC. The points are growth rates derived from the fitting of the experimental data to the simple growth equation (3.31), whereas the solid line is the behaviour predicted by Eq. (3.36) multiplied by a factor of three. The two clusters of points surrounded by the dashed ellipses indicate the data used to recreate the experimental curves in Fig. 3.6

they found that the fits were not improved by allowing the exponent $\delta$ to vary.

They found that while the *shape* of the growth curves predicted by Eq. (3.37) fitted the data extraordinarily well, the measured growth rates $\gamma$ were between a factor of four to thirty times larger than what was predicted by Eq. (3.36). Theoretically this was not unexpected—some of the simplifications in model A described in the previous section are rather drastic. Indeed, before the results of the experiment became known, another paper on the growth of trapped BECs was prepared and submitted for publication [101]. This removed some of the major approximations, and predicted a speed-up of the growth of up to an order of magnitude depending on the particular parameters.

While the MIT experiment was a beautiful demonstration of bosonic stimulation, the quantitative data they published was less than satisfactory. Only one of the experimental growth curves plotted was accompanied by a full set of parameters, i.e. initial and final temperatures, size of the RF cut, and the total number of atoms in the cloud. Further communication with the authors failed to secure more useful data, and so the most quantitative data available was that presented in Fig. 5 of Ref. [35]. This graph plots $\gamma$ against $n_0(\infty)$, with a colour bar giving an indication of the final temperature, and is reproduced in Fig. 3.4.

## 3.6 Model B: inclusion of quasiparticles

One of the limitations of the treatment of condensate growth in model A is that the overall rate factor, $W^+$, is calculated using an equilibrium *Boltzmann* distribution function with a positive chemical potential $\mu$. To improve upon this model the calculation of $W^+$ should be performed using the Bose-Einstein distribution. However, the chemical potential in the Bose-Einstein distribution must be less than the lowest energy level considered, as the distribution is singular at $\varepsilon = \mu$. This is inconsistent with the requirement that $\mu_C(n_0) \to \mu$ in equilibrium if we do not consider the modifications of the lowest energy levels due to the presence of a condensate. Thus, to go beyond the Boltzmann approximation for $W^+$ requires a much more detailed treatment of the condensate band levels.

Therefore a more realistic model of condensate growth was developed to take account of the quasiparticle levels. As the condensate grows, its energy $\mu_C(n_0)$ increases due to the build up of the mean-field and this leads to the *compression* in energy space of the quasiparticle levels above the condensate, since they necessarily lie between $\mu_C(n_0)$ and $E_R$. By definition the levels above $E_R$ are considered to be unaffected by the condensate. Thus, we calculate $W^+$ using the Bose-Einstein formula for the distribution function of the non-condensate band. The derivation of this quantity has not been published but can be found in Appendix B. The result is

$$W^+(n_0) = \frac{4m(ak_BT)^2}{\pi\hbar^3}\left\{[\ln(1-z)]^2 + z^2\sum_{r=1}^{\infty}[z\,z(n_0)]^r[\Phi(z,1,r+1)]^2\right\}, \tag{3.38}$$

where

$$z = \exp\left(\frac{\mu - E_R}{k_BT}\right), \qquad z(n_0) = \exp\left(\frac{\mu_C(n_0) - E_R}{k_BT}\right). \tag{3.39}$$

The function $\Phi$ is the *Lerch transcendent* [108], defined by

$$\Phi(x,s,a) = \sum_{k=0}^{\infty}\frac{x^k}{(a+k)^s}. \tag{3.40}$$

The occupation of the quasiparticle levels above the condensate is incorporated in the model by the inclusion of all the terms in the stochastic master equation for the occupation probabilities of the condensate band Eq. (3.24). The terms involving the functions $W_m^{\pm\mp}(N)$, however, are set to zero as they arise out of the mixing of creation and annihilation operators in the Bogoliubov method. They represent processes involving the transfer of a particle into the condensate band but the destruction of a quasiparticle (and vice versa), and are expected to be negligible. This approximation means that all the excitations of the condensate band are approximated as being particle-like.

Due to the large number of quasiparticle levels, rather than considering each individually they are grouped into energy bins. The increase in the mean energy of each bin due to condensate growth is accounted for phenomenologically by approximating the density of states in the region of compression using a linear fit, such that the total number of states in each bin remains constant. While rather crude, this approximation is not expected to significantly affect the results—a hypothesis confirmed in Chapter 4 of this thesis.

In a similar manner to the derivation of Eq. (3.28), it can be shown that in equilibrium the rates for particle transfer to (from) the condensate band with the corresponding creation (annihilation) of a quasiparticle satisfy

$$W_m^{++}(N) = \exp\left(\frac{\mu - \mu_C(N) - \epsilon_m}{k_B T}\right) W_m^{--}(N), \tag{3.41}$$

and hence the population growth of the bins is described by similar equations to the simple growth equation (3.31)

$$\dot{n}_m = 2W_m^{++}(n_0)\left\{\left[1 - \exp\left(\frac{\mu - \epsilon_m}{k_B T}\right)\right] n_m + g_m\right\}, \tag{3.42}$$

where $\epsilon_m$ is the mean energy of the bin measured relative to the condensate, and $g_m$ is the number of levels contained in the bin. In practice the approximation $W_m^{++}(n_0) \approx W^+(n_0)$ was used, as the range of energies in the condensate band is much narrower than that of $R_{NC}$.

While this model predicted an increased growth rate, the amount by which condensate growth was accelerated was strongly dependent upon the choice of $E_R$. Also, it was observed that the lowest lying quasiparticle levels became very highly occupied before the initiation of condensate growth. Once the condensate population reached a macroscopic number these levels quickly relaxed to their final equilibrium values.

The reason for this behaviour was the neglect of what we call *scattering processes*, depicted schematically in Fig. 3.5. Without the inclusion of the scattering processes, once a particle had entered a quasiparticle level the only way for it to

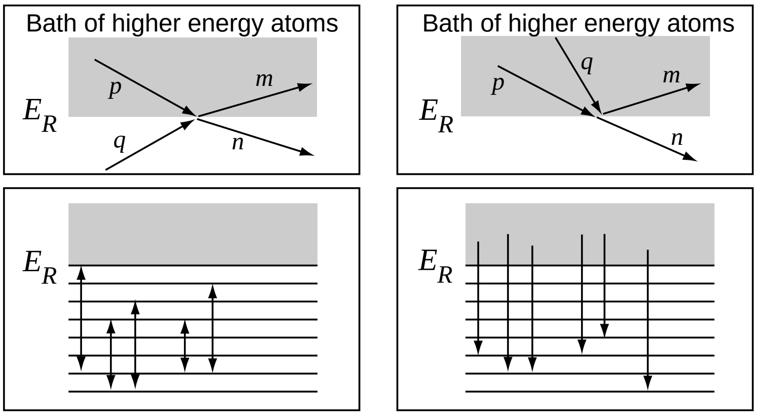

Figure 3.5: The two collision processes that must be included in the description of the condensate band for model B of condensate growth. Left: scattering, right: growth.

end up in the condensate was to first move back into the bath. The more likely route, however, is for an atom from $R_{NC}$ to collide with a quasiparticle and scatter it directly into the condensate level.

Expressions for these scattering rates have been derived from quantum kinetic theory—however, calculating them directly is computationally difficult. Instead, an estimate was derived from the equivalent terms in the quantum Boltzmann equation. The inclusion of these processes in the model had a significant effect on the resulting growth curves. The macroscopic occupation of the lower quasiparticle levels was no longer observed—instead they quickly approached their equilibrium values. The particles that were previously coalescing in these levels were almost immediately scattered into the condensate level. This resulted in a smaller initiation time, and a much sharper onset of condensate growth. In the later stages, however, the curves appeared much the same.

As a test of the approximation of the scattering rates by quantum Boltzmann estimates, further calculations were carried out in which the rates were multiplied by a prefactor that was varied over two orders of magnitude. The prefactor had little effect on the growth curves, however, suggesting that only the *presence* of the scattering terms that was necessary. Significantly, the inclusion of scattering also removed almost all dependence of the growth curves on the exact value chosen for $E_R$.

A full investigation of the details of this model can be found in Refs. [103, 109]. The most important result from this work was the comparison of theoretical growth curves with the data from the experimental paper [35]. Two clusters of points were chosen from the MIT graph reproduced in Fig. 3.4 and these parameters were used

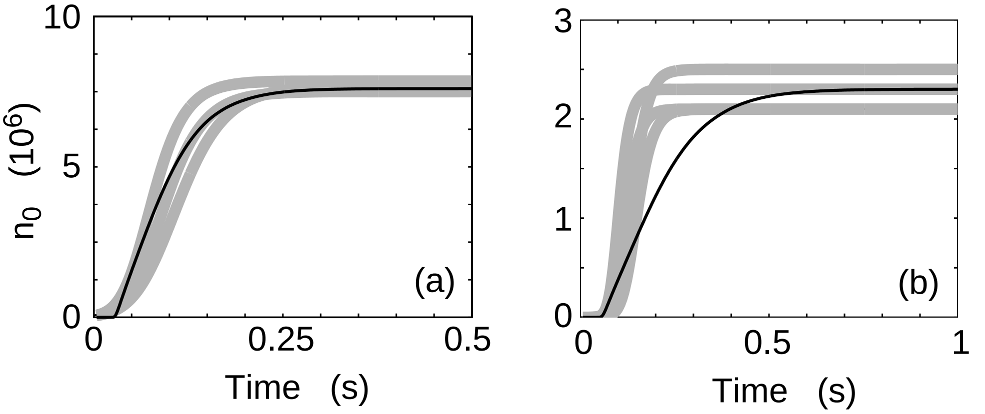

Figure 3.6: Comparison of theoretical curves (black) versus curves fitted to experimental data (grey) taken from Ref. [35] for the growth of condensates in the MIT sodium trap. (a) $n_{0,\mathrm{eq}} = 7.5 \times 10^6$ atoms, $T = 830$ nK, (b) $n_{0,\mathrm{eq}} = 2.3 \times 10^6$ atoms, $T = 590$ nK. The large width of the grey curves is to indicate that these have been fitted to experimental data points, and these will have some scatter.

to plot the approximate solution to the simple growth equation, Eq. (3.37). One cluster was for a condensate of about $7.5 \times 10^6$ atoms at a temperature near 830 nK, whereas the second was for a condensate of $2.3 \times 10^6$ atoms at a temperature of 590 nK.

The theoretical solutions using the more sophisticated model B of condensate growth are plotted in Fig. 3.6, along with the curves from the experimental data. As can be seen, at the higher temperature there is good agreement between theory and experiment. At the lower temperature, however, this is not the case. The condensate growth model generally predicts slower growth rates at lower temperatures, while the opposite was observed in experiments.

## 3.7 Further development

Model B of condensate growth is based on four major approximations:

(i) The part of the vapour with energies higher than $E_R$ is treated as being time-independent.

(ii) The energy levels above the condensate are modified phenomenologically to account for the fact that they must always be greater than the condensate chemical potential, which increases as the condensate grows.

(iii) All levels are treated as being particle-like, on the grounds that detailed calculations [11] have shown that only a very small proportion of excitations of a trapped Bose gas are phonon-like.

(iv) The quantum Boltzmann equation in an ergodic form has been used, in which all levels of a similar energy are assumed to be equally occupied.

In the next chapter we develop a more sophisticated model that will no longer require the first two of these approximations. Abandoning the first means that we are required to take account of all possible collisions, and thus treat the time-dependence of all levels. This comes at a dramatic increase in both the computation time required (hours rather than seconds) and the precision of algorithms required. We also use a density of states that should be closer to the actual density of states as the condensate grows, thereby avoiding the phenomenological modification of energy levels. However, we still treat all of the levels as being particle-like, since it seems unlikely that the few non-particle-like excitations will have a significant effect on the growth as a whole. The ergodic form of the quantum Boltzmann equation is needed to make the computations tractable, and is of necessity retained.

## CHAPTER 4

# GROWTH OF A TRAPPED BOSE-EINSTEIN CONDENSATE

In this chapter we extend earlier models of the growth of a Bose-Einstein condensate [100, 101, 102] to include the full dynamical effects of the thermal cloud by numerically solving a modified quantum Boltzmann equation. We compare our new results with model B of condensate growth described in Sec. 3.6 and Refs. [102, 103, 109], and determine the regime in which the approximations made are valid. We find good agreement with the earlier modelling, except at higher condensate fractions where there is a significant speedup. The discrepancy between theory and experiment remains, however, since the speedup found in these computations does not occur in the parameter regime specified in the experiment. We also investigate what effect the final temperature has on condensate growth, and find it is surprisingly small.

## 4.1 Formalism

The basis of our method is the quantum kinetic theory that was outlined in Chapter 3. This formalism provides a complete framework for the study of a trapped Bose gas in the form of a set of master equations. The full solution of these equations is not feasible, however, and therefore several approximations must be made for any computation. The basic structure of the method used here is essentially the same as that of QKVI [103], the major difference being that all time-dependence of the distribution function is retained. As explained in QKV, QKVI and Ref. [102], quantum kinetic theory leads to a model that can be viewed as a modification of the quantum Boltzmann equation in which

(i) The condensate wave function and energy eigenvalue [the condensate chemical potential $\mu_{\rm C}(n_0)$] are given by the solution of the time-independent Gross-Pitaevskii equation with $n_0$ atoms.

(ii) The excited states above the condensate are the quasiparticle levels appropriate to the condensate wave function. This leads to a density of states for the excited states that is substantially modified from the non-interacting case, as discussed below in Sec. 4.2.2.

(iii) The transfer of atoms between levels is given by a modified quantum Boltzmann equation (MQBE) in the energy representation. This makes the ergodic assumption that the distribution function depends only on energy.

We derive our model from the quantum Boltzmann equation below with these principles in mind.

### 4.1.1 The ergodic form of the quantum Boltzmann equation

The ergodic form of the quantum Boltzmann equation is usually derived by performing the operation

$$\int d^3\mathbf{x} \int d^3\mathbf{K} \;\; \delta(V_{\rm trap}(\mathbf{x}) + \hbar^2 K^2/2m - \varepsilon),$$

on both sides of the full QBE (2.60). Details of this derivation for the classical Boltzmann equation are given in Sec. 4 of Ref. [84], and the application of this method to the QBE is identical. The result is

$$\begin{aligned} g(\varepsilon_p)\frac{df_p}{dt} &= \frac{8ma^2}{\pi\hbar^3}\int d\varepsilon_q \int d\varepsilon_m \int d\varepsilon_n \, g(\varepsilon_{\rm min})\delta(\varepsilon_p + \varepsilon_q - \varepsilon_m - \varepsilon_n) \\ &\quad \times \Big[(1+f_p)(1+f_q)f_m f_n - f_p f_q (1+f_m)(1+f_n)\Big], \end{aligned} \tag{4.1}$$

where we have written $f_p \equiv f(\varepsilon_p)$, $\varepsilon_{\rm min} = \min(\varepsilon_p, \varepsilon_q, \varepsilon_m, \varepsilon_n)$ and the function $g(\varepsilon)$ is the density of states of the system.

In the derivation of Eq. (4.1), the expression for the density of states that naturally occurs is that of the non-interacting gas. This does not allow for any modification of the excitation spectrum due to the mean field that will arise in the formation of a condensate. Thus in this section we give a derivation appropriate to our case, in which the density of states can change with time as the condensate grows. We divide phase space into energy bins labelled by an index $n$ with energies in the range

$$D_n(t) \equiv \left(\epsilon_n(t) - \frac{\delta\epsilon_n(t)}{2}, \epsilon_n(t) + \frac{\delta\epsilon_n(t)}{2}\right), \tag{4.2}$$

and a width of $\delta\varepsilon_n(t)$. The width of each bin changes in time so that the number of states within each bin, $g_n$, is constant.

Starting from the full quantum Boltzmann equation, Eq. (2.60), the ergodic approximation is expressed in terms of this binned description as follows: We set $f(\mathbf{x}, \mathbf{K}, t)$ equal to the value $f_n$, when $\epsilon(\mathbf{x}, \mathbf{K}, t) \equiv \hbar^2\mathbf{K}^2/2m + V_{\text{eff}}(\mathbf{x}, t)$ is inside the $n$th bin, i.e., $\epsilon(\mathbf{x}, \mathbf{K}, t) \in D_n(t)$. Here $V_{\text{eff}}(\mathbf{x}, t)$ is the potential of the trap, as modified by the mean field arising from the presence of the condensate wave function $\psi_0(\mathbf{x})$

$$V_{\text{eff}}(\mathbf{x}, t) = V_{\text{trap}}(\mathbf{x}, t) + n_0(t)U_0|\psi_0(\mathbf{x})|^2. \tag{4.3}$$

Thus we can approximate

$$\frac{\partial f(\mathbf{x}, \mathbf{K}, t)}{\partial t} \to \frac{\partial f_n}{\partial t} \qquad \text{if} \qquad \epsilon(\mathbf{x}, \mathbf{K}, t) \in D_n(t). \tag{4.4}$$

In order to derive the ergodic quantum Boltzmann equation, we define the indicator function $\chi_n(\mathbf{x}, \mathbf{K}, t)$ of the $n$th bin $D_n(t)$ by

$$\chi_n(\mathbf{x}, \mathbf{K}, t) = \begin{cases} 1 & \text{if} \qquad \epsilon(\mathbf{x}, \mathbf{K}, t) \in D_n(t), \\ 0 & \text{otherwise.} \end{cases} \tag{4.5}$$

The number of states in the bin $n$ will be given by $g_n = \int d^3\mathbf{x}\, d^3\mathbf{K}\, \chi_n(\mathbf{x}, \mathbf{K}, t)/h^3$, and is held fixed.

The formal statement of the binned approximation is

$$f(\mathbf{x}, \mathbf{K}, t) \to \sum_n f_n \chi_n(\mathbf{x}, \mathbf{K}, t), \tag{4.6}$$

and the ergodic quantum Boltzmann equation is derived by substituting Eq. (4.6) into the various parts of the quantum Boltzmann equation as follows. For the time derivative term we make this replacement and project onto $D_n(t)$, getting

$$\int \frac{d^3\mathbf{x}d^3\mathbf{K}}{h^3}\chi_n(\mathbf{x},\mathbf{K},t)\frac{\partial f(\mathbf{x},\mathbf{K},t)}{\partial t} \quad\to\quad g_n\frac{\partial f_n}{\partial t}. \tag{4.7}$$

[Note that the expansion of Eq. (4.6) would mean that delta function singularities arise at the upper and lower boundaries of $D_n(t)$, but the condition that $g_n$ is fixed means that these are equal and opposite, and cancel when integrated over $D_n(t)$, giving a result consistent with Eq. (4.7).] We now replace $\partial f(\mathbf{x},\mathbf{K},t)/\partial t$ on the left hand side of Eq. (4.7) by the collision integral that appears on the right hand side of the quantum Boltzmann equation (2.60), and substitute for $f(\mathbf{x},\mathbf{K},t)$ in the collision integral using Eq. (4.6). (The streaming terms in the QBE give no contribution, since the form Eq. (4.6) is a function of the energy $\epsilon(\mathbf{x},\mathbf{K},t)$ only.)

This procedure leads to the *ergodic quantum Boltzmann equation* in the form

$$\begin{aligned} g_n\frac{\partial f_n}{\partial t} &= \frac{4a^2h^3}{m^2}\sum_{pqr}\{f_pf_q(1+f_r)(1+f_n)-(1+f_p)(1+f_q)f_rf_n\} \\ &\quad\times\int\frac{d^3\mathbf{x}d^3\mathbf{K}}{h^3}\int d^3\mathbf{K}_1\int d^3\mathbf{K}_2\int d^3\mathbf{K}_3 \\ &\quad\times\chi_p(\mathbf{x},\mathbf{K}_1,t)\chi_q(\mathbf{x},\mathbf{K}_2,t)\chi_r(\mathbf{x},\mathbf{K}_3,t)\chi_n(\mathbf{x},\mathbf{K},t)\delta\left(\mathbf{K}_1+\mathbf{K}_2-\mathbf{K}_3-\mathbf{K}\right) \\ &\quad\times\delta\left(\epsilon(\mathbf{x},\mathbf{K}_1,t)+\epsilon(\mathbf{x},\mathbf{K}_2,t)-\epsilon(\mathbf{x},\mathbf{K}_3,t)-\epsilon(\mathbf{x},\mathbf{K},t)\right). \end{aligned} \tag{4.8}$$

The final integral is approximated by the method of Ref. [91] to give

$$\begin{aligned} g_n\frac{\partial f_n}{\partial t} &= \frac{8ma^2\bar{\omega}^2}{\pi\hbar}\sum_{pqr}\{f_pf_q(1+f_r)(1+f_n)-(1+f_p)(1+f_q)f_rf_n\} \\ &\quad\times M(p,q,r,n)\Delta(p,q,r,n). \end{aligned} \tag{4.9}$$

where $\bar{\omega}$ is defined in Eq. (2.42), and $\Delta(p,q,r,n)$ is a function that expresses overall energy conservation, and is defined by

$$\Delta(p,q,r,n) = \begin{cases} 1 & \text{when } |\varepsilon_p+\varepsilon_q-\varepsilon_r-\varepsilon_n| \le \frac{1}{2}|\delta\varepsilon_p+\delta\varepsilon_q+\delta\varepsilon_r+\delta\varepsilon_n|, \\ 0 & \text{otherwise.} \end{cases} \tag{4.10}$$

The quantity $M(p,q,r,n)$ which occurs in Eq. (4.9) expresses all the overlap integrals over the states in the bins. It is difficult to calculate exactly, and in our computations we have simply set this to correspond to the value found in Ref. [91]

$$M(p,q,r,n) \quad\to\quad g_{\min(p,q,r,n)}. \tag{4.11}$$

Since we approximate $f(\mathbf{x}, \mathbf{K}, t)$ by a constant value within each bin, energy conservation means that $\bar{E} \equiv \sum_n \varepsilon_n g_n f_n(t)$ is constant. This follows from the full quantum Boltzmann equation, which also implies that

$$\begin{aligned}\sum_{rn} \Delta(p,q,r,n) M(p,q,r,n)(\varepsilon_r + \varepsilon_n) \\ = (\varepsilon_p + \varepsilon_q) \sum_{rn} \Delta(p,q,r,n) M(p,q,r,n).\end{aligned} \tag{4.12}$$

This is the limit to which the binning procedure defines energy conservation.

## 4.2 Details of the model

The most important aspect of our model is the inclusion of the mean-field effects of the condensate. As the population of the condensate increases, the absolute energy of the condensate level also rises due to the atomic interactions. This results in a compression in energy space of the quantum levels directly above the condensate (see Fig. 4.1), and this has an important effect on the evolution of the condensate band.

The correct description of the quantum levels immediately above the ground state requires a quasiparticle transformation when there is a significant condensate population. This is computationally difficult, however, so we make use of a single-particle approximation for these states. This should be reasonable, as most of the growth dynamics will involve higher-lying states that will be almost unaffected by the presence of the condensate. In model B of condensate growth described in Sec. 3.6 this was done using a linear interpolation of the density of states; here we use an approximate treatment based on the Thomas-Fermi approximation.

### 4.2.1 Condensate chemical potential $\mu_{\mathrm{C}}(n_0)$

We consider a harmonic trap with a geometric mean frequency of $\bar{\omega} = (\omega_x \omega_y \omega_z)^{1/3}$. We include the mean-field effects via a Thomas-Fermi approximation for the condensate eigenvalue, which is directly related to the number of atoms in the condensate mode. We use a modified form of this relation in order to give a smooth transition to the correct harmonic oscillator value when the condensate number is small [c.f. Eq. (2.41)]

$$\mu_{\mathrm{C}}(n_0) = \alpha \left[ n_0 + (3\hbar\bar{\omega}/2\alpha)^{5/2} \right]^{2/5}, \tag{4.13}$$

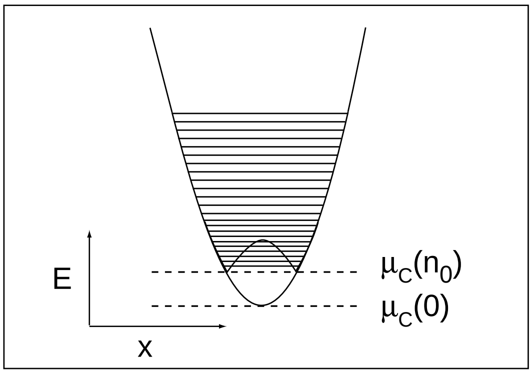

Figure 4.1: Qualitative picture of the compression of the quantum levels above the condensate mode as the condensate eigenvalue increases.

where $\alpha = (15a\bar{\omega}m^{1/2}\hbar^2/4\sqrt{2})^{2/5}$. Thus, for $n_0 = 0$ we have $\mu_C(0) = \varepsilon_0 = 3\hbar\bar{\omega}/2$.

### 4.2.2 Density of states $\bar{g}(\varepsilon)$

The derivation of the density of states that we use is given in Appendix C. Following Timmermans *et al.* [110], we assume a Bogoliubov-like dispersion relation for all particles in the region of the condensate. The expression Timmermans *et al.* derived involved integrals which they did not perform; we have carried these out analytically to give the final result

$$\bar{g}(\varepsilon, n_0) = \frac{\varepsilon^2}{2(\hbar\bar{\omega})^3}\left\{1 + q_1\left(\mu_C(n_0)/\varepsilon\right) + \left(1 - \frac{\mu_C(n_0)}{\varepsilon}\right)^2 q_2\left(\frac{1}{\varepsilon/\mu_C(n_0) - 1}\right)\right\}, \tag{4.14}$$

where

$$q_1(x) = \frac{2}{\pi}\left[\sqrt{x}\sqrt{1-x}(1-2x) - \sin^{-1}(\sqrt{x})\right], \tag{4.15}$$

$$q_2(x) = \frac{4\sqrt{2}}{\pi}\left[\sqrt{2x} + x\ln\left(\frac{1 + x + \sqrt{2x}}{\sqrt{1+x^2}}\right) - \left\{\frac{\pi}{2} + \sin^{-1}\left(\frac{x-1}{\sqrt{1+x^2}}\right)\right\}\right]. \tag{4.16}$$

This function is plotted in Fig. 4.2, along with the density of states for the ideal gas. We see that the density of states of the system varies smoothly as the condensate grows.

As we are assuming that all excitations of the condensate band are particle-like, to be completely consistent we should use a Hartree-Fock dispersion relation

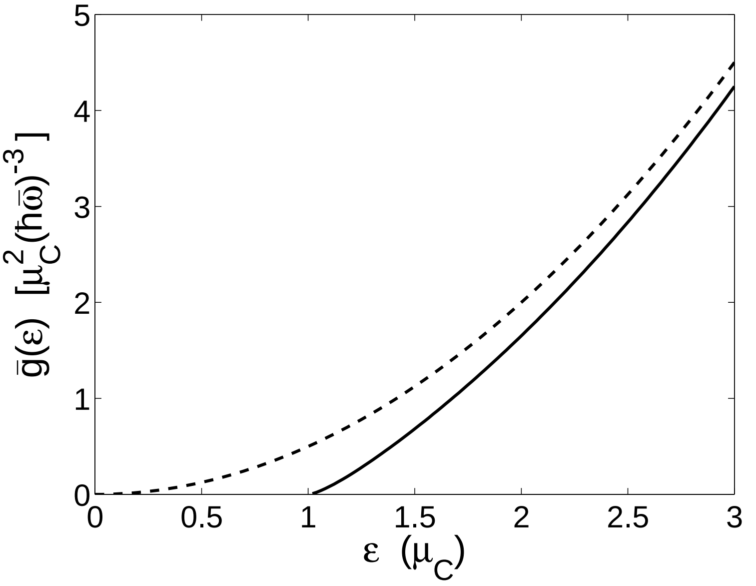

Figure 4.2: The modified density of states including the effect of the condensate mean field (solid curve) compared with the ideal gas density of states (dashed curve) for a harmonic trap.

in the calculation of the density of states. However, we do not expect this small discrepancy to have a noticeable effect on our results.

## 4.3 Numerical methods

### 4.3.1 Representation of the distribution function

The bins we choose for the representation of the distribution function are divided into two distinct regions, as illustrated in Fig. 4.3. The lowest energy region corresponds essentially to the *condensate band* $R_C$ of QKIII, QKVI, and the growth papers [100, 102]. In this region $f_n$ varies rapidly, and so we use a series of fine-grained energy bins up to a fixed energy $E_R \approx 3\mu_{\rm C}(n_{0,\rm max})$, where $n_{0,\rm max}$ is the largest number of particles in the condensate during the simulation. The condensate is a *single* quantum state represented by the lowest energy bin. As the number of particles in the condensate increases, the energy of the condensate level changes according to the Thomas-Fermi approximation of Eq. (4.13). Thus the total energy width of $R_C$ decreases as the condensate grows.

We represent $R_C$ by a fixed number of energy bins of equal width $\delta\varepsilon_n$ with a midpoint at $\varepsilon_n$. As the condensate energy increases, we adjust $\varepsilon_n$ and $\delta\varepsilon_n$ *between* integration time steps, such that all the bins below $E_R$ have equal width. This is

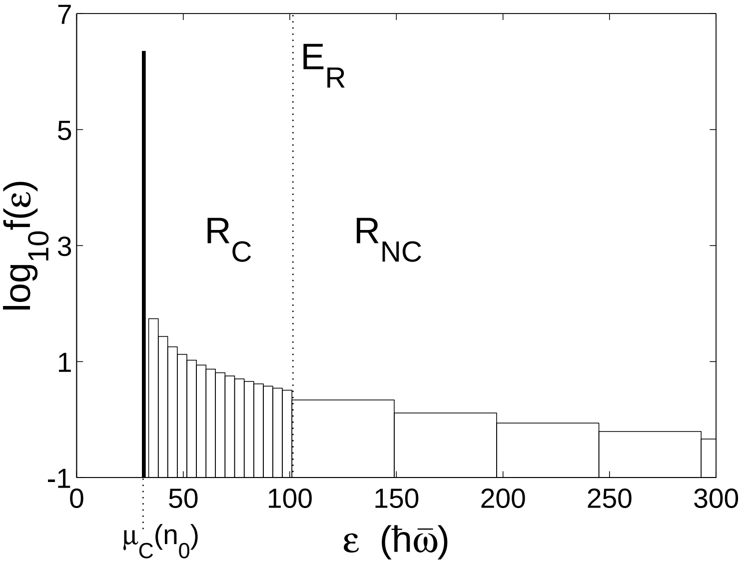

Figure 4.3: The numerical representation of the system with a condensate of $n_0 = 2.3 \times 10^6$ atoms at a temperature of 590 nK. $R_C$ is the condensate band, which is fine-grained, whereas $R_{NC}$ is the non-condensate band, which is coarse-grained. The division between the two bands is fixed at $E_R$. The condensate energy is derived from the Thomas-Fermi approximation.

done by redistributing the particles into new bins after each time step, and thus does not contradict the requirement that $g_n$ is fixed *during* the time step. We find that this is the simplest procedure for the calculation of rates into and out of these levels. We choose the number of bins to be such that the width is not more than about $\delta\varepsilon_n \sim 5\hbar\bar{\omega}$.

The high energy region corresponds to the *thermal bath* of QKIII and the vapour of QKV, as discussed in Chapter 3. This is the region in which $f_n$ is slowly varying, and therefore the energy bins are considerably broader (up to $64\hbar\bar{\omega}$ in the results presented here). To model the bosonic stimulation experiment of Ref. [35], the evaporative cooling is carried out by the sudden removal of the population for all the bins in this region with $\varepsilon_n > \varepsilon_{\text{cut}}$.

### 4.3.2 Solution

There are four different types of collision that can occur given our numerical description of the system. These are depicted in Fig. 4.4, and are

(a) *Growth*: This involves two particles in $R_{NC}$ colliding, resulting in the transfer of one of the particles to the condensate band (along with the reverse process).

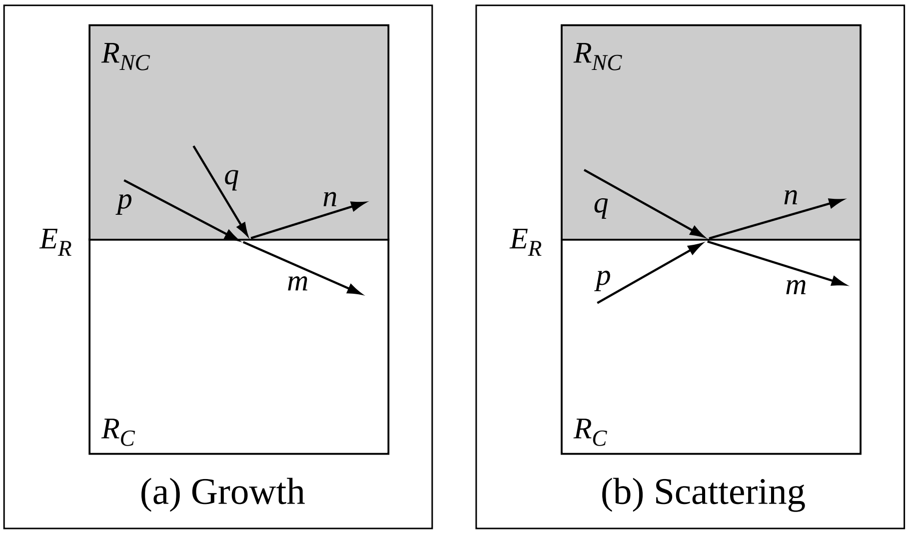

(a) Growth (b) Scattering

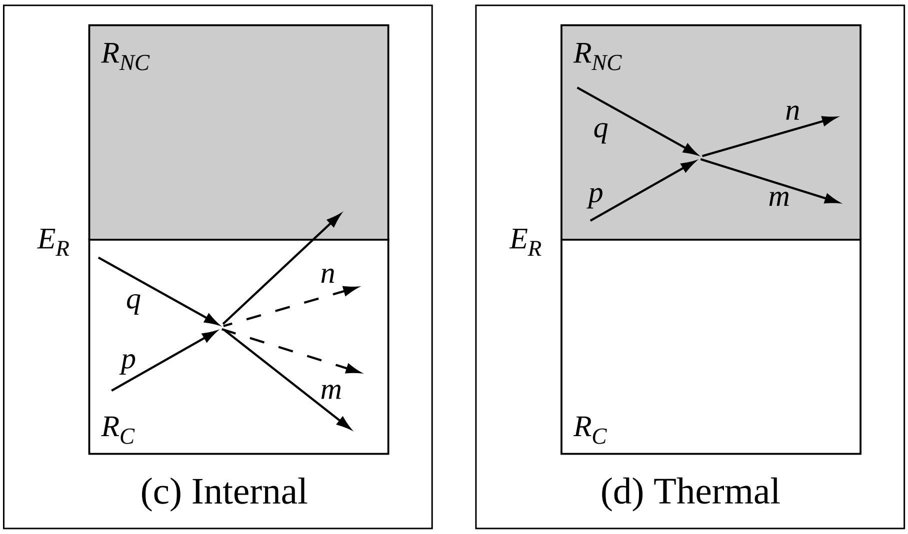

(c) Internal (d) Thermal

Figure 4.4: The four different collision types that can occur in our numerical description.

(b) *Scattering*: A particle in $R_{NC}$ collides with a particle in the condensate band, with one particle remaining in $R_C$.

(c) *Internal*: Two particles within the condensate band collide with at least one of these particles remaining in $R_C$ after the collision.

(d) *Thermal*: Two particles from the non-condensate band collide, and both remain in this band.

Model A of condensate growth [100] considered only process (a). The next calculation using model B [101, 102] included both processes (a) and (b). The calculations presented below include all four processes, allowing us to determine whether the earlier approximations were justified.

The computation of the rates of processes (a) and (b) is difficult because of the different energy scales of the two bands. Our solution is to *interpolate* the distribution function $f_n$ in $R_{NC}$ such that the bin sizes are reduced to be the same as for $R_C$. The rates are then calculated using this interpolated distribution function, now consisting of more than one thousand bins, and the rates for the large bins of the non-condensate band are found by summing the rates of the appropriate interpolated bins.

We have found that these rates are *extremely* sensitive to the accuracy of the numerical interpolation—small errors lead to inconsistencies in the solutions of the MQBE. However, this procedure is more efficient than simply using the same bin size for the whole distribution, as there are only a small number of bins for the condensate band.

### 4.3.3 Algorithm

The algorithm we use to solve the MQBE is summarised as follows:

(1) Calculate the collision summation of Eq. (4.9) for all types of collisions, keeping the density of states and the energies of the levels in the condensate band $R_C$ fixed. The distribution function $f_n(t+\delta t)$ is calculated using an embedded fourth-order Runge-Kutta method with adaptive step-size, using Cash-Karp parameters [111].

(2) As mentioned earlier, we use the approximation of Ref. [91] that $M(p,q,r,n) \rightarrow g_{\min(p,q,r,n)}$. We also express energy conservation in a simplified form, using

the fact that the energy bins will be chosen to be *equally spaced*, by choosing a Kronecker delta form

$$\Delta(p, q, r, n) \quad \rightarrow \quad \delta(p + q, r + n). \tag{4.17}$$

The difference between these two forms clearly goes to zero as the bins become very narrow. We have checked explicitly that in practice energy is conserved to very high accuracy throughout the calculation.

(3) As a result of the time step the condensate population $n_0$ will have changed, along with $\mu_C(n_0)$ and the density of states. This results in the compression of the energies of the excited states above the condensate. The derivation in Sec. 4.1.1 shows that individual quantum states remain in the same energy bin during a time step. Therefore, as the actual energy of each quantum level will shift, the upper and lower boundaries of each bin will be different at the end of the Runge-Kutta time step. The population $g_n f_n$ is the occupation of the shifted energy bin.

(4) As a result of the preceding step, the bins will no longer be of equal width. Therefore, we redistribute the populations $g_n f_n$ into a new set of equally spaced bins, as explained in Sec. 4.3.1. This procedure results in a slight change to $f_n$, the *occupation per energy level* of the $n$th bin.

(5) We now continue with step (1).

The change in $\mu_C(n_0)$ with each time step, and hence the shifts in the energy of the bins in $R_C$, is very small. Therefore, the adjustment of the distribution function due to step (4) is tiny and is much smaller than the change due to step (1).

This algorithm has been tested by altering the position of $E_R$ and the width of the energy bins in both $R_{NC}$ and $R_C$. We have found that the solution is independent of the value of $E_R$ for a wide range of these parameters.

## 4.4 Results

In this section we present the results of simulations modelling the experiments described in Ref. [35]. As explained in Sec. 3.5, in these experiments a cloud of sodium atoms was evaporatively cooled to just above the Bose-Einstein transition temperature, before a rapid RF cut removed the high-energy tail of the distribution. The growth of a condensate was then observed using non-destructive imaging techniques.

We have carried out a full investigation of the effect that varying the initial cloud parameters has on the growth of the condensate for the trap configuration described in Ref. [35]. Here we concentrate on a comparison of these results with the earlier theoretical model B described in Chapter 3. To model the experiments we begin our simulations with an equilibrium Bose-Einstein distribution with temperature $T_i$ and chemical potential $\mu_{\text{init}}$, and truncate it at an energy $\varepsilon_{\text{cut}} = \eta k T_i$. This represents the system at the end of the RF cut. The distribution is then allowed to evolve in time until the gas once again approaches equilibrium, that is, the appropriate Bose-Einstein distribution in the presence of a condensate. This process is depicted in a series of snapshots of the distribution function from a single simulation in Fig. 4.5.

Because of the ergodic assumption, the MQBE that we simulate depends only on the geometric average of the trapping frequencies $\bar{\omega} = (\omega_x \omega_y \omega_z)^{1/3}$. There is likely to be some type of experimental dependence on the actual trap geometry that is not included in our simulation; however, in the regime $kT \gg \hbar\bar{\omega}$ this should be small. The trap parameters of Ref. [35] were $(\omega_x, \omega_y, \omega_z) = 2\pi \times (82.3, 82.3, 18)$ Hz, giving $\bar{\omega} = 2\pi \times 49.6$ Hz.

### 4.4.1 Matching the experimental data

The main source of quantitative experimental data of condensate growth generally available is Fig. 5 of Ref. [35], reproduced as Fig. 3.4 in the previous chapter. This gives growth rates as a function of final condensate number and temperature rather than the initial conditions. Whereas the growth curves calculated in Refs. [100, 102] required these parameters as inputs, the calculations presented here require three different input parameters; the initial number of atoms in the system $N_i$ (and hence the initial chemical potential $\mu_{\text{init}}$), the initial temperature $T_i$, and the position of the cut energy $\eta k T_i$.

Given the parameters supplied in Ref. [35], it is possible to calculate several sets of initial conditions that will result in the final state of the gas that we require. As we know the final condensate number, we can calculate the value of the chemical potential of the gas using the Thomas-Fermi approximation for the condensate eigenvalue, Eq. (4.13). This gives a density of states according to Eq. (4.14), and along with the measured final temperature $T_f$, we can calculate the total energy

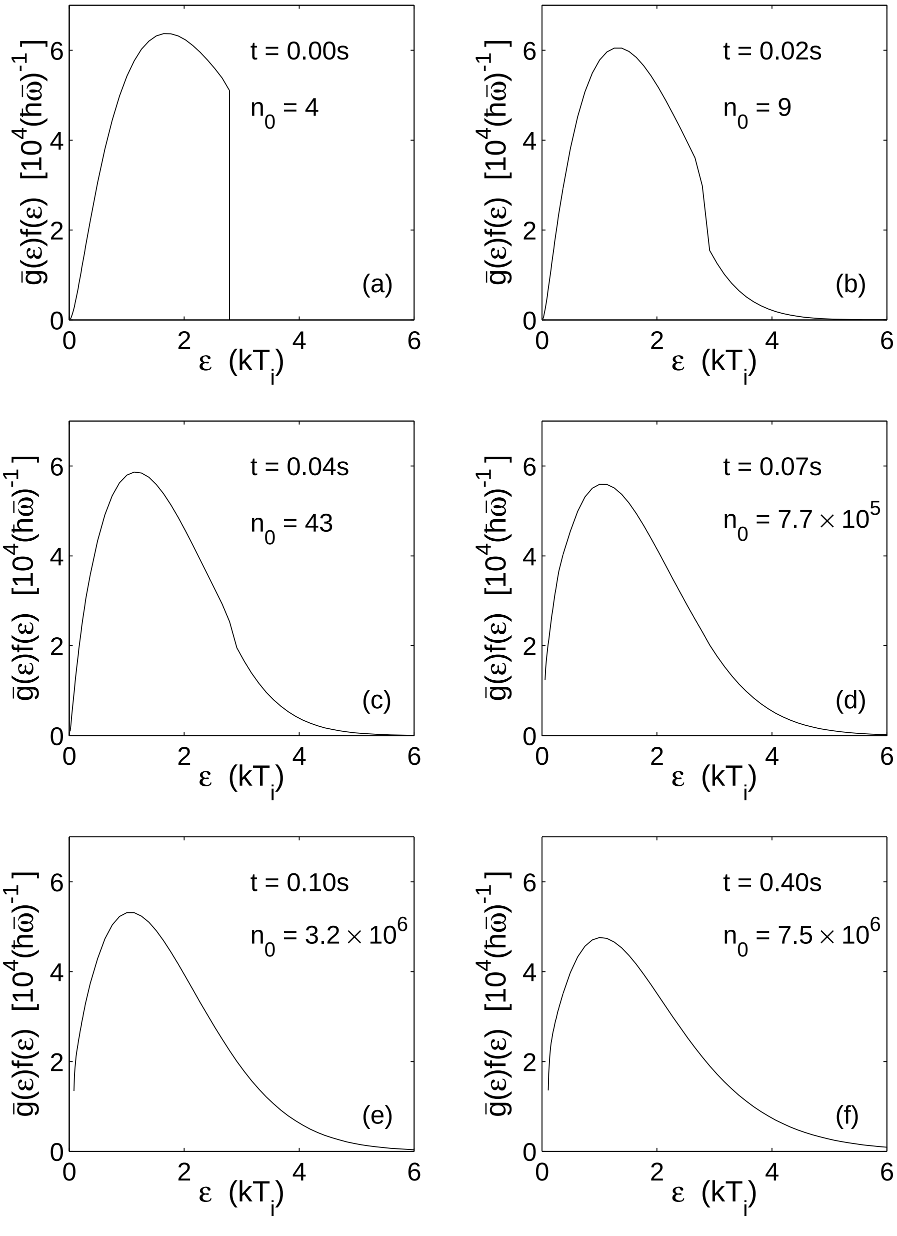

Figure 4.5: Snapshots of the distribution function for a simulation with initial conditions $\mu_{\rm init} = -100\hbar\bar{\omega}$, $T_i = 1119$ nK, and $\eta = 2.83$. This results in a condensate with $n_0 = 7.5 \times 10^6$ atoms at a temperature of $T_f = 830$ nK. For clarity, the condensate itself is not depicted, but the presence of a significant amount of condensate has the effect of displacing the left-hand end of the curves (d)–(f) by an amount $\mu_{\rm C}(n_0)/kT_i$ from the axis. The growth curve for this simulation is shown in Fig. 4.6(a).

$E_{\rm tot}$ and number of atoms $N_{\rm tot}$ in the system at the end of the experiment

$$\begin{aligned} N_{\rm tot} &= n_0 + \sum_{\varepsilon_n > \mu_{\rm C}(n_0)}^{\infty} \frac{g_n}{\exp[\{\varepsilon_n - \mu_{\rm C}(n_0)\}/kT_f] - 1}, & (4.18) \\ E_{\rm tot} &= E_0(n_0) + \sum_{\varepsilon_n > \mu_{\rm C}(n_0)}^{\infty} \frac{\varepsilon_n g_n}{\exp[\{\varepsilon_n - \mu_{\rm C}(n_0)\}/kT_f] - 1}. & (4.19) \end{aligned}$$

This completely characterises the final state of the gas.

We now want to find an initial distribution that would have the same total energy and number of atoms if truncated at $\varepsilon_{\rm cut} = \eta k T_i$ (the parameter $\eta$ is not recorded in the experimental data). If we guess an initial chemical potential for the distribution $\mu_{\rm init}$, we can self-consistently solve for the parameters $T_i$ and $\eta$ from the following nonlinear set of equations

$$\begin{aligned} N_{\rm tot} &= \sum_{\varepsilon_n = 3\hbar\bar{\omega}/2}^{\eta k T_i} \frac{g_n}{\exp[(\varepsilon_n - \mu_{\rm init})/kT_i] - 1}, & (4.20) \\ E_{\rm tot} &= \sum_{\varepsilon_n = 3\hbar\bar{\omega}/2}^{\eta k T_i} \frac{\varepsilon_n g_n}{\exp[(\varepsilon_n - \mu_{\rm init})/kT_i] - 1}. & (4.21) \end{aligned}$$

This gives the input parameters for our simulation, and we can now calculate growth curves starting with initially different clouds, but resulting in the same final condensate number and temperature.

### 4.4.2 Typical results

A sample set of growth curves is presented in Fig. 4.6(a), for a condensate with $7.5 \times 10^6$ atoms at a final temperature of 830 nK and a condensate fraction of 10.4%. The initial parameters for the curves are given in Table 4.1.

It can be seen that the curves are very similar, and arguably it would be difficult to distinguish them in experiment. The main difference is that the further the system starts from the transition point (i.e. the more negative the initial chemical potential), the longer the initiation time but the steeper the growth curve.

#### Effective chemical potential

To facilitate the understanding of these results, we introduce the concept of an effective chemical potential $\mu_{\rm eff}$ for the non-condensate band. We do this by fitting

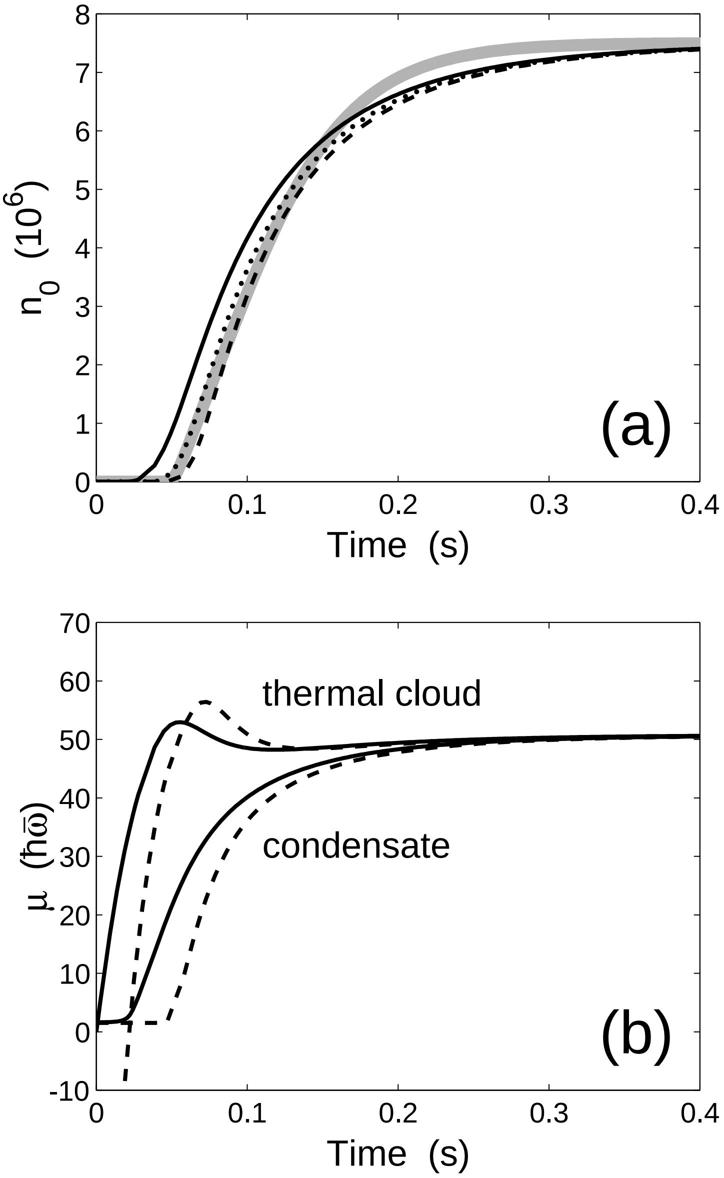

Figure 4.6: Growth of a condensate with $n_0 = 7.5 \times 10^6$, $T_f = 830$ nK. Solid lines $\mu_{\text{init}} = 0$, dotted lines $\mu_{\text{init}} = -40\hbar\bar{\omega}$, dashed lines $\mu_{\text{init}} = -100\hbar\bar{\omega}$. (a) Population of the condensate versus time. The grey curve is the solution for model B of condensate growth. (b) Chemical potential $\mu_{\text{C}}(n_0)$ of the condensate (lower curves) and effective chemical potential $\mu_{\text{eff}}$ of the thermal cloud (upper curves).

| $\mu_{\text{init}}(\hbar\bar{\omega})$ | $T_i$(nK) | $N_i(10^6)$ | $\eta$ | $\varepsilon_{\text{cut}}(\hbar\bar{\omega})$ |
|---|---|---|---|---|
| 0 | 1000 | 89.1 | 3.82 | 1605 |
| -40 | 1080 | 100.1 | 3.31 | 1503 |
| -100 | 1119 | 117.6 | 2.83 | 1419 |

Table 4.1: Parameters for the formation of a condensate with $n_0 = 7.5 \times 10^6$ atoms at a temperature of $T_f = 830$nK from an uncondensed thermal cloud. The growth curves are plotted in Fig. 4.6.

a Bose-Einstein distribution to the lowest energy bins of $R_{NC}$ as a function of time. Obviously, the chemical potential is undefined when the system is not in equilibrium, but as has been noted for the classical Boltzmann equation, the distribution function tends to resemble an equilibrium distribution as evaporative cooling proceeds [112]. The effective chemical potential is not unique—it is dependent on the particular choice of the energy cutoff $E_R$. It gives a good indication of the "state" of the non-condensate, however, since the majority of the particles entering the condensate after a collision come from bins in the region of $E_R$. Here we compute $\mu_{\rm eff}$ using a linear fit to $\ln(1+1/f_n)$ for the first ten bins of the noncondensate band, with the intercept giving $\mu_{\rm eff}$ and the gradient an effective temperature.

#### Interpretation

We find that all the results presented in this chapter can be qualitatively understood in terms of the simple growth equation (3.31), with the vapour chemical potential $\mu$ replaced by the effective chemical potential $\mu_{\rm eff}$ of the thermal cloud.

The simple growth equation requires $\mu_{\rm eff} > \mu_{\rm C}(n_0)$ for condensate growth to occur. In Fig. 4.6(b) we plot the effective chemical potential $\mu_{\rm eff}$ of the thermal cloud and the chemical potential of the condensate $\mu_{\rm C}(n_0)$. This graph helps explain the two effects noted above—longer initiation time and a steeper growth curve for the $\mu_{\rm init} = -100\hbar\bar{\omega}$ case. Firstly, the inversion of the chemical potentials for this simulation occurs at a later time than for $\mu_{\rm init} = 0$, causing the stimulated growth to begin later. This is because for the $\mu_{\rm init} = -100\hbar\bar{\omega}$ simulation the initial cloud is further from the transition point at $t = 0$. Secondly, the effective chemical potential of the thermal cloud rises more steeply in this case, meaning that $[\mu_{\rm eff} - \mu_{\rm C}(n_0)]$ is larger, and therefore the rate of condensate growth is increased.

### 4.4.3 Comparison with model B

In Fig. 4.6(a) we have also plotted the growth curve that is predicted for the same final condensate parameters by model B of condensate growth described in Sec. 3.6 and Ref. [102]. We note that in this model the vapour is treated as being undepleted, with a constant chemical potential and temperature.

For these particular parameters, it turns out that the results of the full calculation of the growth curve give very similar results to model B, with the initial condensate number adjusted appropriately.[1] This is not surprising; indeed, from Fig. 4.6(b) we can see that the approximation of the thermal cloud by a constant chemical potential (i.e. the cloud is not depleted) is good for the region where the condensate becomes macroscopic.

For larger condensate fractions, however, the principal condition assumed in model B that the chemical potential of the vapour can be treated as approximately constant is no longer satisfied. In Fig. 4.7(a) we plot the growth of the same size condensate as in Fig. 4.6, (that is, $7.5\times10^6$ atoms), but at a lower final temperature of 590 nK. In this situation the condensate fraction increases to 24.1%, and so there is considerable depletion of the thermal cloud. The effect of this can be seen in Fig. 4.7(b). The difference between the vapour and condensate chemical potentials $[\mu_{\rm eff} - \mu_{\rm C}(n_0)]$ initially increases to much larger values than for model B, in which $\mu_{\rm eff}$ is held constant at its final equilibrium value. It is this fact that causes more rapid growth in the new calculations.

As the condensate continues to grow, it begins to significantly deplete the thermal cloud, causing $\mu_{\rm eff}$ to decrease from its maximum. It is the "overshoot" of $\mu_{\rm eff}$ from the final equilibrium value that model B cannot take into account. This overshoot only occurs for final condensate fractions of more than about 10%; hence up to this value model B should be sufficient.

### 4.4.4 Effect of final temperature on condensate growth

We have investigated the effect that the final temperature has on the growth of a condensate of a fixed final population. All simulations in this section began with $\mu_{\rm init} = 0$, since the initial chemical potential has little effect on the overall shape of the growth curves. The other parameters $T_i$ and $\eta$ are then determined, and the initial conditions are shown in Table 4.2. The results of these simulations are presented in Fig. 4.8.

We find the somewhat surprising result that the growth curves do not change significantly over a very large temperature range for the same size condensate. In fact, a condensate formed at 600 nK grows more slowly than at 400 nK for these parameters—an effect in qualitative agreement with the trend observed in the MIT experiment. As the temperature is increased further, however, the growth rate increases again, and at a final temperature of 1 $\mu$K the growth rate is faster

---

[1] In the solution of model B the initial condensate number is indeterminate, whereas for the full calculation described in this chapter the initial distribution is Bose-Einstein, with the zero of time corresponding to the removal of the high-energy tail.

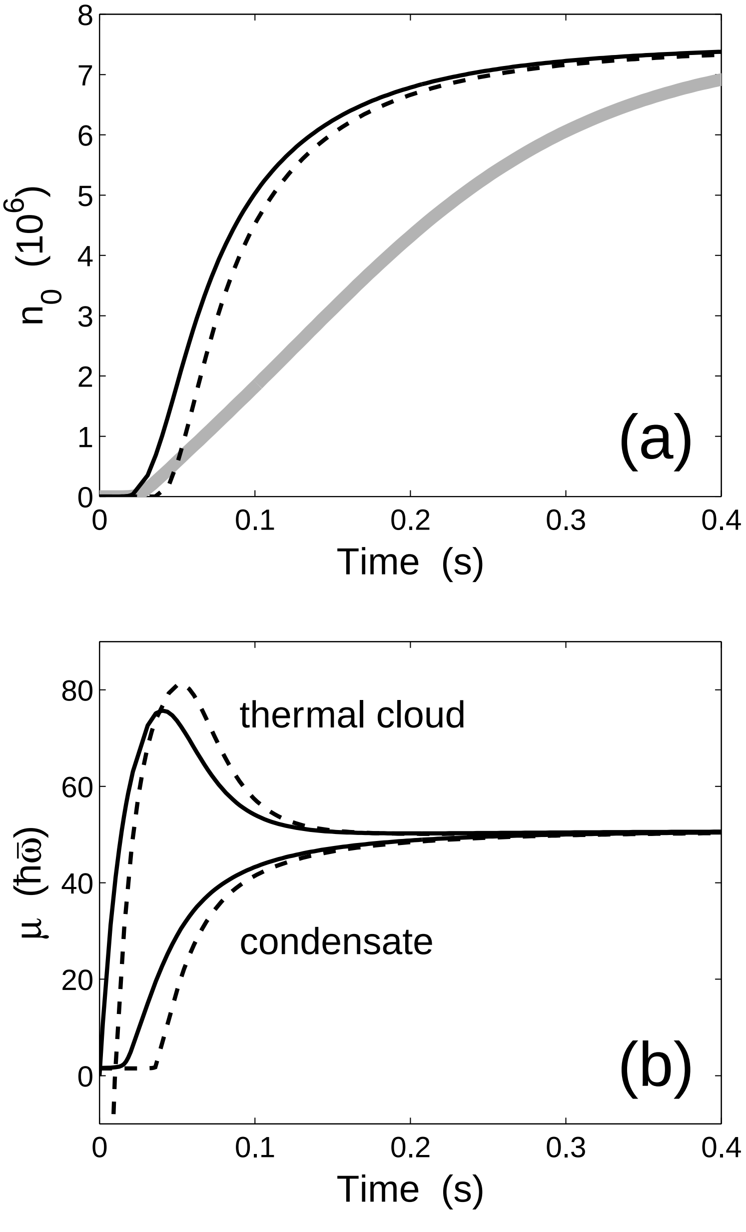

Figure 4.7: Comparison of condensate growth models for a condensate fraction of 24.1%, $n_0 = 7.5 \times 10^6$, $T_f = 590$ nK. Solid lines $\mu_{\text{init}} = 0$, dashed lines $\mu_{\text{init}} = -100\hbar\bar{\omega}$. (a) Population of condensate versus time. The grey line is the solution of model B. (b) Chemical potential of condensate (lower curves) and effective chemical potential of thermal cloud (upper curves).

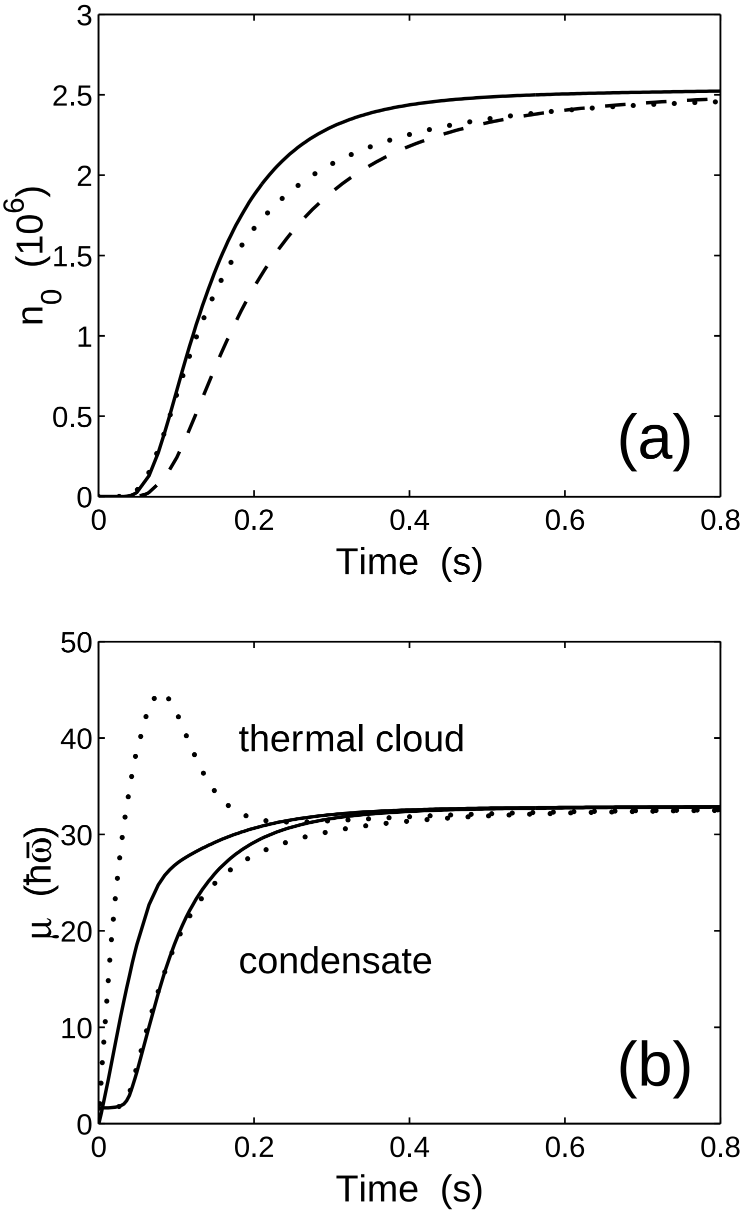

Figure 4.8: Growth of a condensate with a final condensate size of $n_0 = 2.5 \times 10^6$ atoms from a vapour with $\mu_{\text{init}} = 0$. The dotted line is for a final temperature of 400 nK, dashed 600 nK, and solid 1 $\mu$K. (a) Growth curves. (b) Chemical potential of condensate (lower curves) and thermal cloud (upper curves).

| $T_f$(nK) | $T_i$(nK) | $N_i(10^6)$ | $\eta$ | $\varepsilon_{\text{cut}}(\hbar\bar{\omega})$ | Condensate fraction |
|---|---|---|---|---|---|
| 400 | 622.0 | 21.5 | 2.19 | 572 | 0.253 |
| 600 | 707.3 | 31.6 | 4.03 | 1198 | 0.099 |
| 1000 | 1064.8 | 107.7 | 5.87 | 2629 | 0.025 |

Table 4.2: Parameters for the formation of a condensate with $n_0 = 2.5 \times 10^6$ atoms from an uncondensed thermal cloud with $\mu_{\text{init}} = 0$. The growth curves are presented in Fig. 4.8.

than at 400 nK. This effect has also been observed for both larger ($7.5 \times 10^6$) and smaller ($1 \times 10^6$) condensates.

This observation can once again be interpreted using the simple growth equation (3.31). Although $W^+(n_0)$ increases with temperature [approximately as $T^2$ as shown in Eq. (3.38)], the maximum value of $[\mu_{\text{eff}} - \mu_{\text{C}}(n_0)]$ achieved via evaporative cooling decreases with temperature for a fixed condensate number, as the cut required is less severe and the final condensate fraction is smaller. Also, the term in the curly brackets of Eq. (3.31) is approximately proportional to $T^{-1}$ for most regimes. The end result is that the decrease in this term compensates for the increase in $W^+(n_0)$, giving growth curves that are very similar for the different simulations. Once the "overshoot" of the thermal cloud chemical potential ceases to occur (when the evaporative cooling cut is not very severe), the growth rate begins to increase with temperature as predicted by model B.

### 4.4.5 Effect of size on condensate growth

Finally, we have performed simulations of the formation of a condensate of a varying size at a fixed final temperature. The parameters for these simulations are given in Table 4.3, and the growth curves are plotted in Fig. 4.9(a). We find that the larger the final condensate, the more rapidly it grows. The initial clouds required to form the larger condensates not only start at a higher temperature (and thus have a higher collision rate to begin with), but also need to be truncated more severely, causing a larger difference in the chemical potentials as seen in Fig. 4.9(b). Thus, instead of these effects negating each other as in the previous section, here they tend to reinforce one another. This causes the growth rate to be highly sensitive to the final number of atoms in the condensate for a fixed final temperature.

In Fig. 4.9(a) we also plot in grey the lower temperature results of Fig. 3.6(b), computed using model B of condensate growth. This curve has the same parameters as the dashed curve that was computed using the full model. It can be seen that the two methods are in very good agreement with each other for this choice of parameters—but the experimental data disagrees with the theoretical curves. It is this particular set of final parameters for which the discrepancy between theory and experiment remains.

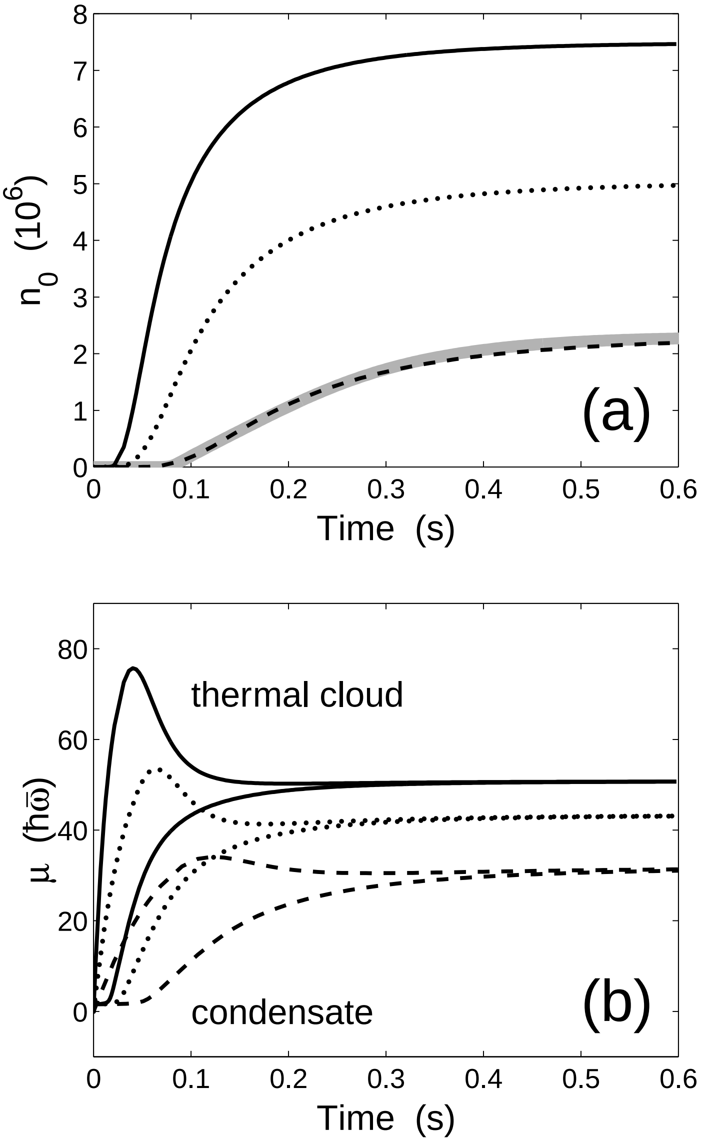

Figure 4.9: Growth of a condensate with a final temperature of 590 nK, starting from an uncondensed thermal cloud with $\mu_{\text{init}} = 0$. Solid line $7.5 \times 10^6$ atoms, dotted line $5.0 \times 10^6$ atoms, dashed line $2.3 \times 10^6$ atoms. The dashed line is for the same parameters as the lower temperature curves in Fig. 3.6. (a) Growth curves, with the solution to model B in grey. (b) Chemical potential of condensate (lower curves) and thermal cloud (upper curves).

| $n_0(10^6)$ | $T_i$(nK) | $N_i(10^6)$ | $\eta$ | $\varepsilon_{\text{cut}}(\hbar\bar{\omega})$ | Condensate fraction |
|---|---|---|---|---|---|
| 2.3 | 692.5 | 29.6 | 4.07 | 1186 | 0.095 |
| 5.0 | 794.6 | 44.7 | 2.91 | 973 | 0.179 |
| 7.5 | 897.9 | 64.6 | 2.29 | 865 | 0.239 |

Table 4.3: Parameters for the formation of condensates at $T_f = 590$ nK from an uncondensed thermal cloud with $\mu_{\text{init}} = 0$. The growth curves are presented in Fig. 4.9.

### 4.4.6 The appropriate choice of parameters

In our computations we have taken some care to make sure that we give our results as a function of the experimentally measured *final* temperature $T_f$ and condensate number $n_0$. Nevertheless, it can be seen from our results that this can give rise to counterintuitive behavior, such as the fact that under the condition of a given final condensate number, the growth rate seems to be largely independent of temperature because of the cancellation noted in Sec. 4.4.4. This effect has its origin in the simple fact that with a sufficiently severe cut, it is impossible to separate the process of equilibration of the vapour distribution from the growth of the condensate. In other words, the attempt to implement the "ideal" experiment in which a condensate grows from a vapour with a constant chemical potential and temperature cannot succeed with a sufficiently large cut. Under these conditions the initial temperature differs quite strongly from the final temperature. Also, the number of atoms required to form the condensate is so large that the vapour cannot be characterised by a slowly varying chemical potential during most of the growth process.

### 4.4.7 Comparison with experiment

#### Comparison with MIT fits

The most quantitative data available from Ref. [35] is in the graph we have reproduced as Fig. 3.4, in which the experimental results are presented as parameters extracted from fits to the simple growth equation (3.31). In Ref. [102] we took two clusters of data from this figure at the extremes of the temperature range for which measurements were made, and compared the theoretical results with the fitted experimental curves. At the higher temperature of 830 nK the results were in good agreement with experiment, but at 590 nK they differed significantly, the experimental growth rate being about three times faster than the theoretical prediction based on model B.

We have performed the same calculations using the detailed model of this chapter. The results for 830 nK are presented in Fig. 4.6 and those for 590 nK are presented in Fig. 4.9. There is a good match between the two theoretical models at *both* temperatures. This means that the more sophisticated calculation presented here does not explain the observed discrepancy between theory and experiment for the lower temperature case.

### Comparison with sample growth curves

In Ref. [35] some specific experimental growth curves are presented, and we shall compare these with our computations. We also compare our results with those of Bijlsma *et al.* [113], whose paper on this subject appeared as a preprint soon after this work was submitted to the cond-mat eprint archive [114]. Their method is derived from the formalism for finite temperature dynamics developed by Zaremba *et al.* [115] and is essentially a quantum Boltzmann equation in an effective potential formed by the trap and Thomas-Fermi condensate. There are some important differences to our own work, however, and their work provides an useful check of our own calculations.

In Fig. 4.10 we show the experimental data from Fig. 3 of Ref. [35], the computation of Fig. 11 of Ref. [113], and our own calculation. This is for the MIT sodium trap, with the simulation parameters taken from Bijlsma *et al.* of $N_i = 60 \times 10^6$, $T_i = 876$ nK and $\eta = 2.5$. We find that this results in a condensate of $6.97 \times 10^6$ atoms at a temperature of 604 nK, and a final condensate fraction of 21.8% after half a second. This agrees with our predictions from the solution of the equations in Sec. 4.4.1 at $t = \infty$ to within 0.2%.

We can see that there is little difference in the results of the two computations for this case, the main discrepancy being that the initiation time for our simulation is a little longer than that of Bijlsma *et al.* This is likely to be due to the fact that their calculation starts with the condensate already occupied with $n_0 = 5 \times 10^4$ atoms, whereas we begin with the equilibrium number given by the Bose distribution of $n_0 = 208$ atoms. However, this difference could be brought about by the use of a slightly different density of states, which could also be the cause of the difference in the final condensate number of approximately $3 \times 10^5$ atoms.

The agreement with the experimental growth curve data is very good for both computations. Model B of condensate growth cannot reproduce the results at this temperature, as is shown by the lower grey curve in Fig. 4.10. This is as we expect—the final condensate fraction is far greater than 10% and in this case the "overshoot" of $\mu_{\text{eff}}$ is significant. These initial conditions are the only situation where we have found that the "speedup" given by the full quantum Boltzmann theory *may* yield a significant improvement of the fit to the experimental data.

We would like to emphasise, however, that the parameters used for this simulation *do not* come from experimental data. The MIT paper [35] does not provide any details of the size of the thermal cloud, or the temperature at which this curve was measured, and as such, a set of unique initial and final parameters of the ex-

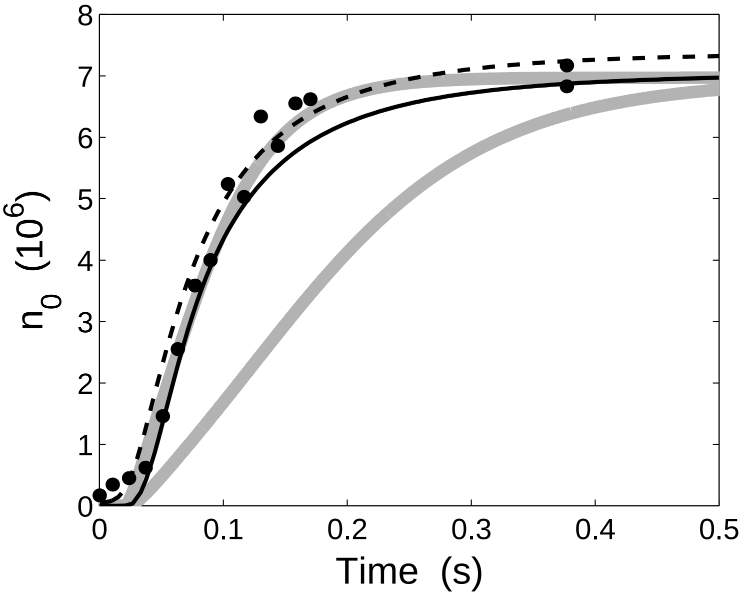

Figure 4.10: A comparison between the results of Fig. 11 of Ref. [113] and our own calculations with the initial conditions $N_i = 60 \times 10^6$ atoms, $T_i = 876$ nK, $\eta = 2.5$. Our data is shown as the solid line and the results from Bijlsma *et al.* are the dashed line. The lower grey curve corresponds to the results of model B for a final temperature of $T_f = 604$ nK matching these initial conditions. The upper grey curve is also for model B, but with what we feel is a more realistic final temperature of $T_f = 830$ nK. The experimental data points are the solid dots.

periment cannot be determined. We have simply taken these parameters from the calculation of Ref. [113].

In fact, it seems likely to us that the final temperature for the experimental curve shown in Fig. 4.10 should be higher. Studying Fig. 3.4 shows that most condensates of $7 \times 10^6$ atoms or more were formed at temperatures above 800 nK. We have therefore performed a second calculation using the simple model B with a final temperature of 830 nK, and this result is shown as the upper grey curve in Fig. 4.10. As can be seen, *this also fits the experimental data extremely well.* The condensate fraction at this higher temperature is 10.2%, meaning that these parameters are very similar to the situation considered in Fig. 4.6, which was originally found to be a good match to experimental data in Ref. [102]. We note that the solution to model B at this higher temperature is also in good agreement with our more detailed calculation for these parameters, which has not been plotted for clarity.

The situation is very different, however, if we compare with the growth curve data of Fig. 4 from Ref. [35] (part (a) of which is reproduced here in Fig. 4.11)

| Quantity | Parameters extracted from experiment | Parameters which give an apparent fit |
|---|---|---|
| $N_i$ ($10^6$) | 40.0 | 40.0 |
| Atoms lost | 60% | 94% |
| Condensate fraction | 7.2% | 51% |
| $T_i$ (nK) | 945.5 | 765 |
| $T_f$ (nK) | 530 | 211 |
| $\eta$ | 2.19 | 0.60 |

Table 4.4: Comparison of the static parameters of the Bose gas that match Fig. 4 of Ref. [35].

with a final condensate population of $1.2 \times 10^6$ atoms. For this particular curve sufficient experimental data is provided such that all relevant cloud parameters can be determined. The MIT figure shows an experimentally measured reduction in the thermal cloud number from $40 \times 10^6$ atoms to about $15 \times 10^6$ over the duration of the experiment. Including the final condensate population gives a total number of atoms in the system of approximately $16.2 \times 10^6$, or a loss of 60% of the atoms. With the three pieces of data taken from the MIT graphs (initial thermal cloud number, final thermal cloud number and final condensate number), we can estimate all the relevant parameters using the equations of Sec. 4.4.1, and these are shown in the left column of Table 4.4.

While the parameters we present here are consistent with the static experimental data, the growth curve corresponding to these parameters (shown in Fig. 4.11) certainly does not fit the dynamical data. We find that to remove such a large proportion of atoms yet still obtain a relatively small condensate, the initial system must be a long way from the transition temperature, with $\mu_{\rm init} = -212\hbar\bar{\omega}$. This means that condensate growth does not occur until the relaxation of the thermal cloud is almost complete, resulting in a very long initiation time. Also, when the growth does begin, the rate is significantly slower than was observed experimentally. This is the parameter regime in which the experimental and theoretical discrepancies lie—at relatively low temperature, but with a condensate fraction of less than ten percent such that model B agrees with the more sophisticated calculation of this chapter.

As well as the computation based on the extracted parameters, in Fig. 4.11 we also present two “apparent fits,” one based on our calculations and another based on a calculation of Bijlsma *et al.* [113]. Here we find the results of the two different formulations are almost identical. The difference appears to be due to

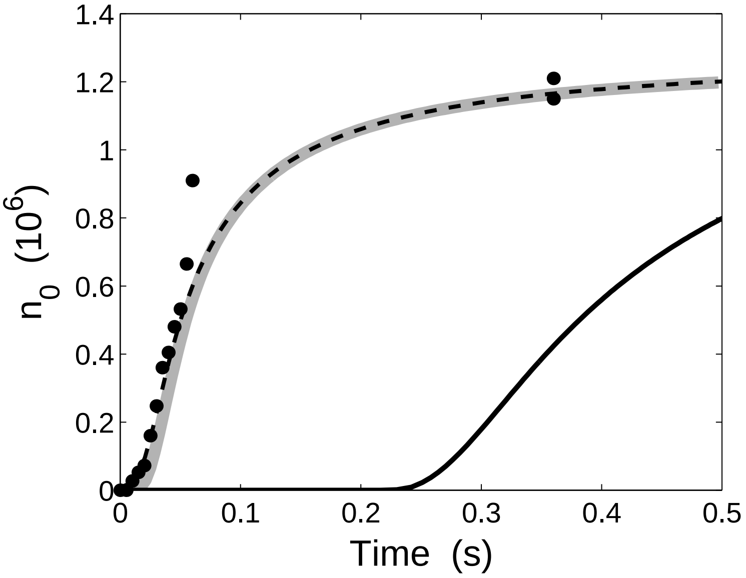

Figure 4.11: A comparison between the data of Fig. 4 of Ref. [35] (large solid dots) and our own calculations. The solid curve shows the growth curve for the static parameters that we have extracted from the experimental data: $N_i = 40 \times 10^6$, $T_i = 945.5$ nK, $\eta = 2.19$. An apparent fit can also be obtained—the parameters for the grey curve (our results) and dashed curve (Bijlsma *et al.*) are $N_i = 40 \times 10^6$ atoms, $T_i = 765$ nK, $\eta = 0.6$. However, as noted in the text, these parameters are not experimentally acceptable.

the initial condensate number—our calculations begin with 295 atoms, whereas Bijlsma *et al.* begin with $10^4$ atoms. The initial parameters chosen in Ref. [113] for this simulation are a system of $N_i = 40 \times 10^6$ atoms at a temperature of $T_i = 765$ nK, and the energy distribution is truncated at $\eta = 0.6$—an extremely severe cut.

However, while the fit to the experimental data looks very good, the initial parameters for these calculations are not consistent with the experiment. An inspection of the final state of the gas explains the situation. The final temperature according to these computations is $T_f = 211$ nK, and the condensate fraction is 51%. Looking at the data of Ref. [35], we find that no final temperatures lower than 500 nK were measured, and the largest condensate fraction reported was 30% (although our analysis of the experimental data from Fig. 3.4 gave a maximum of 17%). The evaporative cooling for these "apparent fit" simulations would remove 94% of the atoms in the trap, and we believe it is very unlikely that this matches any of the experimental situations.

### Speedup of condensate growth compared to model B

We have shown that compared to model B of condensate growth, a significant speedup can occur for condensate fractions larger than 10% . However, this is not sufficient to explain the discrepancy of theory with the experimental results for all of the measured values of temperature and condensate fraction from Fig. 3.4. The only situation in which this speedup might be relevant to the MIT experiment is the single growth curve shown in Fig. 4.10. However, as we have noted, the initial conditions for this figure are quite speculative, and in fact also appear to be unrealistic.

The actual speedup observed in our computations is the same order of magnitude as that achievable with a different condensate fraction, and it is conceivable that the problem could be experimental rather than theoretical—a systematic error in the methodology of extracting the condensate number from the observed data could cause the effect. For a realistic comparison to be made between theory and experiment, sufficient data should be taken to verify all the relevant parameters that have an influence on the results.

Thus one should measure the initial temperature and number of atoms, along with the final temperature, condensate number and the size of the “cut”. In particular it should be noted that in the one case where all of this data is available, substantial disagreement is found between theory and experiment, as is shown in Fig. 4.11.

The work on condensate growth published in QKVI considered in detail a semiclassical method of fitting theoretical spatial distributions to the two-dimensional data extracted by phase-contrast imaging of the system during condensate growth. This method shows that significantly different condensate numbers and temperatures are consistent with the MIT data and methodology [35, 116]. This could be a possible cause of the discrepancy between theory and experiment.

## 4.4.8 Outlook

It remains conceivable, however, that approximations made in this formulation of quantum kinetic theory are not valid in the experimental regime where the discrepancy lies. In this section we summarise the possible further extensions to the model of condensate growth described in this chapter.

The first possible extension is to remove the ergodic approximation, that assumes all levels of a similar energy are equally occupied. From the results of QKII it would seem that any non-ergodicity in the initial distribution would be damped on the time-scale of the growth—therefore the effect of this could be significant if the initial distribution is far from ergodic. It is difficult to know what the exact initial distribution of the system is without performing a detailed three-dimensional calculation of the evaporative cooling, which would require massive computational resources. Also related to this point, we have used the simplified expression of Eq. (4.11) derived in analogy with the work of Holland *et al.* [91] on the ergodic approximation.

The second important approximation is that the low-lying states of the gas are well-described by a single-particle excitation spectrum, so that a density of states description can be used to calculate the collision rates for these levels. The justification for this is that these states are not expected to be important in determining the growth of the condensate. Indeed, in QKVI it was shown that varying these rates by orders of magnitude had little effect on the growth curves.

The third approximation made is that the growth of the condensate level is adiabatic, and that its shape is always well-described by the Thomas-Fermi wave function. This may not be the case, and indeed some collective motion during growth was observed in Ref. [35]. We feel that this may become important for sufficiently large truncations of the thermal cloud, i.e. in experiments that could be considered a temperature "quench". Removing this assumption would require introducing a full description of the low-lying quasiparticle levels, and a time-dependent Gross-Pitaevskii equation for the shape of the condensate—again requiring large computational resources.

The final approximation is that fluctuations of the occupation of the quantum levels are ignored. It seems unlikely that this would have a major effect, as most of the experimental data was averaged over a number of runs.

The agreement between the theory and the single experiment performed so far is generally good, and there is only one regime in which there is significant discrepancy. The removal of these approximations requires a large amount of work, and we feel this is not justified until new experimental data on condensate growth becomes available.

## 4.5 Conclusions

We have extended the earlier models of condensate growth described in Chapter 3, Refs. [100, 101, 102] and QKVI to include the full time-dependence of both the condensate occupation and the thermal cloud. We have compared the results of this more sophisticated calculation with model B and determined that for bosonic stimulation experiments resulting in a condensate fraction of the order of 10%, model B is quite sufficient.

However, for larger condensate fractions the depletion of the thermal cloud becomes important. We have introduced the concept of the effective chemical potential $\mu_{\text{eff}}$ for the thermal cloud as it relaxes, and observed it to overshoot its final equilibrium value in these situations. This results in a much higher growth rate than model B would predict. We have therefore identified a mechanism for a possible speedup of condensate growth that may contribute to eliminating the discrepancy with experiment.

We have also found that the results of these calculations can be qualitatively explained using the effective chemical potential of the thermal cloud, $\mu_{\text{eff}}$, and the simple growth equation (3.31). In particular, the rate of condensate growth for the same size final condensate can be remarkably similar over a wide range of temperatures; in contrast, the rate of growth is highly sensitive to the final condensate number at a fixed temperature.

The model we have developed in this thesis eliminates all the major approximations in the previous calculations of condensate growth apart from the ergodic assumption, whose removal would require massive computational resources. In the absence of experimental data that is sufficiently comprehensive to allow a full comparison between theory and experiment, this does not seem justified at present.

In Sec. 4.4.7 we have compared the results of our simulations to those of Bijlsma *et al.* [113], and found that our formulations are quantitatively very similar, giving growth curves in excellent agreement with each other. The two treatments are based on similar, but not identical methodologies, and have been independently computed. Thus the disagreement with experiment must be taken seriously.

# CHAPTER 5

# A FORMALISM FOR BEC DYNAMICS

The Gross-Pitaevskii equation has been used extensively in the literature to predict the properties of Bose-Einstein condensates near $T = 0$, when there are very few non-condensate atoms present. Both statically and dynamically it has shown excellent agreement with experiment, as discussed in Sec. 2.3.5 of this thesis.

The most successful finite temperature theories of BEC are based on second order perturbation theory, and are limited to the case of thermal equilibrium away from the region of critical fluctuations [54, 55, 56]. As mentioned earlier, these have accurately determined quantities such as excitation frequencies and damping rates of Bose-condensed systems from first principles.

Dynamical theories of condensates in the presence of a thermal cloud pose a much greater challenge. To date, most attempts have had to make use of severe approximations to be able to carry out practical calculations. Some examples of these include

1. The effect of evaporative cooling on the dynamics of condensation in small systems [117].
2. Atom lasers with a restricted number of modes [118].
3. The growth of a trapped Bose-Einstein condensate, as described in the previous two chapters of this thesis.

It has been argued, however, that the Gross-Pitaevskii equation can describe the dynamics of a Bose-Einstein condensate at finite temperature [94, 90, 119, 120]. In the limit that the low-lying modes of the system are highly occupied ($N_k \gg$

1), the classical fluctuations of the field operator $\hat{\Psi}(\mathbf{x},t)$ overwhelm the quantum fluctuations, and these modes may be approximated by a coherent wave function. This is analogous to the situation in laser physics, where the highly occupied laser modes can be well described by classical equations. Very recently two preprints by Svistunov have appeared suggesting the use of the GPE to study the kinetics of strongly non-equilibrium BEC [121, 122].

Despite this proposal appearing in the literature in 1991 [94], very few numerical calculations have been performed. The first was by Damle *et al.* [123], who calculated the approach to equilibrium of a near-ideal superfluid using the GPE, in which they concentrated on the scaling behaviour of the time for condensate formation. More recently, Marshall *et al.* [124] performed two-dimensional simulations of evaporative cooling of a thermal Bose field in a trap. While they qualitatively showed that the GPE appeared to represent a thermal field, there was no quantitative analysis. Finally, a preprint has recently appeared that treats several modes of a homogeneous Bose gas classically [125]. This is close to the treatment we present in this chapter, and indeed, some of the results observed are similar to those presented in Chapter 6. Classical approximations to other quantum field equations have been successful in the calculation of the dynamics of the electroweak phase transition [126].

The main advantage of these methods is that realistic calculations, while still a major computational issue, are feasible—methods for solving the GPE are well developed. In addition, the GPE is non-perturbative and it should be possible to study the region of the BEC phase transition, where perturbation theory often fails.

There are, however, a number of problems associated with the use of the GPE at finite temperature. It is a classical equation, and so in equilibrium it will satisfy the equipartition theorem—all modes of the system will contain an energy $k_B T$. Thus, if we couple the GPE to a heat bath and numerically solve the equation with infinite accuracy, we will observe an ultra-violet catastrophe. Also, the higher the energy of any given mode, the lower its occupation will be in equilibrium and eventually the criterion $N_k \gg 1$ will no longer be satisfied. For these low occupation modes a form of kinetic equation is more appropriate. The solution to both of these problems is to introduce a *cutoff* in the modes represented by the GPE.

In this chapter we develop a formalism in which the low-lying modes of the system are described non-perturbatively by a form of Gross-Pitaevskii equation, coupled to a thermal bath described by a quantum Boltzmann equation. We derive a finite temperature GPE, and discuss the terms that couple the coherent part of the field operator to the thermal bath. In particular we show how a description of loss via elastic collisions arises naturally in the formalism.

In Chapter 6 we present numerical results based on this method, and finally in Chapter 7 we discuss its future use and development.

## 5.1 Decomposition of the field operator

The goal of this formalism is to describe the coherent part of the field operator by a wave function. In this region, the quantum fluctuations of the field can be neglected in comparison to the classical fluctuations. With this in mind, we define the projection operator

$$\hat{\mathcal{P}} = \sum_{\nu\in C} |\nu\rangle\langle\nu|, \tag{5.1}$$

such that operating on the field operator with $\hat{\mathcal{P}}$ gives

$$\begin{aligned}\hat{\mathcal{P}}\hat{\Psi}(\mathbf{x}) &= \sum_{\nu\in C}\phi_\nu(\mathbf{x})\int d^3\mathbf{x}'\ \phi^*_\nu(\mathbf{x}')\hat{\Psi}(\mathbf{x}'),\\ &= \sum_{\nu\in C}\hat{a}_\nu\phi_\nu(\mathbf{x}),\\ &= \hat{\psi}(\mathbf{x}).\end{aligned}\tag{5.2}$$

The region $C$ is *determined* by the requirement that $\langle\hat{a}^\dagger_\nu\hat{a}_\nu\rangle \gg 1$, and the set $\{\phi_\nu\}$ defines some basis in which the field operator is approximately diagonal at the boundary of $C$. We envisage that in any calculation, the boundary of $C$ will be estimated in the construction of the initial wave function. If the particular choice later turns out to be unsatisfactory, the boundary can be adjusted accordingly and the calculation repeated.

We now define the operator $\hat{\mathcal{Q}} = \hat{1} - \hat{\mathcal{P}}$, such that

$$\begin{aligned}\hat{\mathcal{Q}}\hat{\Psi}(\mathbf{x}) &= \sum_{k\notin C}\hat{a}_k\phi_k(\mathbf{x}),\\ &= \hat{\eta}(\mathbf{x}).\end{aligned}\tag{5.3}$$

The operator $\hat{\eta}(\mathbf{x})$ represents the thermal bath, or incoherent region $I$. Quantum fluctuations *are* important for these modes—in fact we will later assume that

$\langle \hat{a}_k \rangle \approx 0$ for the large majority of $k \notin C$.

The full field operator can be represented by

$$\begin{aligned} \hat{\Psi}(\mathbf{x}) &= [\hat{\mathcal{P}} + \hat{\mathcal{Q}}]\hat{\Psi}(\mathbf{x}), \\ &= \hat{\psi}(\mathbf{x}) + \hat{\eta}(\mathbf{x}), \\ &= \sum_{\nu \in C} \hat{a}_\nu \phi_\nu(\mathbf{x}) + \sum_{k \notin C} \hat{a}_k \phi_k(\mathbf{x}), \end{aligned} \tag{5.4}$$

where we indicate indices within $C$ by Greek subscripts, and outside $C$ by Roman subscripts. We shall follow this convention throughout the remainder of this chapter.

## 5.2 Equations of motion

### 5.2.1 The Hamiltonian

We now substitute the decomposition of Eq. (5.4) into the Hamiltonian Eq. (2.1) and find for the non-interacting part

$$\begin{aligned} \hat{H}_0 &= \sum_{\alpha\beta} \langle \alpha | \hat{H}_{sp} | \beta \rangle \hat{a}^\dagger_\alpha \hat{a}_\beta && (5.5a) \\ &+ \sum_{\alpha k} \left[ \langle \alpha | \hat{H}_{sp} | k \rangle \hat{a}^\dagger_\alpha \hat{a}_k + h.c. \right] && (5.5b) \\ &+ \sum_{kj} \langle k | \hat{H}_{sp} | j \rangle \hat{a}^\dagger_k \hat{a}_j, && (5.5c) \end{aligned}$$

where $h.c.$ denotes the hermitian conjugate, and we have defined

$$\langle k | \hat{H}_{sp} | j \rangle = \int d^3\mathbf{x}\, \phi^*_k(\mathbf{x}) \hat{H}_{sp} \phi_j(\mathbf{x}). \tag{5.6}$$

We assume for $k \notin C$ that $\phi_k(\mathbf{x})$ is an eigenstate of $\hat{H}_{sp}$, and so $\hat{H}_0$ simplifies to

$$\hat{H}_0 = \sum_{\alpha\beta} \langle \alpha | \hat{H}_{sp} | \beta \rangle \hat{a}^\dagger_\alpha \hat{a}_\beta + \hbar \sum_k \omega_k \hat{a}^\dagger_k \hat{a}_k, \tag{5.7}$$

as $\langle\alpha|\hat{H}_{sp}|k\rangle = \hbar\omega_k\langle\alpha|k\rangle = 0$. For the interaction part of the Hamiltonian we have

$$\begin{aligned}
\hat{H}_I &= \frac{1}{2}\sum_{\alpha\beta\chi\sigma}\langle\alpha\beta|V|\chi\sigma\rangle\hat{a}^\dagger_\alpha\hat{a}^\dagger_\beta\hat{a}_\chi\hat{a}_\sigma && \text{(5.8a)}\\
&+ \sum_{\alpha\beta\chi n}\left[\langle\alpha\beta|V|\chi n\rangle\hat{a}^\dagger_\alpha\hat{a}^\dagger_\beta\hat{a}_\chi\hat{a}_n + h.c.\right] && \text{(5.8b)}\\
&+ \frac{1}{2}\sum_{\alpha\beta mn}\left[\langle\alpha\beta|V|mn\rangle\hat{a}^\dagger_\alpha\hat{a}^\dagger_\beta\hat{a}_m\hat{a}_n + h.c.\right] && \text{(5.8c)}\\
&+ 2\sum_{\alpha j\chi n}\langle\alpha j|V|\chi n\rangle\hat{a}^\dagger_\alpha\hat{a}_\chi\hat{a}^\dagger_j\hat{a}_n && \text{(5.8d)}\\
&+ 2\sum_{\alpha jmn}\left[\langle\alpha j|V|mn\rangle\hat{a}^\dagger_\alpha\hat{a}^\dagger_j\hat{a}_m\hat{a}_n + h.c.\right] && \text{(5.8e)}\\
&+ \frac{1}{2}\sum_{kjmn}\langle kj|V|mn\rangle\hat{a}^\dagger_k\hat{a}^\dagger_j\hat{a}_m\hat{a}_n, && \text{(5.8f)}
\end{aligned}$$

where the symmetrised matrix element $\langle kj|V|mn\rangle$ is defined in Eq. (2.14). Using Eqs. (5.7) and (5.8) we now derive the Heisenberg equations of motion for the operators in each region.

### 5.2.2 Coherent region

The equation of motion for a coherent region mode is

$$\begin{aligned}
i\hbar\frac{d\hat{a}_\alpha}{dt} &= \sum_\beta\langle\alpha|\hat{H}_{sp}|\beta\rangle\hat{a}_\beta && \text{(5.9a)}\\
&+ \sum_{\beta\chi\sigma}\langle\alpha\beta|V|\chi\sigma\rangle\hat{a}^\dagger_\beta\hat{a}_\chi\hat{a}_\sigma && \text{(5.9b)}\\
&+ \sum_{q\chi\sigma}\langle\alpha q|V|\chi\sigma\rangle\hat{a}^\dagger_q\hat{a}_\chi\hat{a}_\sigma && \text{(5.9c)}\\
&+ 2\sum_{\beta m\sigma}\langle\alpha\beta|V|m\sigma\rangle\hat{a}^\dagger_\beta\hat{a}_m\hat{a}_\sigma && \text{(5.9d)}\\
&+ \sum_{\beta mn}\langle\alpha\beta|V|mn\rangle\hat{a}^\dagger_\beta\hat{a}_m\hat{a}_n && \text{(5.9e)}\\
&+ 2\sum_{qm\sigma}\langle\alpha q|V|m\sigma\rangle\hat{a}^\dagger_q\hat{a}_m\hat{a}_\sigma && \text{(5.9f)}\\
&+ \sum_{qmn}\langle\alpha q|V|mn\rangle\hat{a}^\dagger_q\hat{a}_m\hat{a}_n. && \text{(5.9g)}
\end{aligned}$$

It is at this stage that we make our approximations. The coherent region $C$ is defined by the condition that for all modes $\langle \hat{a}_\nu^\dagger \hat{a}_\nu \rangle \gg 1$, and therefore the quantum fluctuations of the projected field operator in this region can be ignored. Thus we assume that the region $C$ is well approximated by a coherent state, so that we have the expectation value

$$\begin{aligned} \langle \hat{\psi}(\mathbf{x}) \rangle &\equiv \langle \Psi | \hat{\psi}(\mathbf{x}) | \Psi \rangle, \\ &\approx \psi(\mathbf{x}) \langle \Psi | \Psi \rangle, \\ &= \psi(\mathbf{x}). \end{aligned} \tag{5.10}$$

Expanding the coherent state wave function on the basis we find

$$\begin{aligned} \psi(\mathbf{x}) &= \sum_{\nu \in C} \langle \hat{a}_\nu \rangle \phi_\nu(\mathbf{x}), \\ &\equiv \sum_{\nu \in C} c_\nu \phi_\nu(\mathbf{x}). \end{aligned} \tag{5.11}$$

To obtain the finite temperature GPE, we take the expectation value of Eq. (5.9). We find, for example

$$\begin{aligned} \left\langle \sum_{q\chi\sigma} \langle \alpha q | V | \chi\sigma \rangle \hat{a}_q^\dagger \hat{a}_\chi \hat{a}_\sigma \right\rangle &\to \sum_{q\chi\sigma} \langle \alpha q | V | \chi\sigma \rangle \langle \hat{a}_q^\dagger \rangle c_\chi c_\sigma \\ &= \sum_q \langle \alpha q | V | \psi\psi \rangle \langle \hat{a}_q^\dagger \rangle, \end{aligned} \tag{5.12}$$

where the matrix element is time dependent, as the wave function $\psi$ is not a stationary state.

The incoherent region for the most part is best represented by number states. However, this is not always the case. In particular the states within $I$ near the boundary of the two regions will be partially coherent, and this is illustrated in Fig. 5.1. The expectation value $\langle \hat{a}_q^\dagger \rangle$ in this transitional region will not be zero, and so terms such as Eq. (5.12) are retained in our equations. This is different from other mean field theories where linear terms are set to zero. In systems that are partially condensed, however, the effect of these terms will be small, as the transition region will be narrow compared to the full width of the incoherent region.

Taking the expectation value of all terms in Eq. (5.9), the full basis set equation

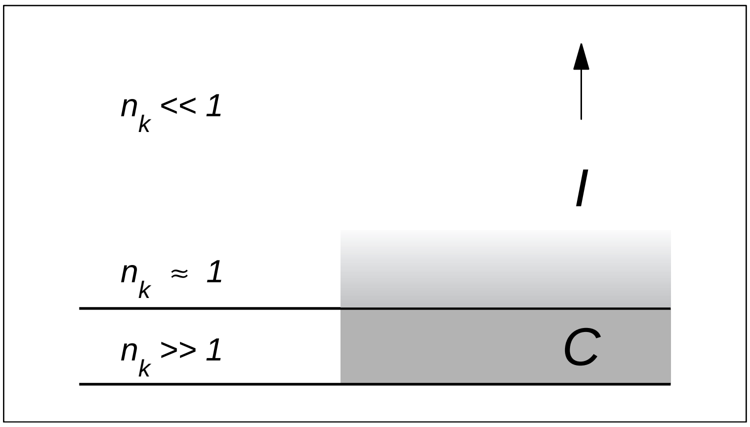

Figure 5.1: An illustrative diagram of the coherent region $C$ and the incoherent region $I$, with the shading an indication of the coherence of the field. The states in $I$ near the boundary with $C$ will be partially coherent.

of motion for a coherent mode of the field is

$$\begin{aligned}
i\hbar\frac{dc_\alpha}{dt} &= \langle\alpha|\hat{H}_{sp}|\psi\rangle && (5.13a)\\
&+ \langle\alpha\psi|V|\psi\psi\rangle && (5.13b)\\
&+ \sum_q \langle\alpha q|V|\psi\psi\rangle\langle\hat{a}_q^\dagger\rangle && (5.13c)\\
&+ 2\sum_m \langle\alpha\psi|V|m\psi\rangle\langle\hat{a}_m\rangle && (5.13d)\\
&+ \sum_{mn} \langle\alpha\psi|V|mn\rangle\langle\hat{a}_m\hat{a}_n\rangle && (5.13e)\\
&+ 2\sum_{qm} \langle\alpha q|V|m\psi\rangle\langle\hat{a}_q^\dagger\hat{a}_m\rangle && (5.13f)\\
&+ \sum_{qmn} \langle\alpha q|V|mn\rangle\langle\hat{a}_q^\dagger\hat{a}_m\hat{a}_n\rangle. && (5.13g)
\end{aligned}$$

We can convert this expression to the spatial representation by applying the operation $\sum_{\alpha\in C}|\alpha\rangle$ to both sides. Using the contact potential approximation and recognising $\sum_{\alpha\in C}|\alpha\rangle\langle\alpha|$ as our projector of Eq. (5.1), this procedure results in the finite temperature Gross-Pitaevskii equation (FTGPE)

$$\begin{aligned}
i\hbar\frac{\partial\psi(\mathbf{x})}{\partial t} &= \hat{H}_{sp}\psi(\mathbf{x}) + U_0\hat{\mathcal{P}}\left\{|\psi(\mathbf{x})|^2\psi(\mathbf{x})\right\} && (5.14a)\\
&+ U_0\hat{\mathcal{P}}\left\{2|\psi(\mathbf{x})|^2\langle\hat{\eta}(\mathbf{x})\rangle + \psi(\mathbf{x})^2\langle\hat{\eta}^\dagger(\mathbf{x})\rangle\right\} && (5.14b)\\
&+ U_0\hat{\mathcal{P}}\left\{\psi^*(\mathbf{x})\langle\hat{\eta}(\mathbf{x})\hat{\eta}(\mathbf{x})\rangle + 2\psi(\mathbf{x})\langle\hat{\eta}^\dagger(\mathbf{x})\hat{\eta}(\mathbf{x})\rangle\right\} && (5.14c)\\
&+ U_0\hat{\mathcal{P}}\left\{\langle\hat{\eta}^\dagger(\mathbf{x})\hat{\eta}(\mathbf{x})\hat{\eta}(\mathbf{x})\rangle\right\}, && (5.14d)
\end{aligned}$$

where $\hat{\eta}(\mathbf{x})$ is defined by Eq. (5.3). The FTGPE describes the full dynamics of the region $C$ and its coupling to an effective thermal bath $\hat{\eta}(\mathbf{x})$. Each of the lines of the FTGPE represents collision processes involving a different number of coherent region states. We describe them briefly here, before a longer discussion in the following section.

The terms on the first line of the FTGPE, Eq. (5.14a), represent purely coherent region dynamics. The first term describes the free evolution of the wave function $\psi$, while the second represents evolution due to two particles from $C$ colliding, with both particles remaining inside the $C$. This line describes the *internal* dynamics of the coherent region, and therefore conserves the normalisation of $\psi(\mathbf{x})$.[1] The collision processes of this line are represented by the dashed outgoing arrows in Fig. 4.4(c), with $R_{NC}$ being interpreted as the incoherent region and $R_C$ the coherent region.

The terms on the second line, Eq. (5.14b), describe two coherent atoms interacting resulting in one remaining in $C$ and one escaping to the incoherent region, along with the reverse process. These are stimulated processes as the terms contain three coherent region labels, and they result in the transfer of some coherence to the bath $\hat{\eta}(\mathbf{x})$ (see Fig. 5.1). However, because of energy conservation these terms represent a boundary effect, and will not be large in general. These processes are depicted by the solid outgoing arrows in Fig. 4.4(c).

The third line, Eq. (5.14c), is generally more important than the second. The first term represents the collision of two coherent atoms, with two incoherent atoms resulting. If the region $C$ represents only a single condensate in thermal equilibrium then this term cannot conserve energy, and therefore it cannot describe real processes.[2] However, it can describe *virtual* processes and thus contributes to the appearance of both the two-body and many-body T-matrices.

The second term of the third line Eq. (5.14c) represents a coherent atom colliding with an incoherent atom, with one atom remaining in each region after the interaction. In equilibrium, this process represents the mean field of the incoherent region acting on $C$, and can be added to the $|\psi(\mathbf{x})|^2$ term of Eq. (5.14a). Away from equilibrium, this term describes *scattering* processes, identical to those described earlier in model B of condensate growth in Sec. 3.6. They are depicted in Fig. 4.4(b).

---

[1] This point will be discussed further in Sec. 6.1.

[2] However, when the coherent region is made up of two or more condensates then the first term of Eq. (5.14c) can describe real processes—we leave further discussion of this point to Sec. 5.3.2.

Finally the fourth line, Eq. (5.14d), represents the collision of two incoherent atoms in which one is transferred to the coherent region $C$. This is the growth process described in the earlier chapters, and is the main contribution to the transfer of population between the coherent and incoherent regions. This process is depicted in Fig. 4.4(a).

### 5.2.3 Incoherent region

The coherence of the majority of levels outside of $C$ is negligible, and therefore the incoherent region is best described in terms of number states. The energy of the quantum levels is large enough that the mean field of the wave function does not significantly affect this region, and so we assume that $\hat{H}_I$ is a small perturbation to $\hat{H}_0$. Therefore kinetic theory can describe the evolution of this part of the quantum field, with the appropriate modifications to treat the coupling to the coherent region.

In the following treatment of the dynamics we use similar techniques to those presented in Sec. 2.4 in the derivation of the quantum Boltzmann equation. We earlier found approximate solutions for the terms on the right-hand side of the relevant equations of motion, and substituted them back in. We follow the same procedure for the expectation values of the combinations of operators on the right-hand side of the FTGPE. Thus we need the equation of motion for the incoherent region operator $\hat{a}_p$. From calculating the commutator with the Hamiltonian of Sec. 5.2.1, we find

$$\begin{aligned} i\hbar\frac{d\hat{a}_p}{dt} &= \hbar\omega_p\hat{a}_p && (5.15a)\\ &+ \langle p\psi|V|\psi\psi\rangle && (5.15b)\\ &+ \sum_q\langle pq|V|\psi\psi\rangle\hat{a}_q^\dagger && (5.15c)\\ &+ 2\sum_m\langle p\psi|V|m\psi\rangle\hat{a}_m && (5.15d)\\ &+ \sum_{mn}\langle p\psi|V|mn\rangle\hat{a}_m\hat{a}_n && (5.15e)\\ &+ 2\sum_{qm}\langle pq|V|m\psi\rangle\hat{a}_q^\dagger\hat{a}_m && (5.15f)\\ &+ \sum_{qmn}\langle pq|V|mn\rangle\hat{a}_q^\dagger\hat{a}_m\hat{a}_n. && (5.15g)\end{aligned}$$

From here we can use the chain rule to derive the other equations needed. These are quite long, and we defer the results to Appendix E.

A kinetic equation for the incoherent region can be derived from Eq. (5.15) using the same techniques as in Sec. 2.4. The result is long and complicated, and is best considered after we have understood all the incoherent region terms in the FTGPE. We postpone presenting and discussing this equation to the end of the chapter.

## 5.3 The individual terms of the FTGPE

In this section we interpret the meaning and find approximate expressions for the terms involving combinations of the bath operator $\hat{\eta}(\mathbf{x})$ on the right-hand side of the FTGPE, Eq. (5.14).

### 5.3.1 The linear terms

There are two terms involving either $\hat{\eta}(\mathbf{x})$ or $\hat{\eta}^\dagger(\mathbf{x})$ in Eq. (5.14). As mentioned earlier, these describe the collision of two coherent atoms, where one particle remains in the region $C$ and the other is transferred to the incoherent region (along with the reverse process). In systems where there is significant population in the incoherent region, these terms will not be very large in comparison to the terms of higher order in $\hat{\eta}$. There is, however, a situation in these terms can be important.

We consider the situation of a static, Thomas-Fermi regime condensate in a harmonic trap at $T = 0$. The condensate is the in lowest eigenstate of the system, and hence the region $C$ is small. Collisions between condensate atoms cannot excite particles out of the ground state, as these processes cannot conserve energy.[3] Thus the linear terms that we are considering are zero in equilibrium. However, these terms can be important at $T = 0$ when the system is out of equilibrium due to a sudden disturbance. Such situation can occur for a condensate with a tunable $s$-wave scattering length.

Recently Bose-Einstein condensation has been observed in $^{85}$Rb by the group of Carl Wieman at JILA, Colorado [43]. This is a remarkable achievement in itself, as the scattering length of this atom is large and negative in zero magnetic field. However, the group made use of a Feshbach resonance in the interatomic potential to tune the scattering length during evaporative cooling to minimise inelastic loss

---

[3] Of course, there can be collisions in which pairs are virtually excited, and these contribute to the two-body T-matrix.

processes [127]. This enabled them to observe the formation of stable condensates with a positive scattering length consisting of several thousand atoms.

Having control over the scattering length, and in particular being able to switch it from being positive to negative in a very short time, allows the experimental investigation of the process of condensate collapse. This has been observed to occur previously for $^7$Li in the experiment at Rice University [128, 129]. However, this group uses a permanent magnetic trap for which the largest stable condensates consist of fewer than 1300 atoms. This means that the condensate is very small and it is difficult to image directly. Because the trap is permanent they cannot use time-of-flight imaging techniques, and therefore they have been restricted in their measurements of collapse. The JILA experiment is much more flexible, and better suited to this purpose.

Experiments investigating the process of collapse have recently been performed at JILA [130]. These begin with a 4000 atom condensate in equilibrium near $T = 0$ with a very large, positive $s$-wave scattering length of $a = +2500a_0$, where $a_0$ is the Bohr radius.[4] At $t = 0$ this is rapidly switched to being small and negative, with a value of $a = -60a_0$. The condensate is then observed to collapse, losing atoms in two large “burns,” before expanding and becoming stable with around 1000 atoms in the final condensate. A thermal cloud with a temperature of $\sim 60$ nK is also observed where there was none previously. The time scale of this collapse is very short, and the inelastic collision rates necessary to account for such a rapid loss of atoms are much larger than theory or previous measurements [131] would predict. However, it has recently been suggested in a preprint by Duine and Stoof that *elastic* collision processes are responsible for the loss of atoms from the condensate [132]. We have investigated this possibility with the formalism we have described in this chapter.

### Our interpretation

The phenomena observed in the experiment at JILA can be attributed mainly to the large change in the interaction energy of the condensate. Although the negative final scattering length results in a system that can only sustain a certain number of atoms in the condensate, we believe very similar results would be obtained experimentally for a condensate with a final scattering length of $a_s = +60a_0$.

This can be understood as follows. The condensate is initially in the Thomas-Fermi regime and has a large spatial extent. When the scattering length is changed,

---

[4] In comparison, the $s$-wave scattering length of $^{87}$Rb is $a \approx +110a_0$.

the interaction energy is reduced so that the large condensate radius can no longer be supported. The potential energy stored in the trap is hence transferred to kinetic energy.

We can interpret the subsequent dynamics using the sudden approximation. The condensate is initially in its ground state for $a = +2500a_0$. After the change in the scattering length, however, the system is in a *superposition* of excited states appropriate to the new value of $U_0$. There is now sufficient energy in the coherent region that collisions out of the condensate can occur. Particles near the boundary of $C$ may interact, with one of the resulting particles being stimulated into the new condensate ground state. For this collision to conserve energy the remaining atom must end up outside the boundary of $C$. This process is purely stimulated, and should be described by the finite temperature GPE, Eq. (5.14), by the terms involving $\langle\hat{\eta}\rangle$ and $\langle\hat{\eta}^\dagger\rangle$.

### Approximate solution

We now find an approximate expression for these terms so that we can substitute them into the FTGPE. We begin with the equation for motion for the single annihilation operator of Eq. (5.15), and eliminate the free evolution via the transformation $\tilde{a}_p = \hat{a}_p \mathrm{e}^{i\omega_p t}$. Taking the expectation value and using Wick's theorem and the RPA, the only terms that survive are

$$i\hbar \frac{d\langle\tilde{a}_p\rangle}{dt} = \langle p\psi|V|\psi\psi\rangle \mathrm{e}^{i\omega_p t} + 2\sum_q \langle pq|V|q\psi\rangle n_q \mathrm{e}^{i\omega_p t}. \tag{5.16}$$

We can also drop the last term in this equation as it does not represent energy conserving processes, and thus we have

$$i\hbar \frac{d\langle\tilde{a}_p\rangle}{dt} = \langle p\psi|V|\psi\psi\rangle \mathrm{e}^{i\omega_p t}, \tag{5.17}$$

which we recognise as the GPE, but for mode $p$ in the incoherent region. If we expand the coherent region wave function on a basis set

$$\psi(\mathbf{x}) = \sum_\sigma \tilde{c}_\sigma \xi_\sigma(\mathbf{x}) \mathrm{e}^{-i\omega_\sigma t}, \tag{5.18}$$

where the coefficients $\tilde{c}_\sigma = c_\sigma e^{i\omega_\sigma t}$, the equation of motion for $\tilde{a}_p$ becomes

$$i\hbar \frac{d\langle \tilde{a}_p \rangle}{dt} = \sum_{\beta\chi\sigma} \tilde{c}_\beta^* \tilde{c}_\chi \tilde{c}_\sigma \langle p\beta|V|\chi\sigma\rangle e^{i\omega_{p\beta\chi\sigma}t}, \tag{5.19}$$

where we have introduced the notation

$$\omega_{pqmn} \equiv \omega_p + \omega_q - \omega_m - \omega_n. \tag{5.20}$$

If we can assume that the basis $\{\xi_\sigma\}$ approximately diagonalises the coherent region Hamiltonian, then the exponential term contains most of the time dependence of Eq. (5.19). We can then use the technique described in Appendix A to write down the approximate solution for $\tilde{a}_p$. Incorporating the free evolution in the result, we find

$$\langle \hat{a}_p \rangle = \sum_{\beta\chi\sigma} \left\{ \frac{c_\beta^* c_\chi c_\sigma \langle p\beta|V|\chi\sigma\rangle}{\hbar\omega_{p\beta\chi\sigma} t} - i\pi c_\beta^* c_\chi c_\sigma \langle p\beta|V|\chi\sigma\rangle \delta(\hbar\omega_{p\beta\chi\sigma}) \right\}. \tag{5.21}$$

As we are mainly interested in the kinetic processes that can occur, we neglect the energy shift described by the principal part (the first term on the right-hand side). The relevant term in the FTGPE in basis form, Eq. (5.13d), is thus

$$i\hbar \frac{dc_\alpha}{dt} = \ldots - 2\pi i \sum_{p\kappa\nu} \langle \alpha\kappa|V|p\nu\rangle c_\kappa^* c_\nu \sum_{\beta\chi\sigma} c_\beta^* c_\chi c_\sigma \langle p\beta|V|\chi\sigma\rangle \delta(\hbar\omega_{p\beta\chi\sigma}), \tag{5.22}$$

where we have expanded all the condensate wave functions in the basis according to Eq. (5.18).

The solution for the mean value $\langle \hat{a}_p^\dagger \rangle$ is simply the hermitian conjugate of Eq. (5.21), and the respective term in the FTGPE, Eq. (5.13c), is therefore

$$i\hbar \frac{dc_\alpha}{dt} = \ldots + \pi i \sum_{p\kappa\nu} \langle \alpha p|V|\kappa\nu\rangle c_\kappa c_\nu \sum_{\beta\chi\sigma} c_\chi^* c_\sigma^* c_\beta \langle \chi\sigma|V|p\beta\rangle \delta(\hbar\omega_{p\beta\chi\sigma}). \tag{5.23}$$

We can see that the Eqs. (5.22) and (5.23) contain coherent region amplitudes $\{c_\alpha\}$ only—this is because all the processes we have included are stimulated.

### Comparison with Duine and Stoof

Our results of the previous section can be simplified somewhat if we assume that the basis that diagonalises the Hamiltonian are plane waves.[5] The representation of the condensate wave function of Eq. (5.11) is then

$$\begin{aligned} \psi(\mathbf{x}) &= \sum_{\nu\in C} c_\nu \phi_\nu(\mathbf{x}), \\ &\rightarrow \frac{1}{(2\pi)^3}\int d^3\mathbf{k}\phi(\mathbf{k})e^{i\mathbf{k}\cdot\mathbf{x}}. \end{aligned} \tag{5.24}$$

The matrix elements for the contact potential are delta functions in momentum space

$$\langle\alpha\beta|V|\chi\sigma\rangle \rightarrow U_0\delta(\mathbf{k}_\alpha+\mathbf{k}_\beta-\mathbf{k}_\chi-\mathbf{k}_\sigma). \tag{5.25}$$

Using Eqs. (5.24) and (5.25) we find that Eqs. (5.22) and (5.23) become

$$\begin{aligned} i\hbar\frac{\partial\phi(\mathbf{k}_\alpha)}{\partial t} &= -2\pi i U_0^2\int\frac{d^3\mathbf{k}_p}{(2\pi)^3}\int\frac{d^3\mathbf{k}_\kappa}{(2\pi)^3}\int\frac{d^3\mathbf{k}_\chi}{(2\pi)^3}\int\frac{d^3\mathbf{k}_\sigma}{(2\pi)^3} \\ &\quad\times\delta(\epsilon(\mathbf{k}_\chi)+\epsilon(\mathbf{k}_\sigma)-\epsilon(\mathbf{k}_p)-\epsilon(\mathbf{k}_\chi+\mathbf{k}_\sigma-\mathbf{k}_p)) \qquad (5.26\text{a}) \\ &\quad\times\phi^*(\mathbf{k}_\kappa)\phi(\mathbf{k}_\alpha+\mathbf{k}_\kappa-\mathbf{k}_p)\phi^*(\mathbf{k}_\chi+\mathbf{k}_\sigma-\mathbf{k}_p)\phi(\mathbf{k}_\chi)\phi(\mathbf{k}_\sigma) \\ &+ \pi i U_0^2\int\frac{d^3\mathbf{k}_p}{(2\pi)^3}\int\frac{d^3\mathbf{k}_\kappa}{(2\pi)^3}\int\frac{d^3\mathbf{k}_\chi}{(2\pi)^3}\int\frac{d^3\mathbf{k}_\sigma}{(2\pi)^3} \\ &\quad\times\delta(\epsilon(\mathbf{k}_\chi)+\epsilon(\mathbf{k}_\sigma)-\epsilon(\mathbf{k}_p)-\epsilon(\mathbf{k}_\chi+\mathbf{k}_\sigma-\mathbf{k}_p)) \qquad (5.26\text{b}) \\ &\quad\times\phi(\mathbf{k}_\kappa)\phi(\mathbf{k}_\alpha+\mathbf{k}_p-\mathbf{k}_\kappa)\phi(\mathbf{k}_\chi+\mathbf{k}_\sigma-\mathbf{k}_p)\phi^*(\mathbf{k}_\chi)\phi^*(\mathbf{k}_\sigma). \end{aligned}$$

This is very similar to the rate that can be derived from the imaginary part of the many-body T-matrix, using the formalism of Duine and Stoof. We are still investigating the similarities of the two approaches.

Using their expression for collisional loss, Duine and Stoof simulated the collapse experiment described earlier using a Gaussian ansatz for the condensate wave function. The behaviour they observed was in good agreement with the experimentally observed condensate shape oscillations and loss of atoms. We have also performed simulations of this experiment, solving the three-dimensional GPE equation using cylindrical symmetry, but including inelastic two and three-body loss terms. These simulations also matched the experimental data for the shape and size of the condensate very well. However, the magnitude of the loss rates required are

---

[5] This is not a good assumption for the trapped case.

much larger than have been measured for $^{85}$Rb [131], and also would result in a condensate lifetime that is much shorter than experimentally observed. The loss term due to elastic collisions is essentially a three-body process in the GPE, and hence is approximately proportional to $|\psi|^4\psi$.

We believe the correct way to simulate the experiment is with the GPE, but using the projection technique we have described with the boundary for the coherent region chosen using the sudden approximation. Any components of the wave function that numerically appear in the incoherent region can then be damped. These calculations have yet to be performed.

### 5.3.2 The anomalous term

We now consider the term involving $\langle\hat{\eta}\hat{\eta}\rangle$ on the third line of the FTGPE, Eq. (5.14c). Expanding this quantity in the incoherent region basis gives

$$\begin{aligned} \langle\hat{\eta}\hat{\eta}\rangle &= \sum_{mn} \phi_m\phi_n\langle\hat{a}_m\hat{a}_n\rangle, \\ &= \sum_{mn} \phi_m\phi_n\langle\tilde{a}_m\tilde{a}_n\rangle e^{-i(\omega_m+\omega_n)t}. \end{aligned} \tag{5.27}$$

Eliminating the free evolution of Eq. (E.2), and using Wick's theorem and the RPA we find

$$\begin{aligned} i\hbar\frac{\partial\langle\tilde{a}_m\tilde{a}_n\rangle}{\partial t} &= \langle mn|V|\psi\psi\rangle \mathrm{e}^{i(\omega_m+\omega_n)t}(1+n_m+n_n) \\ &\quad +\sum_{kj}\langle mn|V|kj\rangle\langle\tilde{a}_k\tilde{a}_j\rangle e^{i\omega_{pqmn}t}(1+n_m+n_n). \end{aligned} \tag{5.28}$$

The first line of this equation describes two particles scattering from the coherent region into states $m$ and $n$. The second line would usually be ignored in the RPA, as it is of higher order than the first line. However this describes the particles from $m, n$ scattering into $k, j$ and then onto other states. This offers the possibility of ladder diagrams, such that the two particles could scatter back into the coherent region without interacting with an additional atom. We retain them as they are of the same form as the quantity on the left hand side of the equation.

Expanding the coherent region wave function in the approximately diagonal basis we have

$$
\begin{aligned}
i\hbar\frac{\partial\langle\tilde{a}_m\tilde{a}_n\rangle}{\partial t} &= \sum_{\chi\sigma}\tilde{c}_\chi\tilde{c}_\sigma\langle mn|V|\chi\sigma\rangle \mathrm{e}^{i\omega_{mn\chi\sigma}t}(1+n_m+n_n) \\
&\quad +\sum_{kj}\langle mn|V|kj\rangle\langle\tilde{a}_k\tilde{a}_j\rangle e^{i\omega_{mnkj}t}(1+n_m+n_n). \qquad (5.29)
\end{aligned}
$$

This has the form of a Lippmann-Schwinger equation in the time domain, and we will see that this is where the T-matrix enters the formalism.

To solve this equation, we start by considering only the first line of Eq. (5.29) as it is the lowest order term. Once again, most of the time dependence is contained within the exponential, and so using the method of Appendix A we find the solution is

$$
\begin{aligned}
\langle\tilde{a}_m\tilde{a}_n\rangle &= \sum_{\chi\sigma}\tilde{c}_\chi\tilde{c}_\sigma\frac{\langle mn|V|\chi\sigma\rangle(1+n_m+n_n)e^{i\omega_{mn\chi\sigma}t}}{\epsilon_\chi+\epsilon_\sigma-\epsilon_m-\epsilon_n} \\
&\quad -i\pi\sum_{\chi\sigma}\tilde{c}_\chi\tilde{c}_\sigma\langle mn|V|\chi\sigma\rangle\delta(\epsilon_\chi+\epsilon_\sigma-\epsilon_m-\epsilon_n). \qquad (5.30)
\end{aligned}
$$

For a single condensate in thermal equilibrium, the energy delta-function can never be satisfied as it requires two low-energy, coherent atoms from within the coherent region to collide and result in two high-energy, incoherent atoms. We will return to this point later in the section.

We assume that the full solution of Eq. (5.29) is of the same form as Eq. (5.30) but with the interaction potential $V$ replaced by a T-matrix

$$
\langle\hat{a}_m\hat{a}_n\rangle = \sum_{\chi\sigma}c_\chi c_\sigma\frac{\langle mn|T|\chi\sigma\rangle}{\epsilon_\chi+\epsilon_\sigma-\epsilon_m-\epsilon_n}. \qquad (5.31)
$$

This is a solution of Eq. (5.29) if the operator $T$ obeys

$$
T(z) = V+\sum_{kj}V|kj\rangle\frac{1+n_k+n_j}{z-\epsilon_m-\epsilon_n}\langle kj|T(z), \qquad (5.32)
$$

where we have identified the parameter $z=\epsilon_\chi+\epsilon_\sigma+i\delta$ as the incoming energy of the two particles in the collision. The small imaginary part $i\delta$ in this parameter generates the delta function term in Eq. (5.30). Equation (5.32) is the definition of a restricted many-body T-matrix, as the indices $k, j$ are defined to be outside the coherent region.

The many-body T-matrix describes collisions in the presence of a medium.

It takes into account the fact that the virtual states that the two particles pass through in the collision may be occupied with the scattering enhanced by a factor of $(1 + n_k + n_j)$. We shall not discuss the many-body T-matrix any further here, but refer the interested reader to the work of Morgan [54], Proukakis [61] and Stoof [60].

If we have $n_k = n_j = 0$ for the incoherent region, we recover our definition of the restricted two-body T-matrix *in vacuo*. If we had not introduced the high-energy cutoff into the theory, then this is exactly $T_{2b}$ as described in Sec. 2.2. Thus the anomalous term introduces the T-matrix into condensate-condensate collisions.

### Elastic loss in condensate collisions

In the previous section we claimed that the delta function in the solution of the anomalous term Eq. (5.30) could not be satisfied for a system with only one condensate. The situation is different when we consider the collision of two condensates.

In the formalism of this chapter, the coherent region $C$ is defined such that it contains all the modes of the condensate whose occupation number satisfies $N_k \gg 1$. If we consider a condensate that has been formed in a harmonic trap, but then quickly released into free space, we can use the sudden approximation and analyse the wave function in terms of a plane-wave basis. The region $C$ will typically be defined by a small spherical or ellipsoidal region in $k$-space about a central wave-vector $\mathbf{K}$. For a condensate released at rest we have $\mathbf{K} = 0$, but by applying a Bragg-pulse to the condensate on release, a momentum $\hbar\mathbf{K}$ can be imparted [133].

For our purposes we consider the initial condensate coherently split equally into two. One "daughter" condensate has momentum $\hbar\mathbf{K}$ in the lab frame, while the other is at rest. However, we can make a Galilean transformation to the centre-of-mass frame, where the two condensates have momenta $-\hbar\mathbf{K}/2$ and $+\hbar\mathbf{K}/2$ respectively.

Now consider this system analysed in terms of the plane-wave basis appropriate after release from the trap. If the relative momenta of each of the condensates is large compared to their momentum width, then the region $C$ will be made up of two distinct regions in $k$-space. This means that in the collision of the two condensates it is possible for an atom from each to collide, and then scatter into any spatial direction with energy being conserved. A large number of these collisions will take both particles outside the region $C$, as depicted in Fig. 5.2. As these processes cause scattering of both particles into modes that are otherwise empty (and are

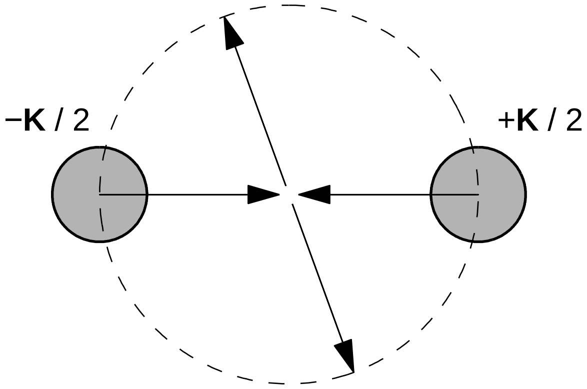

Figure 5.2: A depiction of two condensates colliding in $k$-space in the centre-of-mass frame. The two areas shaded grey centred about $\pm\mathbf{K}/2$ indicate the coherent region $C$. The arrows indicate a possible collision between two coherent particles, in which both end up outside the coherent region. The dashed circle indicates the region of all possible collisions that conserve both energy and momentum.

hence spontaneous), they cannot be represented by the standard GPE.

The proper description of these processes in the formalism described here is via the anomalous term $\langle\hat{\eta}\hat{\eta}\rangle$. In these circumstances the delta function part of Eq. (5.30) can be satisfied, and therefore real transitions can occur. We can see that if the relative momenta of the two condensates is not large, then the two parts of the region $C$ will overlap and most of the circumference of the dashed circle in Fig. 5.2 will lie within $C$. This means that the GPE can describe condensate collisions at low momenta for which spontaneous collisions can be neglected. However, at high relative momenta the methods described here are required.

### Four-wave mixing

Instead of a single Bragg pulse, two separate Bragg pulses can be applied in succession to a condensate after release such that it splits into three distinct parts, each with a different momentum (two moving and one at rest in the lab frame). In a beautiful experiment by the Phillips group at NIST, by carefully adjusting the laser set-up they were able to observe the atom-optical equivalent of four-wave mixing [44].

This experiment can be understood by considering Fig. 5.2. We can imagine a third part to the coherent region corresponding to the third condensate, situated in the figure about the arrow-head at the top of the dashed circle. While the entire dashed region is still available in collisions between atoms from the first two condensates, the presence of third condensate stimulates transitions into this particular mode. This results the formation of a condensate in the region indicated by the arrow pointing downwards. As this is a stimulated collision process, this part of the experiment can be successfully modelled using the ordinary GPE [77, 78].

In fact, the new condensate that appears is entangled with the atoms that are scattered into the third condensate, as the colliding atoms are necessarily correlated. This correlation *cannot* be described by the ordinary GPE, and other methods are required to describe this effect [134]. However, it can be described by the anomalous term in the FTGPE.

### 5.3.3 The scattering term

We now consider the term containing $\langle\hat{\eta}^\dagger\hat{\eta}\rangle$ in the third line of the FTGPE, Eq. (5.14c). A basis set expansion of this quantity gives

$$\langle\hat{\eta}^\dagger\hat{\eta}\rangle = \sum \phi_m^* \phi_n \langle\hat{a}_m^\dagger \hat{a}_n\rangle. \tag{5.33}$$

Eliminating the free evolution, and then using Wick's theorem and the RPA on Eq. (E.3) results in

$$i\hbar \frac{\partial\langle\tilde{a}_m^\dagger \tilde{a}_n\rangle}{\partial t} = 2\sum_{\chi\sigma} \tilde{c}_\chi^* \tilde{c}_\sigma \langle\chi m|V|\sigma n\rangle (n_m - n_n) e^{i\omega_{\chi m\sigma n}t}. \tag{5.34}$$

The solution of Eq. (5.34) differs slightly from that of the anomalous and the linear terms we considered earlier. We previously made the assumption that the approximate solutions were zero at time $t = -\infty$, but this is not the case here.

The diagonal term ($m = n$) of $\langle\tilde{a}_m^\dagger \tilde{a}_n\rangle$ is the ensemble average of the number of particles in mode $n$. For a system at finite temperature in which the incoherent region begins with some population, this will have a non-zero initial value. It appears in the solution of Eq. (5.34) as a constant of integration, determined by the boundary condition. We find

$$\langle\hat{a}_m^\dagger \hat{a}_n\rangle = -2\pi i \sum_{\chi\sigma} c_\chi^* c_\sigma \langle\chi m|V|\sigma n\rangle (n_m - n_n)\delta(\hbar\omega_{\chi m\sigma n}) + n_m \delta_{mn}, \tag{5.35}$$

where the second term on the right-hand side represents the mean field of the incoherent region acting on the coherent region wave function in the FTGPE. We have again neglected the principal part in the solution as the term can describe energy-conserving processes.

The full term in the basis set representation of the FTGPE, Eq. (5.13f) is therefore

$$
\begin{aligned}
i\hbar\frac{dc_\alpha}{dt} &= \ldots + 2\sum_{m\beta} n_m c_\beta \langle \alpha m|V|m\beta\rangle \qquad (5.36) \\
&- 4\pi i \sum_{mn\beta} c_\beta \langle \alpha m|V|n\beta\rangle \sum_{\chi\sigma} c^*_\chi c_\sigma \langle \chi m|V|\sigma n\rangle (n_m - n_n)\delta(\hbar\omega_{\chi m\sigma\sigma})
\end{aligned}
$$

The processes it describes are analogous to the scattering term that was introduced in model B of condensate growth described in Sec. 3.6 of this thesis. It represents an incoherent particle colliding with a coherent particle, with the coherent particle moving between levels within the region $C$ as in Fig. 3.5. In the presence of a condensate this process is recognised as Landau damping. We found that it had an important effect in the description of condensate growth—however in simulations near equilibrium the off-diagonal part of this term is unlikely to be large, as the forward and backward rates will be similar.

### 5.3.4 The growth term

Finally, we consider the term involving $\langle\hat{\eta}^\dagger\hat{\eta}\hat{\eta}\rangle$ on the fourth line of the FTGPE, Eq. (5.14d). This is the most intriguing of the terms arising in the FTGPE, as it will be responsible for the majority of particle exchange between the coherent and incoherent regions. While the linear terms and the anomalous terms can be important in certain circumstances near $T = 0$, in most situations at finite temperature they are small in comparison with this term because of the size difference between the coherent and incoherent region.

From Eq. (E.4), the only terms that survive after taking the expectation value and making use of Wick's theorem and the RPA are

$$
i\hbar\frac{\partial\langle \tilde{a}^\dagger_q \tilde{a}_m \tilde{a}_n\rangle}{\partial t} = 2\sum_\chi \tilde{c}\chi \langle mn|V|q\chi\rangle e^{i\omega_{mnq\chi}t}\{n_q(1+n_m+n_n) - n_m n_n\}, \qquad (5.37)
$$

and as this will have energy matches, the approximate solution is

$$
\langle \tilde{a}^\dagger_q \tilde{a}_m \tilde{a}_n\rangle = 2\pi i \sum_\chi \tilde{c}_\chi \langle mn|V|q\chi\rangle \delta(\hbar\omega_{mnq\chi})\{n_m n_n - n_q(1+n_m+n_n)\}. \qquad (5.38)
$$

Substituting Eq. (5.38) into the basis set version of the FTGPE we find

$$\begin{aligned} i\hbar\frac{dc_\alpha}{dt} &= 2\pi i\sum_{qmn\chi} c_\chi\langle\alpha q|V|mn\rangle\langle mn|V|q\chi\rangle\delta(\hbar\omega_{mnq\chi}) \\ &\quad\times\{n_m n_n - n_q(1+n_m+n_n)\}. \end{aligned} \tag{5.39}$$

This is of the form we expect when making the approximation that the coherent region population $N \gg 1$. The equivalent quantum Boltzmann rate for the growth of a highly occupied level is

$$\begin{aligned} \frac{dN}{dt} &\propto \sum_{qmn}(1+N)(1+n_q)n_m n_n - N n_q(1+n_m)(1+n_n), \\ &\approx \sum_{qmn} N[(1+n_q)n_m n_n - n_q(1+n_m)(1+n_n)], \\ &= \sum_{qmn} N[n_m n_n - n_q(1+n_m+n_n)], \end{aligned} \tag{5.40}$$

and we can see that the right-hand sides of Eqs. (5.39) and (5.40) are similar.

Equation (5.39) is very similar to the growth part of the description of condensate formation described in Chapters 3 and 4. However, rather than describing the rate of change of an occupation number of a generalised energy bin, it describes the growth in amplitude of a given basis component making up the coherent region wave function $\psi$. To calculate this term for inclusion in the GPE, we require

(i) A reasonably good basis and corresponding energies for the coherent region.

(ii) A method of calculating the matrix elements that appear in Eq. (5.39).

While this is not difficult in theory, in practice they need to be calculated at each time step in the evolution of the FTGPE, which may pose more of a problem. We shall address these issues in Chapter 7.

## 5.4 Incoherent region equation of motion

In this section we present the kinetic equation of motion that can be derived for the incoherent region. We find

$$\begin{aligned}
\frac{dn_p}{dt} &= \frac{2\pi}{\hbar}\sum_{q\alpha\beta}|\langle pq|V|\alpha\beta\rangle|^2\delta(\hbar\omega_{pq\alpha\beta})|c_\alpha c_\beta|^2(n_p+n_q+1) && (5.41a)\\
&+ \frac{8\pi}{\hbar}\sum_{\alpha\beta m}|\langle p\alpha|V|m\beta\rangle|^2\delta(\hbar\omega_{p\alpha m\beta})|c_\alpha c_\beta|^2(n_m-n_p) && (5.41b)\\
&+ \frac{4\pi}{\hbar}\sum_{\alpha mn}|\langle p\alpha|V|mn\rangle|^2\delta(\hbar\omega_{p\alpha mn})\\
&\quad\times|c_\alpha|^2\left\{n_m n_n - n_p(1+n_m+n_n)\right\} && (5.41c)\\
&+ \frac{8\pi}{\hbar}\sum_{\alpha qm}|\langle pq|V|m\alpha\rangle|^2\delta(\hbar\omega_{pqm\alpha})\\
&\quad\times|c_\alpha|^2\left\{(n_p+n_q+1)n_m - n_p n_q\right\} && (5.41d)\\
&+ \frac{4\pi}{\hbar}\sum_{qmn}|\langle pq|V|mn\rangle|^2\delta(\hbar\omega_{pqmn})\\
&\quad\times\left\{(1+n_p)(1+n_q)n_m n_n - n_p n_q(1+n_m)(1+n_n)\right\}. && (5.41e)
\end{aligned}$$

We can recognise each of these terms from our previous discussions:

1. The term of Eq. (5.41a) is from the anomalous term, and is only non-zero when we consider condensate collisions.
2. The line of Eq. (5.41b) describes the scattering processes.
3. The two terms of Eqs. (5.41c) and (5.41d) are due to the forward and backward growth terms of the coherent region.
4. The line of Eq. (5.41e) is simply the QBE for the incoherent region.

It may seem surprising that there is no contribution from the linear terms discussed in the previous section. This is because the rates for each of the forward and backward processes contain only stimulated terms and so they cancel; the terms that arise are

$$\frac{2\pi}{\hbar}\sum_{\beta\chi\sigma}|\langle p\beta|V|\chi\sigma\rangle|^2\delta(\hbar\omega_{p\beta\chi\sigma})(|c_\beta c_\chi c_\sigma|^2-|c_\beta c_\chi c_\sigma|^2)=0. \qquad (5.42)$$

The kinetic equation for the incoherent region is thus not very different from the usual QBE, and the couplings to the coherent region can be understood from the previous section.

## 5.5 Outlook

In this chapter we have derived a formalism for calculating the dynamics of a Bose gas in the presence of a significant condensate fraction. We have derived a finite temperature Gross-Pitaevskii equation for the coherent region $C$, and identified and discussed each of the terms that arise. In particular we have explained how the linear terms in the bath operator $\hat{\eta}(\mathbf{x})$ may contribute to loss via elastic collisions in the collapse of a BEC with a negative scattering length. We have also shown how the anomalous term introduces the T-matrix into coherent region collisions, and that this can describe elastic particle loss in condensate collisions at large relative momenta. The terms analogous to the scattering and growth processes of Chapters 3 and 4 have also been discussed. We leave numerical computations based on this formalism to the following chapter, and consider the prospects for experimentally-relevant calculations in Chapter 7.

## Chapter 6

# The projected GPE

In Chapter 5 we developed a formalism to describe the dynamics of a Bose condensate at finite temperature based on the GPE. This description is valid when the low-lying modes of the system are classical, satisfying the criterion $N_k \gg 1$. The condensate and its excitations in the coherent region $C$ are represented by a wave function $\psi(\mathbf{x})$, and this is coupled to a thermal cloud represented by the quantum operator $\hat{\eta}(\mathbf{x})$.

The full dynamics of the coherent region and its coupling to the effective heat bath $\eta(\mathbf{x})$ are contained in the finite temperature Gross-Pitaevskii equation, Eq. (5.14). In principle $\hat{\eta}(\mathbf{x})$ can be described using a form of quantum kinetic theory, and the non-equilibrium dynamics of the entire system will depend on the exchange of energy and particles between $C$ and the bath.

## 6.1 The projected GPE

In this chapter, however, we wish to show that the GPE *alone* can describe evolution of general configurations of the coherent region $C$ towards an equilibrium that can be parameterised by a temperature. We therefore ignore all terms involving $\hat{\eta}(\mathbf{x})$ in Eq. (5.14) and concentrate on the first line

$$i\hbar\frac{\partial\psi(\mathbf{x})}{\partial t} = \hat{H}_{sp}\psi(\mathbf{x}) + U_0\hat{\mathcal{P}}\left\{|\psi(\mathbf{x})|^2\psi(\mathbf{x})\right\}, \tag{6.1}$$

which we call the projected Gross-Pitaevskii equation (PGPE). Although Eq. (6.1) is completely reversible, it is well known that deterministic nonlinear systems with only a few degrees of freedom exhibit chaotic, and hence ergodic behaviour [135].

The projected GPE describes a microcanonical system. However, if the region $C$ is large, then its fluctuations in energy and particle number in the grand canonical ensemble would be small. Hence we expect the final equilibrium state of the projected GPE to be similar to that of the finite temperature GPE coupled to a bath $\hat{\eta}(\mathbf{r})$ with the appropriate chemical potential and temperature. The detailed non-equilibrium dynamics of the system *will* depend on the exchange of energy and particles between $C$ and the bath—however, we leave the coupling of $\psi(\mathbf{x})$ and $\hat{\eta}(\mathbf{x})$ to be addressed in future work.

### 6.1.1 Conservation of normalisation

The PGPE conserves normalisation as the effective projected Hamiltonian is hermitian. The nonlinear term of the GPE can be considered to describe interactions between two particles, and as such there can be collisions in which two coherent atoms collide and one is ejected from the coherent region. However, the projector excludes these terms from the equation of motion, and we demonstrate this below.

Consider the equation of motion in a basis set. By substituting

$$\psi(\mathbf{x}) = \sum_{k \in C} c_k \phi_k(\mathbf{x}), \tag{6.2}$$

into Eq. (6.1), and performing the operation $\int d^3\mathbf{x}\phi_p(\mathbf{x})$ on both sides we find

$$i\hbar \frac{dc_p}{dt} = \hbar\omega_p c_p + U_0 \hat{\mathcal{P}} \sum_{qmn \in C} c_q^* c_m c_n \langle pq|mn\rangle. \tag{6.3}$$

If the state $p \in C$, then all four labels are from the coherent region and there is no transfer of population outside the region. For $p \notin C$ the matrix element $\langle pq|mn\rangle \neq 0$ necessarily, and therefore it seems collisions between states from within the coherent region can transfer population outside of $C$. However, we should not be considering the equations of motion for amplitudes $p \notin C$ in the first place, as they not in the definition of the wave function $\psi(\mathbf{x})$. The projection operation is therefore performed implicitly by the basis set representation.

Numerically solving the GPE using a basis set method requires a triple summation over indices, which is a very time-consuming operation. This suggests that we should instead use the spatial representation of Eq. (6.1), where the nonlinear term is local. However, any spatial grid that is fine enough to provide a good representation of all the states within $C$ will also be able to represent modes outside the region $C$. From Eq. (6.3) we can see that this will cause population to be transferred outside of $C$, and so in this case we need to consider the projection operation explicitly.

Another method of approaching this issue is to assume that *all* modes in the problem can be represented by the GPE, but arbitrarily choose part of the system to be the coherent region. Thus the field operator can be written as

$$\hat{\Psi}(\mathbf{x}) \approx \psi(\mathbf{x}) + \eta(\mathbf{x}), \tag{6.4}$$

where *both* fields are classical. Substituting this into the interaction part of the Hamiltonian Eq. (2.3) and using the contact potential approximation, we have

$$\begin{aligned}
\hat{H}_I/U_0 &= \hat{H}_4 + \hat{H}_3 + \hat{H}_2 + \hat{H}_1 + \hat{H}_0, && (6.5)\\
\hat{H}_4 &= \frac{1}{2}\psi^*\psi^*\psi\psi, && (6.6)\\
\hat{H}_3 &= \psi^*\psi^*\psi\eta + \psi^*\eta^*\psi\psi, && (6.7)\\
\hat{H}_2 &= \frac{1}{2}\psi^*\psi^*\eta\eta + 2\psi^*\eta^*\psi\eta + \frac{1}{2}\eta^*\eta^*\psi\psi, && (6.8)\\
\hat{H}_1 &= \psi^*\eta^*\eta\eta + \eta^*\eta^*\psi\eta, && (6.9)\\
\hat{H}_0 &= \frac{1}{2}\eta^*\eta^*\eta\eta, && (6.10)
\end{aligned}$$

where we have dropped all space and time labels for clarity, and have divided the Hamiltonian into five terms depending on the number of coherent region operators they contain. Considering the Hamiltonian in this form we can easily interpret each of the terms. Each $\psi^*$ creates a particle in the coherent region, and each $\psi$ removes a particle from the coherent region. The $\eta^*$ and $\eta$ perform the same operation outside the region $C$. This allows us to identify which processes each of the terms in the Hamiltonian contribute to the equations of motion for both $\psi$ and $\eta$.

We can now derive equations of motion for $\psi$ and $\eta$ by using functional differentiation. We find

$$i\hbar\frac{\partial\psi}{\partial t} = \hat{\mathcal{P}}\frac{\partial\hat{H}}{\partial\psi^*}, \qquad i\hbar\frac{\partial\eta}{\partial t} = \hat{\mathcal{Q}}\frac{\partial\hat{H}}{\partial\eta^*}. \tag{6.11}$$

As an example, let us consider the contribution to these equations for all interactions involving three coherent and one incoherent state, described by $\hat{H}_3$. We find

| No. of coherent states | $i\hbar\left(\dfrac{\partial\psi}{\partial t}\right) = \hat{\mathcal{P}} \times \ldots$ | $i\hbar\left(\dfrac{\partial\eta}{\partial t}\right) = \hat{\mathcal{Q}} \times \ldots$ |
|---|---|---|
| 4 | $\lvert\psi\rvert^2\psi$ | $0$ |
| 3 | $+2\lvert\psi\rvert^2\eta + \eta^*\psi^2$ | $+\lvert\psi\rvert^2\psi$ |
| 2 | $+2\psi\lvert\eta\rvert^2 + \psi^*\eta^2$ | $+2\lvert\psi\rvert^2\eta + \eta^*\psi^2$ |
| 1 | $+\lvert\eta\rvert^2\eta$ | $+2\psi\lvert\eta\rvert^2 + \psi^*\eta^2$ |
| 0 | $+0$ | $+\lvert\eta\rvert^2\eta$ |

Table 6.1: Classical FTGPE divided into terms representing physical processes involving $n$ coherent states

from Eq. (6.7) and Eq. (6.11).

$$i\hbar\frac{\partial\psi}{\partial t} \sim \hat{\mathcal{P}}\left(2|\psi|^2\eta + \eta^*\psi^2\right), \tag{6.12}$$

$$i\hbar\frac{\partial\eta}{\partial t} \sim \hat{\mathcal{Q}}\left(|\psi|^2\psi\right). \tag{6.13}$$

The results of carrying out this operation for all terms of the Hamiltonian are summarised in Table 6.1. The equations of motion for the system will together conserve both energy and normalisation if *all* terms in any row of the table are included, as this correctly accounts for all forward and backward processes of the same order. We have confirmed this numerically by carrying out coupled simulations of $\psi$ and $\eta$ and including only some of these terms.

We can now see that if we want an equation describing interactions involving four coherent states, but neglecting all processes involving incoherent particles, then this is simply the PGPE.

### 6.1.2 Technical aspects of the projector

We earlier defined the projector $\mathcal{P}$ such that

$$\hat{\mathcal{P}}F(\mathbf{x}) = \sum_{k\in C}\phi_k(\mathbf{x})\int d^3\mathbf{x}'\ \phi_k^*(\mathbf{x}')F(\mathbf{x}'), \tag{6.14}$$

and this operation must be carried out every time that we calculate the nonlinear term in the PGPE. This is numerically a very time consuming operation in general, taking many times longer than calculating $|\psi|^2\psi$ itself.

The operation is somewhat simpler if we use a plane-wave basis in our projector.

In this case we have

$$\hat{\mathcal{P}}F(\mathbf{x}) \;=\; \sum_{\mathbf{k}\in C} e^{+i\mathbf{k}\cdot\mathbf{x}'}\int d^3\mathbf{x}\; e^{-i\mathbf{k}\cdot\mathbf{x}}F(\mathbf{x}), \tag{6.15}$$

which is simply the application of a forward Fourier transformation, followed by an inverse Fourier transformation that only includes the modes in the coherent region. We can accomplish this by simply multiplying the forward transform by a grid of ones and zeros that identify the region $C$ in Fourier space. Thus our numerical procedure is

$$\hat{\mathcal{P}}F(\mathbf{x}) \;=\; \mathrm{IFFT}\Big\{P(\mathbf{k})\times\mathrm{FFT}\left[F(\mathbf{x})\right]\Big\}, \tag{6.16}$$

where FFT and IFFT refer to the forward and inverse fast Fourier transform operations respectively, and $P(\mathbf{k})$ is the representation of the projector $\hat{\mathcal{P}}$ in Fourier space. There are very efficient routines available to carry out FFTs[1], and so we find that it is extremely advantageous numerically to define our projector in the plane-wave basis.

### Implications

For any non-periodic trapping potential, the use of a plane-wave basis is at odds with our requirement that the basis must approximately diagonalise $\psi(\mathbf{x})$ at the boundary of the region $C$. In fact, it may not even satisfy this requirement for a periodic potential if the boundary of the coherent region occurs at a low enough energy.

If we consider a homogeneous system, however, the plane-wave basis will always satisfy our requirements. In this case the effect of a condensate on the excitations of the system is simply to mix modes of momenta $\mathbf{p}$ and $-\mathbf{p}$. Thus even if $\psi(\mathbf{x})$ is not diagonalised at the boundary of $C$, we can still apply the projector cleanly in Fourier space. For these reasons, the simulations that we present in this thesis are for the homogeneous Bose gas. We intend to address the issue of projectors for the trapped Bose gas in future work.

---

[1] See `http://www.fftw.org`, the home of the Fastest Fourier Transform in the West.

## 6.2 Simulations

We have performed simulations for a fully three-dimensional homogeneous Bose gas with periodic boundary conditions. The dimensionless equation we compute is

$$i\frac{\partial\psi(\tilde{\mathbf{x}})}{\partial\tau} = -\tilde{\nabla}^2\psi(\tilde{\mathbf{x}}) + C_{\mathrm{nl}}\hat{\mathcal{P}}|\psi(\tilde{\mathbf{x}})|^2\psi(\tilde{\mathbf{x}}), \tag{6.17}$$

where the normalisation of the wave function has been defined to be

$$\int d^3\tilde{\mathbf{x}}\,|\psi(\tilde{\mathbf{x}})|^2 = 1. \tag{6.18}$$

The nonlinear constant is

$$C_{\mathrm{nl}} = \frac{2mNU_0}{\hbar^2 L}, \tag{6.19}$$

where $N$ is the total number of particles in the system, and $L$ is the period. Our dimensionless parameters are $\tilde{\mathbf{x}} = \mathbf{x}/L$, wave vector $\tilde{\mathbf{k}} = \mathbf{k}L$, energy $\tilde{\varepsilon} = \varepsilon/\varepsilon_L$, and time $\tau = \varepsilon_L t/\hbar$, with $\varepsilon_L = \hbar^2/(2mL^2)$.

### 6.2.1 Parameters

The two parameters that determine all properties of the system are the projector $\hat{\mathcal{P}}$ and the nonlinear constant $C_{\mathrm{nl}}$.

#### Projector $\hat{\mathcal{P}}$

We have chosen a projection operator such that all modes included in the simulations have $|\mathbf{k}| < 15 \times 2\pi/L$, which enables us to use a computationally efficient numerical grid of $32 \times 32 \times 32$ points. This means that 13997 modes are included in the problem.

#### Nonlinearity $C_{\mathrm{nl}}$

We note that the choice of the nonlinear constant determines only the ratio of $NU_0/L$. This means that for a given value of $C_{\mathrm{nl}}$, we can choose the parameters $N$, $U_0$ and $L$ such that our condition $N_{\mathbf{k}} \equiv N|c_{\mathbf{k}}|^2 \gg 1$ is always satisfied for a given physical situation.

We have performed three series of simulations with nonlinearities of $C_{\mathrm{nl}} = 500$, 2000, and 10000. The highest value of $C_{\mathrm{nl}}$ was chosen such that all the states contained in the calculation are phonon-like for a large condensate fraction. The boundary between phonon-like and particle-like states for the homogeneous gas is

$$\frac{\hbar^2 k_0^2}{2m} = n_0 U_0, \tag{6.20}$$

where in this chapter we have defined $N_0$ to be the condensate number within the volume $L^3$, and thus $n_0 = N_0/L^3$ is the condensate density. Converting Eq. (6.20) to dimensionless units we find that

$$\tilde{k}_0 = \sqrt{C_{\mathrm{nl}} \frac{N_0}{N}}, \tag{6.21}$$

and therefore for a condensate fraction of $N_0/N = 1$ we have

$$\begin{aligned} C_{\mathrm{nl}} = 10000 \quad &\rightarrow \quad \tilde{k}_0 \approx 15.9 \times 2\pi, \\ C_{\mathrm{nl}} = 2000 \quad &\rightarrow \quad \tilde{k}_0 \approx 7.12 \times 2\pi, \\ C_{\mathrm{nl}} = 500 \quad &\rightarrow \quad \tilde{k}_0 \approx 3.56 \times 2\pi. \end{aligned}$$

We would ideally like to present results for a smaller value of $C_{\mathrm{nl}}$ that is closer to the ideal gas case of $C_{\mathrm{nl}} = 0$, but we find that such simulations would be too computationally intensive. This is because the equilibration rate is approximately proportional to $C_{\mathrm{nl}}^2$, whereas the minimum time-step required for a given accuracy in the numerical integration of the PGPE only increases slowly with decreasing $C_{\mathrm{nl}}$.

To give an indication of how these dimensionless parameters compare to experimental setups, for $C_{\mathrm{nl}} = 10000$ we can choose $^{87}$Rb atoms with $N = 1.8 \times 10^6$ and $L \approx 26$ $\mu$m to give a number density of about $10^{14}$ cm$^{-3}$—similar to current experiments on BEC in traps.

### 6.2.2 Initial wave functions

We begin our simulations with strongly non-equilibrium wave functions with a chosen total energy $\tilde{E}$. We construct these by populating the amplitudes of the wave function components $c_{\mathbf{k}}$ in the expansion

$$\psi(\mathbf{x}, 0) = \sum_{\mathbf{k} \in C} c_{\mathbf{k}} e^{i\mathbf{k}\cdot\mathbf{x}}. \tag{6.22}$$

The populations $|c_{\mathbf{k}}|^2$ are chosen such that the distribution is as flat as possible, while the phases of the amplitudes are chosen at random [120].

The total energy $\tilde{E}$ is a constraint on the distribution of amplitudes. The energy of a pure condensate is $\tilde{E} = C_{\rm nl}/2$, all of this being due to interactions—the kinetic energy is zero. To have a wave function with an energy not much larger than $C_{\rm nl}/2$, the occupations of the $\tilde{k} = 0$ state and the $\tilde{k} = 2\pi$ states cannot be equal. (We use the notation $k \equiv |\mathbf{k}|$.) Therefore, for the lowest energy simulations the initial condensate population is necessarily larger than the excited state populations.

To ensure that the initial wave functions are sufficiently randomised, we enforce the condition that all 123 states with $\tilde{k} \leq 3 \times 2\pi$ must have some initial population, while all other components may be unoccupied. For low energies, when this distribution including the condensate cannot be totally flat, we keep the populations of the components with $1 \leq \tilde{k}/2\pi \leq 3$ equal, and adjust the condensate population such that the wave function has the energy we require. An example of this situation is shown in Fig. 6.1 for the $\tilde{E} = 7000$ initial wave function in the $C_{\rm nl} = 10000$ simulation series.

For simulations with a sufficiently high total energy $\tilde{E}$ that the inner 123 components may have equal population, we continue to add further shells of higher $k$ to our wave function. The amplitudes of the inner components are readjusted to maintain the required normalisation. This causes the energy of the system to increase monotonically with each new shell until we find two wave functions that bound the energy we are looking for, differing only in their outermost shell. We then adjust the population of the outermost shell downwards until we reach the required energy. An example of an initial wave function produced by this procedure is shown in Fig. 6.2 for the $\tilde{E} = 11000$ case in the $C_{\rm nl} = 10000$ simulation series.

This method is chosen because the problem is nonlinear. In the ideal gas case ($C_{\rm nl} = 0$), we can calculate the kinetic energy (and hence the total energy) of the wave function simply by knowing the distribution of $|c_{\mathbf{k}}|^2$, via

$$\begin{aligned} E_{\rm kin} &= -\frac{\hbar^2}{2m} \int d^3\mathbf{x}\, \psi^*(\mathbf{x}) \nabla^2 \psi(\mathbf{x}), \\ &= -\frac{\hbar^2}{2m} \sum_{\mathbf{k}} |c_{\mathbf{k}}|^2 k^2. \end{aligned} \tag{6.23}$$

However, for $C_{\rm nl} > 0$ we must also add the interaction energy of the wave function

| $C_{\text{nl}}$ | Min. time step ($10^{-6}$) | Max. time step ($10^{-6}$) | Length of evolution $\tau$ |
|---|---|---|---|
| 500 | 4 | 6 | 2.0 |
| 2000 | 1.6 | 4.4 | 0.4 |
| 10000 | 0.45 | 1.2 | 0.2 |

Table 6.2: The typical minimum and maximum time steps for the simulations. The minimum is for high energy simulations, and the maximum for low energy.

to the total energy. This is

$$\begin{aligned} E_{\text{int}} &= \frac{U_0}{2}\int d^3\mathbf{x}\,|\psi(\mathbf{x})|^4, \\ &= \frac{U_0}{16\pi^3}\sum_{\mathbf{pqmn}} c^*_{\mathbf{p}}c^*_{\mathbf{q}}c_{\mathbf{m}}c_{\mathbf{n}}\delta_{\mathbf{p}+\mathbf{q}-\mathbf{m}-\mathbf{n}}, \end{aligned} \tag{6.24}$$

and depends non-trivially on the $\{c_{\mathbf{k}}\}$.

Further images of initial and final state wave functions are shown in Figs. 6.1 and 6.2 in real space, as well as $k$-space.

### 6.2.3 Evolution

The PGPE is evolved in the interaction picture, using a fourth-order Runge-Kutta method with adaptive step size determined by estimating the fifth-order truncation error as described in Appendix D. The acceptable relative truncation error was set to be $10^{-10}$ for all components with an occupation of $\geq 10^{-4}N_0/N$. This resulted in typical time steps as presented in Table 6.2. The duration of each time step ranged from 1.05 seconds on a 900 Mhz AMD Athlon processor, to 1.55 seconds on a 550 Mhz Pentium III and 2.20 seconds on a 300 Mhz Pentium II processor.

We evolve the initial wave functions for at least twice as long as it takes for the system to reach equilibrium, based on the observation of the behaviour of the condensate fraction (see the next section). The time period for each value of $C_{\text{nl}}$ is also given in Table 6.2. Thus the longest of these simulations required $\sim 5\times10^5$ time steps, or nearly six days computational time on the fastest processors available to us.

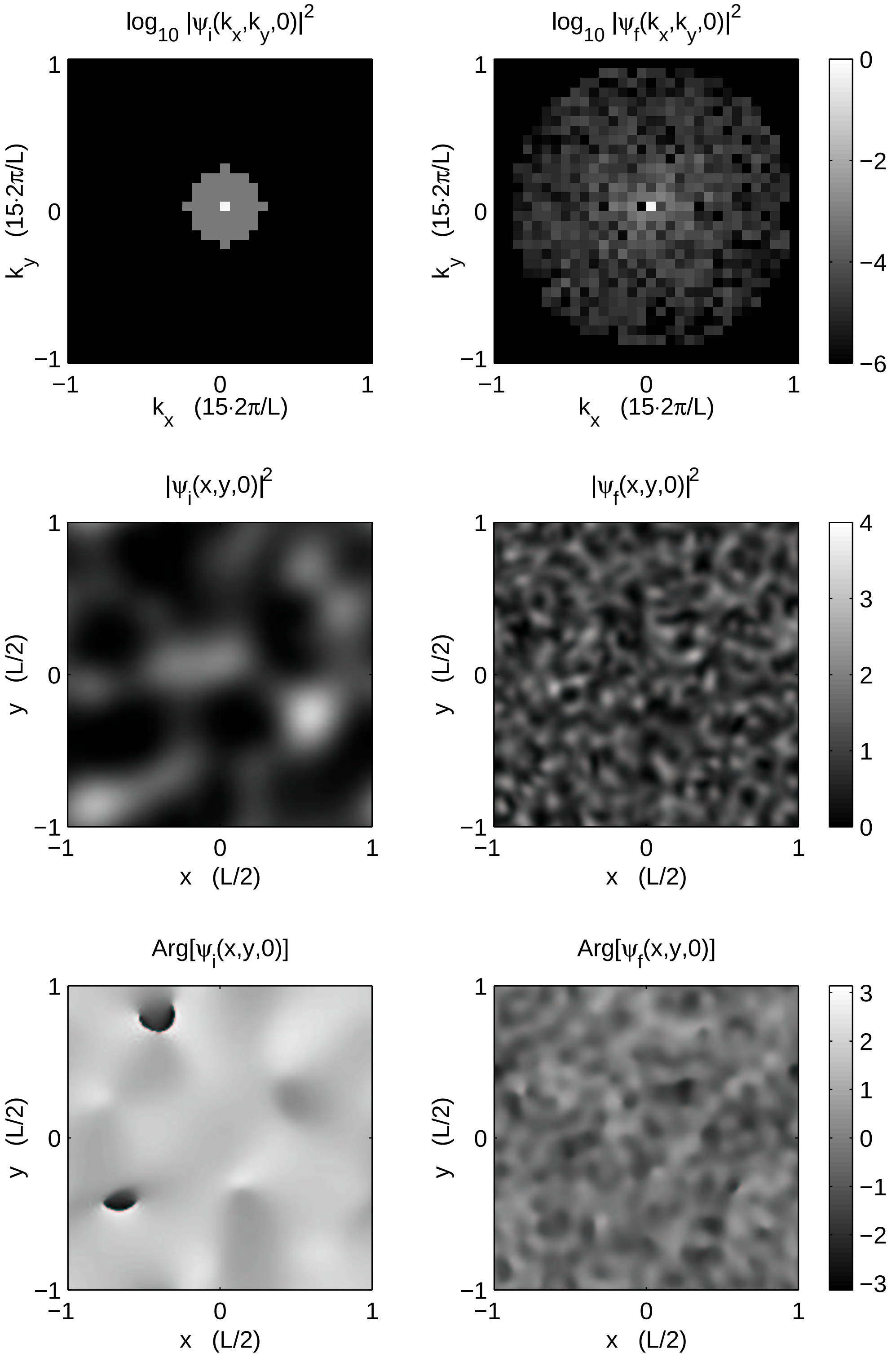

Figure 6.1: Two dimensional slices of wave functions for the $C_{\mathrm{nl}} = 10000$, $\tilde{E} = 7000$ simulations. The initial wave function at $\tau = 0$ is shown on the left, and the final wave function at $\tau = 0.2$ is shown on the right. The top row is the wave function in $k$-space, showing the distribution of the occupations $|c_{\mathbf{k}}|^2$. The middle row is the probability density and the bottom row is the phase in real space.

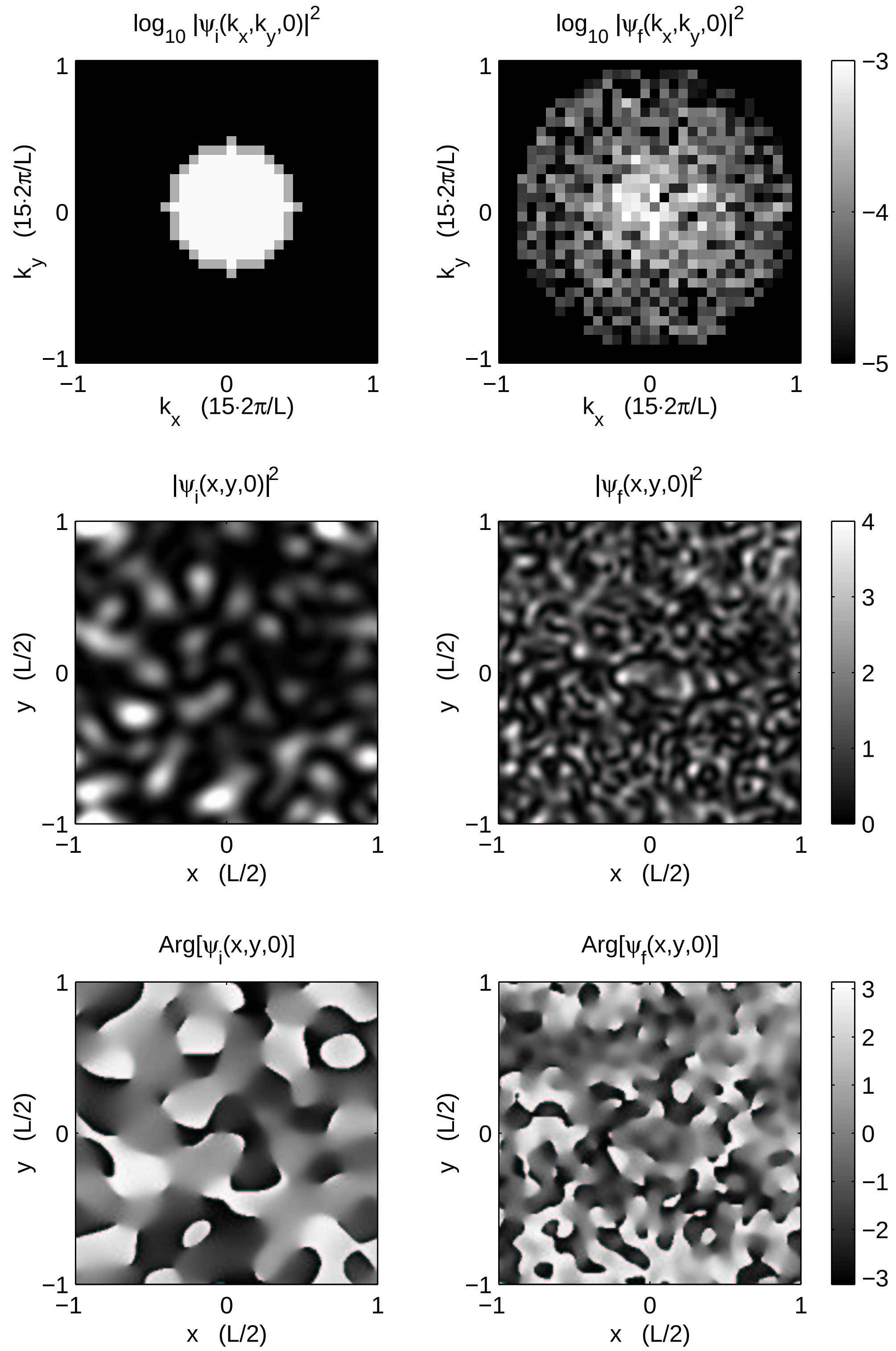

Figure 6.2: Two dimensional slices of wave functions for the $C_{\mathrm{nl}} = 10000$, $\tilde{E} = 11000$ simulations. The initial wave function at $\tau = 0$ is shown on the left, and the final wave function at $\tau = 0.2$ is shown on the right. The top row is the wave function in $k$-space, showing the distribution of the occupations $|c_{\mathbf{k}}|^2$. The middle row is the probability density and the bottom row is the phase in real space.

## 6.3 Evidence for equilibrium

Although the PGPE is completely reversible, the final state wave functions displayed in Figs. 6.1 and 6.2 indicate that the simulations have evolved the system to an apparent equilibrium state. The $k$-space distributions have evolved from initially being flat to a form that is peaked at the centre, and tails away towards the edges. Also, there is a smoothing out of both the phase and density profiles of the real-space wave function. After a certain time of evolution $\tau_{\mathrm{eq}}$, the plots for the wave functions appear to be isomorphic for $\tau > \tau_{\mathrm{eq}}$.

We would like to note that the equilibrium properties depend only on the total energy and momentum of the initial wave function—they are independent of the shape of the distribution in $k$-space. We have performed simulations with non-spherical initial wave functions, and found that they evolve to a spherical equilibrium state. Also, as the GPE conserves momentum, for the condensate to form in the $k = 0$ mode the initial distribution must have zero total momentum. We have performed simulations where the initial distribution had a finite momentum, and observed the condensate to form in a non-zero momentum state.

In theory, to determine the properties of the system at equilibrium we should carry out many different simulations each with the same initial conditions but with different choices of the initial phases of the amplitudes, and then take the ensemble average at a given time. However, this is computationally unfeasible, and instead we assume the ergodic theorem applies, such that the time average of a quantity in a single system at equilibrium is equivalent to the ensemble average over many. This seems a reasonable hypothesis, and thus we time-average over the last 50 wave functions saved all with $\tau > \tau_{\mathrm{eq}}$.

### Condensate occupation

Strong evidence that the simulations have reached equilibrium is provided by the time dependence of the condensate population. For all simulations this settles down to an average value (dependent on the energy $\tilde{E}$) that fluctuates by a small amount. The initial time evolution of the condensate fraction for five different energies with $C_{\mathrm{nl}} = 10000$ is shown in Fig. 6.3.

The average condensate occupation in equilibrium for all simulations for the $C_{\mathrm{nl}} = 10000$ case are presented in Fig. 6.4(a). The fluctuations of the condensate population are indicated by vertical lines at each point, and these are largest for the $\tilde{E} = 9000$ simulation. For comparison, the corresponding curve for the ideal gas is

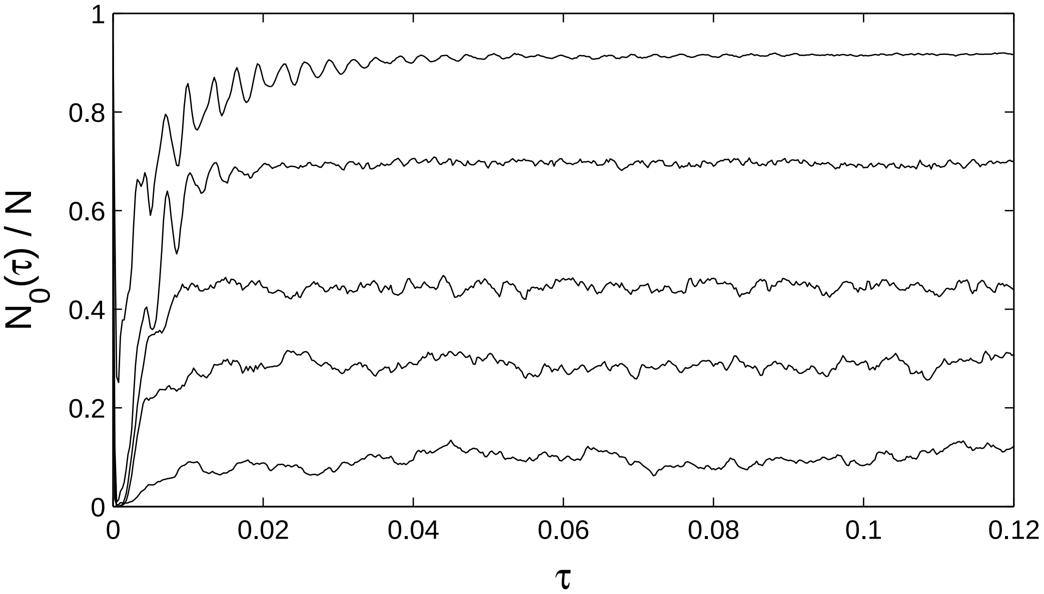

Figure 6.3: Plot of the initial time evolution of $N_0(\tau)/N$ for four different simulation energies with $C_{\rm nl} = 10000$. From top to bottom: $\tilde{E} = 5500, 7000, 8500, 9250, 10000$. The simulations were run until $\tau = 0.2$. Other values of the nonlinearity give qualitatively similar results.

plotted in Fig. 6.4(b). We can see that for $C_{\rm nl} = 0$ the curve is linear up to the transition point, but the $C_{\rm nl} = 10000$ curve displays a distinct bulge. The shape of the corresponding curves for $C_{\rm nl} = 500$ and 2000 fall in between the $C_{\rm nl} = 0$ and 10000 cases.

### Particle distribution

Further evidence of equilibrium is provided by the distribution of the particles in momentum space. Rather than using the plane-wave basis, we transform the wave functions into the quasiparticle basis of quadratic Bogoliubov theory. As was mentioned earlier, for the homogeneous case the expressions are analytic and we can write the quasiparticle amplitude $b_{\mathbf{k}}$ as

$$b_{\mathbf{k}} = u_{\mathbf{k}} c_{\mathbf{k}} - v_{\mathbf{k}} c_{-\mathbf{k}}, \tag{6.25}$$

where we have

$$u_{\mathbf{k}} = \frac{1}{\sqrt{1-\alpha_k^2}}, \qquad v_{\mathbf{k}} = \frac{-\alpha_k}{\sqrt{1-\alpha_k^2}}, \tag{6.26}$$

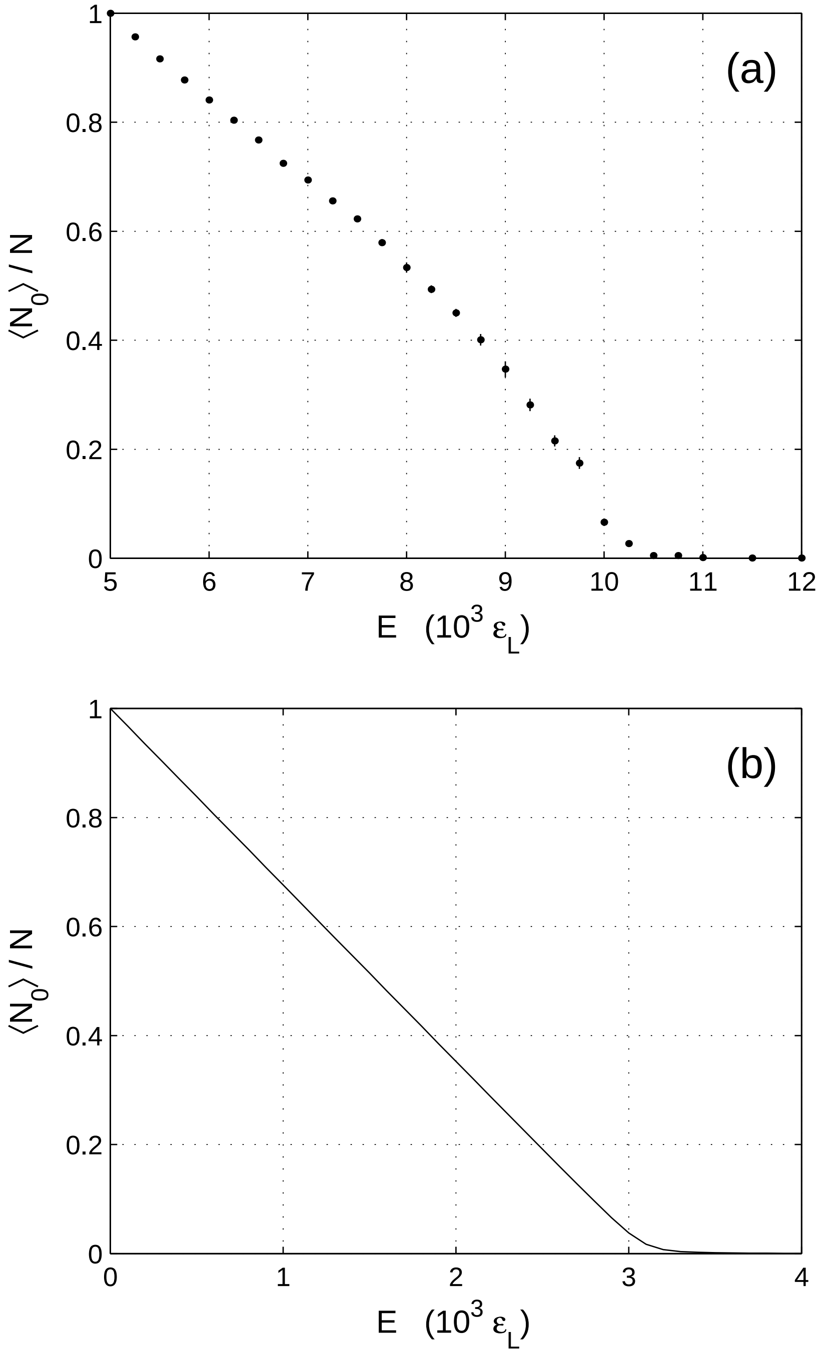

Figure 6.4: (a) Condensate fraction plotted against total energy after each individual simulation has reached equilibrium for $C_{\mathrm{nl}} = 10000$. The barely discernable vertical lines on each point indicate the magnitude of the fluctuations. (b) The curve for the same system, but calculated for the ideal gas.

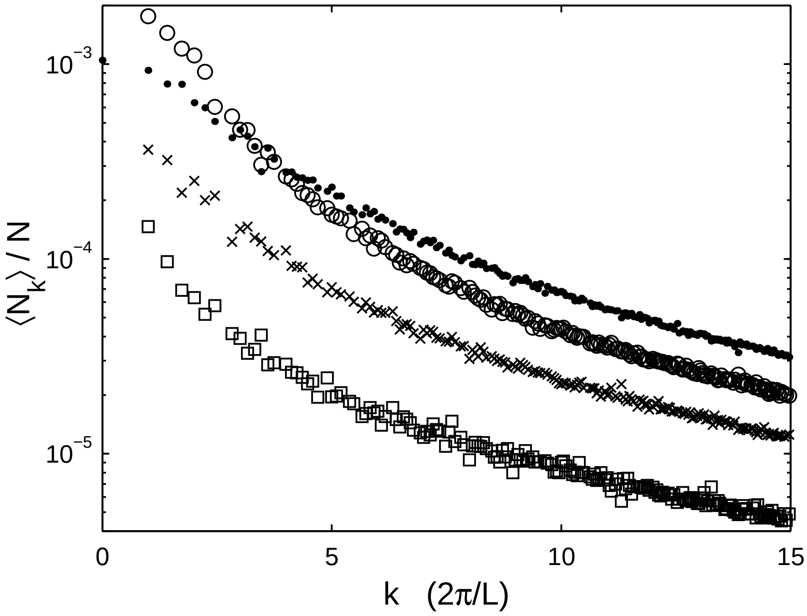

Figure 6.5: Plots of the equilibrium Bogoliubov quasiparticle distributions averaged over time and angle for four different total energies. Squares $\tilde{E} = 6000$, crosses $\tilde{E} = 7500$, circles $\tilde{E} = 9000$, dots $\tilde{E} = 11000$. The mean condensate occupation for the first three distributions is off-axis.

such that for any $\alpha_k$ the normalisation condition $u_{\mathbf{k}}^2 - v_{\mathbf{k}}^2 = 1$ is automatically satisfied. We find the solution is

$$\alpha_k = 1 + y_k^2 - y_k\sqrt{2 + y_k^2}, \tag{6.27}$$

where the dimensionless wave vector $y_k = k/k_0$, and $k_0$ is defined in Eq. (6.20). From Eq. (6.21) we can see that the sole parameters of the transformation are the condensate fraction $\langle N_0 \rangle / N$, and the nonlinear constant $C_{\text{nl}}$.

We average the populations of the quasiparticles states $N_{\mathbf{k}}/N = |b_{\mathbf{k}}|^2$ over time as was described in Sec. 6.3 to give $\langle N_{\mathbf{k}} \rangle / N$, and finally over angle so that we can produce a one dimensional plot of $\langle N_k \rangle / N$. This distribution for four different simulation energies and $C_{\text{nl}} = 10000$ is shown in Fig. 6.5. We can see that the shape of the curves is surprisingly smooth for each energy, suggesting that the system is in equilibrium. The plot of the distribution for any individual wave function is scattered about the average.

We have also determined the fluctuations of the population of the quasiparticle modes. The grand canonical ensemble for the Bose gas predicts the relationship

$$\langle \Delta N_k \rangle^2 = \langle N_k \rangle^2 + \langle N_k \rangle, \tag{6.28}$$

for $k \neq 0$, which in the classical limit $\langle N_k \rangle \gg 1$ gives

$$\langle \Delta N_k \rangle \approx \langle N_k \rangle, \tag{6.29}$$

This is the behaviour that we observe. While we are evolving a microcanonical system, in this case there are such a large number of modes that the remainder of the system acts as a bath for any individual mode.

While the data presented in this section indicates that the PGPE is evolving the system to equilibrium, as yet we have presented no quantitative evidence. To demonstrate conclusively that equilibrium has been reached, we need to be able to assign a temperature to the simulations. One method of achieving this is to fit the simulation data to a predicted quasiparticle distribution, and this is how we proceed in the next section.

## 6.4 Quantitative analysis of distributions

### 6.4.1 Expected distribution

The GPE is the high occupation limit of the full equation for the Bose field operator, Eq. (2.9). Therefore, in equilibrium we expect the mean occupation of mode $k$ to be the classical limit of the Bose-Einstein distribution—i.e. the equipartition relation

$$\langle N_k \rangle = \frac{k_B T}{\varepsilon_k - \mu}. \tag{6.30}$$

Manipulating Eq. (6.30), we find that

$$\varepsilon_k = \frac{k_B T}{\langle N_k \rangle} + \mu. \tag{6.31}$$

The equilibrium condensate occupation according to the equipartition relation will be given by Eq. (6.30) with $\langle N_k \rangle \to \langle N_0 \rangle$ and $\varepsilon_k \to \lambda$. From this expression we can solve for the chemical potential

$$\mu = \lambda - \frac{k_B T}{\langle N_0 \rangle}. \tag{6.32}$$

Substituting this result into Eq. (6.31), and converting to dimensionless units we find

$$\tilde{\varepsilon}_k - \tilde{\lambda} = \tilde{T}\left(\frac{N}{\langle N_k\rangle} - \frac{N}{\langle N_0\rangle}\right), \tag{6.33}$$

where $\tilde{T} = k_B T/(N\varepsilon_L)$ is the dimensionless temperature. Since we determine the distribution $\langle N_k\rangle$ from our simulations, the only unknowns in Eq. (6.33) are the mode energies and the temperature.

## 6.4.2 Bogoliubov theory

In the limit of large condensate fraction $\langle N_0\rangle/N \sim 1$, we expect the Bogoliubov transformation to provide a good basis. The dispersion relation in the homogeneous case is

$$\varepsilon_k - \lambda = \left[\left(\frac{\hbar^2 k^2}{2m}\right)^2 + (c\hbar k)^2\right]^{1/2}, \tag{6.34}$$

where $c = (n_0 U_0/m)^{1/2}$ is the speed of sound, $\varepsilon_k$ is the absolute energy of a mode with wave vector $k$, and $\lambda$ is the condensate eigenvalue. In our dimensionless units this becomes

$$\tilde{\varepsilon}_k - \tilde{\lambda} = \left(\tilde{k}^4 + 2C_{\mathrm{nl}}\frac{\langle N_0\rangle}{N}\tilde{k}^2\right)^{1/2}. \tag{6.35}$$

As we determine the condensate fraction from the numerical results, if the Bogoliubov dispersion relation is valid we can determine a temperature for the simulations by comparing a plot of Eq. (6.33) with Eq. (6.35).

### Results

We have carried out this analysis for all the simulation data. For the $C_{\mathrm{nl}} = 500$ case, the measured distribution is in excellent agreement with the Bogoliubov dispersion relation for all energies, and we have been able to extract the corresponding temperature for each simulation.

However, this is not the case for the more strongly interacting systems. For $C_{\mathrm{nl}} = 2000$, the Bogoliubov relation is a good fit only for simulations with $\tilde{E} \leq 2000$ ($\langle N_0\rangle/N \geq 0.75$), or for energies above the BEC transition point. For the $C_{\mathrm{nl}} = 10000$ case, good agreement is found only for the lowest energy simulation with $\tilde{E} = 5250$ and $\langle N_0\rangle/N \approx 0.96$. Sample fits of the simulation data to the Bogoliubov dispersion relation are shown in Fig. 6.6 for cases where the agreement is good.

The reason for the limited range of agreement is because the Bogoliubov transformation diagonalises only the quadratic Hamiltonian. It neglects the cubic and quartic terms, assuming that they are small (these are discussed in detail below). This is a good approximation for the $C_{\rm nl} = 500$ simulations—at large condensate fraction the dispersion relation is only slightly shifted from the non-interacting relation $\tilde{\varepsilon}_k = \tilde{k}^2$, and at smaller condensate fractions the difference is negligible. Hence we can fit a temperature up to and above the BEC transition.

For the $C_{\rm nl} = 2000$ case the higher order terms become important above $\tilde{E} = 2000$, and for the strongest interaction strength of $C_{\rm nl} = 10000$, they are important almost from the beginning. For these higher energy simulations the shape of Eq. (6.33) no longer agrees with Eq. (6.35), and we must use a more sophisticated theory to predict the dispersion relation.

Above the transition point, however, there is no condensate and the ideal gas dispersion relation is a reasonable description of the system.

### 6.4.3 Second order theory

As the occupation of the quasiparticle modes becomes significant at large interaction strengths, the cubic and quartic terms of the many-body Hamiltonian that are neglected in the Bogoliubov transformation become important. In Ref. [54] Morgan develops a consistent extension of the Bogoliubov theory to higher order that leads to a gapless excitation spectrum. This theory treats the cubic and quartic terms of the Hamiltonian using perturbation theory in the quasiparticle basis. This results in energy-shifts of the excitations away from the Bogoliubov predictions of Eq. (6.34).

Expressions for the energy-shifts of the excitations are given in Sec. 6.2 of Ref. [54]. They have the form

$$\Delta\tilde{\varepsilon}_k = \Delta\tilde{E}_3(k) + \Delta\tilde{E}_4(k) + \Delta\tilde{E}_\lambda(k), \tag{6.36}$$

where $\Delta\tilde{E}_3(k)$ [$\Delta\tilde{E}_4(k)$] is the shift in energy of a quasiparticle in mode $k$ due to the cubic [quartic] Hamiltonian, and $\Delta\tilde{E}_\lambda(k)$ describes the shift due to the change in the condensate eigenvalue. In the high-occupation limit we find

$$\Delta\tilde{E}_4(k) + \Delta\tilde{E}_\lambda(k) = -C_{\rm nl}\tilde{\kappa}\frac{(1+\alpha_k)^2}{1-\alpha_k^2}, \tag{6.37}$$

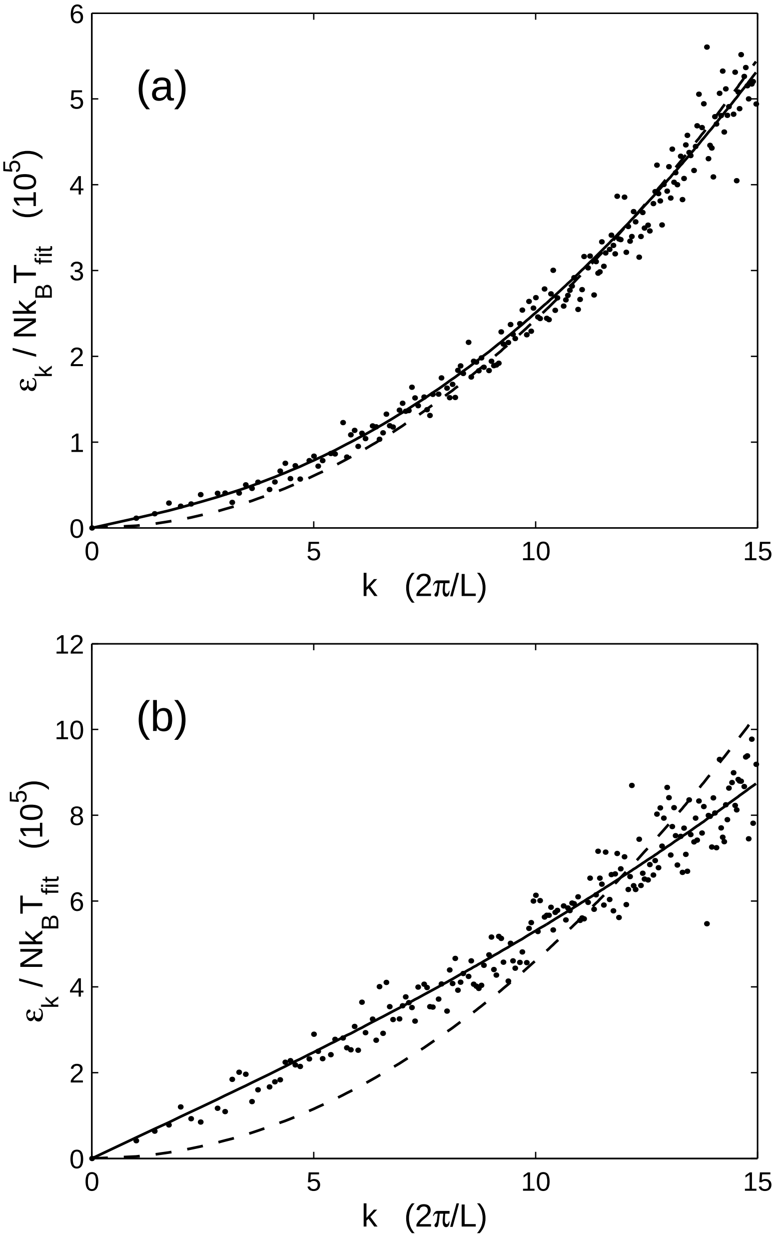

Figure 6.6: Fits of the simulation quasiparticle population data to the Bogoliubov dispersion relation for two cases. For both graphs the solid line is the Bogoliubov curve, while the dashed line is the ideal gas dispersion relation. The temperature is determined by a least-squares fit to the plot of $(N/\langle N_k\rangle - N/\langle N_0\rangle)$, which is shown as the dots. (a) $C_{\mathrm{nl}} = 500$, $\tilde{E} = 500$ and $\langle N_0\rangle/N = 0.929$, with a best fit temperature from Bogoliubov theory of $\tilde{T} = 0.0175$. (b) $C_{\mathrm{nl}} = 10000$, $\tilde{E} = 5250$ and $\langle N_0\rangle/N = 0.957$, with a best fit temperature from Bogoliubov theory of of $\tilde{T} = 0.018$.

where $\tilde{\kappa}$ is the dimensionless anomalous average, defined by

$$\tilde{\kappa} = \sum_k \frac{(N_k + N_{-k})\alpha_k}{N(1-\alpha_k^2)}. \tag{6.38}$$

The expression for $\Delta\tilde{E}_3(k)$ is derived from second-order perturbation theory, and is rather complicated. We have

$$\Delta\tilde{E}_3(k) = \frac{-2C_{\rm nl}}{1-\alpha_k^2}[\Delta\tilde{E}_3^a(k) + \Delta\tilde{E}_3^b(k) + \Delta\tilde{E}_3^c(k)], \tag{6.39}$$

where

$$\begin{aligned}
\Delta\tilde{E}_3^a(k) &= \sum_j \frac{(N_i + N_j)(1-\alpha_i-\alpha_j+\alpha_i\alpha_k+\alpha_j\alpha_k-\alpha_i\alpha_j\alpha_k)^2}{N(z_i+z_j-z_k)(1-\alpha_i^2)(1-\alpha_j^2)}, & (6.40)\\
\Delta\tilde{E}_3^b(k) &= \sum_j \frac{(N_{-i} + N_{-j})(\alpha_i+\alpha_j+\alpha_k-\alpha_i\alpha_j-\alpha_i\alpha_k-\alpha_j\alpha_k)^2}{N(z_i+z_j+z_k)(1-\alpha_i^2)(1-\alpha_j^2)}, & (6.41)\\
\Delta\tilde{E}_3^c(k) &= -2\sum_j \frac{(N_i - N_j)(1-\alpha_j-\alpha_k+\alpha_i\alpha_j+\alpha_i\alpha_k-\alpha_i\alpha_j\alpha_k)^2}{N(z_i-z_j+z_k)(1-\alpha_i^2)(1-\alpha_j^2)}, & (6.42)
\end{aligned}$$

in which $\mathbf{i} = \mathbf{k} - \mathbf{j}$, and

$$z_k = y_k(2+y_k^2)^{1/2} \equiv \tilde{\varepsilon}_k\left(C_{\rm nl}\frac{\langle N_0\rangle}{N}\right)^{-1}, \tag{6.43}$$

is another form of the dimensionless energy of mode $k$, with $y_k = k/k_0$ as earlier.

We have calculated these shifts for our simulations. Our procedure is to:

1. Calculate the quasiparticle populations $N_{\mathbf{k}}$ for the last 50 wave functions of our simulation based on a condensate population $\langle N_0\rangle$, and then average these over time.

2. Calculate the energy shifts for mode $\mathbf{k}$.

3. Average the shifts over angle to give a one-dimensional function of $k$.

A plot of the energy shifts for one particular simulation is presented in Fig. 6.7. As we can see the calculated shifts are not smooth, but this is due to the finite size of the system. The expressions for the energy shifts for $\Delta\tilde{E}_3(k)$ contain poles when energy matches occur, and hence the numerical calculation is performed using an imaginary part in the denominator. We have found that the size of this imaginary

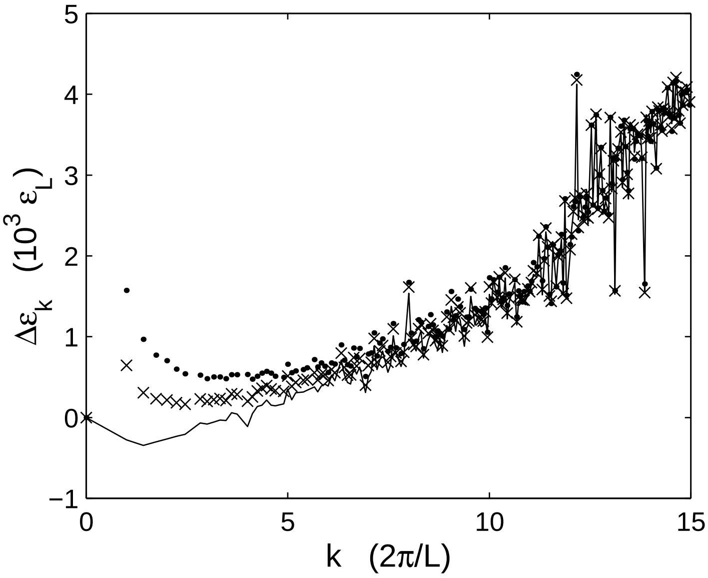

Figure 6.7: The energy shifts calculated using the second order theory of Morgan for the $C_{\rm nl} = 10000$, $\tilde{E} = 7000$ simulation. The crosses are for the quasiparticle transformation using the measured condensate fraction of $N_0/N = 0.6943 \pm 0.004$, the solid line is for $N_0/N = 0.712$, and the dots are for $N_0/N = 0.676$.

part does not affect the shape of the curve in the limit that it is small, but it does affect the amount of scatter in the shifts. We have performed sample calculations allowing $L$ to increase while keeping other parameters of the system constant, and observed that this makes the curve smoother.

The curves plotted in Fig. 6.7 are for the simulation with $C_{\rm nl} = 10000$ and $\tilde{E} = 7000$, with a measured condensate population of $\langle N_0\rangle/N = 0.6943 \pm 0.004$. However, we find that if we use this condensate population in our quasiparticle transformation, we are left with what appears to be a remnant of an infra-red divergence as $k \to 0$ (the crosses in Fig. 6.7).

We have therefore scanned the condensate population used in our quasiparticle transformation over a small range near the measured value, and two more sample curves, shifted from the measured value of $\langle N_0\rangle/N$ by $\pm 0.018$, are presented in Fig. 6.7 (+ solid line, − dots). While the effect of this on the quasiparticle distribution as presented in Fig. 6.5 is invisible to the naked eye, we find that it has a reasonably significant effect on the infra-red behaviour of the shift $\Delta\varepsilon_k$.

We remain unsure as to the origin of this behaviour. It is possible that it is numerical, as both $\Delta\tilde{E}_4(k) + \Delta\tilde{E}_\lambda(k)$ and $\Delta\tilde{E}_3(k)$ separately exhibit infra-red divergence in the expression for the shift. However, it has been shown analytically that these two quantities cancel to third order in the thermodynamic limit to give

$\Delta\varepsilon_k \to 0$ as $k \to 0$ [54]. However, this means that we must numerically calculate two large quantities with sufficiently high accuracy to give a remainder that is small. As an indication of their size, we have $\Delta\tilde{E}_3(k) \sim 10^5$ for $k = 2\pi/L$ for Fig. 6.7, leaving a remnant of $\sim 10^3$. Also, in the sample calculation mentioned earlier, the infra-red remnant shifted towards the origin as $L$ was increased.

Fedichev and Shlyapnikov have calculated the shifts of the quasiparticle energies in the high occupation, thermodynamic limit for the homogeneous Bose gas [55]. They found that for small $k$ the shift was negative, but as $k$ increased it became positive. Qualitatively their curve was similar to the solid line plotted in Fig. 6.7.

Thus, for the higher energy $C_{\rm nl} = 10000$ simulations it was necessary to increase the condensate occupation by up to $\delta\langle N_0\rangle/N = +0.02$ to avoid any remaining infra-red divergence in the energy shift as $k \to 0$. This was not necessary for the $C_{\rm nl} = 2000$ simulations, however, as although there was still an infra-red remnant, it was very small. This oddity is a matter of ongoing investigation. We would like to note however, that the shifts for $\tilde{k} > 5 \times 2\pi$ are largely unaffected by this procedure.

### Results

The shifted energy spectrums are in good agreement with the quasiparticle populations extracted from the simulations, and are a significantly better fit than the Bogoliubov theory of Eq. (6.35) for a large number of cases. We find that almost all the measured distributions for the $C_{\rm nl} = 2000$ case are well described by the second order theory, and it is successful for the $C_{\rm nl} = 10000$ case up until about $\tilde{E} = 7250$. Sample results are presented in Fig. 6.8.

### Breakdown of perturbation theory

The validity of the second order theory is constrained by the requirement [54]

$$\left(\frac{k_B T}{n_0 U_0}\right)(n_0 a^3)^{1/2} \ll 1, \tag{6.44}$$

where $n_0$ is the condensate density. This corresponds in our dimensionless units to

$$\frac{\tilde{T}}{(8\pi)^{3/2}}\left(\frac{C_{\rm nl}}{\langle N_0\rangle/N}\right)^{1/2} \ll 1. \tag{6.45}$$

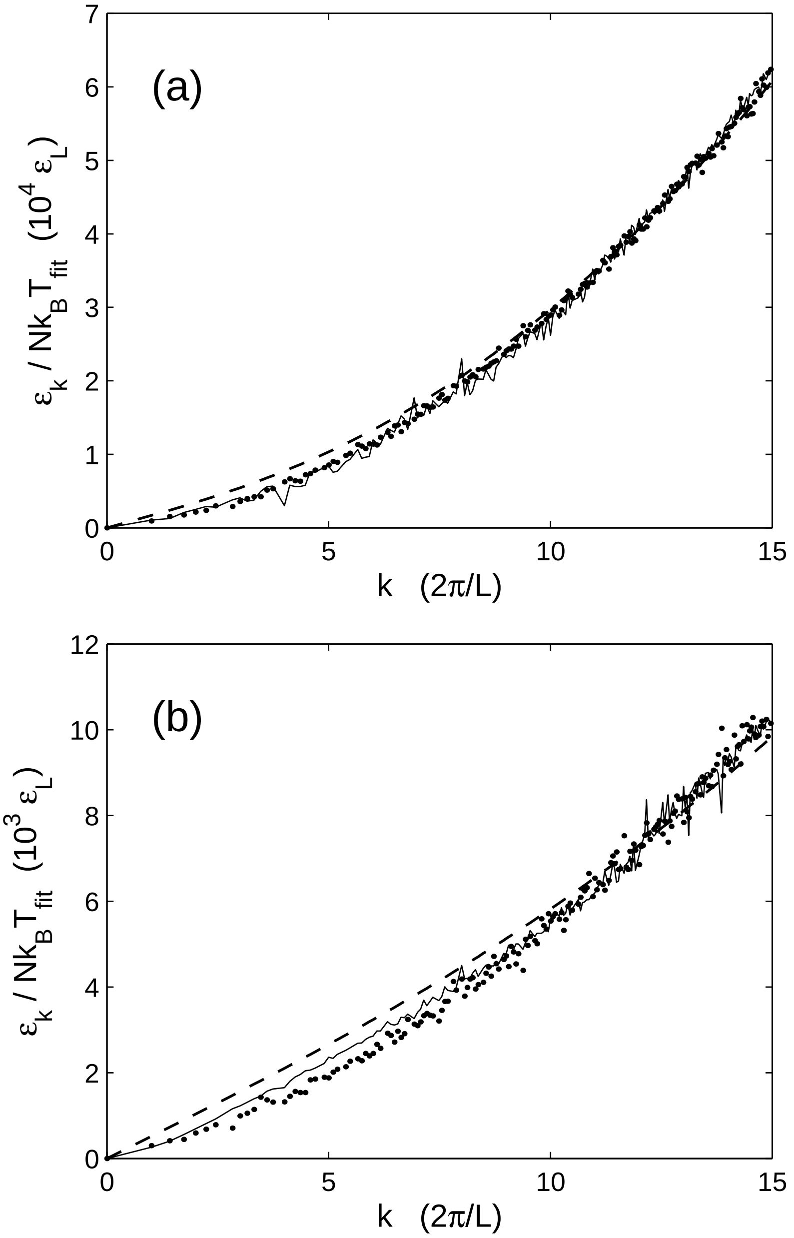

Figure 6.8: Fits of the simulation quasiparticle population data to the full second order theory dispersion relation for two cases. For both graphs the solid line curve is for the full theory and the dashed line is the Bogoliubov curve. The dots are a plot of $(N/\langle N_k\rangle - N/\langle N_0\rangle)$, and the best-fit temperatures are determined by a least-squares fit of this to the dispersion relations. (a) $C_{\rm nl} = 2000$, $\tilde{E} = 3400$ and $\langle N_0\rangle/N = 0.449$, with a second order theory best-fit temperature of $\tilde{T} = 0.1640$. (b) $C_{\rm nl} = 10000$, $\tilde{E} = 7000$ and $\langle N_0\rangle/N = 0.6943$, with a second order theory best-fit temperature of $\tilde{T} = 0.1788$.

For the results of Fig. 6.8(b) with $C_{\rm nl} = 10000$, $\tilde{E} = 7000$ this parameter is 0.17 and so we are beginning to probe the boundary of validity of the theory. At higher $\tilde{E}$ the shifts become of the order of the unperturbed energies, and hence the results are unreliable. In this region even higher order terms are important, and the second order theory can no longer be expected to give good results. From our calculations it seems that this parameter should be $\leq 0.2$ for the theory to be valid.

We would like to emphasise, however, that the GPE suffers no such limitations. It is non-perturbative and thus can be used all the way through the transition region as long as the condition $N_k \gg 1$ is satisfied.

## 6.5 Condensate fraction and temperature

It is usual when considering how the condensate fraction varies with the other properties of the system to plot it against temperature, rather than against energy as we have done in Fig. 6.4. We are now in a position to present this data, and it is displayed in Fig. 6.9.

We can see that a major effect of increasing the nonlinearity is to increase the condensate fraction at any given temperature. However, it seems that the transition temperature is largely unaffected by the size of $C_{\rm nl}$. This can be understood by considering the shape of the dispersion relation.

The Bogoliubov dispersion relation Eq. (6.35) shows that for a given condensate fraction, a larger value of $C_{\rm nl}$ will result in an increase in the energy of any mode $k$ relative to the condensate. This leads directly to the observation that for a fixed condensate fraction, an increase in the nonlinearity must lead to an increase in the temperature. However, as $\langle N_0 \rangle / N \to 0$ in the transition region, the energy-momentum relationship tends towards the ideal gas dispersion relation, and therefore the transition temperature will not be greatly shifted over a wide range of nonlinearities.

We note that we have not assigned a temperature to the $\tilde{E} = 7500$–$10500$, $C_{\rm nl} = 10000$ simulations, and therefore these points are not plotted in Fig. 6.9. We can see from the graph that this means there is a large increase in the energy of the system for a very small increase in temperature in the region of the transition, and hence the specific heat is large.

The specific heat of the ideal Bose gas reaches a maximum at the critical temperature—however, the behaviour displayed here is reminiscent of the lambda point in superfluid $^4$He. In this system the specific heat diverges at the transition

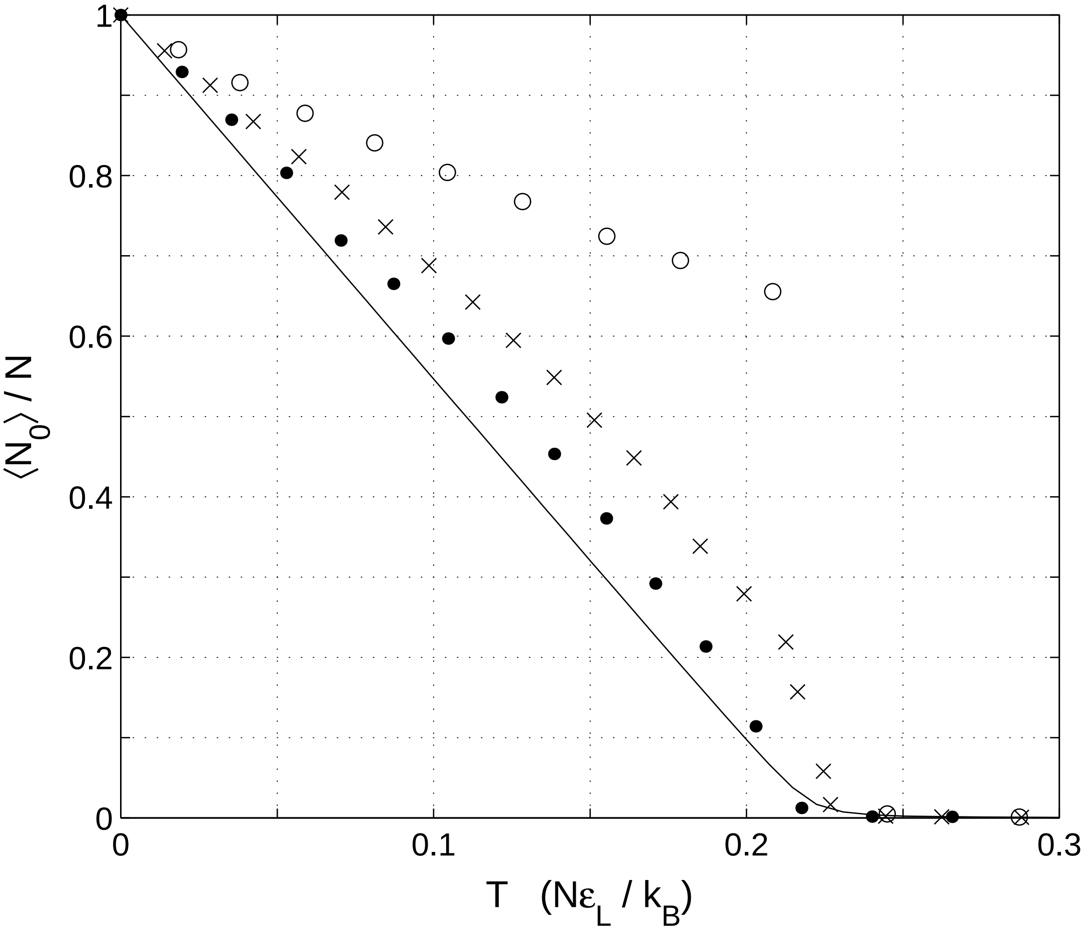

Figure 6.9: Condensate fraction versus temperature for system with $k < 15\pi/L$, but with four different interaction strengths. The open circles are for $C_{\rm nl} = 10000$, crosses for $C_{\rm nl} = 2000$, solid dots for $C_{\rm nl} = 500$, and the solid line is for the ideal gas. Points are missing from the $C_{\rm nl} = 10000$ curve in the range from $\tilde{E} = 7500$–$10500$, corresponding to a temperature of $\tilde{T} = 0.21$–$0.23$. This is where second order perturbation theory breaks down and we are unable to determine a temperature by the methods used in this chapter. The points in this region for the other interaction strengths should also be treated with caution.

temperature. This issue will be be addressed further in the continuation of the work presented in this thesis.

## 6.6 The role of vortices

Another quantity of interest is the vorticity of the system in equilibrium. It has been argued that vortices may be important in the superfluid transition of $^4$He, reducing the superfluid density near the transition point [136]. With this in mind, we have studied the presence of vortex lines and rings in our simulations.

A vortex is a topological excitation, characterised in a wave function by

$$\oint_C \nabla \mathrm{Arg}[\psi(\mathbf{x})] \cdot d\mathbf{l} = 2\pi n, \tag{6.46}$$

where $C$ is a closed contour, and $n$ is a non-zero integer, the sign of which indicates the circulation of the vortex. The continuous variation of the phase from zero to $2n\pi$ around such a contour implies that there must be a discontinuity in the phase within the loop. The only way that this can be physical is for the wave function to have zero amplitude at the spatial position of the phase singularity. The phase profiles characterising the presence of a vortex are clearly visible in the phase plots of the wave functions in Fig. 6.2.

In a two dimensional wave function the centre of vortices are zero-dimensional points, and they can be easily counted to give a measure of the vorticity of the system. However, in three dimensions vortices form lines and rings, and the equivalent quantity of the 2D measure of vorticity would be to calculate the length of all vortex structures in the wave function. This would be a somewhat complicated procedure numerically, and so we have devised a different technique.

We increase the spatial resolution of our wave functions to be 128 × 128 × 128 points, so that the grid spacing is smaller than the vortex healing length $\xi$, defined by

$$\frac{\hbar^2}{2m\xi^2} = n_0 U_0. \tag{6.47}$$

We do this by extending the wave function in $k$-space, and then Fourier transforming to real space. This does not require any extra information, as for $k > 15 \times 2\pi/L$ we have $c_{\mathbf{k}} = 0$. We then count the number of vortex lines passing through every $xy$ plane, and take the average over all planes. It seems that this is a reasonable measure of the vorticity of the wave function, and it should be similar to the measurement of the length of the vortex structures discussed above.

We have analysed the data from the simulations using this procedure. We find that when the energy of the simulation is sufficiently high that there are vortices present, the time evolution of the vorticity is a good indicator for when the system reaches equilibrium. As is the case for the condensate population, the vorticity tends to an equilibrium value which fluctuates by a small amount (much smaller than the fluctuations in the condensate population).

A plot of the vorticity against system energy is shown in Fig. 6.10(a) for the $C_{\mathrm{nl}} = 10000$ simulation (the curves are qualitatively similar for the other nonlinearities). We see that there is a minimum energy required for vortices to be present in the system at equilibrium. Also, as we reach this energy the plot of condensate occupation versus energy appears to dip. This same behaviour is observed for the $C_{\mathrm{nl}} = 500$ and 2000 cases, but it occurs at a higher condensate fraction, and is not as pronounced. There is no corresponding departure from linearity in the ideal gas case, as was seen in Fig. 6.4(b).

The appearance of vortex structures in the $C_{\mathrm{nl}} = 10000$ case also corresponds to the region in which the second order theory of Morgan begins to fail. This is to be expected, as neither Bogoliubov theory or the second order theory take account of topological excitations. This raises the question of why these theories appeared to give a good fit to the measured distribution function when vortices were present for the $C_{\mathrm{nl}} = 2000$ case.

A tentative explanation for this behaviour is the magnitude of the energy of the topological excitations. The energy of a vortex ring is proportional to both $C_{\mathrm{nl}}$ and the superfluid density [136], and it seems quite possible that the energy that makes up these excitations in the low $C_{\mathrm{nl}}$ simulations is only a small fraction of that accounted for by the usual quasiparticle excitations. This is why we have more of them for a given temperature in the lower $C_{\mathrm{nl}}$ simulations. However, in the $C_{\mathrm{nl}} = 10000$ case it seems likely that topological excitations are the cause of the rapid increase in the specific heat near the transition temperature, as suddenly there are many more modes with a significant energy that can be excited. This suggests that the phase transition may be vortex-mediated, however more quantitative analysis is necessary.

A plot of the number of vortex lines versus temperature for all the simulations is shown in Fig. 6.10(b), and this displays a sudden increase in the vorticity near the transition temperature for $C_{\mathrm{nl}} = 10000$. Even the $C_{\mathrm{nl}} = 2000$ case appears to show a small jump in this region. A more in-depth analysis of this behaviour will

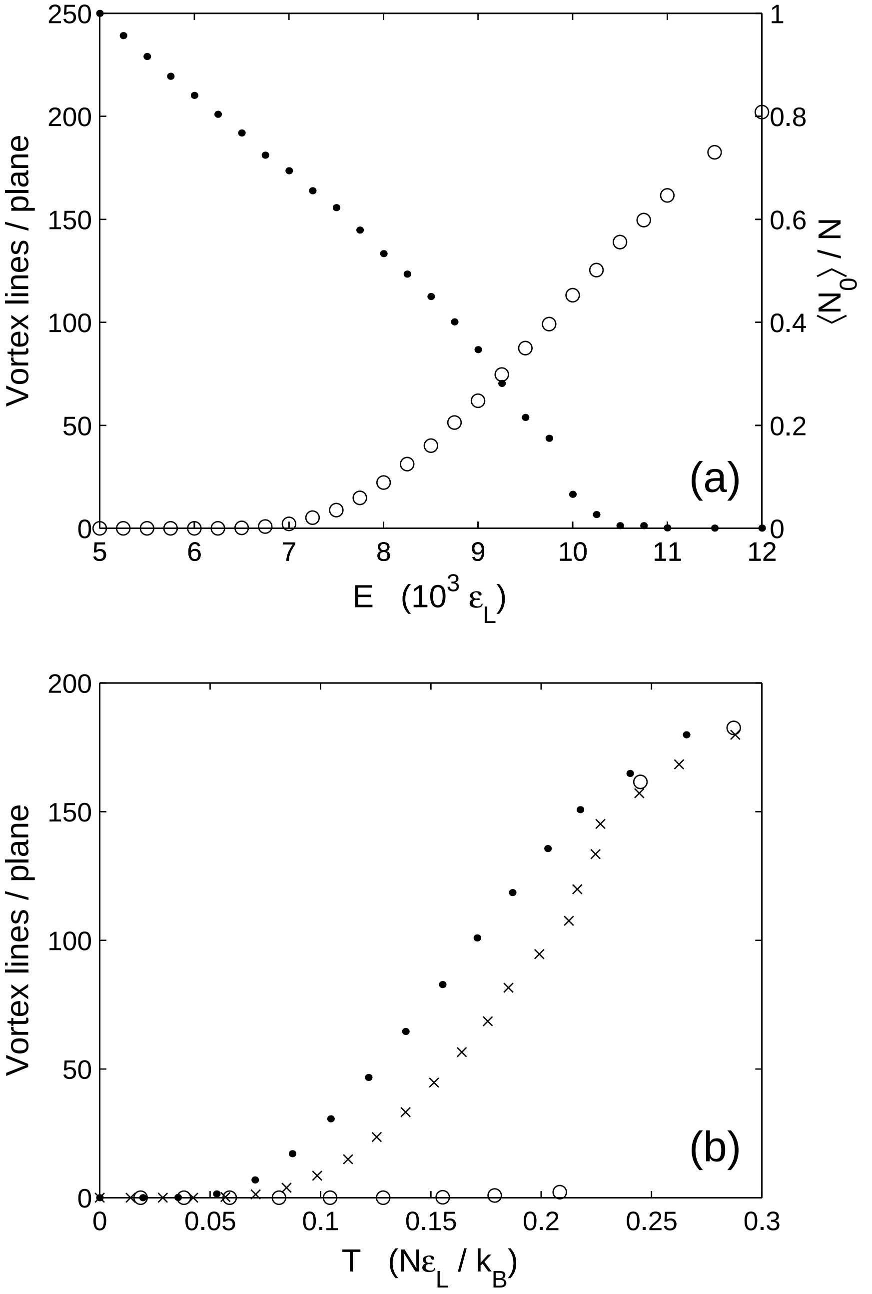

Figure 6.10: The presence of vortices in the simulations. (a) A plot of vorticity for the $C_{\mathrm{nl}} = 10000$ simulation series. The number of vortex lines per plane are indicated by open circles with the scale on the left vertical axis, and the condensate fraction by dots with the scale on the right vertical axis. (b) The number of vortex lines per plane plotted against temperature for all three simulation series. Open circles are $C_{\mathrm{nl}} = 10000$, crosses are $C_{\mathrm{nl}} = 2000$, and dots are $C_{\mathrm{nl}} = 500$.

be carried out in a subsequent extension of the work of this thesis.

## 6.7 Conclusions

We have presented compelling evidence that the projected Gross-Pitaevskii equation is a good approximation to the dynamics of the classical modes of a Bose gas. We have described how to carry out the projection technique for the homogeneous system with periodic boundary conditions, and have shown that starting with a randomised wave function with a given energy, the projected GPE evolves towards an equilibrium state. We have analysed the numerical data in terms of quadratic Bogoliubov theory, and also the gapless, finite temperature theory of Ref. [54] in the classical limit. We have found that both the occupation and energies of the quasiparticles agree quantitatively with the predictions. Also, we have found that increasing the nonlinearity $C_{\mathrm{nl}}$ leads to an increase in the specific heat of the system in the region of the critical temperature, and presented evidence that suggests vortices may play some role in the transition. The projected GPE is a simple equation but it appears to describe very rich physics, only some of which we have considered here. It will remain the topic of further research.

## Chapter 7

# Prospects for future development

In the last part of this thesis we discuss the prospects for further development of the formalism described in Chapter 5.

## 7.1 The PGPE

### 7.1.1 Homogeneous case

The PGPE was studied in the previous chapter for the homogeneous gas with periodic boundary conditions. We have shown that this describes the evolution of the classical modes of the system to an equilibrium which is well described by static theories of BEC. However, there seems to be much more physics in the PGPE that is yet to be understood. Below we describe the next steps in the study of this equation.

1. We would like to be able to assign a temperature to the simulations that appear to have reached equilibrium, but which are not well-described by current equilibrium theories. In this region of critical fluctuations, perturbation theory breaks down but the PGPE remains valid.

   One method of doing this may be to couple the strongly-interacting system to a second that is weakly-interacting, and allow the two to come to equilibrium. Perturbation theory would remain valid for the weakly-interacting system, and so it would be possible to infer the temperature of the strongly-interacting system by measuring the temperature of the second.

2. If this is successful it may be possible to investigate the effect of interactions on the BEC transition temperature. This is a topic of much debate in the commmunity at present [137].
3. Further investigation into the role of vortices in the strongly-interacting gas is required. We would like to be able to describe the energy that they contain, and study the part (if any) that they play in the phase transition.
4. Another system of interest is the homogeneous 2D gas, which cannot undergo Bose-Einstein condensation, but for which a Kosterlitz-Thouless transition can be observed. In this case the occupation of the zero momentum state becomes significant, but fluctuations remain large and there is no off-diagonal long range order. It is known that vortices are important in the phase transition of this system [138]. In two dimensions the PGPE will be much easier to compute.

   Attempts are being made to implement the second order theory in the case that vortices are present in 2D [139]. Rather than having a flat condensate with quasiparticle excitations on top, this assumes that a network of vortices are present, and describes excitations above this. The PGPE will be a useful tool in the development of this theory.
5. The problem of coherence at finite temperature could be studied, a topic particularly important in the discussion of the properties of atom lasers.
6. The shifts and widths of the excitation frequencies of a condensate have been studied at finite temperature, but only in the limit that the amplitudes are small. The PGPE would allow us to consider the frequency and rate of decay of large amplitude excitations where nonlinear effects are important.

### 7.1.2 Inhomogeneous case

The implementation of the projector $\hat{\mathcal{P}}$ is the bottleneck in considering the Bose gas at finite temperature in a trap. It may be possible to develop a suitable approximation for the projector, or simply to use a finite size grid to effectively carry out a lattice simulation that restricts the energies considered. Another option is to make use of supercomputing resources.

If a scheme can be developed for the application of the projector, whether it is simply by brute force or possibly by the use of a clever approximation, there are several situations that could be investigated:

1. Many of the issues considered in the homogeneous case are also important for trapped gases. In particular, the study of vortices in a trap at finite temperature could be very fruitful, along with the issues of coherence and the properties of large amplitude excitations.

2. The issue of condensate collapse could be addressed, as discussed in Sec. 5.3.1.

3. Collisional loss in four-wave mixing with atomic BECs could be studied.

As can be seen, there are still many possibilities to be considered using the PGPE.

## 7.2 The FTGPE

The next step in the development of this formalism will be to begin to include the terms involving the bath operator $\hat{\eta}(\mathbf{x})$ in the computations. In the homogeneous case this should be relatively straightforward.

Rather than calculating the dynamics of the incoherent region as well as those of the coherent region, a useful first step will be to assume that the incoherent region is in quasi-equilibrium, and can be described by a chemical potential $\mu$ and temperature $T$. This is reminiscent of the procedure of QKIII, which treated the region $R_{NC}$ as being fully thermalised. Indeed, this thesis along with other studies in the literature suggests that this approximation can be a good one.

The first term to consider will be the growth term, $\hat{\eta}^{\dagger}\hat{\eta}\hat{\eta}$, as described by Eq. (5.39). Taking the incoherent region to be thermalised will leave an integral of the form of the quantity $W^{\pm}$ from quantum kinetic theory, which can easily be carried out. This will result in an expression for the rate into each quasiparticle level of the coherent region based on its energy. This description would in fact be very similar to model B of condensate growth, but without the scattering terms.

While neglecting the scattering term will not give the exact dynamics as suggested by our earlier studies of condensate growth, it will be a good first estimate. This procedure provides one possible coupling of the PGPE to a weakly interacting system that has a well-defined temperature.

The next term to include will be the scattering term, as in Eq. (5.37). This will be more difficult, as it involves the calculation of matrix elements and a summation over two condensate indices.

From the studies of condensate growth in quantum kinetic theory, it seems reasonable that the remaining terms can be neglected in the limit that the incoherent region is large. This will almost always be the case due to the definition of the coherent region. The terms linear in $\hat{\eta}$ will be boundary terms, and the anomalous term will mainly contribute to the renormalisation of the interaction strength. When the incoherent region is small and these terms can be significant, both the growth and the scattering terms are not likely to be important. In this situation we envisage evolving the FTGPE, but only using the extra terms to describe the loss from the coherent region.

## 7.3 Limitations

While the formalism developed in this thesis is applicable for a wide range of systems, there are two situations where it is not valid.

### Low temperature

At temperatures slightly above zero, there will be an intermediate regime where the $T = 0$ GPE is not valid due to the presence of a thermal fraction, but for which there are an insufficient number to be treated using kinetic theory.

### Small systems

Small systems are the only major situation that cannot be described by this formalism, when the criterion $N_k \gg 1$ is not satisfied for any modes except for the condensate. In this regime quantum fluctuations are important, and the quantum nature of the modes must be considered. In this regime, the coherent state phase-space equations (know as the positive-$P$ representation) are equivalent to the relevant quantum equations if the phase-spase boundary terms vanish. Such a description has been considered by Drummond and Corney [117].

## 7.4 Final conclusions

In this final chapter of this thesis we have considered possible future applications of both the projected and finite temperature Gross-Pitaevskii equations, and have shown that there is still much to be understood. We have also briefly discussed the limitations of the formalism.

While the formalism is by no means perfect, it is based on the principle that it should lead to calculations that can feasibly be performed. There is little to be gained by developing an elegant method that turns out to be computationally impossible. We have based our approach on the GPE, a subject of much research for $T = 0$, and have shown it to be an excellent approximation for the classical modes of a Bose gas. We remain hopeful that from this description it will be possible to model real experiments on Bose-Einstein condensates in laboratories.

# APPENDIX A

# APPROXIMATE SOLUTION OF OPERATOR EQUATIONS

We often have equations of the following form that we wish to solve approximately to substitute into another equation of motion

$$i\hbar \frac{d\tilde{A}(t)}{dt} = U_0 \tilde{F}(t) \exp(-i\Delta\omega t), \tag{A.1}$$

where $\tilde{F}(t)$ represents a sum over operators that is slowly varying on the scale of $\Delta\omega$. The formal solution to this equation is

$$\tilde{A}(t) = \frac{U_0}{i\hbar} \int_{t_0}^{t} dt' \tilde{F}(t') \exp(-i\Delta\omega t'). \tag{A.2}$$

As we assume that $\tilde{F}(t')$ is slowly varying we can move it outside the integral, replacing the argument with the end value of the integral $t$

$$\tilde{A}(t) = \frac{U_0}{i\hbar} \tilde{F}(t) \int_{t_0}^{t} dt' \exp(-i\Delta\omega t'). \tag{A.3}$$

We now have the challenge of integrating the exponential in such a way that we get a finite answer. The standard way to do this is to add a small imaginary part $i\epsilon$ to $\Delta\omega$, carry out the integral and then let $\epsilon \to 0$. We eventually only want the contribution from the upper limit of the integral, so the sign of $\epsilon$ is chosen such that the integral converges as the limit is taken to $t_0 = -\infty$

$$\begin{aligned} \int_{t_0}^{t} dt' \frac{\mathrm{e}^{-i\Delta\omega t'}}{i} \quad &\Rightarrow \quad \lim_{\epsilon\to 0} \int_{t_0}^{t} dt' \frac{\mathrm{e}^{-i(\Delta\omega + i\epsilon)t'}}{i}, \\ &= \quad \lim_{\epsilon\to 0} \left[ \frac{\mathrm{e}^{-i(\Delta\omega+i\epsilon)t'}}{\Delta\omega + i\epsilon} \right]_{t'=t_0}^{t'=t}. \end{aligned} \tag{A.4}$$

The trick is now to multiply through by $(\Delta\omega - i\epsilon)/(\Delta\omega - i\epsilon)$ so that

$$\tilde{A}(t) = \frac{U_0}{\hbar} \tilde{F}(t) \lim_{\epsilon\to 0} \left[ \left( \frac{\Delta\omega}{\Delta\omega^2 + \epsilon^2} - \frac{i\epsilon}{\Delta\omega^2 + \epsilon^2} \right) \mathrm{e}^{-i(\Delta\omega+i\epsilon)t'} \right]_{t'=t_0}^{t'=t}. \tag{A.5}$$

Now we have

$$\lim_{\epsilon\to 0} \frac{\Delta\omega}{\Delta\omega^2 + \epsilon^2} = \frac{1}{\Delta\omega}, \tag{A.6}$$

$$\lim_{\epsilon\to 0} \frac{i\epsilon}{\Delta\omega^2 + \epsilon^2} = i\pi\delta(\Delta\omega), \tag{A.7}$$

as the left-hand side of Eq. (A.7) is a Lorentzian that tends to a delta function, with the area under the curve being equal to $\pi$. The other trick that we use is to extend the lower limit of the integration to $-\infty$, so we drop the term involving $t_0$. Thus the final result is

$$\tilde{A}(t) = U_0 \tilde{F}(t) \frac{\mathrm{e}^{-i\Delta\omega t}}{\hbar\Delta\omega} - i\pi U_0 \tilde{F}(t) \delta(\hbar\Delta\omega). \tag{A.8}$$

This is essentially a proof of the standard result

$$\frac{1}{x + i\epsilon} = P\left(\frac{1}{x}\right) - i\pi\delta(x), \tag{A.9}$$

which is short for

$$\int \frac{dx f(x)}{x + i\epsilon} = P \int \frac{dx f(x)}{x} - i\pi \int dx f(x) \delta(x). \tag{A.10}$$

This is a result of a ‘well-known theorem from complex function theory’ as stated on page 61 of Mattuck [140], and the reader is referred to Ref. [141].

# Appendix B

# Derivation of the rate $W^+$

In this appendix we give the derivation of the formula for the rate $W^+$ calculated using the Bose-Einstein distribution function in the integral. We begin from Eq. (3.26) which we reproduce here for the reader's convenience

$$W^+(N) = \frac{4ma^2}{\pi\hbar^3}\int d\varepsilon_1\, d\varepsilon_2\, d\varepsilon_3\, f_1 f_2 (1+f_3)\, \delta(\varepsilon_1+\varepsilon_2-\varepsilon_3-\mu_C(N)). \quad \text{(B.1)}$$

For clarity we split this into two integrals

$$W^+(N) = \frac{4ma^2}{\pi\hbar^3}\,(A+B)\,, \quad \text{(B.2)}$$

where

$$A = \int d\varepsilon_1\, d\varepsilon_2\, d\varepsilon_3\, f_1 f_2\, \delta(\varepsilon_1+\varepsilon_2-\varepsilon_3-\mu_C(N)), \quad \text{(B.3)}$$

$$B = \int d\varepsilon_1\, d\varepsilon_2\, d\varepsilon_3\, f_1 f_2 f_3\, \delta(\varepsilon_1+\varepsilon_2-\varepsilon_3-\mu_C(N)). \quad \text{(B.4)}$$

For the distribution function we use the expansion

$$\begin{aligned} f(\varepsilon) &= \frac{1}{e^{\beta(\varepsilon-\mu)}-1} = \frac{e^{-\beta(\varepsilon-\mu)}}{1-e^{-\beta(\varepsilon-\mu)}}, \\ &= e^{\beta(\varepsilon-\mu)}\sum_{m=0}^{\infty} e^{-m\beta(\varepsilon-\mu)}, \\ &= \sum_{m=1}^{\infty} e^{-m\beta(\varepsilon-\mu)}, \end{aligned} \quad \text{(B.5)}$$

and so integrating over the delta functions we have

$$\begin{aligned} A &= \sum_{mn=1}^{\infty} \int d\varepsilon_1\, d\varepsilon_2\, e^{\beta\mu(m+n)} e^{-\beta(m\varepsilon_1+n\varepsilon_2)}, && \text{(B.6)} \\ B &= \sum_{mnp=1}^{\infty} \int d\varepsilon_1\, d\varepsilon_2\, e^{\beta\mu(m+n+p)} e^{-\beta[(m+p)\varepsilon_1+(n+p)\varepsilon_2]+p\beta\mu_C(N)}. && \text{(B.7)} \end{aligned}$$

Carrying out the integrals from $E_R$ to infinity results in

$$\begin{aligned} A &= (k_BT)^2 \sum_{mn=1}^{\infty} \frac{e^{\beta(\mu-E_R)(m+n)}}{m+n}, && \text{(B.8)} \\ B &= (k_BT)^2 \sum_{mnp=1}^{\infty} \frac{e^{\beta\mu(m+n+p)+p\beta\mu_C(N)-\beta(m+n+2p)E_R}}{(m+p)(n+p)}. && \text{(B.9)} \end{aligned}$$

Both of the sums in these results can be carried out to some extent. If we define the "fugacities"

$$z = e^{\beta(\mu-E_R)}, \qquad z(N) = e^{\beta(\mu_C(N)-E_R)}, \tag{B.10}$$

then for $A$ we have

$$\begin{aligned} \frac{e^{\beta(\mu-E_R)(m+n)}}{m+n} &= \left(\sum_{m=1}^{\infty} \frac{z^m}{m}\right)^2, \\ &= [\ln(1-z)]^2 \qquad \text{for } z < 1, && \text{(B.11)} \end{aligned}$$

and for $B$

$$\begin{aligned} \sum_{mnp=1}^{\infty} \frac{e^{\beta\mu(m+n+p)+p\beta\mu(N)-\beta(m+n+2p)E_R}}{(m+p)(n+p)} &= \sum_{p=1}^{\infty} [z.z(N)]^p \left(\sum_{m=1}^{\infty} \frac{z^m}{m+p}\right)^2, && \text{(B.12)} \\ &= z^2 \sum_{p=1}^{\infty} [z.z(N)]^p \left(\sum_{m=0}^{\infty} \frac{z^m}{m+p}\right)^2, && \text{(B.13)} \\ &= z^2 \sum_{p=1}^{\infty} [z.z(N)]^p \Phi(z,1,p+1), && \text{(B.14)} \end{aligned}$$

where the function $\Phi$ is the *Lerch transcendent* [108] defined by

$$\Phi(x,s,a) = \sum_{k=0}^{\infty} \frac{x^k}{(a+k)^s}. \tag{B.15}$$

Thus the final result is

$$W^+(N) \;=\; \frac{4m(ak_BT)^2}{\pi\hbar^3}\left\{[\ln(1-z)]^2 + z^2\sum_{r=1}^{\infty}[z\,z(n_0)]^r[\Phi(z,1,r+1)]^2\right\}, \quad \text{(B.16)}$$

which was quoted in the Chapter 3 as Eq. (3.39). For $z \ll 1$ the second term can be neglected with respect to the first, and using the approximation

$$[\ln(1-z)]^2 \approx [1-(1-z)]^2 = z^2, \quad \text{(B.17)}$$

we find

$$W^+(N) \;=\; \frac{4m(ak_BT)^2}{\pi\hbar^3}e^{2\beta\mu}, \quad \text{(B.18)}$$

which is very similar to the Boltzmann estimate Eq. (3.30) given in the main text.

## Appendix C

# Semiclassical density of states

In this appendix we outline the derivation of the density of states for a general system. In particular we derive the harmonic oscillator density of states, both for the ideal gas, and for a gas interacting with a Bose-Einstein condensate using the Thomas-Fermi approximation for the condensate wave function. The result is Eq. (4.14) in the main text.

The classical expression for the density of states is

$$g(\varepsilon) = \frac{1}{h^3}\int d^3\mathbf{r}\int d^3\mathbf{p}\;\delta[\varepsilon - \varepsilon(\mathbf{r},\mathbf{p})], \tag{C.1}$$

where $\varepsilon(\mathbf{r},\mathbf{p})$ is the dispersion relation. It is simple to show that a property of the delta function is

$$\delta[y - f(x)] \equiv \delta[x - f^{-1}(y)]\left|\frac{\partial f}{\partial x}\right|^{-1}. \tag{C.2}$$

Therefore, assuming that the energy is a function of the magnitude of the momentum only i.e. $\varepsilon(\mathbf{p}) = \varepsilon(|\mathbf{p}|)$, we can integrate over the momentum coordinate in Eq. (C.1) to find

$$g(\varepsilon) = \frac{1}{2\pi^2\hbar^3}\int d^3\mathbf{r}[p(\varepsilon,\mathbf{r})]^2\left|\frac{\partial\varepsilon}{\partial p}\right|^{-1}. \tag{C.3}$$

## C.1 Harmonic oscillator

For an anisotropic harmonic trap the entire position dependence of the dispersion relation is contained in the external potential

$$V(\mathbf{r}) = \frac{m}{2}\left(\omega_x x^2 + \omega_y y^2 + \omega_z z^2\right). \tag{C.4}$$

If we make the change of variable

$$x' = \frac{\omega_x}{\bar{\omega}}x, \qquad y' = \frac{\omega_y}{\bar{\omega}}y, \qquad z' = \frac{\omega_z}{\bar{\omega}}z, \tag{C.5}$$

where we define the geometric mean of the trap frequencies $\bar{\omega} = (\omega_x\omega_y\omega_z)^{1/3}$, we find

$$V(r) = \frac{m}{2}\bar{\omega}^2 r^2. \tag{C.6}$$

We can then carry out carry out the angular part of the integral of Eq. (C.3) for the density of states to leave us with

$$g(\varepsilon) = \frac{4}{2\pi\hbar^3}\int r^2 dr[p(\varepsilon, r)]^2 \left|\frac{d\varepsilon}{dp}\right|^{-1}, \tag{C.7}$$

The integral extends from zero to the maximum radius of a particle with energy $\varepsilon$, found by putting $p = 0$ in the dispersion relation and solving for $r_{\max}$.

## C.2 Ideal gas

For the ideal gas the dispersion relation is everywhere

$$\varepsilon(r, p) = p^2/2m + V(r), \tag{C.8}$$

so

$$\frac{\partial\varepsilon}{\partial p} = \frac{p}{m}, \qquad \text{and} \qquad p(\varepsilon, r) = \sqrt{2m}\sqrt{\varepsilon - V(r)}. \tag{C.9}$$

We find that the upper bound of the integral of Eq. (C.7) is

$$r_{\max} = \left(\frac{2\varepsilon}{m\bar{\omega}}\right)^{1/2}, \tag{C.10}$$

and substituting this, along with Eq. (C.9) into Eq. (C.7) we find that

$$g(\varepsilon) = \frac{16}{2\pi}\frac{\varepsilon^2}{(\hbar\bar{\omega})^3}\int_0^1 dx x^2\sqrt{1-x^2}, \tag{C.11}$$

which is a standard integral, the result giving us ideal gas density of states for a harmonic trap

$$g(\varepsilon) = \frac{\varepsilon^2}{2(\hbar\bar{\omega})^3}. \tag{C.12}$$

## C.3 Thomas-Fermi approximation

For an interacting gas in the presence of a Bose-condensate, the largest contribution to the mean field experienced by non-condensed particles is due to the condensate itself. If the condensate is large and static, we can approximate its mean field using the Thomas-Fermi approximation for the density profile, i.e.

$$U_0|\psi(\mathbf{r})|^2 = \begin{cases} \mu_C(n_0) - V(\mathbf{r}) & \text{if} \quad \mu_C(n_0) > V(\mathbf{r}), \\ 0 & \text{otherwise.} \end{cases} \tag{C.13}$$

An approximate Bogoliubov dispersion relation can be used in the region of the condensate

$$\varepsilon(r,p) \;=\; \left[\left(\frac{p^2}{2m}\right)^2 + \frac{p^2}{m}[\mu_C(n_0) - V(r)]\right]^{1/2} + \mu_C(n_0), \tag{C.14}$$

where $\mu_C(n_0)$ has been added to this expression, as the standard Bogoliubov relation measures quasiparticle energies relative to the condensate eigenvalue. Thus we have

$$\frac{\partial\varepsilon}{\partial p} = \frac{p^3/m + 2[\mu_C(n_0) - V(r)]p/m}{2\left[(p^2/2m)^2 + [\mu_C(n_0) - V(r)]p^2/m\right]^{1/2}}. \tag{C.15}$$

Inverting the dispersion relation for the condensate region Eq. (C.14) we find

$$\frac{p(\varepsilon,r)^2}{2m} = \sqrt{[\mu(n_0) - V(r)]^2 + [\varepsilon - \mu(n_0)]^2} - [\mu(n_0) - V(r)]. \tag{C.16}$$

Outside the condensate region defined by

$$r > r_{TF} = \frac{[2\mu_C(n_0)]}{m\bar{\omega}}^{1/2}, \tag{C.17}$$

the ideal gas dispersion relation Eq. (C.8) is used. Writing out the entire integral we have

$$\begin{aligned} g(\varepsilon) &= \frac{(2m)^{3/2}}{\pi\hbar^3}\int_0^{r_{TF}} r^2 dr \mu\left(\frac{\varepsilon}{\mu}-1\right)\frac{\left[\sqrt{\mu^2\left(1-\frac{V}{\mu}\right)^2+\mu^2\left(\frac{\varepsilon}{\mu}-1\right)^2}-\mu\left(1-\frac{V}{\mu}\right)\right]^{1/2}}{\left[\mu^2\left(1-\frac{V}{\mu}\right)^2+\mu^2\left(\frac{\varepsilon}{\mu}-1\right)^2\right]^{1/2}} \\ &+ \frac{(2m)^{3/2}}{\pi\hbar^3}\int_{r_{\rm TF}}^{r_{\max}} r^2 dr\sqrt{\mu}\sqrt{\frac{\varepsilon}{\mu}-\frac{V}{\mu}} \end{aligned} \tag{C.18}$$

where we have used the shorthand notation $\mu = \mu_C(n_0), V = V(r)$. This is easily transformed into

$$\begin{aligned} g(\varepsilon) &= \frac{4}{\pi}\frac{\mu^2}{(\hbar\bar{\omega})^3}\left(\frac{\varepsilon}{\mu}-1\right)\int_0^1 dx\sqrt{1-x}\frac{\left[\sqrt{\left(\frac{\varepsilon}{\mu}-1\right)^2+x^2}-x\right]^{1/2}}{\left[\left(\frac{\varepsilon}{\mu}-1\right)^2+x^2\right]^{1/2}} \\ &+ \frac{4}{\pi}\frac{\mu^2}{(\hbar\bar{\omega})^3}\int_1^{\varepsilon/\mu} dx\sqrt{x}\sqrt{\frac{\varepsilon}{\mu}-x}. \end{aligned} \tag{C.19}$$

These are standard integrals that can be found in tables [142]. The final result for the density of states for a harmonic trap in the presence of a condensate is

$$\bar{g}(\varepsilon, n_0) = \frac{\varepsilon^2}{2(\hbar\bar{\omega})^3}\left\{1+q_1\left(\mu_{\rm C}(n_0)/\varepsilon\right)+\left(1-\frac{\mu_{\rm C}(n_0)}{\varepsilon}\right)^2 q_2\left(\frac{1}{\varepsilon/\mu_{\rm C}(n_0)-1}\right)\right\}, \tag{C.20}$$

where

$$q_1(x) = \frac{2}{\pi}\left[\sqrt{x}\sqrt{1-x}(1-2x)-\sin^{-1}(\sqrt{x})\right], \tag{C.21}$$

$$q_2(x) = \frac{4\sqrt{2}}{\pi}\left[\sqrt{2x}+x\ln\left(\frac{1+x+\sqrt{2x}}{\sqrt{1+x^2}}\right)\left\{\frac{\pi}{2}+\sin^{-1}\left(\frac{x-1}{\sqrt{1+x^2}}\right)\right\}\right]. \tag{C.22}$$

## APPENDIX D

# NUMERICAL METHODS

In this appendix we describe some of the numerical techniques we have used to solve the time-dependent Gross-Pitaevskii equation.

## D.1 Preliminaries

The dimensionless form of the GPE is

$$i\frac{\partial\psi(\mathbf{x})}{\partial\tau} = -\nabla^2\psi(\mathbf{x}) + V_{\mathrm{trap}}(\mathbf{x})\psi(\mathbf{x}) + C_{\mathrm{nl}}|\psi(\mathbf{x})|^2\psi(\mathbf{x}). \tag{D.1}$$

We choose to write this in the form

$$i\frac{\partial\psi(\mathbf{x})}{\partial\tau} = (\hat{D} + \hat{N})\psi(\mathbf{x}). \tag{D.2}$$

where we have defined the operators

$$\hat{D} = -\nabla^2, \qquad \hat{N} = V_{\mathrm{trap}}(\mathbf{x}) + C_{\mathrm{nl}}|\psi(\mathbf{x})|^2. \tag{D.3}$$

The dispersion operator $\hat{D}$ contains only spatial derivatives, while the nonlinear operator $\hat{N}$ is local in space. In the numerical solution of this equation we begin with a real-space wave function and evolve it in time.

### D.1.1 Calculation of $\hat{D}$

The calculation of derivatives on a numerical grid can be carried out by finite differencing techniques, based on a Taylor series expansion of the function. However, these are only accurate to a given order, and are less accurate near the edge of the grid. Instead, we make use of a spectral method to calculate the operator $\hat{D}$ which is limited only by the numerical representation of the function. This can be carried out by the use of numerical fast Fourier transforms (FFTs), and takes about the same amount of computational time as a high-order finite difference method.

With the forward and reverse Fourier transforms defined as

$$\begin{aligned} \psi(\mathbf{k}) &= \frac{1}{2\pi}\int d^3\mathbf{x}\,\psi(\mathbf{x})\,e^{+i\mathbf{k}\cdot\mathbf{x}}, \\ \psi(\mathbf{x}) &= \int d^3\mathbf{k}\,\psi(\mathbf{k})\,e^{-i\mathbf{k}\cdot\mathbf{x}}, \end{aligned} \tag{D.4}$$

we have

$$\begin{aligned} -\nabla^2\psi(\mathbf{x}) &= -\nabla^2\int d^3\mathbf{k}\,\psi(\mathbf{k})\,e^{-i\mathbf{k}\cdot\mathbf{x}}, \\ &= \int d^3\mathbf{k}\,k^2\psi(\mathbf{k})\,e^{-i\mathbf{k}\cdot\mathbf{x}}, \\ &= \int d^3\mathbf{k}\,k^2\,e^{-i\mathbf{k}\cdot\mathbf{x}}\times\frac{1}{2\pi}\int d^3\mathbf{x}'\,e^{+i\mathbf{k}\cdot\mathbf{x}'}\psi(\mathbf{x}'). \end{aligned} \tag{D.5}$$

So the numerical procedure can be summarised as

$$-\nabla^2\psi = \mathrm{IFFT}\left\{k^2\times\mathrm{FFT}[\psi]\right\}, \tag{D.6}$$

i.e. transform the wave function to $k$-space, multiply each component by $k^2$ and transform back.

### D.1.2 Choice of grid

To facilitate efficient numerics we choose to represent our wave function on a grid with $2^{n_i}$ points in each dimension $i$, where $n_i$ is a positive integer. Algorithms for computing FFTs are fastest for these grid sizes. The definition of a spatial grid and the corresponding Fourier space grid can be a source of confusion, and in this section we describe our choice of grid.

Discrete Fourier transforms treat the function being transformed as periodic, so we must be careful to ensure that the end points are not represented twice in our definition. This is especially important when evolving wave functions with periodic boundary conditions.

For example, consider a grid for a system defined between $-L/2$ and $L/2$. If we have $n$ grid points then the spacing of the points should be $dx = L/n$, and we should choose the $x$-grid as either

$$\begin{aligned} x_i &= -\frac{L}{2}, dx - \frac{L}{2}, 2dx - \frac{L}{2}, \ldots, \frac{L}{2} - 2dx, \frac{L}{2} - dx, \qquad \text{or} \qquad (D.7) \\ x_i &= \frac{dx - L}{2}, \frac{3dx - L}{2}, \ldots, \frac{L - 3dx}{2}, \frac{L - dx}{2}. \qquad (D.8) \end{aligned}$$

The corresponding $k$-grid for the discrete Fourier transform will be

$$k_i = 0, \frac{2\pi}{L}, \frac{4\pi}{L}, \ldots, \frac{2\pi[\mathrm{fl}(n/2)]}{L}, \frac{-2\pi[\mathrm{fl}(n/2) - 1]}{L}, \ldots, -\frac{4\pi}{L}, -\frac{2\pi}{L}. \qquad (D.9)$$

where $\mathrm{fl}(x)$ indicates that any decimal part of $x$ should be truncated. This is important when $n$ is odd.

## D.2 Symmetrised split-step method (SSM)

We now consider methods for solving the GPE. From here on we drop all space labels for our wave function, but include time labels.

The GPE is written as

$$i\frac{\partial\psi(\tau)}{\partial\tau} = (\hat{D} + \hat{N})\psi(\tau). \qquad (D.10)$$

Neglecting the time dependence of the operator $\hat{N}$, we can write the formal solution to the GPE as

$$\psi(\tau + \delta\tau) = e^{-i(\hat{D}+\hat{N})\delta\tau}\psi(\tau). \qquad (D.11)$$

Using the Baker-Hausdorff identity

$$e^{x\hat{D}}e^{x\hat{N}} = e^{x(\hat{D}+\hat{N})+x^2[\hat{D},\hat{N}]/2+x^3[\hat{D}-\hat{N},[\hat{D},\hat{N}]]/12+\ldots}, \qquad (D.12)$$

then if $\delta\tau$ is small then we can approximate Eq. (D.11) by

$$\psi(\tau + \delta\tau) = e^{-i\hat{D}\delta\tau}e^{-i\hat{N}\delta\tau}\psi(\tau). \qquad (D.13)$$

This gives us a procedure for evolving the wave function $\psi(\tau)$ by an amount $\delta\tau$, assuming that the change in $\hat{N}$ is negligible over the time step.

In fact, we can improve the accuracy of this method to third order by symmetrising the expression to cancel the $x^2$ term of Eq. (D.12). We therefore have the following scheme to propagate the wave function in time

$$\psi(\tau+\delta\tau) = e^{-i\hat{N}\delta\tau/2} e^{-i\hat{D}\delta\tau} e^{-i\hat{N}\delta\tau/2} \psi(\tau). \tag{D.14}$$

This is known as the symmetrised split-operator method (SSM).

We gain some computational advantage by splitting $\hat{N}$ and not $\hat{D}$, as the latter is more time-consuming numerically. We find

$$e^{-i\hat{D}\delta\tau}\psi \;=\; \text{IFFT}\left\{ e^{ik^2\delta\tau} \times \text{FFT}[\psi] \right\}. \tag{D.15}$$

This algorithm is often mentioned in the literature as the method used to solve the time dependent GPE.

## D.3 Fourth order Runge-Kutta

Solving a differential equation by use of a Runge-Kutta method involves propagating the solution by making several Euler-type steps over a time interval, and then combining the information at the end of the step to match a Taylor series expansion. Further details of their derivation can be found in Ref. [111], and several formulae can be found in Ref. [143].

One of the most commonly used methods is the fourth order Runge-Kutta formula (RK4). If the time derivative of our wave function $\psi$ is given by

$$i\frac{\partial\psi(\tau)}{\partial\tau} = f(\psi(\tau),\tau), \tag{D.16}$$

then to propagate it from $\tau$ to $\tau+\delta\tau$ we calculate

$$\begin{aligned}
k_1 &= -i\delta\tau f(\psi(\tau),\tau), \\
k_2 &= -i\delta\tau f(\psi(\tau)+k_1/2,\tau+\delta\tau/2), \\
k_3 &= -i\delta\tau f(\psi(\tau)+k_2/2,\tau+\delta\tau/2), \\
k_4 &= -i\delta\tau f(\psi(\tau)+k_3,\tau+\delta\tau), \\
\psi(\tau+\delta\tau) &= \psi(\tau)+\frac{k_1}{6}+\frac{k_2}{3}+\frac{k_3}{3}+\frac{k_4}{6}+O[(\delta\tau)^5].
\end{aligned} \tag{D.17}$$

From *Numerical Recipes*, Ref. [111]

> “For many scientific users, fourth-order Runge-Kutta is not just the

> first word on ODE integrators, but the last word as well. In fact, you can get pretty far on this old workhorse ..."

This algorithm requires only four derivative evaluations per time step, and one addition to the wave function for each of these evaluations. It therefore has a lot of "bang for its buck", and this contributes to its popularity.

### D.3.1 RK4IP

An algorithm developed by R. J. Ballagh and co-workers at the University of Otago combines the use of an interaction picture (IP) with the RK4 method. We define

$$\psi^{\mathrm{I}(\tau_0)}(\tau) = e^{+i\hat{D}(\tau-\tau_0)}\psi(\tau), \tag{D.18}$$

where $\psi^{\mathrm{I}(\tau_0)}(\tau)$ is the interaction picture wave function at time $\tau$ with time origin at $\tau_0$. Note that for $\tau = \tau_0$ that the interaction picture and normal picture wave functions are the same.

Substituting Eq. (D.18) into Eq. (D.11) the GPE becomes

$$i\frac{\partial\psi^{\mathrm{I}(\tau_0)}}{\partial\tau}(\tau) = \hat{N}^{\mathrm{I}(\tau_0)}\psi^{\mathrm{I}(\tau_0)}(\tau), \tag{D.19}$$

where we have the IP operator

$$\hat{N}^{\mathrm{I}(\tau_0)} = e^{+i\hat{D}(\tau-\tau_0)}\hat{N}e^{-i\hat{D}(\tau-\tau_0)}. \tag{D.20}$$

The computation of the operator $e^{+i\hat{D}(\tau-\tau_0)}$ is very time consuming numerically, as it involves two Fourier transforms. Therefore the direct application of the algorithm outlined in Eq. (D.17) for the IP would be very slow. However, the use of clever techniques is able to reduce the total number of transforms required to eight per step, the same number that would be required without using the interaction picture.

#### Algorithm

We begin with the normal picture wave function $\psi(\tau = 0)$ and wish to propagate the wave function to $\tau = \delta\tau$. We define the interaction picture origin to be in the middle of the step at $\tau = \delta\tau/2$, and so

$$\psi^{\mathrm{I}}(0) = e^{+i\hat{D}\delta\tau/2}\psi(0). \tag{D.21}$$

We have at $\tau = 0$

$$\begin{aligned} k_1 &= -i\delta\tau \hat{N}^{\mathrm{I}}\psi^{\mathrm{I}}(0), \\ &= -i\delta\tau \left[ e^{+i\hat{D}\delta\tau/2}\hat{N}e^{-i\hat{D}\delta\tau/2} \right] \times \left[ e^{+i\hat{D}\delta\tau/2}\psi(0) \right], \\ &= -i\delta\tau e^{i\hat{D}\delta\tau/2}\hat{N}\psi(0), \end{aligned} \tag{D.22}$$

where two of the exponential operations have cancelled each other.

The quantities $k_2$ and $k_3$ are calculated at $\tau = \delta\tau/2$, which is the origin of the interaction picture. Here we have $\hat{N}^{\mathrm{I}} \equiv \hat{N}$, and so

$$\begin{aligned} k_2 &= -i\delta\tau \hat{N}(\psi^{\mathrm{I}}(0) + k_1/2), \\ k_3 &= -i\delta\tau \hat{N}(\psi^{\mathrm{I}}(0) + k_2/2). \end{aligned} \tag{D.23}$$

For $k_4$ at $\tau = \delta\tau$

$$k_4 = -i\delta\tau e^{-i\hat{D}\delta\tau/2}\hat{N}e^{+i\hat{D}\delta\tau/2}(\psi^{\mathrm{I}}(0) + k_3). \tag{D.24}$$

Finally we assemble all the components, which gives us the wave function at $\tau = \delta\tau$ but in the interaction picture with origin at $\tau = \delta\tau/2$. We therefore transform the origin of the interaction picture to $\tau = \delta\tau$, which also is the normal picture wave function at the end of the step. We thus have

$$\psi(\delta\tau) = e^{+i\hat{D}\delta\tau/2}\left\{ \psi^{\mathrm{I}}(0) + \frac{k_1}{6} + \frac{k_2}{3} + \frac{k_3}{3} + \frac{k_4}{6} \right\}. \tag{D.25}$$

However, there is still a saving to be made. From Eq. (D.25) we can see that all terms are operated on by $e^{+i\hat{D}\tau/2}$, but the last operation applied to $k_4$ in Eq. (D.24) is $e^{-i\hat{D}\tau/2}$. So instead we define

$$k_4^* = -i\delta\tau \hat{N}e^{+i\hat{D}\delta\tau/2}(\psi^{\mathrm{I}}(0) + k_3), \tag{D.26}$$

so that the final wave function is given by

$$\psi(\delta\tau) = e^{+i\hat{D}\delta\tau/2}\left\{ \psi^{\mathrm{I}}(0) + \frac{k_1}{6} + \frac{k_2}{3} + \frac{k_3}{3} \right\} + \frac{k_4^*}{6}. \tag{D.27}$$

In summary, the procedure to calculate $\psi(\delta\tau)$ from $\psi(0)$ is as follows:

$$\begin{aligned}
\psi^{\mathrm{I}}(0) &= e^{i\hat{D}\delta\tau/2}\psi(0), \\
k_1 &= -i\delta\tau e^{i\hat{D}\delta\tau/2}\hat{N}\psi(0), \\
k_2 &= -i\delta\tau\hat{N}(\psi^{\mathrm{I}}(0)+k_1/2), \\
k_3 &= -i\delta\tau\hat{N}(\psi^{\mathrm{I}}(0)+k_2/2), \\
k_4^* &= -i\delta\tau\hat{N}e^{+i\hat{D}\delta\tau/2}(\psi^{\mathrm{I}}(0)+k_3), \\
\psi(\delta\tau) &= e^{+i\hat{D}\delta\tau/2}\left\{\psi^{\mathrm{I}}(0)+\frac{k_1}{6}+\frac{k_2}{3}+\frac{k_3}{3}\right\}+\frac{k_4^*}{6}.
\end{aligned} \tag{D.28}$$

This algorithm has been used successfully in both Oxford and New Zealand since 1996 to evolve the GPE.

One difficulty faced when using this algorithm is the choice of step-size. It must be relatively short such that numerical accuracy is not compromised, however this must be balanced with the fact that the computations must finish on a reasonable time scale.

After using this algorithm in many varied situations, we still find it difficult to determine whether the answer has converged. The only way to be sure is to halve the step size and recompute the results. If the final state is the same, then it is a reasonable assumption that the original step-size was sufficient. However, repeating the simulation with one that takes twice as long seems like a waste of resources, especially if it turns out that the longer time step was sufficiently accurate.

We have therefore developed an algorithm base on a Runga-Kutta method, but with an adaptive step size. We specify an acceptable truncation error per time step at the beginning of a calculation, and the algorithm adjusts the size of each step along the way. This has the advantage that it can take large steps through relatively “easy” territory, but slows down when the terrain is more difficult. The cost is a more computationally intensive, complicated algorithm; however, at the start of the development it was likely that the benefits would outweigh the costs.

## D.4 Adaptive step size algorithm (ARK45)

The algorithm we base our method on is an embedded Runge-Kutta, as described in Ref. [111]. An interesting fact about Runge-Kutta formulas is that for orders $M > 4$, either $M + 1$ or $M + 2$ evaluations of the derivative are required—this is one reason the fourth order method is popular. However, Fehlberg discovered

| $i$ | $a_i$ | $b_{ij}$ | | | | | $c_i$ | $c_i^*$ |
|---|---|---|---|---|---|---|---|---|
| 1 | | | | | | | $\frac{37}{378}$ | $\frac{2825}{27648}$ |
| 2 | $\frac{1}{5}$ | $\frac{1}{5}$ | | | | | 0 | 0 |
| 3 | $\frac{3}{10}$ | $\frac{3}{40}$ | $\frac{9}{40}$ | | | | $\frac{250}{621}$ | $\frac{18575}{48384}$ |
| 4 | $\frac{3}{5}$ | $\frac{3}{10}$ | $-\frac{9}{10}$ | $\frac{6}{5}$ | | | $\frac{125}{594}$ | $\frac{13525}{55296}$ |
| 5 | 1 | $-\frac{11}{54}$ | $\frac{5}{2}$ | $-\frac{70}{27}$ | $\frac{35}{27}$ | | 0 | $\frac{277}{14336}$ |
| 6 | $\frac{7}{8}$ | $\frac{1631}{55296}$ | $\frac{175}{512}$ | $\frac{575}{13824}$ | $\frac{44275}{110592}$ | $\frac{253}{4096}$ | $\frac{512}{1771}$ | $\frac{1}{4}$ |
| j = | | 1 | 2 | 3 | 4 | 5 | | |

Table D.1: Cash-Karp parameters for the embedded Runga-Kutta method.

a fifth order RK formula, using six derivative evaluations, whose results could be combined in a second manner to give a fourth order method. The comparison of the results of the two formulae gives a measure of the fifth-order truncation error which can be used to monitor the step-size.

The general form of a fifth-order Runge-Kutta formula for our equation is

$$\begin{aligned} k_1 &= -i\delta\tau f(\psi(\tau),\tau), \\ k_2 &= -i\delta\tau f(\psi(\tau)+b_{21}k_1,\tau+a_2\delta\tau), \\ &\ldots \\ k_6 &= -i\delta\tau f(\psi(\tau)+b_{61}k_1+\ldots+b_{65}k_5,\tau+a_6\delta\tau), \\ \psi(\tau+\delta\tau) &= \psi(\tau)+c_1k_1+c_2k_2+\ldots+c_6k_6+O[(\delta\tau)^6]. \end{aligned} \tag{D.29}$$

The embedded fourth-order formula is

$$\psi(\tau+\delta\tau)^* = \psi(\tau)+c_1^*k_1+c_2^*k_2+\ldots+c_6^*k_6+O[(\delta\tau)^5]. \tag{D.30}$$

and in our algorithm, we use the Cash-Karp set of parameters given in Table D.1.

The truncation error is given by

$$\Delta_m = \psi(\tau+\delta\tau)-\psi(\tau+\delta\tau)^*. \tag{D.31}$$

However, this notation hides the fact that $\psi$ is actually a grid from which we need to extract a single measure of the error.

### D.4.1 Interaction picture

We would like to make use of the interaction picture with the adaptive step size. However, for this algorithm it seems we would require many applications of the operator $e^{+i\hat{D}\delta\tau}$, and this would be very inefficient. The previous algorithm was able to reduce the number of $e^{+i\hat{D}\delta\tau}$ operations due to choosing the IP time origin in a convenient place—however, this is not possible in general.

Our solution is to evolve the GPE in $k$-space rather than real space. The dispersion operation is then easy to calculate as it will require no Fourier transforms and is simply an array multiplication. To calculate the nonlinear term we transform $\psi$ back into real space. This will require twelve transforms, as there are six derivative calculations in the RK formula—the same number as would be required without using the IP.

Evolving in $k$-space has another advantage. In Chapter 6 we project the wave function onto the coherent region $C$ at each derivative. This must be carried out in $k$-space, so using a real space algorithm would require many Fourier transforms even for the RK4IP method.

### D.4.2 Step size

According to Eqs. (D.29) and (D.30), the fifth order truncation error should scale with $(\delta\tau)^5$. However, we have a grid of measured errors, which leads to the question: How should we choose a suitable measure? The problem is more difficult in Fourier space, as the wave function components vary over orders of magnitude, and so the relative error on the smaller components will be larger than the ones than the ones that are most important.

There is no single best way to make this measure; here we detail a scheme we have devised that seems to work well. We find the components of the wave function whose amplitudes are no smaller than $10^{-3}$ times the largest. We then calculate the relative error for each of these components on a time step $\delta\tau$, and we use the largest error as $\Delta_m$ to use in the step determining procedure. At the beginning of the calculation we set a tolerance on the maximum truncation error for each time step, $\Delta_{\text{tol}}$. Typically this is between $10^{-6}$ and $10^{-10}$ depending on the situation.

We accept a time step of $\delta\tau_n$ if $\Delta_m \leq \Delta_{\text{tol}}$. It is rejected if $\Delta_m > \Delta_{\text{tol}}$, and the step must be calculated again. The size of the next time step $\delta\tau_{n+1}$ is determined by

$$\delta\tau_{n+1} = \begin{cases} 0.92\delta\tau_n \left|\dfrac{\Delta_{\text{tol}}}{\Delta_m}\right|^{1/5} & \text{if } \Delta_m \leq \Delta_{\text{tol}}, \\ \\ 0.92\delta\tau_n \left|\dfrac{\Delta_{\text{tol}}}{\Delta_m}\right|^{1/4} & \text{if } \Delta_m > \Delta_{\text{tol}}. \end{cases} \tag{D.32}$$

For further details of this choice see Ref. [111]. We find that this procedure leads to at least 99% of all steps being accepted.

## D.5 Comparison of algorithms

### D.5.1 Soliton in 1D

To compare some of the characteristics of the algorithms discussed in this appendix, we make use of a known soliton solution to the 1D GPE. If we begin with a wave function

$$\psi(x,0) = N\text{sech}(x), \tag{D.33}$$

where $N$ is a positive integer, and propagate this wave function with the equation

$$i\frac{\partial\psi(x,\tau)}{\partial\tau} = \frac{\partial^2\psi(x,\tau)}{\partial x^2} - 2|\psi(x,\tau)|^2\psi(x,\tau), \tag{D.34}$$

the wave function envelope will reform itself completely every $\delta\tau = n\pi/2$ where $n$ is an integer. In this time the phase will have advanced by $n\pi/2$. If we propagate Eq. (D.34) to one of these times, we can compare the final state with the initial wave function and measure the accuracy of the algorithm.

We have evolved the $N = 6$ soliton to $\tau = \pi$ using all three algorithms described in this appendix. For these simulations we used an $x$-grid of $N_{\text{pts}} = 4096$ points, with a range of 40. A sample plot of the evolution is presented in Fig. D.1.

The figures of merit we use for each simulation are the average error per point

$$\text{Error} = \frac{\sum_{i=1}^{N_{\text{pts}}} \left| |\psi(x_i,\pi)|^2 - |\psi(x_i,0)|^2 \right|}{N_{\text{pts}} \sum_{i=1}^{N_{\text{pts}}} |\psi(x_i,0)|^2}, \tag{D.35}$$

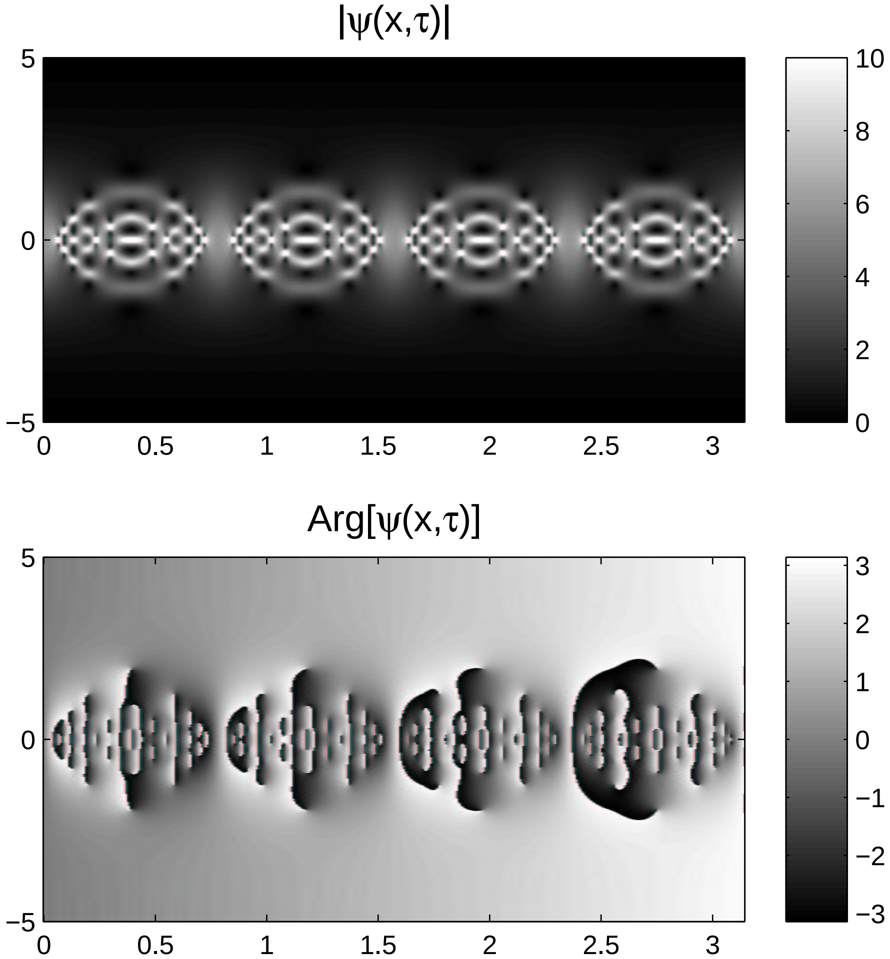

Figure D.1: The evolution of the $N = 6$ soliton for a time period of $\tau = \pi$.

| Algorithm | Time / step (s) |
|---|---|
| SSM | 0.0115 |
| RK4IP | 0.0315 |
| ARK45 | 0.1320 |

Table D.2: A comparison of the time per step for each algorithm for the 1D soliton simulation.

and the relative change in the normalisation of the wave function

$$\text{Change in norm } = \left| \frac{\sum_{i=1}^{N_{\text{pts}}} |\psi(x_i,\pi)|^2 - \sum_{i=1}^{N_{\text{pts}}} |\psi(x_i,0)|^2}{N_{\text{pts}} \sum_{i=1}^{N_{\text{pts}}} |\psi(x_i,0)|^2} \right|. \tag{D.36}$$

The results of this analysis are presented in Fig. D.2

We can see from Fig. D.2 that for a given number of time steps, the ARK45 method requires the least number of steps for a given accuracy, followed by the RK4IP and then the SSM. The slope of the curve of errors should give the order of the method—both ARK45 and RK4IP have a slope of four, whereas the SSM has a slope of about three. Both the ARK45 and RK4IP curves tail off at around $10^{-10}$—this is most likely due to the $x$-range of the grid, which would have to be increased for any further increase in accuracy. On average, the RK4IP algorithm requires about five times, and the SSM about 100 times more steps than the ARK45 method for the same accuracy.

However, this is not the complete picture, as we have not taken into account the computational time taken per step. The SSM only requires two FFTs per step, the RK4IP needs eight, and the ARK45 twelve. The average time per step for each simulation is given in Table D.2. As we can see, although ARK45 requires five times fewer time steps than RK4IP, each step is about four times as long!

In Fig. D.2(b) we show the change in relative normalisation for all the simulations. We see by comparison with Fig. D.2(a) that for the RK4IP and ARK45 methods that this is a good measure of the average error of the simulation. This is useful knowledge, as usually in carrying out numerical calculations we do not have an analytic solution to compare our final state with.

However, the normalisation does not give an indication of the accuracy of the SSM. This is because every operation applied to the wave function is unitary as is seen in Eq. (D.14). The normalisation actually increases with the number of steps—this is most likely due to the accumulation of numerical noise with each step.

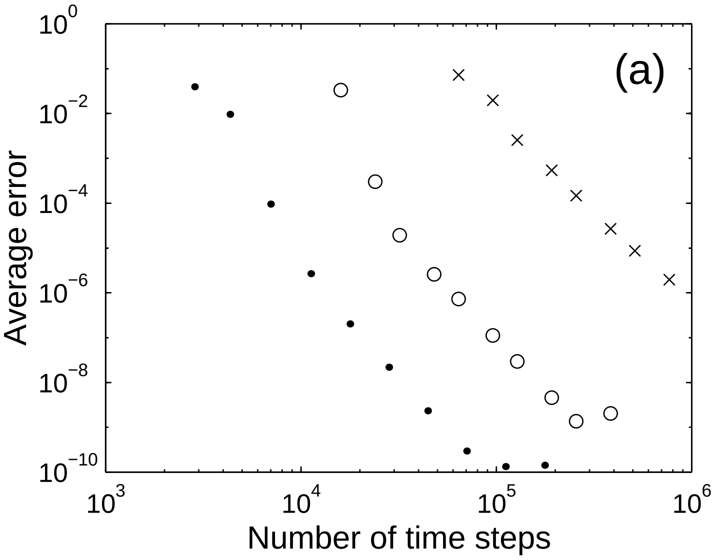

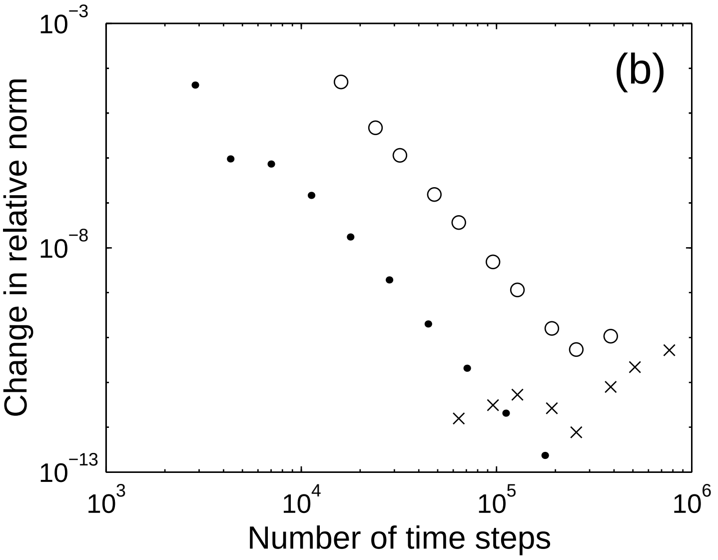

Figure D.2: The figures of merit for the 1D $N = 6$ soliton simulations, plotted against the number of steps for each algorithm. For both figures the crosses are for the SSM, the open circles are for the RK4IP method, and the dots are for the ARK45 algorithm. The ARK45 tolerances ranged from $10^{-3}$ to $10^{-12}$. (a) The average error as defined by Eq. (D.35). (b) The relative change in normalisation as defined by Eq. (D.36).

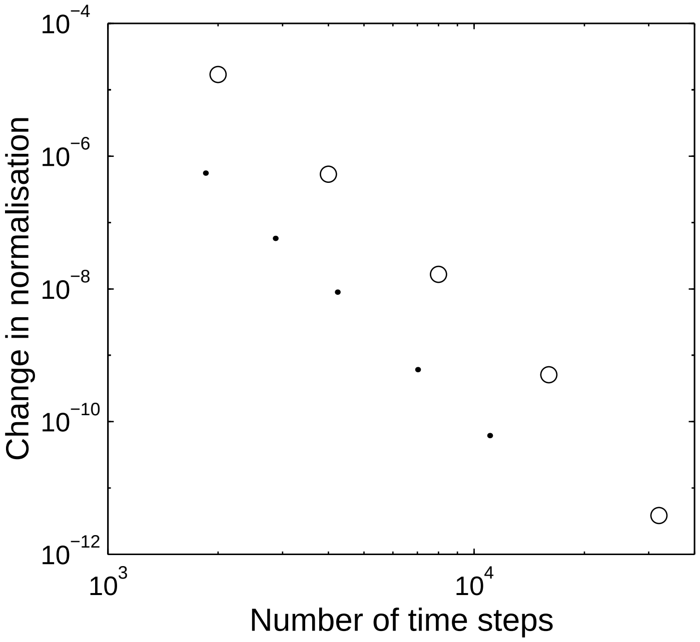

Figure D.3: The relative change in normalisation for a 2D condensate collision, as depicted in Fig. D.4. The open circles are for the RK4IP method, and the dots are for the ARK45 algorithm. The tolerances specified for the ARK45 method were from $10^{-6}$ to $10^{-10}$.

### D.5.2 Condensate collision in 2D

The 1D soliton simulation carried out in the previous section is perhaps not a fair test for these algorithms when it comes to simulating the GPE. It is a particular tough simulation due to the sharpness of some of the structures that appear in the wave function, as can be seen in Fig. D.1.

We therefore present a brief analysis for a 2D GPE simulation involving the collision of two condensates in a harmonic trap, for the RK4IP and ARK45 methods only. We begin with two ground state $C_{\mathrm{nl}} = 88$ condensates, separated by a distance of ten harmonic oscillator (h.o.) units in an isotropic harmonic trap. The grid is $512 \times 512$ points, and spans 40 h.o. units in total. We run this simulation for two h.o.p̃eriods ($\tau = 4\pi$). A plot of the change in relative normalisation after this time is given in Fig. D.3, and snapshots of the first part of the evolution are shown in Fig. D.4.

We can see a similar trend in Fig. D.3 as we saw in Fig. D.2, although the difference in the number of time steps is only about a factor of 2–3 here. On measuring the computational time per step, we find that the RK4IP algorithm is about two and a half times faster than the ARK45. Thus it seems that we are

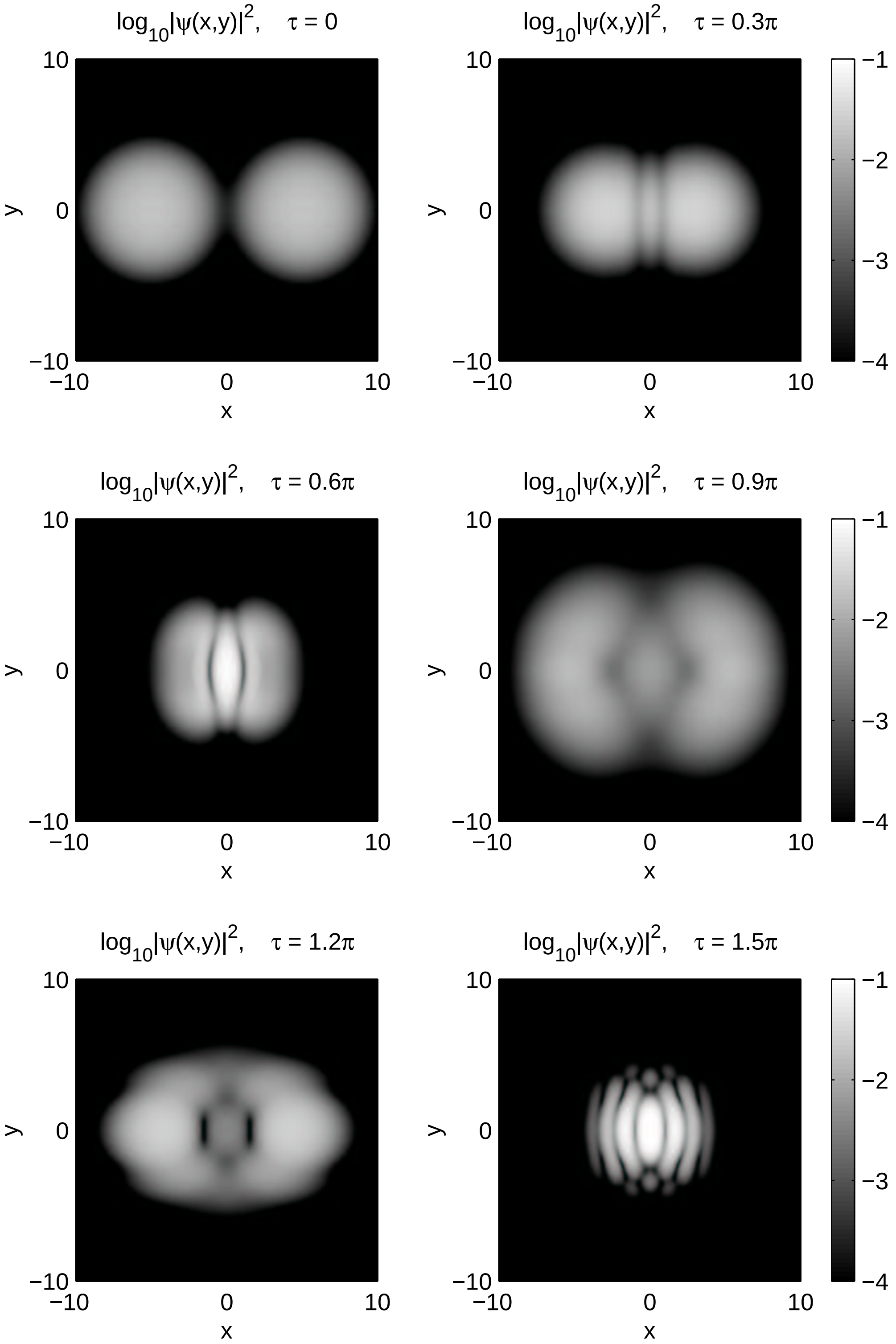

Figure D.4: A collision of two $C_{\mathrm{nl}} = 88$ condensates in a 2D isotropic harmonic trap.

gaining very little by the use of the more sophisticated algorithm.

We would like to make two points. Although any individual run is only slightly faster than the RK4IP method, the ARK45 algorithm allows the user to simply specify a truncation tolerance per step. The RK4IP method, on the other hand, requires an explicit choice of step-size to be made at the outset. Therefore it may turn out that that fewer simulations need to be run using ARK45 to give an acceptable result.

Finally, the ARK45 algorithm has only been developed recently, and has not yet been optimised fully. It is possible that further work will improve its efficiency.

# APPENDIX E

# INCOHERENT REGION EQUATIONS

In this Appendix we give the Heisenberg equations of motion for all the operator combinations that appear in the basis set version of the FTGPE of Eq. (5.13). The single operator term is

$$
\begin{aligned}
i\hbar \frac{d\hat{a}_p}{dt} &= \hbar\omega_p \hat{a}_p && \text{(E.1a)}\\
&+ \langle p\psi|V|\psi\psi\rangle && \text{(E.1b)}\\
&+ \sum_q \langle pq|V|\psi\psi\rangle \hat{a}_q^\dagger && \text{(E.1c)}\\
&+ 2\sum_m \langle p\psi|V|m\psi\rangle \hat{a}_m && \text{(E.1d)}\\
&+ \sum_{mn} \langle p\psi|V|mn\rangle \hat{a}_m\hat{a}_n && \text{(E.1e)}\\
&+ 2\sum_{qm} \langle pq|V|m\psi\rangle \hat{a}_q^\dagger\hat{a}_m && \text{(E.1f)}\\
&+ \sum_{qmn} \langle pq|V|mn\rangle \hat{a}_q^\dagger\hat{a}_m\hat{a}_n, && \text{(E.1g)}
\end{aligned}
$$

which is Eq. (5.15) reproduced from the main text. The equation of motion for $\hat{a}_p^\dagger$ is simply the hermitian conjugate.

The other equations of motion can be found either by calculating the commutator with the Hamiltonian, or using the chain rule.

We have

$$i\hbar\frac{d(\hat{a}_m\hat{a}_n)}{dt} = \hbar(\omega_m+\omega_n)\hat{a}_m\hat{a}_n \tag{E.2a}$$

$$+ \langle m\psi|V|\psi\psi\rangle\hat{a}_n + \langle n\psi|V|\psi\psi\rangle\hat{a}_m \tag{E.2b}$$

$$+ \langle mn|V|\psi\psi\rangle \tag{E.2c}$$

$$+ \sum_k\left[\langle kn|V|\psi\psi\rangle\hat{a}_k^\dagger\hat{a}_m + \langle km|V|\psi\psi\rangle\hat{a}_k^\dagger\hat{a}_n\right] \tag{E.2d}$$

$$+ 2\sum_k\left[\langle n\psi|V|k\psi\rangle\hat{a}_k\hat{a}_m + \langle m\psi|V|k\psi\rangle\hat{a}_k\hat{a}_n\right] \tag{E.2e}$$

$$+ \sum_{kj}\left[\langle m\psi|V|kj\rangle\hat{a}_n\hat{a}_k\hat{a}_j + \langle n\psi|V|kj\rangle\hat{a}_m\hat{a}_k\hat{a}_j\right] \tag{E.2f}$$

$$+ 2\sum_k\langle mn|V|k\psi\rangle\hat{a}_k \tag{E.2g}$$

$$+ 2\sum_{kj}\left[\langle km|V|j\psi\rangle\hat{a}_k^\dagger\hat{a}_j\hat{a}_n + \langle kn|V|j\psi\rangle\hat{a}_k^\dagger\hat{a}_j\hat{a}_m\right] \tag{E.2h}$$

$$+ \sum_{kj}\langle mn|V|kj\rangle\hat{a}_k\hat{a}_j \tag{E.2i}$$

$$+ \sum_{qkj}\left[\langle mq|V|kj\rangle\hat{a}_q^\dagger\hat{a}_n\hat{a}_k\hat{a}_j + \langle nq|V|kj\rangle\hat{a}_q^\dagger\hat{a}_m\hat{a}_k\hat{a}_j\right], \tag{E.2j}$$

$$i\hbar\frac{d(\hat{a}_m^\dagger\hat{a}_n)}{dt} = \hbar(\omega_n-\omega_m)\hat{a}_m^\dagger\hat{a}_n \tag{E.3a}$$

$$+ \langle n\psi|V|\psi\psi\rangle\hat{a}_m^\dagger - \langle\psi\psi|V|m\psi\rangle\hat{a}_n \tag{E.3b}$$

$$+ \sum_k\left[\langle kn|V|\psi\psi\rangle\hat{a}_k^\dagger\hat{a}_m^\dagger - \langle\psi\psi|V|km\rangle\hat{a}_k\hat{a}_n\right] \tag{E.3c}$$

$$+ 2\sum_k\left[\langle n\psi|V|k\psi\rangle\hat{a}_m^\dagger\hat{a}_k - \langle k\psi|V|m\psi\rangle\hat{a}_k^\dagger\hat{a}_n\right] \tag{E.3d}$$

$$+ \sum_{kj}\left[\langle n\psi|V|kj\rangle\hat{a}_m^\dagger\hat{a}_k\hat{a}_j - \langle kj|V|m\psi\rangle\hat{a}_k^\dagger a_j^\dagger\hat{a}_n\right] \tag{E.3e}$$

$$+ 2\sum_{kj}\left[\langle kn|V|j\psi\rangle\hat{a}_m^\dagger\hat{a}_k^\dagger\hat{a}_j - \langle j\psi|V|km\rangle\hat{a}_j^\dagger a_k\hat{a}_n\right] \tag{E.3f}$$

$$+ \sum_{qkj}\left[\langle qn|V|kj\rangle\hat{a}_m^\dagger\hat{a}_q^\dagger\hat{a}_k\hat{a}_j - \langle kj|V|qm\rangle\hat{a}_j^\dagger a_k^\dagger\hat{a}_q\hat{a}_n\right], \tag{E.3g}$$

and

$$\begin{align}
i\hbar\frac{d(\hat{a}_q^\dagger\hat{a}_m\hat{a}_n)}{dt} &= i\hbar\left[\hat{a}_q^\dagger\frac{d(\hat{a}_m\hat{a}_n)}{dt}+\frac{d(\hat{a}_q^\dagger)}{dt}\hat{a}_m^\dagger\hat{a}_n\right] \notag\\
&= \hbar(\omega_m+\omega_n-\omega_q)\hat{a}_q^\dagger\hat{a}_m\hat{a}_n \tag{E.4a}\\
&+ \langle m\psi|V|\psi\psi\rangle\hat{a}_q^\dagger\hat{a}_n+\langle n\psi|V|\psi\psi\rangle\hat{a}_q^\dagger\hat{a}_m \tag{E.4b}\\
&+ \langle mn|V|\psi\psi\rangle\hat{a}_q^\dagger-\langle\psi\psi|V|q\psi\rangle\hat{a}_m\hat{a}_n \tag{E.4c}\\
&+ \sum_k\Big[\langle kn|V|\psi\psi\rangle\hat{a}_q^\dagger\hat{a}_k^\dagger\hat{a}_m+\langle km|V|\psi\psi\rangle\hat{a}_q^\dagger\hat{a}_k^\dagger\hat{a}_n \tag{E.4d}\\
&\quad -\langle\psi\psi|V|kq\rangle\hat{a}_k\hat{a}_m\hat{a}_n] \tag{E.4e}\\
&+ 2\sum_k\big[\langle n\psi|V|k\psi\rangle\hat{a}_q^\dagger\hat{a}_k\hat{a}_m+\langle m\psi|V|k\psi\rangle\hat{a}_q^\dagger\hat{a}_k\hat{a}_n \tag{E.4f}\\
&\quad -\langle k\psi|V|q\psi\rangle\hat{a}_k^\dagger\hat{a}_m\hat{a}_n\Big] \tag{E.4g}\\
&+ \sum_{kj}\big[\langle m\psi|V|kj\rangle\hat{a}_q^\dagger\hat{a}_n\hat{a}_k\hat{a}_j+\langle n\psi|V|kj\rangle\hat{a}_q^\dagger\hat{a}_m\hat{a}_k\hat{a}_j \tag{E.4h}\\
&\quad -\langle kj|V|q\psi\rangle\hat{a}_k^\dagger a_j^\dagger\hat{a}_m\hat{a}_n\Big] \tag{E.4i}\\
&+ 2\sum_k\langle mn|V|k\psi\rangle\hat{a}_q^\dagger\hat{a}_k \tag{E.4j}\\
&+ 2\sum_{kj}\Big[\langle km|V|j\psi\rangle\hat{a}_q^\dagger\hat{a}_k^\dagger\hat{a}_j\hat{a}_n+\langle kn|V|j\psi\rangle\hat{a}_q^\dagger\hat{a}_k^\dagger\hat{a}_j\hat{a}_m \tag{E.4k}\\
&\quad -\langle j\psi|V|kq\rangle\hat{a}_k^\dagger\hat{a}_j\hat{a}_m\hat{a}_n\Big] \tag{E.4l}\\
&+ \sum_{kj}\langle mn|V|kj\rangle\hat{a}_q^\dagger\hat{a}_k\hat{a}_j \tag{E.4m}\\
&+ \sum_{rkj}\big[\langle mr|V|kj\rangle\hat{a}_q^\dagger\hat{a}_r^\dagger\hat{a}_n\hat{a}_k\hat{a}_j+\langle nr|V|kj\rangle\hat{a}_q^\dagger\hat{a}_r^\dagger\hat{a}_m\hat{a}_k\hat{a}_j \tag{E.4n}\\
&\quad -\langle kj|V|rq\rangle\hat{a}_k^\dagger\hat{a}_j^\dagger\hat{a}_r\hat{a}_m\hat{a}_n\Big]\,. \tag{E.4o}
\end{align}$$

## APPENDIX F

# EFFECTS OF TEMPERATURE UPON THE COLLAPSE OF A BOSE-EINSTEIN CONDENSATE IN A GAS WITH ATTRACTIVE INTERACTIONS

In this appendix we present research carried out on the excitation spectrum of Bose-Einstein condensates with a negative *s*-wave scattering length. It have been published as Ref. [144] and is reproduced essentially verbatim. It is included in this thesis to provide a complete record of work carried out in the course of the D. Phil.

## F.1 Abstract

We present a study of the effects of temperature upon the excitation frequencies of a Bose-Einstein condensate formed within a dilute gas with a weak attractive effective interaction between the atoms. We use the self-consistent Hartree-Fock Bogoliubov treatment within the Popov approximation and compare our results to previous zero temperature and Hartree-Fock calculations. The metastability of the condensate is monitored by means of the $l = 0$ excitation frequency. As the number of atoms in the condensate is increased, with $T$ held constant, this frequency goes to zero, signalling a phase transition to a dense collapsed state. The critical number

for collapse is found to decrease as a function of temperature, the rate of decrease being greater than that obtained in previous Hartree-Fock calculations.

## F.2 Introduction

Mean field theories of the Bose-Einstein condensation of trapped alkali vapours have been extremely successful both qualitatively and quantitatively in determining the excitation frequencies of the condensates, especially at relatively low temperatures ($\leq 0.7\ T_c$) [145, 146]. These calculations have been based upon the Popov approximation to the Hartree-Fock Bogoliubov (HFB) treatment, where the anomalous average of the fluctuating field operator is neglected.[1] In all cases the study has been of alkali vapours with positive *s*-wave scattering lengths (i.e., repulsive effective interactions). The case of attractive interactions ($^7$Li for example, as used in experiments at Rice University [148]) has not been treated in this manner. Calculations have, rather, been based on the zero temperature Gross-Pitaevskii equation (GPE) [149] or upon a Hartree-Fock variational calculation [150].

There are two main reasons why the HFB formalism was not used in the Hartree-Fock study referred to above. Firstly, in the case of negative scattering length, the HFB-Popov collective excitations of a homogeneous system are unstable at long wavelengths. Houbiers and Stoof therefore found it more appealing to use the Hartree-Fock method, which has stable excitations at long wavelengths [150]. In the case of the trapped gas this does not present a problem, as one is saved from the infra-red limit by the finite zero-point energy of the trap. From an alternative viewpoint, the finite size of the condensate eliminates very long wavelength excitations. The HFB-Popov theory is hence quite applicable for trapped gases.

Secondly, there is the possibility that atoms with an attractive effective interaction can undergo a BCS-like pairing transition.[2] This possibility is in fact included in the full theory that Houbiers and Stoof develop. However, in their numerical calculations, they ignore the possibility of pairing and the results presented are based on a Hartree-Fock treatment of Bose-Einstein condensation alone. If one is going to assume that their is no BCS transition, then a better description would appear to be that of the HFB-Popov formalism. This is the treatment adopted in

---

[1] The corrections due to the inclusion of the anomalous terms are treated in Ref. [147], and only become important at temperatures greater than about $0.7\ T_c$ in the cases studied previously.

[2] Strictly the transition is an Evans-Rashid phase transition. We will still refer to the pairing transition, however, as a BCS or BCS-like transition as we feel this conveys the nature of the phenomenon more clearly.

this letter.

The purpose of the present investigation is to determine the stability of the condensate against mechanical collapse, and the effects thereon of thermal excitations. It has been shown in the homogeneous limit that the condensate is unstable at the densities required for BEC [151] . In the trap, the additional kinetic energy can stabilise the condensate and a metastable state is possible. This state decays on a timescale which is long compared to the lifetime of the experiment, but only exists for condensates below a certain size. At some critical condensate number the condensate becomes unstable and collapses. This instability is characterised by the monopolar collective excitation going soft [149] (viz., the excitation frequency goes to zero). Various predictions for the critical number, $N_c$, have been made at zero temperature using the GPE and at finite temperatures using the Hartree-Fock treatment. Here we investigate the effects of temperature upon the collapse via the HFB-Popov approach as described briefly below.

## F.3 Method

We make the usual decomposition of the Bose field operator into condensate and noncondensate parts; $\hat{\psi}(\mathbf{r}) \equiv \Phi(\mathbf{r}) + \tilde{\psi}(\mathbf{r})$. The condensate wave function $\Phi(\mathbf{r})$ is then defined within the Popov approximation by the generalised Gross-Pitaevskii equation (GPE)

$$\left[-\frac{\nabla^2}{2m} + V_{ext}(\mathbf{r}) + g n_0(\mathbf{r}) + 2g\tilde{n}(\mathbf{r})\right] \Phi(\mathbf{r}) = \mu\Phi(\mathbf{r})\,. \tag{F.1}$$

Here, $n_0(\mathbf{r}) \equiv |\Phi(\mathbf{r})|^2$ and $\tilde{n}(\mathbf{r}) \equiv \langle\tilde{\psi}^\dagger(\mathbf{r})\tilde{\psi}(\mathbf{r})\rangle$ are the condensate and noncondensate densities respectively. The Popov approximation[152, 153, 154] consists of omitting the anomalous correlation $\langle\tilde{\psi}(\mathbf{r})\tilde{\psi}(\mathbf{r})\rangle$, but keeping $\tilde{n}(\mathbf{r})$. The condensate wave function in Eq. (F.1) is normalised to $N_0$, the total number of particles in the condensate. $V_{ext}(\mathbf{r})$ is the external confining potential and $g = 4\pi\hbar^2 a/m$ is the interaction strength determined by the $s$-wave scattering length $a$. For $^7$Li the value of $a$ used is -27.3 Bohr radii. The condensate eigenvalue is given by the chemical potential $\mu$.[3]

The usual Bogoliubov transformation, $\tilde{\psi}(\mathbf{r}) = \sum_i [u_i(\mathbf{r})\hat{\alpha}_i - v_i^*(\mathbf{r})\hat{\alpha}_i^\dagger]$, to the new

---

[3] This is strictly true only when the number of noncondensate particles is a small fraction of the total. Near and above $T_c$, the chemical potential is fixed as in Ref. [155].

Bose operators $\hat{\alpha}_i$ and $\hat{\alpha}_i^\dagger$ leads to the coupled HFB-Popov equations[152]

$$\begin{aligned}\hat{\mathcal{L}}u_i(\mathbf{r}) - gn_0(\mathbf{r})v_i(\mathbf{r}) &= E_i u_i(\mathbf{r}) \\ \hat{\mathcal{L}}v_i(\mathbf{r}) - gn_0(\mathbf{r})u_i(\mathbf{r}) &= -E_i v_i(\mathbf{r})\,,\end{aligned} \tag{F.2}$$

with $\hat{\mathcal{L}} \equiv -\nabla^2/2m + V_{ext}(\mathbf{r}) + 2gn(\mathbf{r}) - \mu \equiv \hat{h}_0 + gn_0(\mathbf{r})$. These equations define the quasiparticle excitation energies $E_i$ and the quasiparticle amplitudes $u_i$ and $v_i$. Once these quantities have been determined, the noncondensate density is obtained from the expression[152]

$$\begin{aligned}\tilde{n}(\mathbf{r}) &= \sum_i \left\{|v_i(\mathbf{r})|^2 + \left[|u_i(\mathbf{r})|^2 + |v_i(\mathbf{r})|^2\right] N_0(E_i)\right\} \\ &\equiv \tilde{n}_1(\mathbf{r}) + \tilde{n}_2(\mathbf{r})\,,\end{aligned} \tag{F.3}$$

where $\tilde{n}_1(\mathbf{r})$ is that part of the density which reduces to the quantum depletion of the condensate as $T \to 0$. The component $\tilde{n}_2(\mathbf{r})$ depends upon the Bose distribution, $N_0(E) = (e^{\beta E} - 1)^{-1}$, and vanishes in the $T \to 0$ limit.

Rather than solving the coupled equations in Eq. (F.2) directly, we introduce the auxiliary functions $\psi_i^{(\pm)}(\mathbf{r}) \equiv u_i(\mathbf{r}) \pm v_i(\mathbf{r})$ which are solutions of a pair of uncoupled equations (a more detailed discussion of the method is presented in Ref. [146]). The two functions are related to each other by $\hat{h}_0\psi_i^{(+)} = E_i\psi_i^{(-)}$. We note that the collective modes of the condensate can be shown to have an associated density fluctuation given by $\delta n_i(\mathbf{r}) \propto \Phi(\mathbf{r})\psi_i^{(-)}(\mathbf{r})$.

To solve these equations we introduce the normalised eigenfunction basis defined as the solutions of $\hat{h}_0\phi_\alpha(\mathbf{r}) = \varepsilon_\alpha\phi_\alpha(\mathbf{r})$ and diagonalise the resulting matrix problem. The lowest energy solution gives the condensate wave function $\Phi(\mathbf{r}) = \sqrt{N_0}\phi_0(\mathbf{r})$ with eigenvalue $\varepsilon_0 = 0$.

The calculational procedure can be summarised for an arbitrary confining potential as follows: Eq. (F.1) is first solved self-consistently for $\Phi(\mathbf{r})$, with $\tilde{n}(\mathbf{r})$ set to zero. Once $\Phi(\mathbf{r})$ is known, the eigenfunctions of $\hat{h}_0$ required in the expansion of the excited state amplitudes are generated numerically. The matrix problem is then set up to obtain the eigenvalues $E_i$, and the corresponding eigenvectors $c_\alpha^{(i)}$ are used to evaluate the noncondensate density. This result is inserted into Eq. (F.1) and the process is iterated, keeping the condensate number $N_0$ and temperature $T$ fixed. The level of convergence is monitored by means of the noncondensate number, $\tilde{N}$ and the iterations are terminated once $\tilde{N}$ is within one part in $10^7$ of its value on the previous iteration.[4] In this way, we generate the self-consistent densities, $n_0$ and $\tilde{n}$, as a function of $N_0$ and $T$.

## F.4 Results

We consider first the case of $T = 0$ for an isotropic harmonic trap with a frequency equal to the geometric average of the frequencies corresponding to the Rice trap [148], $\bar{\nu} = 144.6$ Hz. This is the geometry considered previously by Houbiers and Stoof [150] and with whom we find qualitative agreement. There are several signatures of collapse of the condensate with increasing condensate number $N_0$. First, we can look at the behaviour of the convergence parameter (the total number of particles in the noncondensate for a given condensate number and temperature) used to monitor the convergence of the solution to the HFB-Popov equations. In Fig. F.1 we show $\tilde{N}$ as a function of iteration number for the three values $N_0 = 1243$, 1244, and 1245. The convergence is clear in the first two cases, whereas in the final case the algorithm diverges catastrophically and no stable solution can be found. We therefore identify the critical number, $N_c$, of atoms in the condensate as 1244, beyond which the condensate is no longer metastable, but unstable to the formation of a dense solid phase. This value of $N_c$ is slightly greater than the value of 1241 obtain by Houbiers and Stoof using the Hartree-Fock approximation. A second, more physical indicator of the collapse is the observed strong dependence of the excitation frequencies on the number of condensate atoms. In particular, we find that the $l = 0$ mode goes soft as $N_0$ approaches the critical number found above. We shall focus on this criterion for the instability in the following.

We next consider a trap with confining frequency 150 Hz. The excitation frequencies are again calculated as a function of the number of particles in the condensate, both at $T = 0$ and at finite temperature. The lowest lying modes at temperatures of 0, 200, and 400 nK are shown in Fig. F.2. The lowest mode is the $l = 1$ Kohn mode, which corresponds to a rigid centre of mass motion. For a harmonic trap the excitation frequency of this mode should be identically equal to the trap frequency. However, the dynamics of the noncondensate are neglected in this treatment and the calculated excitations are those of the condensate alone, moving in the effective *static* potential $V_{eff} = V_{ext} + 2g\tilde{n}(\mathbf{r})$. Due to the presence of the

---

[4] For calculations at high temperatures the high lying states are simply harmonic oscillator states, which are populated according to the Bose distribution. The convergence criterion is based solely on the self-consistent states calculated from Eq. (F.3).

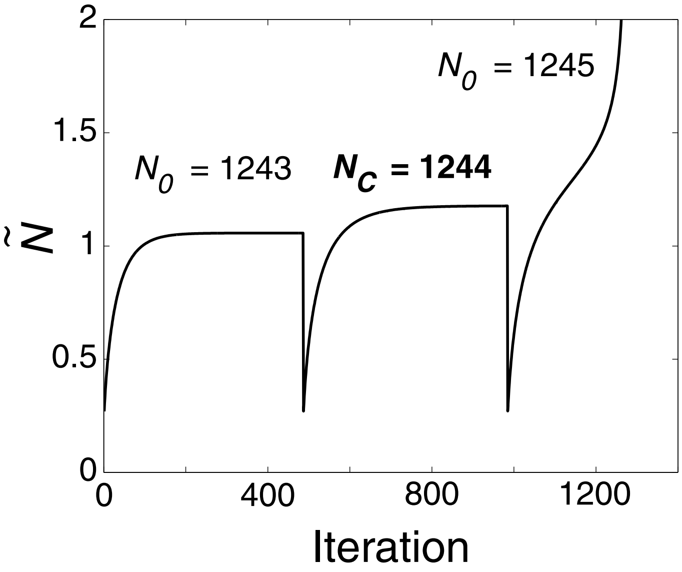

Figure F.1: Noncondensate number as a function of the numerical iteration number for a trap corresponding to the Rice experiment. For $N_0 = 1243$ and $N_0 = 1244$, where $N_0$ is the number of atoms in the condensate, a converged solution is obtained with a self-consistent value for $\tilde{N}$ which varies by less than one part in $10^8$ between iterations. For $N_0 = 1245$ no stable solution can be found. The critical number is identified as $N_c = 1244$ which is the condensate number for which the $l = 0$ mode frequency goes to zero.

noncondensate, the effective potential is not parabolic and hence the generalised Kohn theorem does not apply. The Kohn theorem is approximately obeyed for low temperatures and low particle numbers since the noncondensate is either small, or relatively uniform over the extent of the condensate and hence does not introduce a significant anharmonicity. It is only for higher temperatures near $N_c$ where the noncondensate density is both large and sharply peaked around the centre of the trap that there is a marked deviation from the trap frequency.

As mentioned above, the softening of the $l = 0$ breathing mode is a signature of the instability from a metastable condensate to a completely collapsed state. For $T = 0$ the critical number, $N_c$, is found to be 1227, which is slightly lower than that obtained in the previous case with a stronger confining potential. This is the change in the critical number expected [149] on the basis of the dependence $N_c \propto 1/\sqrt{\omega_0}$, which shows that the critical number increases as the trap confinement is relaxed. With increasing temperature, the frequency of the $l = 0$ mode is found to go to zero at lower condensate numbers. This is because the attractive nature of the interactions with the thermal cloud creates an effective potential for the condensate which is stiffer than the applied external potential [150]. The peak density of

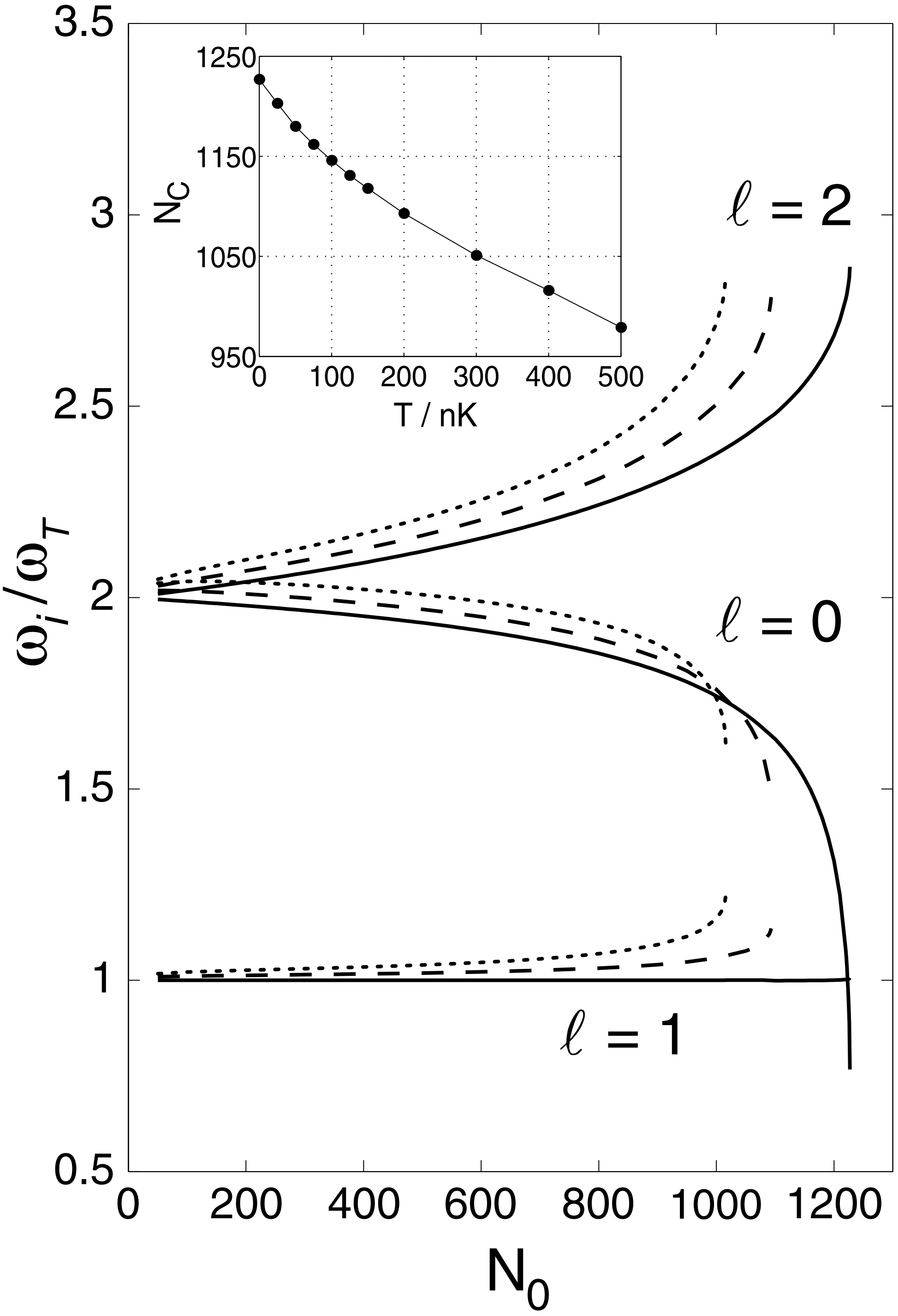

Figure F.2: Low lying mode frequencies as a function of condensate number for $T = 0$ (solid), $T = 200$ nK (dashed), and $T = 400$ nK (dotted) for a trap with a confining frequency of 150 Hz. Note the softening of the $l = 0$ mode for large $N_0$ and the decrease in the critical number at which the mode goes soft as the temperature is increased. The variation of the critical number as a function of temperature is shown in the inset.

the condensate hence increases with temperature (for fixed $N_0$) and the critical condensate number is reduced. The critical number for 200 nK, as obtained from the failure to find a converged solution at larger $N_0$, is $N_c = 1093$. That for $T = 400$ nK is $N_c = 1016$. The temperature dependence of the critical condensate number as a function of temperature is shown in the inset of Fig. F.2.

It should be noted that the total number of trapped atoms, $N$, varies for each point in the figure. Alternatively one could vary $T$ (and hence $N_0$) keeping $N$ fixed, which would give a critical temperature for collapse. Experimentally evaporative cooling removes atoms. A certain total number, corresponding to the transition temperature, is reached at which condensation occurs. Further cooling (removal of atoms) then proceeds to a point where a second critical temperature (or total number) is reached, at which point the second phase transition (i.e. collapse) is observed. However for the experiments on $^7$Li the difference between the critical temperatures for BEC and collapse is extremely small. Cooling thus results in repeated collapse and growth, reducing $N$ until a stable $N_0$ is reached [156].

The collapse occurs because as one increases $N_0$, the peak noncondensate density increases due to the interactions. This in turn creates a tighter and tighter effective potential for the condensate, which eventually results in collapse. Fig. F.3 shows the noncondensate density at 100 nK for a range of $N_0$. The dotted curve is for $N_0 = 50$, the dashed-dot-dot curve that for $N_0 = 1000$. Note that for a large change in $N_0$ the peak noncondensate density has changed relatively little. The next three curves are for $N_0 = 1100$, 1130, and 1146, the final figure being the critical number. The peak noncondensate density increases rapidly over this range. This is a cooperative effect; the tighter effective potential reduces the frequency of the lowest collective mode. This leads to a growth in the population of this low lying mode, which has a density localised near the centre of the condensate, increasing the peak noncondensate density.

The variation of the critical number with temperature is shown in the inset to Fig. F.2. The rate of decrease of $N_c$ with $T$ is significantly greater in the HFB-Popov treatment than in the Hartree-Fock treatment (see Fig. 8 of Ref. [150]). This is due to the different excitation spectra calculated in the two formalisms. In our treatment we calculate (and populate) the collective excitations, which include the low lying $l = 0$ mode. Near collapse this mode has a much lower frequency than the lowest single particle excitation of the Hartree-Fock spectrum. The population of excited states is therefore underestimated in the Hartree-Fock treatment, and as a result, the thermal population of the state is lower than it is with the HFB-Popov

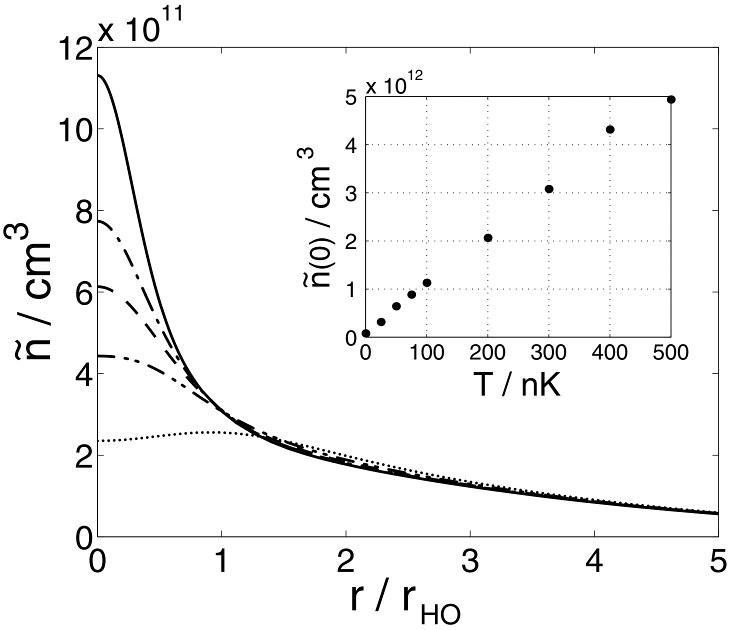

Figure F.3: Noncondensate density for a range of $N_0$ at a temperature of 100 nK in a spherical harmonic trap of frequency 150 Hz. The curves, in increasing order of peak density, are for $N_0 = 50$, 1000, 1100, 1130, and 1146. The final figure is the critical number. The inset shows the peak noncondensate density as a function of temperature at the critical number.

spectrum. The noncondensate population, and hence peak density, increases more rapidly as a function of temperature in our calculation (c.f. inset to Fig. 3 and Fig. 7 of Ref. [150]). This is what gives rise to the more rapid reduction in the critical number as the temperature is increased.

## F.5 Conclusions

We have presented the first self-consistent HFB-Popov calculations for a dilute gas of atoms with attractive effective interactions. We have studied the collective mode frequencies of such a gas and using these frequencies, investigated the phase transition from metastable Bose-Einstein condensate to a collapsed dense phase. The results from these calculations are in general agreement with previous Hartree-Fock results, but we feel that the HFB-Popov approach is the more appropriate one to use if only a BEC transition is assumed to take place. We find a significantly greater dependence of the critical number upon temperature in the HFB-Popov treatment.

If one includes the possibility of a BCS-like pairing transition then this is not the appropriate approach as the omitted pair correlations (the so called anomalous average) are very important. Indeed the pair correlation term, $\langle\tilde{\psi}(\mathbf{r})\tilde{\psi}(\mathbf{r})\rangle$, becomes the order parameter for the BCS-like transition. The possibility of such a transition, or the existence of mixed phases containing both BEC and BCS macroscopic quantum states is currently under investigation.

## Acknowledgments

This work was supported by grants from the Natural Sciences and Engineering Research Council of Canada and from the United Kingdom Engineering and Physical Sciences Research Council. We would like to thank Henk Stoof and Keith Burnett for many helpful and enlightening discussions.

# BIBLIOGRAPHY

[1] S. N. Bose, Z. Phys. **26**, 178 (1924).

[2] A. Einstein, Sitzber. Kgl. Preuss. Akad. Wiss. 261 (1924).

[3] A. Einstein, Sitzber. Kgl. Preuss. Akad. Wiss. 3 (1925).

[4] K. Huang, *Statistical Mechanics* 2nd ed. (John Wiley, 1987).

[5] F. London, Nature **141**, 643 (1938).

[6] L. D. Landau, J. Phys. USSR, **5**, 71 (1941).

[7] L. Tisza, J. Phys. Radium, **1** 164, 350 (1940).

[8] N. N. Bogoliubov, J. Phys. **11**, 23 (1947).

[9] K. Burnett, Contemp. Phys. **37**, 1 (1996).

[10] A. S. Parkins and D. F. Walls, Phys. Rep. **303**, 1 (1998).

[11] F. Dalfovo, S. Giorgini, L. P. Pitaevskii, and S. Stringari, Rev. Mod. Phys. **71**, 463 (1999).

[12] A. Griffin, D. W. Snoke, and S. Stringari, eds., *Bose-Einstein Condensation* (Cambridge University Press, New York, 1995).

[13] M. Inguscio, S. Stringari and C. Wieman, eds., *Bose-Einstein Condensation in Atomic Gases*, (IOS Press, Amsterdam, 1999).

[14] E. Schrödinger, *Statistical Thermodynamics* (Cambridge University Press, Cambridge, 1952).

[15] M. Anderson, J. R. Ensher, M. R. Matthews, C. E. Wieman and E. A. Cornell, Science **269**, 198 (1995).

[16] K. B. Davis, M-O. Mewes, M. R. Andrews, N. J. van Druten, D. S. Durfee, D. M. Kurn, and W. Ketterle, Phys. Rev. Lett. **75**, 3969 (1995).

[17] C. C. Bradley, C. A. Sackett, J. J. Tollet, and R. Hulet, Phys. Rev. Lett. **75**, 1687 (1995); *ibid.* **79**, 1170 (1997).

[18] D. G. Fried, T. C. Killian, L. Willman, D. Landhuis, S. C. Moss, D. Kleppner, and T. J. Greytak, Phys. Rev. Lett. **81**, 3881 (1998).

[19] C. J. Foot, Contemp. Phys. **32**, 369 (1991).

[20] S. Chu, Rev. Mod. Phys. **70**, 685 (1998).

[21] C. Cohen-Tannoudji, Rev. Mod. Phys. **70**, 707 (1998).

[22] W. D. Phillips, Rev. Mod. Phys. **70**, 721 (1998).

[23] H. F. Hess, Phys. Rev. B **34**, 3476 (1986).

[24] W. Petrich, M. H. Anderson, J. R. Ensher, and E. A. Cornell, Phys. Rev. Lett. **74**, 3352 (1995).

[25] M. -O. Mewes, M. R. Andrews, N. J. van Druten, D. M. Kurn, D. S. Durfee, and W. Ketterle, Phys. Rev. Lett **77**, 416 (1996).

[26] D. S. Jin, J. R. Ensher, M. R. Matthews, C. E. Wieman, and E. A. Cornell Phys. Rev. Lett. **77**, 420 (1996).

[27] M.-O. Mewes, M. R. Andrews, N. J. van Druten, D. M. Kurn, D. S. Durfee, C. G. Townsend, and W. Ketterle, Phys. Rev. Lett. **77**, 988 (1996).

[28] D. S. Jin, J. R. Ensher, M. R. Matthews, C. E. Wieman, and E. A. Cornell, Phys. Rev. Lett. **77**, 420 (1996).

[29] M. R. Andrews, D. M. Kurn, H.-J. Miesner, D. S. Durfee, C. G. Townsend, S. Inouye, and W. Ketterle, Phys. Rev. Lett. **79**, 553 (1997); *ibid.* **80**, 2967 (1998).

[30] D. M. Stamper-Kurn, H.-J. Miesner, S. Inouye, M. R. Andrews, and W. Ketterle, Phys. Rev. Lett. **81**, 500 (1998).

[31] M.-O. Mewes, M. R. Andrews, D. M. Kurn, D. S. Durfee, C. G. Townsend, and W. Ketterle, Phys. Rev. Lett. **78**, 582 (1997).

[32] S. Inouye, T. Pfau, S. Gupta, A. P. Chikkatur, A. Görlitz, D. E. Pritchard, and W. Ketterle, Nature **402**, 641 (1999).

[33] E. W. Hagley, L. Deng, M. Kozuma, J. Wen, K. Helmerson, S. L. Rolston, and W. D. Phillips, Science **283**, 1706 (1999).

[34] I. Bloch, T. W. Hänsch, and T. Esslinger, Phys. Rev. Lett. **82**, 3008 (1999).

[35] H.-J. Miesner, D. M. Stamper-Kurn, M. R. Andrews, D. S. Durfee, S. Inouye, and W. Ketterle, Science **279**, 1005 (1998).

[36] C. J. Myatt, E. A. Burt, R. W. Ghrist, E. A. Cornell, and C. E. Wieman, Phys. Rev. Lett. **78**, 586 (1997).

[37] D. S. Hall, M. R. Matthews, J. R. Ensher, C. E. Wieman, and E. A. Cornell, Phys. Rev. Lett. **81**, 1539 (1998).

[38] D. S. Hall, M. R. Matthews, C. E. Wieman, and E. A. Cornell Phys. Rev. Lett. **78**, 1543 (1999).

[39] D. M. Stamper-Kurn, M. R. Andrews, A. P. Chikkatur, S. Inouye, H.-J. Miesner, J. Stenger, and W. Ketterle, Phys. Rev. Lett. **80**, 2027 (1998).

[40] H.-J. Miesner, D. M. Stamper-Kurn, J. Stenger, S. Inouye, A. P. Chikkatur, and W. Ketterle, Phys. Rev. Lett. **82**, 2228 (1999).

[41] D. M. Stamper-Kurn, H.-J. Miesner, A. P. Chikkatur, S. Inouye, J. Stenger, and W. Ketterle, Phys. Rev. Lett. **83**, 661 (1999).

[42] S. Inouye, M. R. Andrews, J. Stenger, H.-J. Miesner, D. M. Stamper-Kurn, and W. Ketterle, Nature **392**, 151 (1998).

[43] S. L. Cornish, N. R. Claussen, J. L. Roberts, E. A. Cornell, and C. E. Wieman, Phys. Rev. Lett. **85** 1795 (2000).

[44] L. Deng, E. W. Hagley, J. Wen, M. Trippenbach, Y. Band, P. S. Julienne, J. E. Simsarian, K. Helmerson, S. L. Rolston, and W. D. Phillips, Nature **398**, 218 (1999).

[45] L. V. Hau, S. E. Harris, Z. Dutton, and C. H. Behroozi, Nature **397**, 594 (1999).

[46] O. M. Maragó, S. A. Hopkins, J. Arlt, E. Hodby, G. Heckenblaikner, and C. J. Foot, Phys. Rev. Lett. **84**, 2056 (2000).

[47] C. Raman, M. Köhl, R. Onofrio, D. S. Durfee, C. E. Kuklewicz, Z. Hadzibabic, and W. Ketterle, Phys. Rev. Lett. **85**, 2502 (1999).

[48] R. Onofrio, C. Raman, J. M. Vogels, J. R. Abo-Shaeer, A. P. Chikkatur, and W. Ketterle, Phys. Rev. Lett. **85**, 2228 (2000).

[49] M. R. Matthews, B. P. Anderson, P. C. Haljan, D. S. Hall, C. E. Wieman, and E. A. Cornell, Phys. Rev. Lett. **83**, 2498 (1999).

[50] B. P. Anderson, P. C. Haljan, C. E. Wieman, and E. A. Cornell, Phys. Rev. Lett. **85**, 2857 (2000).

[51] K. W. Madison, F. Chevy, W. Wohlleben, and J. Dalibard, Phys. Rev. Lett. **84**, 806 (2000).

[52] F. Chevy, K. W. Madison, and J. Dalibard, Phys. Rev. Lett. **85**, 2223 (2000).

[53] M. Le Bellac, *Thermal Field Theory*, (Cambridge University Press, Cambridge, 1996).

[54] S. A. Morgan, J. Phys. B **33**, 3847 (2000); D. Phil thesis, University of Oxford (1999).

[55] P. O. Fedichev and G. V. Shlyapnikov, Phys. Rev. A **58**, 3146 (1998).

[56] S. Giorgini, Phys. Rev. A **61**, 063615 (2000).

[57] M. Rusch, S. A. Morgan, D. A. W. Hutchinson, and K. Burnett, Phys. Rev. Lett. **85**, 4844 (2000).

[58] J. R. Taylor, *Scattering Theory* (Wiley, New York, 1972).

[59] K. Burnett, pg. 265 in Ref. [13].

[60] H. T. C. Stoof, M. Bijlsma, and M. Houbiers, J. Res. Natl. Inst. Stand. Technol. **101**, 443 (1996).

[61] N. P. Proukakis, D. Phil. thesis, University of Oxford (1997).

[62] N. P. Proukakis, K. Burnett, and H. T. C. Stoof, Phys. Rev. A **57**, 1230 (1998).

[63] L. P. Pitaevskii, Zh. Eksp. Teor. Fiz (**40**), 646 (1961) [Sov. Phys. JETP **13**, 451 (1961)]; E. P. Gross, Nuovo Cimento **20**, 454 (1961); E. P. Gross, J. Math. Phys. **4**, 195 (1963).

[64] M. Edwards and K. Burnett Phys. Rev. A **51**, 1382 (1995).

[65] M. Holland and J. Cooper, Phys. Rev. A **53**, R1954 (1996).

[66] Y. Castin and R. Dum, Phys. Rev. Lett. **77**, 5315 (1996).

[67] U. Ernst, J. Schuster, F. Schreck, A. Marte, A. Kuhn, and G. Rempe, Appl. Phys. B **67**, 719 (1998).

[68] M. Edwards, P. A. Ruprecht, K. Burnett, R. J. Dodd, and C. W. Clark, Phys. Rev. Lett. **77**, 1671 (1996).

[69] A. L. Fetter, Phys. Rev. A **53**, 4245 (1996).

[70] K. G. Singh and D. S. Rokshar, Phys. Rev. Lett. **77**, 1667 (1996).

[71] V. M. Pérez-García, H. Michinel, J. I. Cirac, M. Lewenstein, and P. Zoller, Phys. Rev. Lett. **77**, 5320 (1996).

[72] S. Stringari, Phys. Rev. Lett. **77**, 2360 (1996).

[73] W. Hoston and L. You, Phys. Rev. A **53**, 4254 (1996).

[74] H. Wallis, A. Röhrl, M. Naraschewski, and A. Schenzle, Phys. Rev. A **55**, 2109 (1997).

[75] M. R. Andrews, C. G. Townsend, H.-J. Miesner, D. S. Durfee, D. M. Kurn, and W. Ketterle, Science **275**, 637 (1997).

[76] A. Röhrl, M. Naraschewski, A. Schenzle, and H. Wallis, Phys. Rev. Lett. **78**, 4143 (1997).

[77] M. Trippenbach, Y. B. Band, and P. S. Julienne, Opt. Express **3**, 530 (1998).

[78] M. Trippenbach, Y. B. Band, and P. S. Julienne, Phys. Rev. A, **62** 023608 (2000).

[79] D. Guèry-Odelin and S. Stringari, Phys. Rev. Lett. **83**, 4452 (1999).

[80] O. M. Maragó, G. Heckenblaikner, E. Hodby, and C. J. Foot, cond-mat/0101213.

[81] B. Jackson, J. F. McCann, and C. S. Adams, Phys. Rev. A 61, 051603(R) (2000).

[82] H. Wu and C. J. Foot, J. Phys. B **29**, 321 (1996).

[83] M. Holland, J. Williams, K. Coakley, and J. Cooper, Quantum Semiclass. Opt. **8**, 571 (1996).

[84] O. J. Luiten, M. W. Reynolds, and J. T. M. Walraven, Phys. Rev. A **53**, 381 (1996).

[85] C. A. Sackett, C. C. Bradley, and R. G. Hulet, Phys. Rev. A **55**, 3797 (1997).

[86] G. A. Bird, *Molecular Gas Dynamics and the Direct Simulation of Gas Flow* (Clarendon, Oxford, 1994).

[87] C.R. Monroe, E. A. Cornell, C. A. Sackett, C. J. Myatt, and C. E. Wieman, Phys. Rev. Lett. **70**, 414 (1993).

[88] E. A. Uehling and G. E. Uhlenbeck, Phys. Rev. **43**, 552 (1933).

[89] D. W. Snoke and J.P. Wolfe, Phys. Rev. B **39**, 4030 (1989).

[90] Yu. Kagan, B. V. Svistunov, and G. V. Shlyapnikov, Zh. Eksp. Teor. Fiz. **101**, 528 (1992) [Sov. Phys. JETP **75**, 387 (1992)].

[91] M. Holland, J. Williams, and J. Cooper, Phys. Rev. A **55**, 3670 (1997).

[92] M. Yamashita, M. Koashi, and N. Imoto, Phys. Rev. A **59**, 2243 (1999).

[93] J. P. Blaizot and G. Ripka, *Quantum Theory of Finite Systems* (The MIT Press, Cambridge, 1986).

[94] B. V. Svistunov, J. Moscow Phys. Soc. **1**, 373 (1991).

[95] C. W. Gardiner and P. Zoller, Phys. Rev. A **55**, 2902 (1997).

[96] D. Jaksch, C. W. Gardiner, and P. Zoller, Phys. Rev. A **56**, 575 (1997).

[97] C. W. Gardiner and P. Zoller, Phys. Rev. A **58**, 536 (1998).

[98] D. Jaksch, C. W. Gardiner, and P. Zoller, Phys. Rev. A **58**, 1450 (1998).

[99] C. W. Gardiner and P. Zoller, Phys. Rev. A **61**, 033601 (2000).

[100] C. W. Gardiner, P. Zoller, R. J. Ballagh, and M. J. Davis, Phys. Rev. Lett. **79**, 1793 (1997).

[101] C. W. Gardiner, M. D. Lee, R. J. Ballagh, M. J. Davis, and P. Zoller, cond-mat/9801027 (1998).

[102] C. W. Gardiner, M. D. Lee, R. J. Ballagh, M. J. Davis, and P. Zoller, Phys. Rev. Lett. **81**, 5266 (1998).

[103] M. D. Lee and C. W. Gardiner, Phys. Rev. A **62**, 033606 (2000).

[104] M. J. Davis, C. W. Gardiner, and R. J. Ballagh, Phys. Rev. A. **62**, 063608 (2000);cond-mat/9912439

[105] C. W. Gardiner, *Quantum Noise*, (Springer Series in Synergetics Vol. 56, Springer-Verlag, 1991).

[106] C. W. Gardiner, Phys. Rev. A **56**, 1414 (1997).

[107] M. D. Giradeau, Phys. Rev. **113**, 755 (1959).

[108] A. Erdelyi *et al.*, *Higher Transcendental Functions v1* (McGraw Hill, 1955).

[109] M. D. Lee, M.Sc. Thesis, Victoria University of Wellington (1998).

[110] E. Timmermans, P. Tommasini, and K. Huang, Phys. Rev. A **55**, 3645 (1997).

[111] W. H. Press, S. A. Teukolsky, W. T. Vetterling, and B. P. Flannery, *Numerical Recipes in C* (Cambridge University Press, Cambridge, 1992).

[112] O. J. Luiten, M. W. Reynolds, and J. T. M. Walraven, Phys. Rev. A **53**, 381 (1996); M. J. Davis, B.Sc. Honours thesis, University of Otago (1996).

[113] M. Bijlsma, E. Zaremba, and H. T. C. Stoof, cond-mat/0001323; Phys. Rev. A **62**, 063609 (2000).

[114] An eprint server for many fields of physics can be found at `http://arXiv.org`.

[115] E. Zaremba, T. Nikuni and A. Griffin, J. Low Temp. Phys. **116**, 277 (1999).

[116] W. Ketterle, D. S. Durfee and D. M. Stamper-Kurn, pg. 67 in Ref. [13].

[117] P. D. Drummond and J. F. Corney, Phys. Rev. A **60**, R2661 (1999).

[118] M. Holland, K. Burnett, C.W. Gardiner, J. I. Cirac and P. Zoller, Phys. Rev. A **54**, R1757 (1996).

[119] Yu. Kagan and B. V. Svistunov, Zh. Eksp. Teor. Fiz. **105**, 353 (1994) [Sov. Phys. JETP **78**, 187 (1994)].

[120] Yu. Kagan and B. V. Svistunov, Phys. Rev. Lett. **79**, 3331 (1997).

[121] B. Svistunov, cond-mat/0009295.

[122] B. Svistunov, cond-mat/0009368.

[123] K. Damle, S. N. Majumdar, and S. Sachdev, Phys. Rev. A **54**, 5037 (1996).

[124] R. J. Marshall, G. H. C. New, K. Burnett, and S. Choi, Phys. Rev. A **59**, 2085 (1999).

[125] K. Gòral, M. Gajda, and K. Rzążewski, cond-mat/0011165.

[126] G. D. Moore and N. Turok, Phys. Rev. D **55**, 6538 (1997).

[127] J. L. Roberts, N. R. Claussen and J. P. Burke, Jr., C. H. Greene, E. A. Cornell, and C. E. Wieman, Phys. Rev. Lett. **81**, 5109 (1998).

[128] C. A. Sackett, H. T. C. Stoof and R. G. Hulet, Phys. Rev. Lett. **80**, 2031 (1998).

[129] J. M. Gerton, D. Strekalov, I. Prodan, and R. G. Hulet, Nature **408**, 692 (2000).

[130] S. L. Cornish, private communication (2000).

[131] J. L. Roberts, N. R. Claussen, S. L. Cornish and C. E. Wieman, Phys. Rev. Lett. **85**, 728 (2000).

[132] R. A. Duine and H. T. C. Stoof, cond-mat/0007320.

[133] M. Kozuma, L. Deng, E. W. Hagley, J. Wen, R. Lutwak, K. Helmerson, S. L. Rolston, and W. D. Phillips, Phys. Rev. Lett, **82**, 871 (1999).

[134] E. V. Goldstein and P. Meystre, Phys. Rev. A **59**, 3896 (1999).

[135] L. E. Reichl, *A Modern Course in Statistical Physics*, (University of Texas Press, Austin, 1980).

[136] G. A. Williams, J. Low. Temp. Phys. **89**, 91 (1992).

[137] G. Baym, J.-P. Blaizot, M. Holzmann, F. Laloë, and D. Vautherin, Phys. Rev. Lett. **83**, 1703 (1999).

[138] J. M. Kosterlitz and D. J. Thouless, J. Phys. C **6**, 1181 (1972).

[139] M. D. Lee, S. A. Morgan, and K. Burnett, private communication (2000).

[140] Richard D. Mattuck, *A Guide to Feynmann Diagrams in the Many-Body Problem*, 2nd ed. (Dover, New York, 1992).

[141] Philippe Dennery and Andre Drzywicki, *Mathematics for Physicists* (Dover, New York, 1996).

[142] I. S. Gradshteyn and I. M. Ryzhik, Alan Jeffrey, editor, 5th ed. *Table of Integrals, Series, and Products* (Academic Press, London, 1994).

[143] M. Abramowitz and I. A. Stegun, Sec. 25.5, *Handbook of Mathematical Functions* (Dover, New York, 1968)

[144] M. J. Davis, D. A. W. Hutchinson, and E. Zaremba, J. Phys. B, **32**, 3993 (1999).

[145] R. J. Dodd, M. Edwards, C. W. Clark, and K. Burnett, Phys. Rev. A **57**, R32 (1998).

[146] D. A. W. Hutchinson, E. Zaremba, and A. Griffin, Phys. Rev. Lett. **78**, 1842 (1997).

[147] D. A. W. Hutchinson, R. J. Dodd, and K. Burnett, Phys. Rev. Lett. **81**, 2198 (1998).

[148] C. C. Bradley, C. A. Sackett, and R. G. Hulet, Phys. Rev. Lett. **78**, 985 (1997).

[149] P. A. Ruprecht, M. J. Holland, K. Burnett, and M. Edwards, Phys. Rev. A **51**, 4704 (1995).

[150] M. Houbiers and H. T. C. Stoof, Phys. Rev. A **54**, 5055 (1996).

[151] H. T. C. Stoof, Phys. Rev. A **49**, 3824 (1994).

[152] A. Griffin, Phys. Rev. B **53**, 9341 (1996) and references therein.

[153] V. N. Popov, *Functional Integrals and Collective Modes* (Cambridge University Press, New York, 1987), Ch. 6.

[154] H. Shi, G. Verachaka, and A. Griffin, Phys. Rev. B **50**, 1119 (1994).

[155] V. V. Goldman, I. F. Silvera, and A. J. Leggett, Phys. Rev. B **24**, 2870 (1981).

[156] C. A. Sackett, J. M. Gerton, M. Welling, and R. G. Hulet, Phys. Rev. Lett. **82**, 876 (1999).